PHOTO-INDUCED CHARGE TRANSFER REACTIONS IN QUANTUM DOT BASED SOLAR CELLS

Josep Albero Sancho

Dipòsit Legal: T. 729-2012

Ph.D. Thesis

Photo-Induced Charge Transfer Reactions in Quantum Dot Based Solar Cells

Josep Albero Sancho

Supervised by Dr. Emilio Palomares Gil and Dr. Eugenia Martínez Ferrero

(Instituto Catalán de Investigación Química – Universidad Rovira i Virgili)

Tarragona, Noviembre 2011

UNIVERSITAT ROVIRA I VIRGILI

UNIVERSITAT ROVIRA I VIRGILI
PHOTO-INDUCED CHARGE TRANSFER REACTIONS IN QUANTUM DOT BASED SOLAR CELLS
Josep Albero Sancho
Dipòsit Legal: T. 729-2012

Emilio Palomares Gil, Group Leader at the Institute of Chemical Research of Catalonia (ICIQ) in Tarragona, and Research Professor of the Catalan Institution for Research and Advanced Studies (ICREA) in Barcelona, and **Eugenia Martínez Ferrero**, Senior Scientist in CETEMMSA

CERTIFY:

That the present research study, entitled “Photo-Induced Charge Transfer Reactions in Quantum Dot Based Solar Cells” presented by Josep Albero Sancho for the award of the degree of Doctor, has been carried out under our supervision in ICIQ and that he fulfills the requirements to obtain a “European Doctorate Mention”.

Tarragona, Noviembre 2011

Prof. Dr. Emilio Palomares Gil

Dr. Eugenia Martínez Ferrero

ICIQ
Institut Català d’Investigació Química

UNIVERSITAT ROVIRA I VIRGILI

UNIVERSITAT ROVIRA I VIRGILI
PHOTO-INDUCED CHARGE TRANSFER REACTIONS IN QUANTUM DOT BASED SOLAR CELLS
Josep Albero Sancho
Dipòsit Legal: T. 729-2012

"*There is plenty of room at the bottom*"

Richard Feynman

UNIVERSITAT ROVIRA I VIRGILI
PHOTO-INDUCED CHARGE TRANSFER REACTIONS IN QUANTUM DOT BASED SOLAR CELLS
Josep Albero Sancho
Dipòsit Legal: T. 729-2012

UNIVERSITAT ROVIRA I VIRGILI
PHOTO-INDUCED CHARGE TRANSFER REACTIONS IN QUANTUM DOT BASED SOLAR CELLS
Josep Albero Sancho
Dipòsit Legal: T. 729-2012

To whom it may concern

UNIVERSITAT ROVIRA I VIRGILI
PHOTO-INDUCED CHARGE TRANSFER REACTIONS IN QUANTUM DOT BASED SOLAR CELLS
Josep Albero Sancho
Dipòsit Legal: T. 729-2012

ACKNOWLEDGEMENTS

The completion of this project would not have been possible without the invaluable help and support of many people, to only some of whom it is possible to give particular mention here.

Above all, I would like to thank my principal supervisor Dr. Emilio Palomares. This thesis would not have been possible without his help, scientific chats, support and patience. But specially, for all the efforts to convince me to believe in myself. I am also extremely grateful to my second supervisor, Dr. Eugenia Martínez, for the good advice and support. She has been invaluable on both an academic and a personal level.

I would like to thank Toni Sanchez for his helpful discussions during our running sessions. Uncountable times we have forgotten time discussing…whatever. I also want to thank Amparo Forneli to share with me all her invaluable experience, always teaching me in and out of the lab. I cannot forget all the other partners in the group, either first generation with Anna, Miquel, John, Eva…, as the second generation with Laia, Lydia, Ivan, James, Núria, Taye, Margherita, Aurelien, Ma, Bea…Thank you all for your help and for such a friendly environment in the lab.

I am also grateful to Dr. Javier Perez for his help and discussions, as well as for the photophysical characterisation systems. This Thesis would not have been possible without him. I want also to thank Dr. John N. Clifford for his explanations on photophysical characterization, English corrections and research suggestions.

I also want to thank my family for all support and understanding, although from time to time they still ask me “exactly, what is your job about?”. To my friends, they do not even know if this is a real job or not, but anyway they encourage me to continue. And last but not least, I am extremely grateful to Maria. Thank you to the brim for your patience with me, and for your priceless encourage and support. Thank you to make life look so easy.

General Index

UNIVERSITAT ROVIRA I VIRGILI
PHOTO-INDUCED CHARGE TRANSFER REACTIONS IN QUANTUM DOT BASED SOLAR CELLS
Josep Albero Sancho
Dipòsit Legal: T. 729-2012

UNIVERSITAT ROVIRA I VIRGILI
PHOTO-INDUCED CHARGE TRANSFER REACTIONS IN QUANTUM DOT BASED SOLAR CELLS
Josep Albero Sancho
Dipòsit Legal: T. 729-2012

Abstract

Semiconductor nanocrystals, also known as quantum dots, are semiconductor nanostructures with sizes in the range of 1–10 nm, where carrier motion is restricted in all three spatial dimensions. While the bulk semiconductor material, whose size is bigger than its Bohr exciton radius, has energy spectra considered as "continuous", quantum dots present discrete energy states (atom-like) due to the quantum confinement that size restrictions generate in these materials.

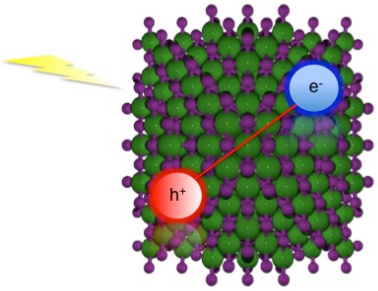

Illustration of a quantum dot with the exciton confined in the nanocrystal. The green dots represent the Cd atoms and the purple dots represent Se atoms.

One of the most striking properties that quantum confinement produces in these materials is the possibility to fine tune the optical properties just by changing the quantum dot size. For example, the absorption and emission spectra of CdSe quantum dots can be tuned through the visible part of the spectrum (500–700 nm), simply by increasing the nanoparticle size from 2 to 6 nm.

The ability to fine tune the absorption spectrum with the particle size makes these nanocrystals very attractive for many applications in the photovoltaics, LED and bio-medicine fields. Moreover, quantum confinement provides another important property for these materials for photovoltaics applications: the possibility of multiple exciton generation. This property could provide solar cells prepared with these materials the possibility to overcome the theoretical efficiency limit proposed by Shockley and Queisser in 1961.

Semiconductor nanocrystals can be synthesised comprising many different materials (CDSe, CdS, PbSe, PbS, ZnS, InP, AsGa, etc.) and morphologies (dots, nanorods, nanofibres, nanoarrows, tetrapods, etc.). Furthermore, there are several

techniques for quantum dot synthesis. However, the most employed in the last decades is the synthesis based on the pyrolysis of organometallic precursors through fast injection in hot coordinating solvents (~300ºC), allowing perfect separation between nucleation and growth. This was proposed by Murray and co-workers in the 1980's. With this methodology a high nanoparticle size control is possible, and it is reproducible, fast and easy to carry out.

For all these reasons, the use of quantum dots in photovoltaics has become widespread in the last decade. Three different architectures have been proposed for quantum dot based photovoltaic devices. The Schottky cell; a variation of the dye sensitised solar cells (Graetzel Cells), where the dye is substituted by quantum dots; and polymer/quantum dot bulk heterojunction solar cells.

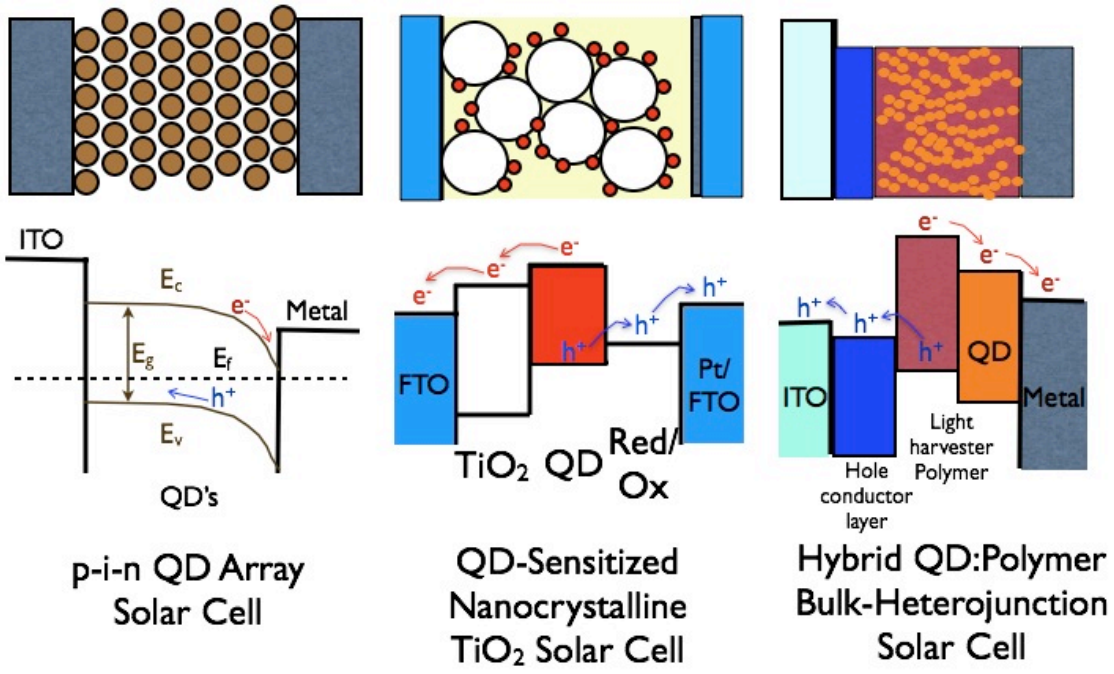

Illustration of the different kinds of quantum dot based solar cells and their main working principles.

All these kinds of devices have attracted much attention during the last years due to the low cost of both materials and production that they present. Many research groups have become interested in this new technology. Indeed, the number of scientific publications in this field has increased considerably. The majority of these reports have focused on obtaining high efficiencies, increasing the light-to-energy conversion by more than 400% for some cases during the last 5 years. Nevertheless, such efficiencies are still low (~4%) if compared with devices with similar architectures using organic materials (~10%) instead of quantum dots. Moreover, little attention has been paid to the study of the interfacial reactions that limit device efficiency. For this reason, a fundamental study of the charge transfer reactions that take place in the device and the understanding of the processes that

limit the device efficiencies under working conditions is necessary to achieve similar efficiencies to the ones observed for similar bulk heterojunction devices containing polymer.

In this Thesis we study the charge recombination dynamics of quantum dot sensitised TiO_2 electrodes and polymer/quantum dot bulk heterojunction films and solar cells.

First of all, we have studied the recombination dynamics at the interface between quantum dots and organic molecules, where the quantum dots act as electron acceptors, and between quantum dots and titania nanoparticles, where the quantum dots act as electron donors. We demonstrate efficient photo-induced charge separation both where the quantum dot acts as electron donor and where they act as electron acceptors. In addition, we observe that the quantum dot size affects the recombination kinetics between quantum dots and titania nanoparticles.

We also studied the effect of the nanocrystal deposition method, as well as the influence of inorganic coatings (ZnS, TiO_2) upon the charge recombination reactions. We employed Transient Absorption Spectroscopy (TAS), a technique previously employed to study the recombination dynamics in dye sensitised solar cells. In our case, we observe, that the deposition techniques which provide higher nanocrystal loads, are the ones with faster recombination kinetics. We also demonstrate, that the addition of such coatings has a positive effect on the recombination kinetics.

Charge transfer reactions in mesoporous titania films co-sensitised with quantum dots and dyes was also investigated. We found clear evidence of the presence of photo-induced charge transfer between quantum dots and dyes, improving hole scavenging and slowing down the recombination kinetics.

We also investigated the charge transfer reactions taking place between quantum dots and a semiconductor polymer (P3HT). We studied the charge separation, and recombination dynamics between the polymer and the quantum dots as a function of the nanocrystal concentration in the polymeric matrix. The use of fluorescence spectroscopic techniques allowed us to observe the charge separation kinetics. This was found to be faster than nanoseconds, independent of the nanocrystal concentration. In addition, the charge separation yield was found to be close to 90% in samples with a 50:50 (w:w) ratio. On the other hand, TAS was used to study the recombination dynamics. We obtained very dispersive dynamics even at low concentrations. Moreover, we observe that the increase in the nanocrystal concentration modifies positively the film morphology, generating

preferential pathways where the electrons can move for long lifetimes through a random walk mechanism.

We investigated the influence of organic molecules (which act as capping ligands on the quantum dot surface) on the charge separation and recombination reactions. We observed that in addition to the dipole moment effects that such molecules produce in the charge transfer reactions, the chemical nature of these molecules produce quantum dot aggregates, and therefore modifications in film nanomorphology, disturbing the pathways that we found to be fundamental to the recombination process.

Another studied aspect is the effect of the nanocrystal structures on the charge transfer reactions. Quantum dots, nanorods and tetrapods were synthesised and mixed with P3HT in different ratios. We observed that although in the elongated structures higher charge separation was achieved compared with the spherical nanocrystals, the charge recombination of these elongated nanostructures was much faster.

Finally, a study of charge recombination in complete devices under working conditions was realised with PCPDTBT polymer : CdSe quantum dot bulk heterojunction solar cells. We found using the charge extraction technique that these devices are able to store an excess of charges exponentially with increasing light bias, as it has been showed for polymer:fullerene bulk heterojunction solar cells. Moreover, from transient photovoltage measurements we found that these devices present non-geminative recombination dynamics as the organic devices also have. However, the carrier lifetime dependency with the charge density in these devices was found to be higher when compared to organic solar cells. We also investigated if the origin of the strong carrier lifetime dependency with the charge density arises from recombination events related with the presence of the metal contacts that these devices use. We observed that the processes that may eventually occur at the electrodes interface are not affecting significantly the dynamics, and are assumed to happen in shorted timer scale, therefore are not observed with the techniques employed along this thesis. Therefore, the origin of the strong dependency of the carrier lifetime was either attributed to superficial defects present in the quantum dots due to the capping molecules or because of trap states present in the crystalline quantum dot surface.

UNIVERSITAT ROVIRA I VIRGILI
PHOTO-INDUCED CHARGE TRANSFER REACTIONS IN QUANTUM DOT BASED SOLAR CELLS
Josep Albero Sancho
Dipòsit Legal: T. 729-2012

UNIVERSITAT ROVIRA I VIRGILI
PHOTO-INDUCED CHARGE TRANSFER REACTIONS IN QUANTUM DOT BASED SOLAR CELLS
Josep Albero Sancho
Dipòsit Legal: T. 729-2012

Chapter 1 - General Introduction

The use of semiconductor nanocrystals with quantum properties in solar photovoltaic devices has attracted great interest in the last 20 years. Such nanocrystal-based photovoltaic devices have usually been labeled as third-generation or "next-generation" photovoltaics. The recent advances in synthetic methods, and the improved knowledge of quantum dot photophysics has opened new possibilities for these inexpensive materials to be incorporated into device structures with potential efficiencies higher than other third-generation photovoltaic devices (dye-sensitized solar cells or organics solar cells). Nevertheless, the still poor understanding of the interfacial charge transfer reactions that take place between the nanocrystals and other materials present in the device has limited the efficiency of these devices up to now.

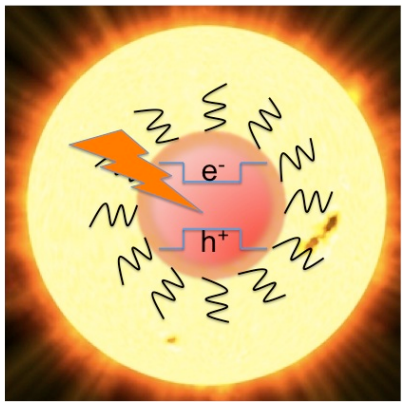

TABLE OF CONTENTS

1 Quantum Dots.

1.1. Characteristics of Semiconductor Quantum Dots.

Quantum dots are a class of quasi-zero-dimensional nanoparticles in which carrier motion is restricted in all three spatial dimensions. The bulk crystalline structure is preserved in the semiconductor nanocrystals, however, due to the three-dimensional quantum confinement of this material, quantum dots have atomic-like discrete energy spectra that are strongly size dependent.[1]

In quantum dots, the boundaries between molecular and bulk regimes are not well defined and are material dependent. A representative scheme of the different electronic energy states of a nanocrystal in the transition from discrete molecules to bulk material is shown in Figure 1. The size regime of the semiconductor nanocrystals take place in a range from hundreds to many thousands of atoms per particle. The lower limit of this range is determined by the stability of the bulk crystalline structure with respect to isomerization into molecular structures. The upper limit corresponds to sizes for which the energy level spacing is approaching the thermal energy kT (T is temperature and k is Boltzmann's constant), meaning that carriers become mobile inside the nanocrystal.[2, 3]

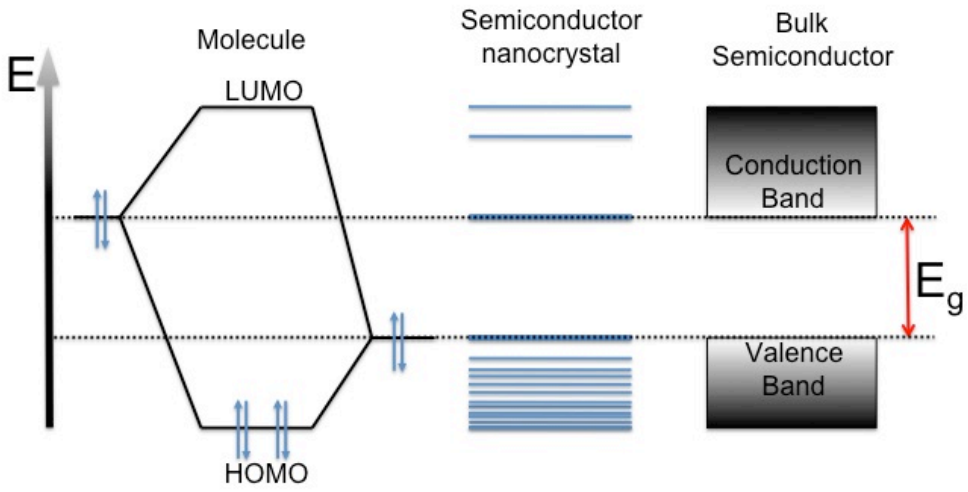

Figure 1. Scheme of the electronic energy states for discrete molecules, nanocrystals and bulk semiconductor materials.

A natural length scale of electronic excitations in bulk semiconductors is given by the Bohr exciton radius (r_{Bohr}) which is determined by the strength of the electron-hole (e – h) Coulomb interaction, which is also called as exciton. In quantum dots with sizes that are comparable to or smaller than r_{Bohr}, the dimensions of the nanoparticles itself define the spatial extent of the e – h pair

state (but not the strength of e – h Coulomb coupling), and hence the size of the spatial confinement of electronic wave-functions, which is known as the "quantum confinement". As the quantum dot size is reduced, the electronic excitations shift to higher energy, and the oscillator strength is concentrated into just a few transitions.[4, 5]

By using this effect, it is possible to continuously tune the quantum dots energy gap (E_g) by more than 1 eV, and so, the optical properties by simply changing nanocrystals dimensions.[6] The change in optical properties as a function of size is one of the most striking properties of semiconductor nanocrystals. The shifts in absorption onset in colloidal prepared II – VI nanocrystals, such as CdS and CdSe, and III – V like InP can be a large fraction of the band gap and can result in tuning across a major portion of the visible spectrum.[7] For example, the band gap in CdSe quantum dots may be tuned from deep red (700 nm) to green (500 nm) by reducing the nanoparticle diameter from 80 to 20 Amstrongs. An example of this is presented in Figure 2.

Figure 2. Digital picture of CdSe colloidal quantum dots prepared at ICIQ of different size illuminated with UV light.

In addition to the tuneable energy gap, another distinct feature of the quantum dot regime is the development of discrete, well separated energy states that replace the continuous energy bands of a bulk semiconductor material, as it have been depicted in Figure 1. In the absence of band mixing effects, each bulk band gives rise to an independent series of quantised states.

An important consequence of strong confinement of the electronic states in quantum dots is a strong enhancement of Coulomb interactions. Not only the exciton binding energy, which provides a measure of the e – h interaction strength, but also the bi-exciton binding energy, which is a measure of the strength of the exciton – exciton interaction. In bulk semiconductors, these energies are inversely proportional to the natural exciton and bi-exciton radius. For instance, in bulk CdSe, the exciton and bi-exciton binding energies are of 16 meV and 4.5 meV,

respectively. In contrast, in semiconductor nanocrystals Coulomb interaction energies become size dependent and for spherical nanoparticles approximately as R^{-1} (R is the quantum dot radius), which leads to a rapid increase of these energies (up to more than 100 meV for exciton and as large as tens of meV in bi-exciton binding energies) with decreasing nanocrystal size.[3]

Besides affecting spectral energies of single and multi-exciton transitions, carrier - carrier interactions have a strong effect on the dynamical behaviour of the e - h system in quantum dots. Specifically, they enhance certain energy relaxation and e - h recombination channels. For example, in bulk semiconductor, where a continuous energy spectrum is present, the electronic states can dissipate energy and cool via emission of phonons. Instead, quantum dots have a quantised spectrum with energy gaps (50-200 meV) greatly exceeding phonon energies (acoustic ~ 2meV, optical ~ 20 meV). Hence, the carrier cooling would be much slower due to the requirement of multi-phonon emission. This phenomena is usually known as the "phonon bottleneck".[8] However, investigations into electron cooling (1P →1S) in high quality colloidal CdSe quantum dots found that as the dots became smaller and the energy gaps larger, the electron cooling rates increased, in direct opposition to expectations from the "phonon bottleneck".[2] Those results could be explained in terms of a new confinement mediated relaxation channel in quantum dots: the Auger relaxation process (Auger recombination). In this process, the e - h recombination energy is not released as a phonon but is instead transferred to a third particle (an electron or hole) that is present in the nanocrystal. In addition to auger recombination, other exciton relaxations mechanisms have been found in quantum dots. For instance, Guyot-Sionnest et al. showed that electron cooling is greatly slowed upon spatially decoupling the hole. In this situation, the electron cooling rate was sensitive to the surface ligands, thereby suggesting some ligand based relaxation channel.[9]

A promising consequence that also arises from the strong carrier - carrier interactions is the possibility of direct photogeneration of multiexcitons by single photons (carrier multiplication), which is the opposite effect to Auger recombination, see Figure 3.[10] Carrier multiplication has been shown to be inefficient in the bulk form to be useful for energy conversion purposes, but an initial proposal in 2001 and several early experimental reports over the past decade have suggested significantly increased carrier multiplication efficiency from nanocrystal materials. If carrier multiplication were to become a very efficient process in nanocrystals, it would led to internal quantum efficiencies in converting light quanta into charge carriers that could greatly exceed 100% (100% is defined as 1 photon creates 1 e - h pair). As an example, it has been published that the

absorption of a single high-energy photon by a PbSe nanocrystal produced up to seven excitons, which corresponds to a quantum efficiency of 700%. Such large yields of charge carriers would have the potential to appreciable improve the performance of photovoltaic cells and could greatly advance solar fuel producing technologies.[3]

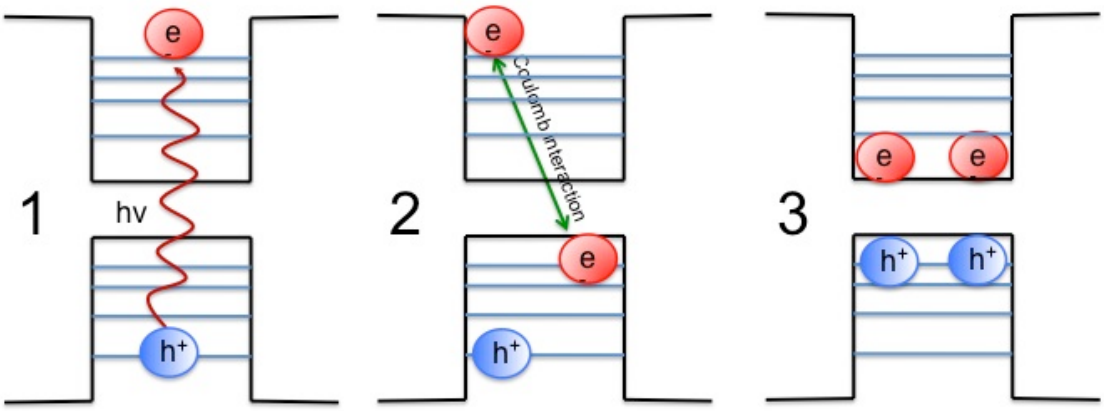

Figure 3. Schematic depiction of carrier multiplication. (1) Electron-hole pair is photogenerated by a photon. (2) An electron in Valence band gets excited via Coulomb interaction leaving a hole. (3) Two excitons have been created by a single photon. The reverse process is referred to be Auger recombination.

However, more recent experimental and theoretical work using improved methods has found carrier multiplication in nanocrystals to be weaker than initially reported. It seems that some of the early high carrier multiplication yield results were likely due to an unrelated non-carrier multiplication signal than can resemble a true carrier multiplication signal.[11] Recently, Bawendi et al. pointed out three main challenges that must be overcome before carrier multiplication in nanocrystals may result in appreciable solar conversion efficiency boosts. First, search for a bulk material which carrier multiplication had a high yield throughout most of the visible spectrum. Then, new methods must be developed to preserve the high carrier multiplication yield from the bulk while boosting the photovoltage via quantum confinement. Finally, solar cell device design and fabrication methods should be developed to effectively translate the increased nanocrystal energy gap E_g into a higher cell photovoltage.[12]

1.2 Optical properties of Semiconductor Quantum Dots.

The unique optical properties of quantum dots are exploited in a large variety of applications essentially in the fields of biological labelling and optoelectronics. In the nanometer size scale many physical properties of the semiconductor nanocrystals change with respect the bulk material. The physical properties of quantum dots, and in particular the optical ones, are strongly size-dependent. For instance, the line-width of the photoluminescence peak is directly related to the

size dispersion of the nanocrystals. Briefly, the most relevant optical properties in nanocrystals semiconductor are discussed.

1.2.1 Absorption.

Absorption of a photon by the nanocrystals occurs if photon energy exceeds the quantum dot energy gap. Due to quantum confinement, decreasing the particle size results in a blue-shift of the absorption onset. A relatively sharp absorption feature near the absorption onset corresponds to the first excitonic peak, which can be correlated to the lowest excited state. While its position depends on the band gap and, consequently, on the particle size, its form and width is strongly influenced by the size distribution, as well as the shape and stoichiometry of the nanocrystals. Therefore poly-disperse samples typically exhibit only a shoulder in the absorption spectrum at the position of the excitonic transition. Less pronounced absorption features in the shorter wavelength range corresponds to excited states of higher energy. It has been observed that the larger the number of such spectral features and the more distinctly they are resolved in the absorption spectrum, the smaller is the size dispersion of the samples.[5, 13] For non-spherical nanocrystals, the excitons in nanorods and in the arms of branched nanocrystals are confined mostly along the diameter since the length often exceeds the exciton radius by several times. In all cases, quantum confinement can enhance the oscillator strength for absorption. Therefore, broad tunability of the band gap within a single-material system (see Figure 4) will enable optimal performances in photovoltaics. In addition, the crystalline nature of these particles imparts a large density of electronic states, yielding huge extinction coefficients and broad absorption spectra that are not possible organic chromophores.[1, 14]

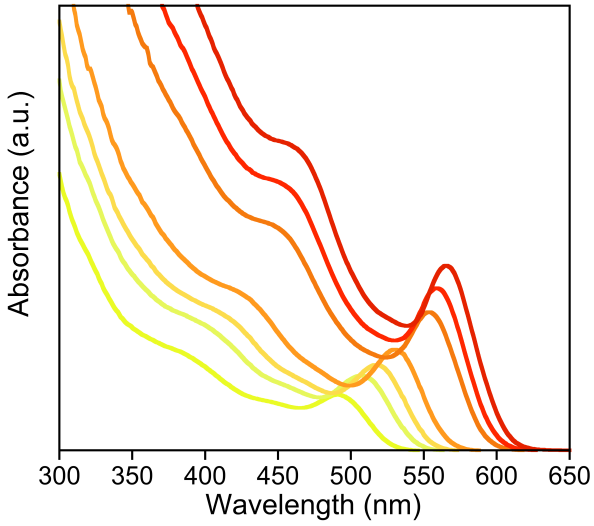

Figure 4. UV-Vis spectrum of colloidal CdSe quantum dots prepared at ICIQ of different sizes in solution (from 2 to 3.5 nm).

In addition of the size-dependent band gap of nanocrystals, due to the quantum confinement there is a second effect: the size-dependent extinction coefficient (ε). The extinction coefficient is a measurement of how strongly a species absorbs light at a given wavelength, per mass unit or per molar concentration, respectively. It is an intrinsic property of the species; the actual absorbance (A) of a sample is dependent on the sample path length (l) and the concentration (c) of the species via the Lambert-Beer law (Equation 1),

$$A = \varepsilon \cdot l \cdot c \qquad \text{(Eq. 1)}$$

The experimental determination of the extinction coefficient has been found to be a non trivial task in semiconductor nanocrystals. However, Xiaogang Peng et al. found empirical fitting functions of the extinction coefficient, which were found to be size dependent. The empirical formulas were obtained for several nanocrystals (CdSe, CdTe and CdS), and they were obtained from two different approaches, obtaining comparable results. The fitting functions are the following ones:

$$\text{For CdTe: } \varepsilon = 3450 \cdot \Delta E \cdot (D)^{2.4}$$

$$\text{For CdSe: } \varepsilon = 1600 \cdot \Delta E \cdot (D)^{3}$$

$$\text{For CdS : } \varepsilon = 5500 \cdot \Delta E \cdot (D)^{2.5}$$

where, ΔE is the transition energy corresponding to the first excitonic peak in eV, and D is the diameter of the nanocrystals.

Therefore, in the case of CdTe, CdSe and CdS nanocrystals, the extinction coefficient of nanocrystals in the quantum confinement size regime increases as their size approximately in a square to a cubic function. The extinction coefficient was found to be independent of the temperature, the nature of the surface capping groups, the refractive index of the solvents, the photoluminescence quantum yield of the nanocrystals and the methods employed for the synthesis of the nanocrystals.[15]

1.2.2 Photoluminescence.

Photoluminescence, which is the process of luminescence generation through excitation by photons, is formally divided into two categories, fluorescence and phosphorescence, depending upon the electronic configuration of the excited state and the emission pathway. In nanocrystals, fluorescence is the property of a

semiconductor to absorb photons with an energy $h\nu_e$ superior to its band gap, and after charge carrier relaxation to the lowest excited state, to emit at a longer wavelength (lower energy $h\nu_f$) after a time interval, called the emission lifetime (τ).

The emitted photons have an energy corresponding to the band gap of the nanocrystals and for this reason the emission colour can be tuned by changing the particle size. For example, CdSe nanocrystals can be tuned through quantum confinement to emit fluorescent light throughout the visible spectrum, making them useful for both biological imaging and many types of optoelectronic devices. The photoluminescence spectra are usually composed by a single-peak. An example of the typical emission spectra in colloidal CdSe quantum dots of different sizes is shown in Figure 5. However, there are many examples in the bibliography where new emission bands, red-shifted with respect to the original ones, can appear. This feature has been explained in terms of emission from trap states in the quantum dot surface.

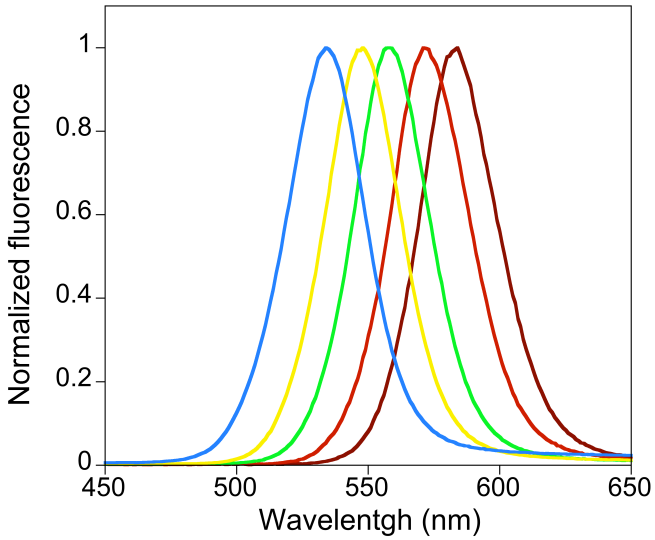

Figure 5. Photoluminiscence spectra of colloidal CdSe quantum dots prepared at ICIQ of five different sizes

The capping ligands can also change the surface properties.[16] They are know to act as hole scavengers which quench photoluminescence of CdSe nanocrystals, varying the emission lifetime and the surface passivation of dangling bonds. Due to spectral diffusion and the size distribution of nanocrystals, the room temperature luminescence line-widths of ensembles lie for the best samples of CdSe quantum dots in the range of 20 – 25 nm (full width at half maximum, FWHM).

In a colloidal quantum dot photoluminiscence spectrum, the maximum of the emission peak are red-shifted by ca. 10 – 20 nm as compared to the first excitonic peak in the absorption spectrum. This phenomenon is usually referred to as Stokes-

shift and has its origin in the particular structure of the exciton energy levels inside the quantum dot.[13]

The fluorescence lifetime decay of quantum dots is one of the most controversial optical properties. Photoluminiscence decay dynamics of colloidal quantum dots differ from those of organic dyes in two important ways. On the one hand, extremely long (tens of nanoseconds at room temperature to microseconds at low temperature) lifetimes are observed; on the other hand, the decays exhibit multiexponential dynamics. These decays dynamics are usually analysed using a de-convoluted fit, which is expressed in Equation 2.

$$F(t) = A + \sum_i B_i \cdot \exp(-t / \tau_i) \qquad \text{(Eq. 2)}$$

, where A and B are constants and τ is the lifetime.

The explanation for the origin of multiexponential emission decay of nanocrystal semiconductors in solution has been studied in detail and ascribed to the trapping sites within the nanocrystals. These surface defects give rise to trap states that lie within the bandgap, and are the responsible of this characteristic emission dynamics.[17, 18] A decay curve of the exciton emission of CdSe quantum dots is showed in Figure 6. The emission decay parameters obtained from fitting of the experimental points to equation 2 and are shown below:

$$F(t) = 0.85 + 0.025 \cdot \exp(\frac{-t}{0.1}) + 0.002 \cdot \exp(\frac{-t}{0.79}) + 0.0004 \cdot \exp(\frac{-t}{3.95}); \chi = 1.1$$

In this case, the Time Correlated Single Photon Counting (TCSPC) technique was used to measure the lifetime decay, with a typical instrument response of 350 ps. However, other studies employing other techniques, with faster resolution, have found up to 5 different decays dynamics from the picosecond to the nanosecond time range.

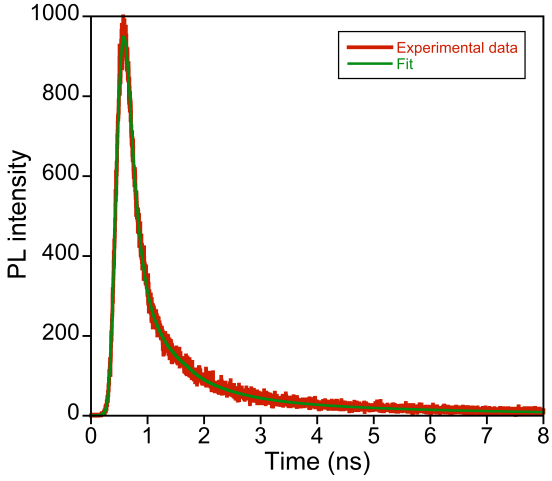

Figure 6. Emission lifetime decay of colloidal CdSe quantum dots prepared at ICIQ.

1.2.3 Other optical properties: The blinking phenomenon and fluorescence quantum yield.

Spectroscopic investigations of single semiconductor nanocrystals revealed that their emission under continuous excitation turns “on” and “off” intermittently. However, detailed understanding of the blinking phenomenon has not yet been achieved. This blinking is a common feature also for other nanostructured materials, like porous Si or epitaxially grown InP quantum dots, as well as chromophores at the single molecule level such as polymer segments or organic dye molecules. However, the origin of the intermittence is completely different for quantum dots and single dye molecules. For the latter resonant excitation into a single absorbing state takes place. Due to spectral shifting events the excitation is no longer in resonance and a dark period begins. On the other hand, quantum dots are excited non-resonantly into a large density of states above the band edge. The sequence of “on” and “off” periods appears randomly on a time scale varying over several orders of magnitude up to minutes and follows temporal statistics described by an inverse power law. Transition from an “on” to an “off” state of the nanocrystal occurs by photo-ionisation, which implies trapping of a charge carrier in the surrounding media (loosing bonds on the surface, solvent, etc.). Since a single delocalized electron or hole still rests in the nanocrystal core, when continuous excitation is applied, this gives rise to fast (nanosecond time scale) non-radiative relaxation through Auger processes. Mechanisms for a return to the “on” state are the recapture of the localised charge carrier into the core or the capture of an opposite charge carrier from traps in the proximity. Both pathways can be accompanied by a reorganisation of the charge distribution around the quantum dot. As a consequence, the local electric field changes leading to a Stark shift of the photoluminescence peak.[13]

Due to the blinking phenomenon the emission efficiency of a nanocrystals population, expressed in terms of the fluorescence quantum yield (Q.Y.), is not close to the theoretical value of 1 due to a certain number of nanocrystals are in “off” states. Furthermore, the Q.Y. may be additionally reduced as a result of quenching caused by surface trap states. As both of these limiting factors are closely related to the quality of the nanocrystal surface, they can be considerably diminished by its improved passivation. Elimination of these traps can be achieved by proper chemical modification of the particle surface. For instance, after substitution of the tri n-octylphosphine oxide (TOPO) cap on CdSe quantum dots by molecules with amine functional groups, an increase of the Q.Y. from about 10% to values of 40 – 50% has been reported.[19]

Nevertheless, in cases where ligand exchange is not desirable, an alternative and suitable method widely applied can be achieved by growing hetero-epitaxially an inorganic passivation shell around the nanocrystals core. The resulting core/shell system not only improves the fluorescence Q.Y. but the stability against photo-oxidation as well by proper choice of the core and shell materials, to tune the emission wavelength in a large spectral window. At the same time, shell growth reduces the number of surface dangling bonds, which can act as trap states for charge carriers and reduce the fluorescence Q.Y. One of the most usual system is ZnS/CdSe. The ZnS shell significantly improves the fluorescence Q.Y. and stability against photo-bleaching. Shell growth is usually accompanied by a small red shift (5-10 nm) of the excitonic peak in the UV-Vis absorption spectrum and the photoluminescence wavelength. This observation is attributed to a light increase in the quantum dot size, therefore, in the quantum confinement.[13]

1.3. Quantum dot Synthesis.

Initiated by pioneering work in the early 1980s, the research on semiconductor nanocrystals went through a remarkable progress after the development of an "easy" chemical synthesis method in 1993, which allowed for the preparation of samples with a low size dispersion. Numerous synthetic methods deriving from the original one[20] have been reported in the literature in the last 20 years. Nowadays, a much better understanding of the influence of the different reaction parameters has been achieved, allowing for the rational design of synthetic protocols. Nonetheless, nanocrystals can be synthesised from a variety of different methods and in several different surroundings as can be seen in the following section.

1.3.1. Quantum Dot Fabrication Procedures.

Fabrication of nanocrystals embedded in a glass matrix by means of diffusion-controlled growth is based on commercial technologies developed for fabrication of colour cut-off filters and photochromic glasses. In this technique nucleation, normal growth and competitive growth are characterised by different activation energies, which makes it possible to obtain crystallites of the same size that have experienced somewhat different growth conditions by a proper choice of the temperature / time combination.

Sol-gel technology offers an alternative way of inorganic glass fabrication that does not include high temperature treatment. Porous glasses developed in this way contain nanometer-size voids that can be impregnated with nanocrystals or dye molecules. However, the sol-gel technique in its present state encounters

serious problems in providing a continuous size control and narrow size distribution. Optical spectra of these systems are usually rather broad because of the wide size distribution.

Semiconductor nanocrystals have been also fabricated in ionic crystals. alkali halide crystals heavily doped with copper were found to contain nano–meter–size copper halide crystallites. Nevertheless, the crystallites developed in this way were found to possess a cubic rather than spherical shape.

Nanocrystals of CdS, PbI_2, and Ge have been fabricated in zeolites. Synthesis of semiconductor clusters inside the cages provides a kind of a quantum dot array consisting of the crystallites with a very sharp size distribution and thus showing rather small inhomogeneous broadening of optical spectra. However, zeolite matrices do not provide any possibility to vary the nanocrystal size. The latter is determined by the cage dimensions. Another problem that prevents a wide application of nanocrystals in zeolites is the very small size of samples. Typically, zeolites are available with no more than 100 μm in all three dimensions.

Composite semiconductor–glass films are used to develop Si and Ge nanocrystals embedded in a SiO_2 matrix. The method is based on a planar magnetron radio frequency sputtering of Si or Ge in a hydrogen or argon environment on a silicon substrate with a thin film of native silicon oxide.

In spite of the rich amount of quantum dot fabrication processes, chemical synthesis allows the fabrication of colloidal nanocrystals with nearly atomic precision. Not only can colloidal quantum dots be prepared in a variety of compositions as nearly spherical particles, elongated nanorods, or nanostructures of other complex shapes such as tetrapods, also by using modern fabrication techniques it is possible to combine in one nanocrystal material of different compositions and, for instance, obtain all–semiconductor heteroparticles or hybrid semiconductor–metal structures. The ability to precisely control quantum dot composition, size, and shape provides great flexibility in engineering the material electronic properties.[5]

1.3.2. The Chemical Method.

Procedures to fabricate nanocrystals have advanced over the past two decades. However, the study of nanocrystals was revolutionised when Murray et al. [20] developed a synthesis based on the pyrolysis of organometallic precursors by injection into a hot coordinating solvent, allowing the separation of the nucleation and subsequent growth steps. The method involved the decomposition of

molecular precursors, for example molecules that deliver the monomers of the nanoparticles, at relatively high temperatures. Precursors are injected swiftly into a hot solvent. Thereby, the monomers are freed quickly leading to a high over saturation of monomers.

The use of organic solvents, over aqueous ones, has the advantage that one can tune the reaction temperature over a wide range, and also in this environment the specific reactants can be exhaustively explored. Temperature and composition of the solvent exert strong influence on the growth kinetics and on the shape of the nanocrystals.[21, 22] Also, through the reaction environment the crystalline phase of the material can be influenced. In general the solvent serves two purposes. The main purpose is to solubilise and disperse the nanocrystals and the reactants involved in the growth. The second is to control the speed of the reaction. To do so, the solvent molecules need to bind and unbind dynamically on the surface of the growing crystals. Once a molecule detaches from the surface of the nanocrystal, it can grow. When referring to these characteristics the solvent can be a mixture of different species, including pure solvent and pure surfactants.

The role of the surfactant is of great interest. The surfactant molecules exhibit two domains, one non-polar, generally a long alkyl chain, and a polar head group. The shape of the non-polar group as well as the binding strength of the polar group influences the growth dynamics. In short, the non-polar tail biases the diffusion properties, whereas the polar head group mainly affects the binding efficiency. Initially, tri-n-octylphosphine oxide (TOPO) and tri-n-octylphospine (TOP) were proposed as surfactants, which are still frequently used. Other types of ligands are phosphonic acids, derived-amines and fatty acids, such as hexylphosphonic acid, hexadecyl amine or oleic acid. A scheme of the structure of the most used ligands is shown in Figure 7.

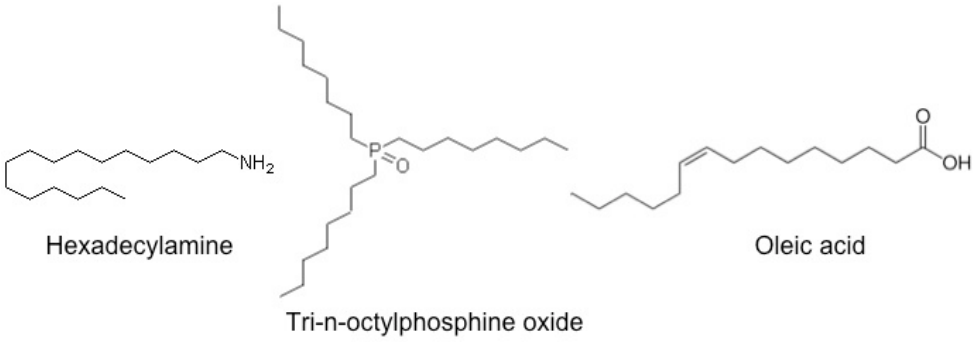

Figure 7. Structures of the most common surfactants employed in quantum dot synthesis.

Most of these compounds are solids at room temperature and melt only at temperatures higher than 50ºC. All these molecules are quite bulky, with a small

anchoring group for bonding onto the surface of nanocrystals and a long hydrocarbon chain. Without rapid dynamics of these bulky surface ligands, it would be difficult to get both the right growth rate and the well-passivated surface of the resulting nanocrystals. Ligands with strong anchoring groups to the surface are known to be not good candidates for synthesising nanocrystals. This is because the anchoring groups would not allow them to be dynamic through a medium-level thermal excitation in the reaction temperature range.[13]

In many cases, the well known TOPO ligand is used in Technical degree (90%). This is due, one the one hand, to the obvious lower price of the reagent compared with the more purified ones (i.e. 99%). On the other hand, it has been reported that beneficial impurities in commercial TOPO (90%) dramatically assist the growth of high-quality colloidal nanocrystals (CdSe). The different impurities enhance the growth of quantum dots, rods, and wires. The di-n-octylphosphine oxide (DOPO) assists the growth of near-isotropic quantum dots; di-n-octylphosphinic acid (DOPA), mono-n-octylphosphinic acid (MOPA) and n-octylphosphonic acid (OPA) assist the growth of rods, and DOPA assists the growth of wires. However, these impurities could have a negative effect when the nanocrystals are used in photovoltaics applications. They could act as electric isolators or hole scavengers, slowing or even avoiding the transport of the carriers between different nanoparticles.[23]

Since Murray et al.[20] reported the synthesis of high quality cadmium chalcogenides nanocrystals using dimethyl cadmium ($Cd(CH_3)_2$) as the cadmium precursor, the synthesis of CdSe nanocrystals using this precursor has been well developed over the other kind of cadmium chalcogenides such as CdTe or CdS. Nonetheless, $Cd(CH_3)_2$ is extremely toxic, pyrophoric, expensive, unstable at room temperature, and explosive at elevated temperatures by releasing large amount of gas. Due to these reasons, the $Cd(CH_3)_2$ based-synthesis required very restricted equipment and conditions and are not suited for large-scale synthesis. Despite the $Cd(CH_3)_2$ precursor, Xiaogang Peng et al.[24] initialised the use of CdO, and they found that this new synthetic scheme worked significantly better than the $Cd(CH_3)_2$ related ones. They identified that $Cd(CH_3)_2$ decomposes in hot TOPO and generates insoluble metallic precipitate. With a strong ligand $Cd(CH_3)_2$ is immediately converted into cadmium complex. After the formation of the complex, an injection of Se dissolved in TBP generates high-quality CdSe nanocrystals. This result implies that $Cd(CH_3)_2$ may not be necessary, if the complex can be generated by other means, for example from $CdCl_2$, $Cd(CH_3COO)_2$ or CdO. High-quality CdSe nanocrystals have been indeed yielded from these complex.

The reactions are usually performed in a three-necked flask connected to a schelenk line with one of the necks, see Figure 8. The remaining two necks are sealed with rubber septa and serve for measurement of temperature inside the flask and for the injection of the reactants. The reaction is carried out under an inert atmosphere, as some of the reactants may be pyrophoric and also some types of nanocrystals may be sensitive to air. After filling the flask with the organic solvent and surfactants molecules, these organic molecules are melted from the solid state to a liquid and the flask is evacuated and kept under vacuum at temperatures between 130ºC -180ºC for 10-20 minutes to remove volatile impurities. This step is crucial for most synthesis. Before starting the actual reaction the flask is flushed with an inert gas (generally nitrogen or argon).

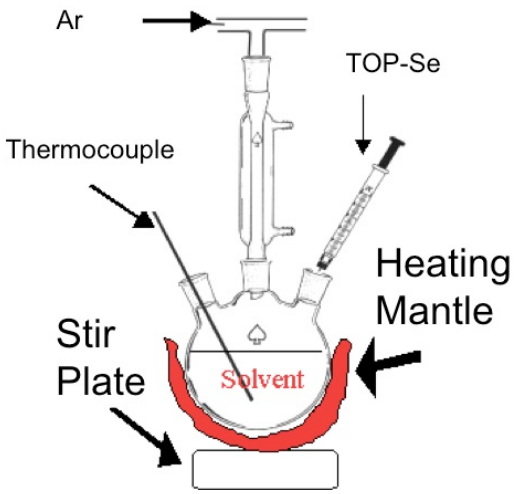

Figure 8. Scheme of the colloidal quantum dot reaction set up.

On the other hand, the reaction monomers can be introduced in many different ways. At least one species should be in the liquid form. Through this, one can determine the start of the formation of nanocyrstals by the quick injection of this compound and thus determine a sharp nucleation event. For the growth of II/VI semiconductor nanocrystals the elemental chalcogens are introduced into the reaction as a complex with either TOP or TBP. The complex is formed by dissolving the chalcogen in liquid TOP or TBP. Generally, for the formation of the complex it is sufficient to simply stir this solution for some minutes. At a temperature close to 300ºC the Cd ions bind to the surfactants. After that, the chalcogen complex is injected and the nucleation sets in shortly after injection.[13]

High-quality nanocrystals have been grown under high temperatures, typically between 250 and 350ºC. These high temperatures could be needed because, on the one hand, this is the only way to maintain a dynamic bonding of the surface ligands at the nanocrystals, “on” and “off” the surface periodically. On the other hand, the high temperature is necessary for the growth of single-

crystalline nanoparticles with desired surface structures. Unfortunately, there are no solid data to support these assumptions although it is a known fact that II–VI and III–V semiconductor nanocrystals synthesised at relatively low temperatures do not show the same optical quality as those grown under high temperatures.

Experimentally, the separation of nucleation and growth can be achieved by rapid injection of the reagents into the hot solvent, which raises the precursor concentration in the reaction flask above the nucleation threshold ("hot–injection method").[25] The hot–injection leads to an instantaneous nucleation, which is quickly quenched by the fast cooling of the reaction mixture (the solution to be injected is at room temperature) and by decreasing supersaturation after the nucleation burst. Another possibility relies on attaining the degree of supersaturation necessary for homogeneous nucleation via the in situ formation of reactive species upon supply of thermal energy ("heating–up method").[26] In an ideal case all crystallisation nuclei are created at the same time and undergo identical growth. During the growth stage it is possible to carry out subsequent injections of precursors on order to increase the mean particle size without deterioration of the narrow size distribution as long as the concentration corresponding to the critical supersaturation is not exceeded.[27]

Crystal growth from solution is in many cases followed by a second distinct growth process, which is referred to as Ostwald ripening. It consists of the dissolution of the smallest particles because of their high surface energy and subsequent redeposition of the dissolved matter onto the bigger ones. Using the hot–injection or heating–up synthesis methods it is possible to obtain samples with 5–10% standard deviation from the mean size without post–preparative size fractionation.[13]

A further modification of the high temperature methods consistes of the appropriate selection of coordinating and non–coordinating solvents, with the goal to determine their influence on the nucleation and growth kinetics of the nanocrystals and to fine–tune the reactivity of the precursors aiming at obtaining a narrow size distribution of the order of 5%. Recently, studies have been undertaken by means of NMR spectroscopy, giving important insight into the chemical reactions occurring during the formation of Cd–chalcogenide quantum dots using the hot–injection method.[28]

1.3.3. Synthesis of Nanocrystals with Different Shapes.

Already in very small nanocrystals different crystalline facets can be identified. Due to the small size of these facets the disposition of only a few atoms

onto one of them changes its nature completely. The shape of a crystal depends on the relative speeds at which the individual facets grow. In this case, the speed of grow of a facet is measured as the speed at which the distance of its centre to the centre of the entire crystal increases. The faster a crystal grows on one facet the more likely to disappear is this facet.

Shape-controlled growth of crystals has been a tough question for the classic theories of crystallisation. The most cited classic model for shape-control is the Wulff facets argument, or Gibbs-Curie-Wulff theorem, which suggests that the shape of a crystal is determined by the relative specific surface energy of each face or facet of the crystals. Moreover, the surface energy depends strongly by the choice of the surfactants. Therefore, following this argument, if the surfactants bind stronger to one face than to its neighbouring face, new monomers are more likely to be incorporated into this neighbouring facets. However, this theorem seems to be not very useful in practice, since this works in thermodynamic equilibrium and the most frequent shape-evolution occurs far away from the thermodynamic equilibrium and must be overcome by the use of high monomer concentrations.[29]

A variety of shapes of CdSe nanocrystals have already been reported in the literature,[21, 30] see Figure 9. It is clear that the concentration of existing monomers in the reaction solution plays a role for the determination and evolution of the shapes of the resulting nanocrystals. For a given solution system, the required monomer concentration in the reaction solution increases in the following order: dots, rice grains, rods and then branched structures. The most thermodynamically stable shape is the dot. By increasing the remaining monomer concentration in the solution, dot-shape nanocrystals can be converted to an elongated shape, and those elongated shapes will evolve to a dot-shape if the remaining monomer concentration is not high enough.

The wurtzite is generally the crystalline structure in CdSe nanocrystals. In the wurtzite structure the choice of the growth axis is relatively straightforward. Through its high symmetry of the unique c-axis is distinguished from the others axes. In CdE (E=S, Te, Se) nanocrystals it serves as the directional axis for the asymmetric growth. But the asymmetric growth is not restricted to materials that display a hexagonal structure. CaF_2 nanorods grow in the cubic fluorite structure. PbSe grows in the highly symmetric cubic rock salt structure, but with the help of bulky surfactants a unique growth direction can be assigned and nanowires are formed.[13]

Shape control of nanocrystals can be achieved by further manipulation of the growth kinetics. The growth of the CdSe nanocrystals with the wurtzite structure is highly anisotropic when the system is kinetically over-driven by an extremely high monomer concentration. Wurtzite CdSe is intrinsically an anisotropic material, and when the overall growth rate is fast, growth is generally faster along this axis. If the overall growth is slow, a nearly spherical, but still faceted, shape that minimises surface area is favoured. If the growth rate is increased, the result is a rod-like faceted shape where the long axis is the c-axis of the wurtzite crystal structure. In order to maintain control of the growth rates in this over-driven regime, it is necessary to change the surfactants that are used.

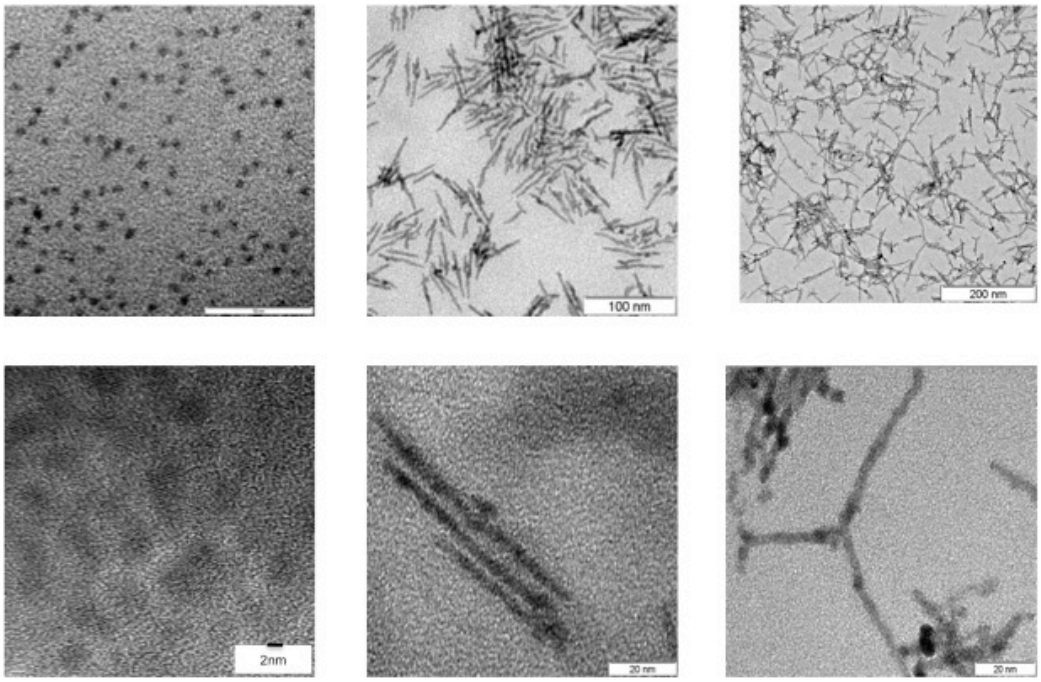

Figure 9. TEM images of CdSe nanocrystals synthesised at ICIQ with different shapes. The images in the left are quantum dots, in the centre nanorods and the images in the right are tetrapods.

Pure TOPO is not a suitable surfactant for growing rod-like CdSe in a controllable manner. Growth in pure TOPO occurs so quickly at the high monomer concentrations desired for the growth of rods that the resulting rod-like particles are often insoluble and too big in all three dimensions. Technical grade TOPO contains additional components, which apparently act to slow the growth. Addition of a molecule that coordinates more strongly than TOPO to cadmium can be used to adjust the growth rate, and hence the shape of the nanocrystals. Phosphonic acids are the most usual ligands used, in addition of TOPO, to control the kinetic growth.

The first works on growing CdSe rods were performed with the organometallic cadmium precursor ($Cd(CH_3)_2$).[31] Nonetheless, recent results imply that organometallic precursors are not necessary. Further, those alternative

precursors generally provide a better control over the shape as they are chemically more stable. The formation of elongated shapes seems not to depend on the nature of the ligand, as long as the ligand can provide a high remaining monomer concentration after the nucleation stage. Further optimisation of the shape control has been achieved in the last years through manipulating the composition of the reaction solvent, the stock solution, the reaction temperature, the injection methods, etc...[32]

A higher level of complexity is observed in branched nanocrystals. An example of such structures is the tetrapod. It is composed of four rods that are fused together in a central core. This shape is observed in several materials, such as ZnO, ZnSe, ZnS, CdSe, CdTe, Pt and Fe_2O_3. Generally, the growth mode of the tetrapods is driven by the same mechanism as the growth of the rods. During growth monomers are deposited onto the high energy facets of the arms, for example on their tips, whereas deposition of monomers onto the lateral facets of the arms is hindered. The main difference in the growth process resides in the nucleation event and the very early stage of the growth, when the core of the tetrapod is formed. There exist two competing models which explain the four arm shape: the octa–twin model and the polymorphism model. To date it is not yet decided which of the models describes the tetrapods the best. In the case of CdE tetrapods there is very little experimental evidence for either of the models. Some experiments seem to point towards the octa–twin model. It is possible to constantly tune the average number of branches in the tetrapod increasing the concentration of a single reactant. This fact can not be explained by the polymorphism model. Therefore we can assume that at least in a synthesis scheme similar to that employed in this kind of branched structures a considerable fraction of the branched nanocrystals is formed according to the octa–twin model.[13]

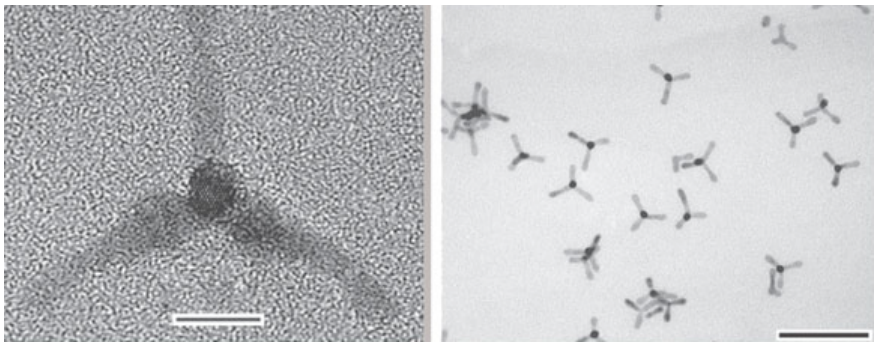

Figure 10. HR-TEM images of CdSe tetrapods from reference 30. The scale bar is 100 nm.

2. Quantum Dots in Molecular Photovoltaics.

2.1. Molecular Photovoltaics. State-of-the-art.

Photovoltaic solar cells are systems which operate absorbing photons from the incident solar radiation and transforming this energy in electric charges. The first photovoltaic devices were based on bulk inorganic semiconductors (for example diffused silicon p–n junction), which were able to create negative electrons and positive holes by absorbing photons with higher energy than the semiconductor energy gap. This bulk semiconductor has a relatively high dielectric constant, and at room temperature the photogenerated charges are uncorrelated and move freely in the conduction and valence bands of the semiconductor. In this case an internal electric field is required to efficiently separate the free electrons and holes, and thus, can be collected at the oppositely charged electrodes. This electric field is commonly produced by a p–n junction in the device. Schottky junctions between a semiconductor and metal or liquid contacts with appropriate work functions differences relative to the semiconductor material can also be used. The main drawback of this devices is the elevated energy consumption necessary to process the inorganic semiconductor, usually crystalline silicon. And therefore, the high production cost that this technology presents.

A second generation solar cells appeared latter in order to reduce the high cost of first generation solar cells by employing thin film technologies. Such technology is based on the reduction of the amount (from hundreds to few microns thick) of material required in creating a solar cell. This technology has enjoyed large investment due to the success of the first generation and the promise of lower cost and flexibility compared to wafer silicon cells, but they have not become mainstream solar products due to their lower efficiency and corresponding larger area consumption per watt production. Cadmium telluride (CdTe), copper indium gallium selenide (CIGS) and amorphous silicon (A–Si) are some of the most common materials used in thin film technologies, where CdTe solar cells are the most cost competitive among them.

Finally, third generation solar cells have recently appeared including dye–sensitized solar cells, organic photovoltaics cells, quantum dot based solar cells, tandem/multijunction cells, intermediate band solar cell, hot–carrier cells, upconversion and downconversion technologies and solar thermal technologies. Traditional solar cells have had several major drawbacks that need to be worked upon to constantly overcome barriers for high performance. Low efficiency and high cost are the foremost factors that are needed to be overcome for a much more robust technology to be in place. For that reason, new solar cells that are less

expensive, flexible, compact, light weight, and efficient are being developed using alternative materials. One example is the use of tandem/multijunction solar cells to generate very high efficiencies. GaAs based multijunction devices are the most efficient solar cells to date. They have reached a record of 42.3%. However, some of the other examples, including organic materials (polymers and conjugated polymers), quantum dots and dye sensitized solar cells, have been proposed as low cost technologies.

One of the fundamental factors for organic materials is that they offer very high possibilities for improving parameters such as charge generation, separation, molecular mass, band gap (determining the ability to harvest light efficiently in different parts of the solar spectrum), molecular energy levels, rigidity and molecule-to-molecule interactions. They are also extremely light weight and flexible making them easy to work with and combine with other molecules. Additionally, these organic materials are compatible with plastics and other flexible substrates; and devices can therefore be fabricated with low cost, high throughput printing techniques that consume less energy and require less capital investment than silicon-based devices and other thin film technologies.[33, 34]

2.2. Organic Photovoltaic Devices.

Organic photovoltaic have become highly popular during the last 20 years. Organic photovoltaics, although not a precise definition, typically summarises the third generation of photovoltaic technologies which contain at least one organic semiconductor or molecule in the active light absorbing layer. The most popular technologies are: dye-sensitized solar cells; all-organic solid-state approaches, such as, small molecule which can be gas phase deposited or solution processed, polymer solar cells and polymer/fullerene solar cells; and the hybrid solar cells, either consisting of inorganic nanoparticles dispersed into a semiconducting polymer matrix or by inorganic nanostructurated semiconductor templates such as ZnO or TiO_2 filled with organic semiconductors.[35] The most popular of those devices will be briefly explained below:

-The interest in dye-sensitized cells has increased considerably since the report from O'Regan and Grätzel in 1991.[36] This photoelectrochemical cell is based on electron transfer from light-excited dye molecules to an inorganic semiconductor with a large band gap. By using nanostructured TiO_2 that has pores on the nanometer scale, enough light can be absorbed to achieve useful efficiencies. These devices have shown efficiencies up to 12% over small areas (< 0.25 cm^2) and 5-8% over somewhat larger areas. A schematic representation of this kind of cell is shown in Figure 11. The device consists of two glass substrates

coated with a transparent conducting oxide such as SnO_2:F (FTO). One of the substrates acts as a photoelectrode, consisting of a porous layer (2 – 20 μm) of a semiconductor, typically TiO_2. A monolayer of sensitising dye is absorbed on to the nanocrystalline oxide film. The second substrate is coated with platinum, which acts as a catalyser, and serves as the counter electrode. In a complete cell, photo- and counter electrode are clamped together and the space between the electrodes and the voids between the TiO_2 particles are filled with an electrolyte containing a redox couple, usually iodide/tri-iodide (I^-/I_3^-) in a non-viscous organic solvent. Photons enter through the photoactive electrode and can be absorbed by sensitiser molecules. These excited molecules inject electrons into the conduction band of the metal oxide nanoparticles, leaving an oxidised molecule on the TiO_2 surface. The injected electrons percolate through the interconnected TiO_2 particles to the substrate and are fed into an electrical circuit, where work can be delivered. The oxidised sensitiser is reduced by the electron donor (I^-) present in the electrolyte. The triiodide produced in this way diffuses to the counter electrode where it is reduced back to iodide by metallic platinum via electrons from external circuit.[34]

Now-a-days, on one hand, great efforts are being done on the substitution of the organic solvents based electrolytes by ionic liquids or solid state redox mediators in order to increase the stability of these devices. On the other hand, a lot of research is being done to find panchromatic dyes that absorb the complete solar spectrum. Other approaches are to increase the light absorption over the complete solar spectrum using dye molecule cocktails, or the substitution of the organic dyes by quantum dots.

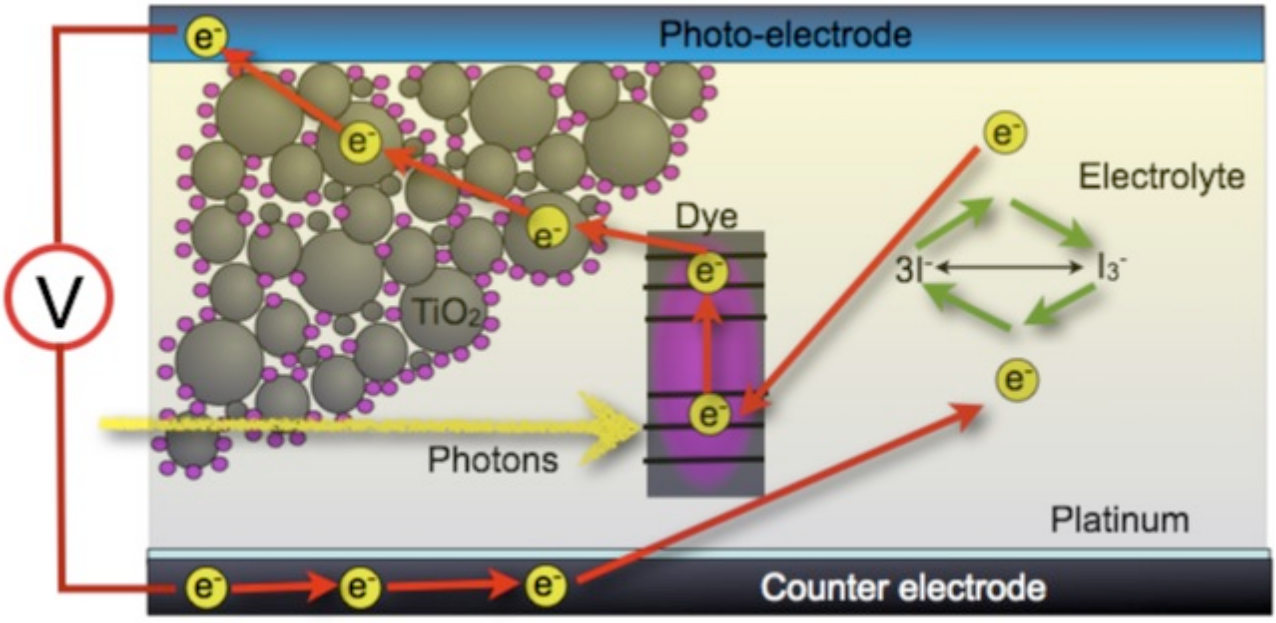

Figure 11. Schematic representation of a dye sensitized solar cell.

–Energy conversion efficiencies of organic photovoltaic cells made from pristine conjugated polymers were typically of the order of 0.001–0.1%, heavily limited by the excitonic nature of conjugated semiconductors. The discovery of photoinduced electron transfer in composites of conjugated polymers and fullerenes provided a molecular approach to achieving higher performances from solution processed systems. For photovoltaic cells made from a bilayer of a conjugated polymer and the electron–accepting fullerene C_{60}, monochromatic energy efficiencies of 1% have been measured. This conversion efficiency is limited due to the small charge–generating regions around the interface. Consequently, interpenetrating phase–separated p–type/n–type network composites, for example, bulk heterojunction, appear to be ideal for photovoltaic composites. By controlling the morphology of the phase separation, so that an interpenetrating network is formed, high interfacial areas can be achieved within a bulk material.[34]

Figure 12 details the processes which influence device performance. In brief, firstly, the incident light (Process 1 in the Figure 12) generates electron–hole pairs at the p–type donor material due to electron transitions from π–HOMO to π*–LUMO bands. The generation of an electron–hole pair (Process 2 in the Figure 12) results in an excited but neutral state with a limited lifetime; this state is termed an exciton and consists of an electron and a hole pair bound by an energy ($E_{ex.}$) similar or higher than the energy gap between the limits of the permitted bands (LUMO and HOMO bands, respectively). The exciton diffuses (Process 3 in the Figure 12) inside the donor material as long as recombination of the hole–electron pair which make up the exciton, called Geminative recombination, do not take place. Föster or Dexter transfers can take place between an excited molecule and a molecule that receives the excitation. If the diffusion length is sufficiently long so that the exciton meets the interface with the acceptor, hole and electron separation may occur. The exciton splitting (Process 4 in the Figure 12) takes place at the donor–acceptor interface, provided the LUMO level of the acceptor is lower than the excitonic state located at the bottom of the conduction band of the donor. The condition which must be fulfilled is that the exciton binding energy should be higher than the difference of the ionisation energy (I_{IP}) of the donor and the electronic affinity (χ_{Ea}) of the acceptor. This energy difference ($I_{IP} - \chi_{Ea}$) is the energy of electron and hole just after the charge transfer at the donor–acceptor interface.

Once the exciton has been dissociated the free charges must travel towards the electrodes (Process 6 in the Figure 12). This transport involves the classic mechanism for hopping processes in organic materials. In this step losses due to trapping carriers or other recombination events (Non–Geminative recombination) that prevent the photo–generated charges reaching the electrodes may happen

(Process 5 in the Figure 12). Finally, the charges that have not been lost on the way are collected at the respective electrodes.

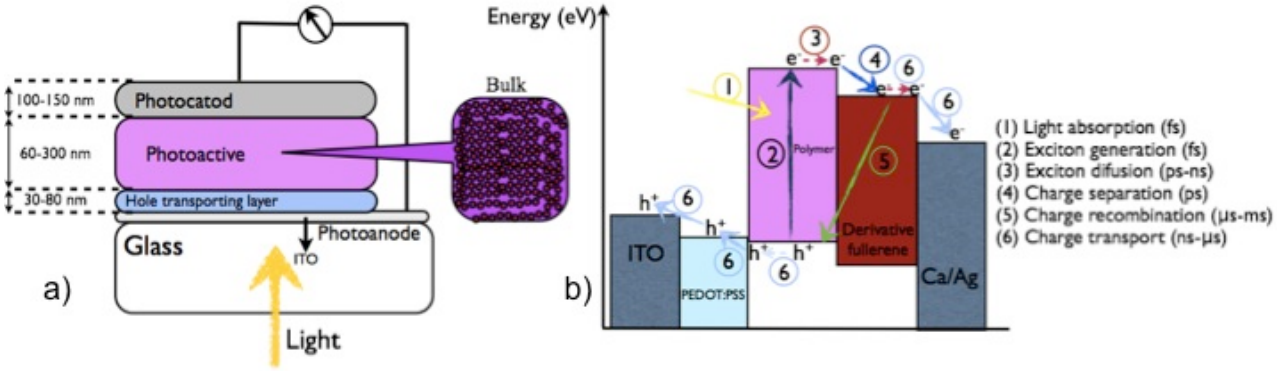

Figure 12. Schematic representation of a) polymer/fullerene bulk heterojunction solar cell and b) an energy diagram of the typical device components with the charge transfer processes.

During the last decade, progress in polymer/fullerene bulk heterojunction solar cells has been so fast that new efficiency records, up to 9%,[37] have frequently appeared in the bibliography. This fast enhancement of the efficiencies has been due, basically, to the development of novel donor materials. The rapid progress with the poly-(3-hexylthiophene) (P3HT) semiconductor polymer platform stimulated the development of new semiconductor polymers based on polyfluorenes (i.e. PFO-DBT or PF10TT) or polycarbazoles (i.e. PCDTBT) . Later, more attention has been paid to low band gap polymers such as poly[2,1,3-benzothiadiazole-4,7-diyl[4,4-bis(2-ethylhexyl)-4H-cyclopenta[2,1-b:3,4-b']dithiophene-2,6-diyl]] (PCPDTBT) or thieno[3,4-c]pyrrole-4,6-dione and dithieno[3,2-b:2',3'-d]silole copolymer (PDTSTPD).

Progress with alternative acceptor materials has not been as visible as for donor polymers. Switching from the C_{60} to C_{70} based fullerenes has proven to give an efficiency improvement for various donors. However, as a main drawback, the fullerene derivatives present high production cost and poor absorption in the solar spectrum region. This has motivated the research of new materials whose production is cheaper and wich contribute to the overall photocurrent in the devices absorbing light in the visible part of the spectrum.[35]

-Hybrid devices incorporating organic and inorganic materials are used due to the prospect of combining the advantages of both types of materials. One class of photovoltaic devices showing particular promise is based on composites of conjugated polymers and semiconducting nanocrystals, including quantum dots. This is due to the recent development of novel polymers, which provide high performance in organic photovoltaics, and the unique optical and electronic properties of inorganic nanocrystals. Quantum dots are materials in which the

crystal dimensions are reduced to the point where quantum confinement of excitations affects the electronic structure of the material. Quantum confinement leads to increasing effects such as a size-dependent optical gap and novel non-linear optical properties. High quality, monodisperse nanocrystals can be prepared by chemical procedures, permitting the electronic to be tuned by varying the size of nanocrystals.[33] In addition, new methodologies, such as synthesis through microfluidics and microwave reactors, have been developed to scale up the quantum dot reactions. CdSe nanoparticles of more definite crystallinity have been synthesised in capillary tubing using high temperatures and surfactants similar to those used for pyrolytic preparations in bulk solutions. Chip-based microreactors, however, are advantageous since "macro"-fabrication systems can be designed to make rapid and complex changes in reaction conditions while retaining superior scalability.[38] In the last years, many companies have appeared which are able to produce colloidal quantum dots with a competitive cost (i.e. Invitrogen, Evident Technologies, PlasmaChem, etc).

Furthermore, metal oxide nanostructures have been also used in combination with semiconductor polymers. Inorganic materials, such us, ZnO, TiO_2, Nb_2O_5, can be synthesised as nanoparticles or nanostructures (i. e. nanowires or nanorods), which provide the device preferential pathways were the electrons and holes can flow. These hybrid polymer:inorganic solar cells can take advantage of the beneficial properties of both types of materials: solution processing of polymer semiconductors and high electron mobility of inorganic semiconductors. It is also well-known that in these kinds of devices the electrodes present an improved stability against moisture. However, these devices have not reached promising efficiencies due basically to the difficult percolation of the semiconductor polymers in the nanostructured electrodes and the non-balanced electron and hole mobilities.[39, 40]

2.3. Quantum Dot Based Solar Cells.

Three different quantum dot based solar cell configurations are under study now-a-days: photoelectrodes composed of quantum dot arrays, quantum dot sensitized solar cells and quantum dots dispersed in organic semiconductor polymer matrices. All these three configurations can be seen in Figure 13.

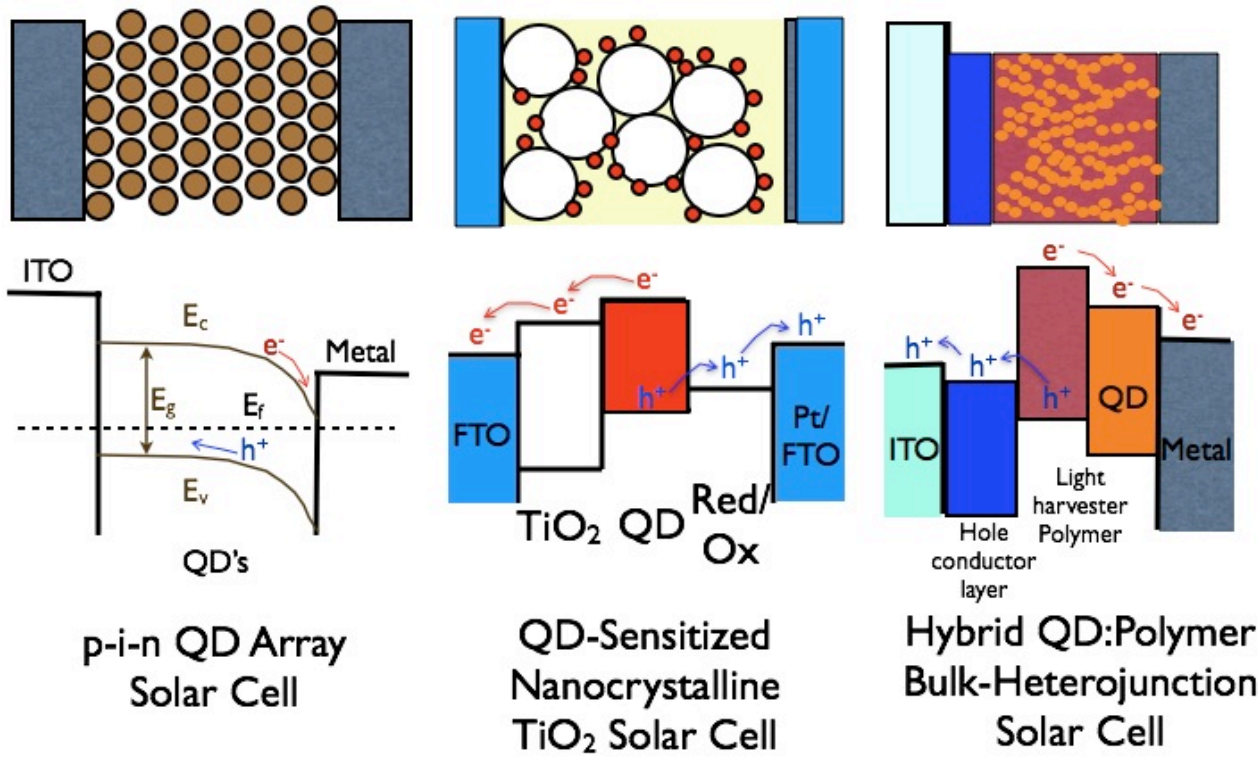

Figure 13. The different QD solar cell configurations (on the top), and the energy diagrams of each one (on the bottom).

2.3.1. Schottky Junction Based Quantum Dot Solar Cells.

The junction between a p-type semiconductor and a low work function metal (Al, Ca, Mg, etc.); or between a n-type semiconductor and a deep work function metal (Au, Pt, etc) forms a Schottky contact. When a semiconductor comes in contact with a metal surface it undergoes Fermi level equilibration. For a bulk semiconductor the conduction and valence bands bend to form a space charge region. The space charge region layer, which is dependent on the carrier density, can extend up to a few microns. When such semiconductor-metal junction is subjected to bandgap excitation the band bending rectifies the flow of photogenerated charge carriers to produce photocurrent in a solar cell.

In a quantum dot array photoelectrode, the semiconductor nanocrystals are formed into an ordered 3-D array with inter-quantum dot spacing sufficiently small such that strong electronic coupling occurs to allow facile electron transport. Several strategies have been used to bring together the nanocrystals, such as, ligand exchange to replace original oleate ligands with much shorter ones or treatment with bidentate thiol molecules. If the nanocrystals have the same size and are aligned, then this system is a 3-D analogue to a 1-D superlattice and the miniband structures formed therein. In the case of semiconductor nanocrystals, band bending occurs only inside the quantum dot film. A depletion region is stablished and the resultant electric field separates electron-hole pairs. Electrons

flow into the metal, and holes to a transparent deep-work-function ohmic contact such as ITO (Indium dopped Tin Oxide) or FTO (Fluor dopped Tin Oxide). The moderately delocalized but still quantised 3-D states could be expected to produce multiple exciton generation. Also, the slower carrier cooling and delocalized electrons could permit the transport and collection of hot carriers to produce a higher photopotential in a photovoltaic cell.[10, 41]

Significant progress has been made in forming 3-D arrays of both colloidal and epitaxial IV-VI, II-VI, and III-V semiconductor nanocrystals. The former systems have been formed via evaporation, crystallization or self-assembly of colloidal quantum dot solutions containing a reasonably uniform quantum dot size distribution. Although the process can lead to a close-packed quantum dot film, they exhibit a significant degree of disorder. Concerning the III-V materials, arrays of epitaxial quantum dot layers have been formed by successive deposition of epitaxial quantum dot layers. Since the first observation of a photovoltaic effect from PbS colloidal quantum dots in 2005, rapid progress has been achieved in this field. The AM1.5G efficiency has now reached 5.5%. Various device architectures, including metal/QD film, oxide/QD film, organic layer/QD film and QD film/QD film have been explored.[42]

While Schottky devices benefit from straightforward fabrication, their efficiency is limited by three factors: First, light absorption begins at the transparent conductive oxide side, requiring that the highest density of photogenerated electrons travel through much of the film thickness before reaching the electron-collecting Schottky contact. These carriers are vulnerable to losses via recombination; Second, for an ideal Schottky junction, the barrier height is typically limited to 0.67 E_g, while practical devices the V_{OC} is often lower because of the Fermi level pinning by defects states at the metal/semiconductor interface; and Third, a minimal barrier to hole injection is present at the electron extracting electrode of the Schottky device, limiting shunt resistance and promoting back recombination.

Depleted heterojunction solar cells have recently been shown to overcome each of the key limitations of the Schottky architecture. In the highest-efficiency colloidal quantum dots reported to date, a p-n heterojunction was formed by bringing together two semiconductors of opposite doping type and generally different composition and bandgap. For efficient dissociation of photogenerated carriers, the donor and acceptor materials should form a type II heterojunction: the electron acceptor (n type material) should have a lower conduction band level while the electron donor (p-type material) should attract holes. Quantum size-effect

tuning provides an added degree of freedom, beyond material composition alone, in the manipulation of the band position of the quantum dots. In addition, multi-junction solar cells made from a combination of quantum dots of different sizes have been recently reported forming tandem solar cells. Using the size-effect tuning of a single colloidal quantum dot material (PbS), and a graded recombination layer to provide a progression of work functions from the hole accepting electrode in bottom cell to the electron accepting electrode in the top cell, allowing matched electron and hole currents to meet and recombine. This tandem solar cell has an open-circuit voltage of 1.06 V, equal to the sum of the two constituent single-junction devices, and a solar power conversion efficiency of up to 4.2%.[42-45]

2.3.2. Quantum Dot Sensitised Solar Cell.

The quantum dot sensitized solar cell configuration is a variation of the promising type of photovoltaic device based on dye-sensitisation of nanocrystalline TiO_2 layers. In this photovoltaic device, as it has been previously explained, dye molecules are chemisorbed onto the surface of TiO_2 nanoparticles that have been sintered into a highly porous nanocrystalline film. Upon photoexcitation of the dye molecules, electrons are efficiently injected from the excited state of the dye into the conduction band of the TiO_2, resulting in charge separation and producing a photovoltaic effect.

In quantum dot sensitized solar cells dye molecules are substituted for quantum dots, but the main device working principle (see section 2.2.) is very similar to dye sensitized solar cells. The use of semiconductor materials as sensitisers comes from the 1990's. However, it has only been in the last years when quantum dot sensitised solar cells have attracted more attention due to the development of technology which has enable the preparation and characterisation of quantum dots and thin layers in a easy way. The experience obtained in the research with dye sensitised solar cells permits the transfer at many of the developments and knowledge in this field to QDSSC.[33, 41]

Nevertheless, further effects such as photoinduced band-edge movement can occur in quantum dot sensitised solar cell, depending on the composition of the cell material. There is a wider variety of materials used in the preparation of quantum dot sensitised solar cells, for example the polysulfide aqueous electrolyte which is used instead of the typical Iodine based electrolyte. The Iodine/Iodide based electrolytes cannot be used in QDSSC due to the corrosive behaviour that iodine has on the quantum dots. Structural differences, exist with DSC such as quantum dot coverage is less than a monolayer. And the lack of ideal counter electrodes for certain electrolytes must be considered to understand the working

principle of a specific quantum dot sensitised solar cell configuration. The pH of aqueous electrolytes shift the band edges of oxide semiconductors, and thus influences the energy–level alignment. Furthermore, the pH can affect the density of surface traps, and electron accumulation in such states can lead to photoinduced band–edge movement, which is not observed with the organic electrolyte containig I^-/I_3^- in dye sensitised solar cells. Furthermore, the quantum dot coverage of the nanostructured electron conductor can affect the recombination kinetics and subsequently the cell performance.[46, 47]

Semiconductor nanocrystal such as CdS, PbS, Bi_2S_3, Sb_2S_3, CdSe and InP which absorb light in the visible part of the solar spectra, can serve as sensitisers as they are able to transfer electrons to semiconductors such as TiO_2, ZnO or SnO_2. Possible advantages of nanocrystals over dye molecules are the facile tuning of effective band gaps down to the IR range by changing their sizes and compositions, efficient exciton multiplication from single absorbed photons, better photostability upon long term irradiation and resistivity toward oxygen and water over molecular counterparts and better heterojunction formation with solid hole conductors.

One of the main advantages of using QDSSC is the fact that the same type of semiconductor can be prepared in many different ways. This offers enormous versatility to the fabrication process. Quantum dots can be absorbed on to the metal oxide surface from colloidal quantum dot solution or produced in situ. In the following sections different techniques to deposit nanocrystals on the metal oxide surface will be described. The properties of the semiconductor material and the final performance of the solar cell depend strongly of the preparation method. Colloidal QD's present good performance but low QD loading, however, growth of QD's in situ confers high semiconductor loading but could lead to higher internal recombination. The preparation method also affects the charge transfer kinetics.[48, 49]

Photoinduced charge transfer reactions in semiconductor nanocrystals have been studied during the past decades. Although the charge relaxation dominates in a nanometer sized semiconductor, the charge separation can be greatly improved by coupling it with another semiconductor particle having favourable energetics. This process has been widely studied in semiconductors such CdS, PbS, Bi_2O_3, CdSe and InP, which absorb light in the visible, because they are able to transfer electrons to large bandgap semiconductors such as TiO_2, ZnO or SnO_2. By controlling the size of the nanocrystals one can vary the energetics of the nanoparticles. Increased band energies of quantum dots can thus be utilised to

promote, suppress or rectify the electron transfer between two semiconductor nanostructures,[50] as can be seen in Figure 14.

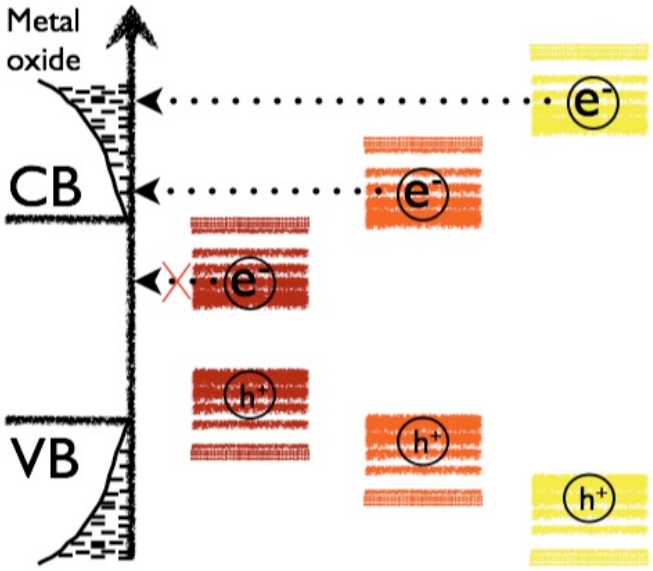

Figure 14. Scheme of the modulation of energy levels (and hence the charge injection) by size control.

Most of the early studies on semiconductor nanocrystals reported were limited to elucidation of the photophysical and photochemical properties of such materials. However, there have been many efforts to study the principal charge transfer reactions in QDSSC: charge separation, charge recombination, charge regeneration and charge transport. A schematic representation of these processes and the time scales of each one is depicted in Figure 15. Quantum dots subjected to bandgap excitation undergo charge separation if the reaction is thermodynamically and kinetically favoured. Efficient charge separation requires that electron injection (Process 3 in Figure 15) must be faster than the excited state decay to ground (Process 2 in Figure 15). The kinetic competition between these two processes is therefore critical. In addition, this reaction only will take place if the alignment of the quantum dot and metal oxide conduction bands is energetically favourable (there must be enough ΔG^{o}). We can find similar scenarios for the rest of the processes. The redox couple must regenerate (Process 6 in Figure 15) the oxidised nanocrystal before electrons from the metal oxide conduction band recombine (Process 4 in Figure 15) and the transport (Process 7 in Figure 15) must be fast enough in order to avoid charge losses (Processes 4 and 5 in Figure 15) before they are collected in the electrodes. The competitions between injection, regeneration, transport and recombination kinetics must remain favourable for efficient conversion efficiency. Therefore, the study of the kinetics and dynamics of reaction of all those processes is one of the main challenges in order to optimise the device configuration and improve the device overall efficiency.

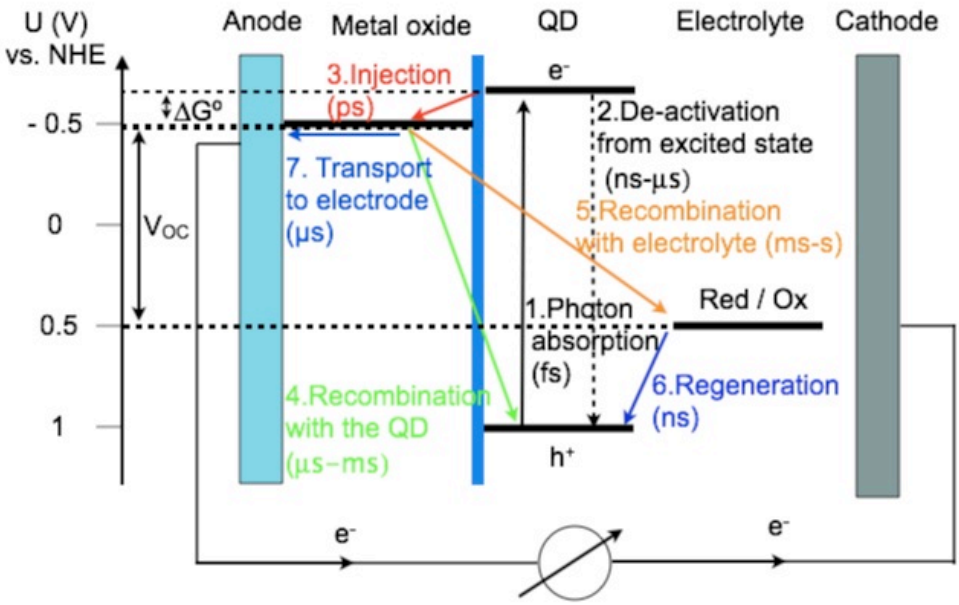

Figure 15. Diagram representing the ideal energetics and kinetics of QDSSC function.

One of the factors that could influence the charge transfer processes is the quantum dot deposition method in the mesoporous metal oxide layer. A brief description of the deposition methods employed in this kind of solar cell is explained below.

2.3.2.1. Successive Ionic-Layer Adsorption and Reaction. SILAR

The successive ionic–layer adsorption and reaction (SILAR) process has been applied for a long time to deposit metal chalcogenides on top of various substrates, and is considered as one of the most effective ways to prepare quantum dot sensitisers on mesoporous metal oxides. The important criteria for making efficient quantum dots sensitisers over mesoporous metal oxide films by in situ deposition are, on the one hand, quantum dots should grow conformally and homogeneously along the surface, without clogging the oxide mesopores, and on the other hand, it should be possible to control the final quantum dot sizes to achieve efficient charge separation from quantum dots to electron and hole acceptors. The flexibility of the SILAR deposition process, including the ability to control the size and distribution density of the deposited nanocrystals by changing precursor concentrations and the number of SILAR cycles, makes it very promising and versatile for general deposition of metal chalcogenide quantum dots directly onto mesoporous substrates. In addition, recent studies have found that the performance of the SILAR process can be improved if it is carried out in alcohol solvents (EtOH or MeOH) , not under the usual aqueous conditions. The low surface tension of the alcohol solvent leads to better penetration into the mesopores with fast removal from mesopores

during drying, which facilitates conformal quantum dot growth along the oxide surfaces and thus results in improved overall efficiencies.

In the SILAR approach dissolved cationic and anionic precursors are in separate vessels. For one deposition cycle the bare nanostructured electrode is dipped into the precursor solution containing the metal cation. After rinsing, the electrode is dipped into the second precursor solution containing the anion, and a second rinsing step completes the deposition cycle. The average quantum dot size can be controlled by the number of deposition cycles, thus, with each SILAR cycle, the nanocrystal deposit became larger in size and denser in distribution. However, the sharp excitonic features observed in colloidal quantum dots are not detected here, reflecting a comparatively broad size distribution in the SILAR-deposited quantum dots. Nevertheless, narrow spectral features are not critical to the performance of these quantum dots in this kind of solar cell.

This method has been used in particular to prepare metal sulfides, but recently it was expanded to metal selenides and tellurides. The SILAR process opens new possibilities for constructing novel structures such as multilayered or hybrid sensitisers. For example the multilayered (CdS)/CdSe/(ZnS)-sensitizers, which have exhibited short-circuit currents comparable to those of dye sensitised solar cells.[51-53]

2.3.2.2. Chemical Bath Deposition. CBD

Chemical bath deposition, is also know as solution growth or controlled precipitation. In the CBD method, the solution chemistry is chosen such that a spontaneous reaction from liquid phase is possible. When the ionic product exceeds the solubility product, precipitation occurs and ions combine on the substrate and in the solution to form nuclei which result in thin film formation on the substrate and the precipitation in the solution.

Chemical bath deposition has been used to deposit quantum dot films of metal sulfides and selenides onto wide bandgap semiconductors. Direct growth is done by immersing the wide bandgap nanostructured electrode (usually a metal oxide) into a solution that contains the cationic and anionic precursors, which react slowly in one bath. For sulfide quantum dots the CBD technique is often based on the slow release of S^{2-} from a precursor such as thiourea. For selenides Na_2SO_3 is commonly used to reduce selenium to form Na_2SeO_3 complex which slowly releases Se^{2-} in the presence of metal cations, for example Cd^{2+} or Pb^{2+}. Compared to the SILAR process, this CBD process for preparing CdSe-modified electrodes is inefficient (takes a few hours or overnight), poorly controlled (in size and density of

the quantum dots) and unselective (not only deposited over the electrode surfaces but also nucleated in bulk solution as well as on the side walls of the deposition container).[46, 48, 49]

2.3.2.3. Linked Assisted Deposition of Colloidal Nanocrystals.

Monodisperse quantum dots are pre-synthesised using capping agents to control nanocrystal shape, size and subsequently the absorption spectrum and luminescence. After synthesis the metal oxide electrode is soaked in a solution of a bifunctional molecular linker (usually (COOH)-R-SH, where R is a short alkyl chain). The carboxyl group attaches to the nanostructured metal oxide film, while the thiol remains free to connect to the quantum dot. The modified film is immersed in the quantum dot solution for adsorption of quantum dot onto the metal oxide electrodes, which typically involves fractional ligand exchange.

Direct adsorption was recently proposed for deposition of monodisperse quantum dots without molecular linkers to the surface of the metal oxide nanostructure. The principle of this method includes solvent/nonsolvent precipitation of quantum dots from the solution onto the mesoporous electrodes. This precipitation process cannot be easily controlled due to the tendency of the quantum dots to agglomerate in solution, leading to uneven and polydisperse coverage by aggregates. In addition, only a low surface of the metal oxide nanostructure coverage of approximately 15% was achieved with this method, and the attachment mechanism remained unclear.[46-49]

2.3.2.4. Electrophoretic Deposition. EPD.

The in situ routes, commonly employed to prepare quantum dots onto nanostructured semiconductor, either CBA or SILAR, provide high surface coverage of quantum dots, with good anchoring to the electrodes, but the control over the size is limited and the size distribution is broad. This problem may be solved by fabricating quantum dot sensitised solar cells with monodisperse quantum dots prepared ex situ. This approach can take advantage of the large developments in controlling the growth of monodisperse and highly crystalline quantum dots of different materials. However, this ex situ growth approach requires, in a second step, facile methods to incorporate the quantum dots onto the electrodes. The most common is use a linker-based approach. This method has two main drawbacks; first, due to the high aspect ratio porosity of the electrode and lack of driving force for deposition, long deposition times are needed (> 8 hours) to achieve reasonable coverage and optical density of the absorbing sensitiser. Second, mostly poor photoelectric responses could be achieved, likely because of the presence of a barrier for electron injection introduced by the linker molecule. A modified ex situ

approach is to employ electrophoretic deposition of semiconductor nanocrystals in mesoporous TiO_2.

EPD was previously employed to deposit semiconductor, metallic, and insulating nonaparticles on conductive substrates and polymers. EPD on the TiO_2 electrodes provides a driving force leading to highly effective quantum dot deposition on the mesoporous metal oxide surface. This allows to shorten the fabrication time considerably, and high coverage is achieved in 2 hours. For EPD of quantum dots the electrodes are soaked in quantum dot solution and a DC voltage is applied for a certain time. This method produce a light broadening of the nanocrystals absorption features upon deposition compared with the solution absorbance, and the band gap of the quantum dots on the electrodes shows slight changes.[54]

2.3.3. Polymer-Quantum Dot Solar Cells.

Bulk heterojunction concept in inorganic/organic hybrid solar cells is similar to that used in organic/organic solar cells. Excitons created upon photoexcitation are separated into free charge carriers at interfaces between two semiconductors in a composite thin film such as a conjugated polymer and fullerene mixture. Electrons will then be accepted by the material with the higher electron affinity (electron acceptor, usually fullerene in the case of organics or inorganic nanocrystal in the case of hybrids), and the hole by the material with the lower ionisation potential, which also acts as the electron donor.

Bulk heterojunctions hybrid solar cells have been demonstrated with various semiconducting polymers (MEH-PPV: poly-2-methoxy, 5-(2'-ethyl)-hexyloxy-p-phenylenevinylene), APFO-3: poly(2,7-(9,9-dioctyl-fluorene)-alt-5,5-(4',7'-di-2-thienyl-2',1',3'-benzothiadiazole), P3HT, PCDTBT, etc blends containing CdSe, $CuInS_2$, CdS or PbS semiconductor quantum dots. These devices are promising for several reasons:[33, 55]

- Inorganic semiconductor nanocrystals have high absorption coefficients and photoconductivity. The well-known fullerene derivative PCBM-C_{60} have good electronic properties, allowing transport of electron towards the electrode very efficiently. However, this fullerene does not present any great absorption feature in the visible range of the spectra, the semiconductor polymer being the only light harvester in this organic photovoltaic solar cell. The substitution of this fullerene with semiconductor nanocrystals may provide efficient light harvesting from 1400 nm to the ultraviolet region.

– The n– or p– type doping level of the nanocrystalline materials can easily be varied by synthetic routes so that, charge transfer in composites of n– or p– type semiconducting materials can be studied. Actually, the same semiconductor nanocrystal (for example CdSe), can act as an light harvester and electron donor in quantum dot sensitized solar cell and also, as an electron acceptor in bulk heterojuntion solar cells. Moreover, electron transport in such nanocrystals is indeed faster (electron mobility of CdSe = 600 $cm^2/V{\cdot}s$) than electron mobility in polymers (the P3HT electron mobility is $1.5{\cdot}10^{-4}$ $cm^2/V{\cdot}s$), which usually have higher hole transport properties (hole mobility in P3HT is $3{\cdot}10^{-3}$ $cm^2/V{\cdot}s$), making semiconductor nanocrystals excellent electron transport materials in hybrid solar cells.[56, 57]

– Band gap tuning in quantum dots with different nanoparticle sizes can be used for realisation of devices architectures, such as tandem solar cells in which the different bandgaps can be obtained by modifying a parameter in the chemical reaction. A substantial interfacial area for charge separation is provided by nanocrystals, which have high surface area to volume ratios.

– The use of solution processable materials provides these devices the capability of large scale at low cost production and the possibility to obtain devices on flexible substrates as for organic photovoltaics.

Molecular photovoltaic devices based on semiconductor quantum dots, as the electron acceptor materials, and semiconductor polymers, as the electron donor, has recently been studied in greater depth. The performance of this type of molecular photovoltaic device is still far from the efficiency of the organic bulk heterojunction solar cell, with record efficiency devices of 4.1% at 1 sun.[58] However, it represents a serious candidate as a top efficient solar cell because it combines many of the properties of the different organic and inorganic photovoltaic devices. Yet, more fundamental studies regarding the control of the blend nanomorphology and understanding of interfacial charge transfer reactions taking place under working conditions are needed to reach similar or higher efficiencies than those of their respective molecular counter–parts.

Initial experiments using hybrid quantum dot polymer thin devices were conducted during the 1990's after the initial observations of efficient charge generation and charge transport in CdS/PVK (PVK: N–polyvinyl carbazole) blends.[59] The initial studies based on the use of induced electrical fields determined that under such high bias conditions, Frenkel excitons were formed in the nanocrystal, and applied fields were necessary to facilitate the separation of closely spaced electron–hole pairs with strong Coulombic attraction. However, such high voltages

are far from the device working conditions usually observed in molecular photovoltaic solar cells, which are typically < 1 V, and thus this preliminary observation had to be revised for efficient devices working under standard sun-simulated irradiation settings (100 mW/cm^2).

In 1996, devices with higher efficiencies were produced by Greenham et al., combining CdS or CdSe nanocrystals with polymer MEH-PPV.[60] A rapid increase in the number of studies of hybrid nanocrystal/polymer devices emerged, establishing a new hot topic for molecular photovoltaic devices, which could be divided into three categories: the study of the different capping agents to achieve different performances, the role of the different crystal nanomorphologies in determining solar cell performance and the interfacial charge transfer reactions between the nanocrystal and the polymer.

The key observation in the seminal paper by Greenham was the effect of the quantum dot capping ligand over the initial charge transfer process between the polymer and the CdSe quantum dots. They observed that electron injection from the polymer to the nanocrystals through a layer of the TOPO ligand, the most widely used organic ligand in the synthesis of quantum dots, did not occur. When the TOPO ligand was removed by treatment with pyridine, efficient electron injection was observed by monitoring the photoluminiscence quenching of the polymer. Moreover, the ratio between the organic hole conductor and the nanocrystal was also studied, and it was found that with a ratio 90 – 95% (wt %) of CdSe versus polymer, the devices internal quantum efficiency was 12%, leading to devices with light-to-energy conversion efficiency of 0.2% when illuminated with sun-simulated solar radiation of 5 mW/cm^2 intensity. This result was also explained in terms of film morphology and the different polymer/nanocrystal phase segregation observed for TOPO and pyridine-capped quantum dots. Although efficient exciton separation was shown at the nanocrystal/polymer interface, the charge transport to the contacts was shown to be poor, and low efficiencies were recorded.

Related to the effect of the ligand capping, in 2006, Cao and coworkers carried out a complete study of different routes to sensitise CdSe nanocrystals capped with oleic acid and observed that the organic solvent used to prepare the hybrid blend was also crucial in obtaining higher device performances.[61] In fact, the CdSe/MEH-PPV solar cell efficiency increased from 0.2 to 0.85% when using toluene or chlorobenzene, respectively. Other groups using the same organic hole conductor polymer but different nanocrystal quantum dot with lower band gaps

such as PbS also showed hindered charge transfer efficiency depending on the alkyl chain length.[62]

The capping ligand, solution conditions, and thermal annealing all influence the phase separation that determines efficient charge separation and charge transport. An extended study with different capping ligands pointed to n-butylamine capped CdSe quantum dots as the best alternative to mix with the polymer P3HT (poly-3-hexylthiophene), followed by annealing at 110ºC to remove the ligands on the quantum dots and the oxygen adsorbed in the polymer. The resulting device showed 1.8% efficiency under standard conditions due to the preferential morphology and short length of the ligand chain.[63]

It is worth noting that other strategies apart from ligand exchange have been developed in order to increase the overall device efficiency. Recent results by Krüger and coworkers have showed that the reduction of the capping ligand sphere by acid treatments to the quantum dots results in better device performance. After this acid washing the CdSe nanocrystals leads to thinner capping spheres that aggregate when mixed with P3HT or PCPDTBT, assisting electron transport and showing better interaction with the polymer. This results in improvement exciton separation, giving efficiencies up to 2.8 % under AM 1.5G 100 mW/cm^2 illumination.[64]

Therefore, it is clear that there is considerable room to engineer strategies that can enhance the charge transfer efficiency to improve exciton separation at the polymer-nanocrystal interface. One example of new approaches consisting of the "in situ" synthesis of the nanocrystals inside the polymer matrix. Such nanocrystals lacking capping organic ligands show similar phase segregation to colloidal quantum dots in which the capping organic ligands have been removed following either annealing or chemical treatment. An example of this approach was presented by Haque and coworkers where CdS nanocrystals are synthesised inside the semiconductor organic polymer matrix, obtaining efficiencies of 2.17% at 1 sun.[65, 66] The nanocrystals are widely distributed within the polymer matrix. However, there is a major concern regarding the amount of nanocrystals obtained within the polymer, since only between 40 and 50 % in weight of the nanocrystals have been obtained, which is sufficient for charge separation but not enough to create the necessary percolation pathways for the charges to be extracted trough the device contacts. In a similar way, the fabrication of PPV/CdTe hybrid solar cells completely from aqueous solution have been recently published. In this case, CdTe quantum dots were synthesised using 2-mercaptoethylamine as a capping ligand, making them water soluble. The monomer of the PPV (poly (p-phenylenevinylene)) polymer,

that is water soluble, was polymerised in the presence of a CdTe quantum dots solution, therefore the formation of the polymer were realised in situ within the quantum dots solution. The devices prepared in this way showed performances of 2.14% at 1 sun.[67]

A first breakthrough in this type of solar cell came with the control of the semiconductor nanocrystal structure on going from quantum dots to nanorods or branched morphologies. Alivisatos and coworkers reported in 2002 the use of a CdSe nanorod blend with the polymer P3HT with power conversion efficiencies under standard conditions of 1.7 %. Moreover, they showed that the control of the nanocrystal shape, from dots to nanorods, as well as the nanocrystal length had an outstanding impact on device performance. The variation of the nanorod radius changes the quantum size effect and thus permits the control of the band gap . The authors reported that the length of the nanorod and its orientation control the electron transport through the device. As the nanorods become longer, the devices display improved 1D transport characteristics and move toward a nanowire regime. In devices containing shorter nanorods (7 nm × 7 nm), the electron transport is dominated by hopping, whereas those with longer nanorods allow the electron transport through band conduction. In fact, the device that contained the longer nanorods, 7 nm × 60 nm, displayed the better performance of 1.7% at 1 sun. Moreover, the authors observed by Transmission Electron Microscopy (TEM) analysis of the device cross-section that the nanorods were partially ordered perpendicularly to the substrate favouring electron transport in the direction of the electrode. However, when longer nanorods were used to increase the electron percolation routes, the authors found it more difficult to solubilise them and thus to disperse them in the polymer. Some strategies using binary solvent mixtures to control the phase separation have been developed to solve this drawback.[68, 69]

The increase in the aspect ratio of the nanorods leads to the construction of branched nanocrystals. This can be done through the control of the surfactant/ inorganic precursor ratio, the injection volume of reactants during the synthesis, and the monomer concentration.[21] These 3D structures influence the charge extraction and transport in the devices by proving larger interfacial contact area and direct pathways for charge collection. The first reported example combined CdSe tetrapods with the polymer MDMO-PPV (poly-2-methoxy-5-(3',7'-dimethyl-octyloxy)-p-phenylenevinylene) and gave 1.8% efficiency at 1 sun.[70] The device showed improved short-circuit external quantum efficiency compared with CdSe nanorod containing devices prepared under the same conditions, which is believed to be due to the existence of favoured electron transport in the film as a consequence of the shape of the tetrapods that are unable to lie flat on the

substrate. The same authors improved the solution processing of the device 2 years later by using a high boiling point solvent (1,2,4-trichlorobenzene, T = 219ºC) that induced the formation of a bilayer with tetrapod-rich composition near the top electrode and a polymer-rich layer near the bottom electrode. This arrangement favours efficient charge collection and extraction, giving an efficiency value of 2.4%.[71] Because of the lack of near-red light absorption (600-700 nm) in the red region of the solar spectrum, the MDMO-PPV polymer was replaced by the red-absorbing poly-fluorene copolymer APFO-3. Although the spectral response was indeed extended to 650nm, with an external quantum efficiency maximum of 44% at 565 nm, the solar power conversion efficiency was still only 2.4%, matching the best results obtained for P3HT where the fill factor was higher.[72]

As had also occurred with the use of dots, the highest improvement in elongated nanocrystal-containing solar cells was achieved through the control of the film postmodification annealing step. The use of high boiling point solvents such as 1,2,4trichlorobenzene in combination with CdSe nanorods allowed efficiencies of up to 2.8% when annealing the film at 150ºC.[73] The high boiling point of the solvent and its extended drying times induced the formation of larger scale polymer structures like fibrils that increase the roughness of the nanocomposite film but most importantly provide pathways for hole transport toward the electrode. Similar observations have been reported when applying vapour annealing treatment using benzene-1,3-dithiol at 120ºC. The annealing step indeed removes the bulky capping ligands, inducing nanocrystal aggregation and phase separation that improves charge collection and transport and yields an overall 2.65% efficiency.[74] Following the results on the use of red absorbing polymers and post-annealing treatment of tetrapod/polymer films, Rumbles and coworkers constructed, using the small-band gap polymer PCPDTBT devices with an external quantum efficiency increase of 55% in the range between 630 and 720 nm, leading an improvement in the final efficiency of 3.13%.[75]

Many other alternative procedures has been carried out in order to obtain more efficient devices. For example, modifying the thiophene units at the polymer terminal, allowing the polymer to bind to the nanorods favouring dispersion and contact between the nanorods and the polymer.[76] However, the device record efficiency recorded up to now has been obtained with CdS quantum dots and crystalline P3HT nanowires. The CdS quantum dots were bounded to the P3HT nanowires through solvent-assisted grafting and ligand exchange, leading to controlled organic-inorganic phase separation and an improved maximum power conversion efficiency of 4.1% under AM 1.5 solar illumination.[58]

Despite the rapid understanding regarding the device efficiency versus morphology, the number of studies on the interfacial charge transfer reactions occurring between the semiconductor polymer and the quantum dots continues to remain small, leaving this area unexplored. Initial experiments using photoinduced absorption spectroscopy (PIA) on MDMO-PPV/CdSe[77] and APFO-3/CdSe[72] systems showed that at low laser intensities, monomolecular charge recombination of long-lived separated species occurs, whereas upon increased laser excitation energies, this process becomes bimolecular. The control of the interface between the nanocrystal and the semiconductor polymer is of great interest since it can modify the dynamics of electron transfer. The fine-tuning of the traps at the surface of the nanocrystals using molecules might prevent or enhance some charge transfer processes.

Because at its simplicity, photoluminiscence spectroscopy has been widely used. Pure conductive polymers such as P3HT or PPV have strong photoluminiscence, and if its intensity is quenched in the presence of nanoparticles, this is an indication for successful transfer of the excited electron to the acceptor material. However, if the absorption spectrum of the acceptor overlaps with the photoluminiscence spectrum of the donor polymer, one cannot conclude from this technique alone, if only the electron is transferred or if the entire electron-hole pair is transferred by Förster resonance energy transfer. Thus, photoluminiscence spectroscopy has become a complement to other spectroscopic techniques, such us PIA, light-induced electron spin resonance (L-ESR) or transient absorption spectroscopy (L-TAS), to study the electron transfer processes.[55]

In addition to the morphology, the dimensionality of the quantum dot electron acceptor also plays a major role in the charge transfer dynamics. Very recently, Dayal and coworkers performed flash photolysis time-resolved microwave conductivity experiments on CdSe nanoparticle/P3HT devices where the nanoparticles were dots, rods, or tetrapods[75] The photoconductivity transients, fitted by multi-exponential functions, revealed significant differences between the different shapes, indicating that the high aspect ratio of nanorods and tetrapods favours charge separation, probably by providing pathways for the electrons to move away from the dissociation site and enhancing the generation of carriers that can survive up to the microsecond time scale. Additionally, the structure of the tetrapods permits that at least one branch stays perpendicular to the substrate, that is, in the direction of electron collection, leading to higher photocurrent and fill factor values than those of the nanorod-containing devices.

The current status of research on polymer/quantum dot bulk heterojunction solar cells demands particular attention to be paid to the elementary processes and limiting factors. Semiconductor nanocrystals have advantages as electron acceptors when compared to fullerene derivatives because of their absorption properties. Furthermore, the possibility to use elongated nanocrystals has demonstrated to have a positive effect on the device performance. Nevertheless, efficiencies reported for hybrid solar cells are still lower than those of state-of-the-art polymer/fullerene solar cells. Studies of charge carrier recombination kinetics are needed to illustrate the role of the surface chemistry of colloidal semiconductor nanocrystals as well as the nanocrystal morphology in the device operational performance. For the future development of the field it is also necessary to obtain a more detailed understanding of the charge transfer processes that limit the device performance under working conditions.

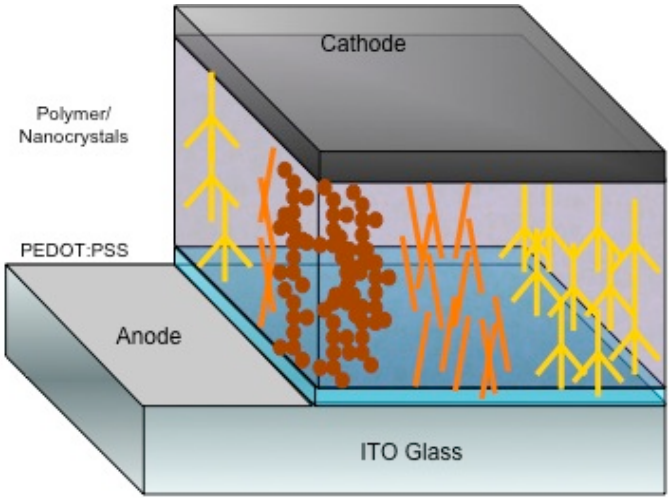

Figure 16. Representation of a polymer-nanocrystal (dot, rods and tetrapods) bulk heterojunction solar cell.

Bibliography.

1. A. P. Alivisatos, *Science*, 1996, **271**, 933-937.
2. V. I. Klimov, *J. Phys. Chem. B*, 2000, **104**, 6112-6123.
3. V. I. Klimov, *J. Phys. Chem. B*, 2006, **110**, 16827-16845.
4. A. L. Efros and M. Rosen, *Annu. Rev. Sci.*, 2000, **30**, 475-521.
5. S. V. Gaponenko, *Optical Properties of Semiconductor Nanocrytals*, Cambridge University Press, Cambridge, 1998.
6. V. I. Klimov, *Annu. Rev. Phys. Chem.* , 2007, **58**, 635-673.
7. D. J. Norris, A. Sacra, C. B. Murray and M. G. Bawendi, *Phys. Rev. Lett.*, 1994, **72**, 2612-2615.
8. P. Kambhampati, *Acc. Chem. Res.* , 2011, **44**, 1-13.
9. P. Guyot-Sionnest, B. Wehrenberg and D. Yu, *J. Chem. Phys.* , 2005, **123**, 074709.
10. A. J. Nozik, M. C. Beard, J. M. Luther, M. Law, R. J. Ellingson and J. C. Johnson, *Chem. Rev.* , 2010, **110**, 6873-6890.
11. M. C. Beard, *J. Phys. Chem. Lett.*, 2011, **2**, 1282-1288.
12. G. Nair, L.-Y. Chang, S. M. Geyer and M. G. Bawendi, *Nano Lett.*, 2011, **11**, 2145-2151.
13. A. L. Rogach, *Semiconductor Nanocrystal Quantum Dots*, SpringerWienNowYork, Wien (Austria), 2008.
14. D. J. Milliron, I. Gur and A. P. Alivisatos, *MRS Bulletin*, 2005, **30**, 41-44.
15. W. W. Yu, L. Qu, W. Guo and X. Peng, *Chem. Mater.*, 2003, **15**, 2854-2860.
16. D. R. Baker and P. V. Kamat, *Langmuir*, 2010, **26**, 11272-11276.
17. M. D. Garrett, M. J. Bowers, J. R. McBride, R. L. Orndorff, S. J. Pennycook and S. J. Rosenthal, *J. Phys. Chem. C*, 2008, **112**, 436-442.
18. K. E. Knowles, E. A. McArthur and E. A. Weiss, *ACSNANO*, 2011, **5**, 2026-2035.
19. S. N. Sharma, H. Sharma, G. Singh and S. M. Shivaprasad, *Mat. Chem. Phys.*, 2008, **110**, 471-480.
20. C. B. Murray, D. J. Norris and M. G. Bawendi, *J. Am. Chem. Soc.*, 1993, **115**, 8706-8715.
21. L. Manna, E. C. Scher and A. P. Alivisatos, *J. Am. Chem. Soc.*, 2000, **122**, 12700-12706.
22. Z. A. Peng and X. Peng, *J. Am. Chem. Soc.*, 2001, **123**, 1389-1395.
23. F. Wang, R. Tang and W. E. Buhro, *Nano Lett.*, 2008, **8**, 3521-3524.
24. Z. A. Peng and X. Peng, *J. Am. Chem. Soc.*, 2001, **123**, 183-184.
25. C. d. M. Donegá, P. Liljeroth and D. Vanmaekelbergh, *Small*, 2005, **1**, 1152-1162.
26. J. Park, J. Joo, S. G. Kwon, Y. Jang and T. Hyeon, *Angew. Chem.*, 2007, **46**, 4630-4660.
27. L. Qu, W. W. Fu and X. Peng, *Nano Lett.*, 2004, **4**, 465-469.
28. R. Gomes, A. Hassinen, A. Szczygiel, Q. Zhaos, A. Vantommes, J. C. Martins and Z. Hens, *J. Phys. Chem. Lett.*, 2011, **2**, 145-152.
29. Z. A. Peng and X. Peng, *J. Am. Chem. Soc.*, 2002, **124**, 3343-3353.
30. Y. Yin and A. P. Alivisatos, *Nature*, 2005, **437**, 664-670.
31. W. U. Huynh, X. G. Peng and A. P. Alivisatos, *Adv. Mater.*, 1999, **11**, 923.
32. X. Peng, *Adv. Mater.*, 2003, **15**, 459-463.
33. S.-S. Sun and N. S. Sariciftci, *Organic Photovoltaics: Mechanisms, Materials, and Devices*, Taylor & Francis Group, United States of America, 2005.
34. C. Brabec, V. Dyakonov, J. Parisi and N. S. Sariciftci, *Organic Photovoltaics: Concepts and Realization*, Springer, Germany, 2003.
35. C. J. Brabec, S. Gowrisanker, J. J. M. Halls, D. Laird, S. Jia and S. P. Willians, *Adv. Mater.*, 2010, **22**, 3839-3856.

36. B. O'Regan and M. Graetzel, *Nature*, 1991, **353**, 737-740.
37. R. F. Service, *Science*, 2011, **332**, 293.
38. E. M. Chan, R. A. Mathies and A. P. Alivisatos, *Nano Lett.*, 2003, **3**, 199-201.
39. W. J. E. Beek, M. M. Wienk and R. A. J. Janssen, *Adv. Func. Mater.*, 2006, **6**, 1112-1116.
40. I. Gonzalez-Valls and M. Lira-Cantu, *Energy Environ. Sci.*, 2009, **2**, 19-34.
41. A. J. Nozik, *Nano Lett.*, 2010, **10**, 2735-2741.
42. J. Tang and E. H. Sargent, *Adv. Mater.*, 2011, **23**, 12-29.
43. X. Wang, G. I. Koleilat, J. Tang, H. Liu, I. J. Kramer, R. Debnath, L. Brzozowski, D. A. R. Barkhouse, L. Levina, S. Hoogland and E. H. Sargent, *Nature Photonics*, 2011, **5**, 480-484.
44. D. A. R. Barkhouse, R. Debnath, I. J. Kramer, D. Zhitomirsky, A. G. Pattantyus-Abraham, L. Levina, L. Etgar, M. Grätzel and E. H. Sargent, *Adv. Mater.*, 2011, **23**, 3134-3138.
45. P. R. Brown, R. R. Lunt, N. Zhao, T. P. Osedach, D. D. Wanger, L.-Y. Chang, M. G. Bawendi and V. Bulovic, *Nano Lett.*, 2011.
46. I. Mora-Seró, S. Gimenez, F. Fabregat-Santiago, R. Gomez, Q. Shen, T. Toyoda and J. Bisquert, *Accounts of chemical research*, 2009, **42**, 1848-1857.
47. I. Mora-Seró and J. Bisquert, *J. Phys. Chem. Lett.*, 2010, **1**, 3046-3052.
48. E. M. Barea, M. Shalom, S. Gimenez, I. Hod, I. Mora-Seró, A. Zaban and J. Bisquert, *J. Am. Chem. Soc.*, 2010, **132**.
49. I. Mora-Seró, S. Giménez, T. Moehl, F. Fabregat-santiago, T. Lana-Villareal, R. Gómez and J. Bisquert, *Nanotechnology*, 2008, **19**, 424007-424014.
50. P. V. Kamat, *J. Phys. Chem. C*, 2008, **112**, 18737-18753.
51. H. M. Pathan, B. R. Sankapal, J. D. Desai and C. D. Lokhande, *Mat. Chem. Phys.*, 2002, **78**, 11-14.
52. H. Lee, M. Wang, P. Chen, D. R. Gamelin, S. M. Zakeeruddin, M. Grätzel and M. K. Nazeeruddin, *Nano Lett.*, 2009, **9**, 4221-4227.
53. H. Lee, H. C. Leventis, S.-J. Moon, P. Chen, S. Ito, S. A. Haque, T. Torres, F. Nüesch, T. Geiger, S. M. Zakeeruddin, M. Grätzel and M. K. Nazeeruddin, *Adv. Func. Mater.*, 2009, **19**, 1-8.
54. A. Salant, M. Shalom, I. Hod, A. Faust, A. Zaban and U. Banin, *ACSNANO*, 2010, **4**, 5962-5968.
55. H. Borchert, *Energy Environ. Sci.*, 2010, **3**, 1682-1694.
56. B. R. Saunders and M. L. Turner, *Advances in Colloid and Interface Science*, 2008, **138**, 1-23.
57. E. v. Hauff, J. Parisi and V. Dyakonov, *Thin Solid Films*, 2006, **511-512**, 506-511.
58. S. Ren, L.-Y. Chang, S.-K. Lim, J. Zhao, M. Smith, N. Zhao, V. Bulovic, M. Bawendi and S. Gradecak, *Nano Lett.*, 2011, **11**, 3998-4002.
59. Y. Wang and N. Herron, *J. Luminiscence*, 1996, **70**, 48-59.
60. N. C. Greenham, X. Peng and A. P. Alivisatos, *Phys. Rew. B: Cond. Matter*, 1996, **54**, 17628-17637.
61. L. Han, D. Qin, X. Jiang, Y. Liu, L. Wang, J. Chen and Y. Cao, *Nanotechnology*, 2006, **17**, 4736.
62. T.-W. F. Chang, S. Musikhin, L. Bakueva, L. Levina, M. A. Hines, P. W. Cyr and E. H. Sargent, *Appl. Phys. Lett.*, 2004, **84**, 4295-4297.
63. J. D. Olson, G. P. Gray and S. A. Carter, *Solar Energ. Mat. & Solar Cells*, 2009, **93**, 519-523.
64. Y. Zhou, F. S. Riehle, Y. Yuan, H.-F. Scheiermacher, M. Niggemann, G. A. Urban and M. Kruger, *Appl. Phys. Lett.*, 2010, **96**, 013304.
65. S. Dowland, T. Lutz, A. Ward, S. P. King, A. Sudlow, M. S. Hill, K. C. Molloy and S. A. Haque, *Adv. Mater.*, 2011, **23**, 2739-2744.

66. H. C. Leventis, S. P. King, A. Sudlow, M. S. Hill, K. C. Molloy and S. A. Haque, *Nano Lett.*, 2010, **10**, 1253-1258.
67. W. Yu, H. Zhang, Z. Fan, J. Zhang, H. Wei, D. Zhou, B. Xu, F. Li, W. Tian and B. Yang, *Energy Environ. Sci.*, 2011, **4**, 2831-2834.
68. W. U. Huynh, J. J. Dittmer and A. P. Alivisatos, *Science*, 2002, **295**, 2425-2427.
69. W. U. Huynh, J. J. Dittmer, W. C. Libby, G. L. Whiting and A. P. Alivisatos, *Adv. Func. Mater.*, 2003, **13**, 73-79.
70. B. Sun, E. Marx and N. C. Greenham, *Nano Lett.*, 2003, **3**, 961-963.
71. B. Sun, H. J. Snaith, A. S. Dhoot, S. Westenhoff and N. C. Greenham, 2005, **J. Appl. Phys.** , 014914.
72. P. Wang, A. Abrusci, H. M. P. Wong, M. Svensson, M. R. Andersson and N. C. Greenham, *Nano Lett.*, 2006, **6**, 1789-1793.
73. B. Sun and C. Greenham, *Phys. Chem. Chem. Phys.*, 2006, **8**, 3557-3560.
74. Y. Wu and G. Zhang, *Nano Lett.*, 2010, **10**, 1628-1631.
75. S. Dayal, N. Kopidakis, D. C. Olson, D. S. Ginley and G. Rumbles, *Nano Lett.*, 2010, **10**, 239-242.
76. J. Liu, T. Tanaka, K. Siluva, A. P. Alivisatos and J. M. J. Frechet, *J. Am. Chem. Soc.*, 2004, **126**, 239-242.
77. M. Pientka, J. Wisch, S. Boger, J. Parisi, V. dyakonov, A. Rogach, D. Talapin and H. Weller, *Thin Solid Films*, 2004, **451-452**, 48-53.

Chapter 2 - Charge Transfer Dynamics in Quantum Dot -TiO_2 Films.

Understanding the charge recombination reactions at the different interfaces in quantum dot sensitised solar cells is key to improving their light-to-energy conversion efficiency. For that reason, we have studied the interfacial recombination kinetics between nanocrystal quantum dots and TiO_2 electrodes. The effect of the quantum dot coating and deposition mode on the charge recombination reactions have been investigated by Laser-Transient Absorption Spectroscopy. Subsequent co-sensitisation with ruthenium molecular dyes of the Quantum Dots-TiO_2 electrodes, even in the presence of inorganic coatings, has been also studied, indicating the presence of photo-induced charge transfer between the quantum dots and the dye molecules.

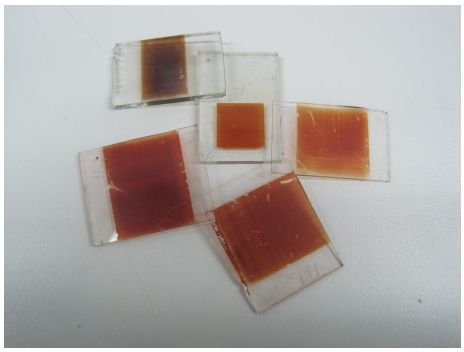

TABLE OF CONTENTS

1. Objectives.

1.- The main objective of this chapter is the study of the charge transfer processes in quantum dot sensitised TiO_2 mesoporous films. This will be carried out by paying attention to the sensitisation process, the addition of passivating layers and the use of hole scavenger dye molecules.

The interfacial charge transfer reactions occurring between the electrons at the TiO_2 nanoparticles and the oxidised quantum dot are of great interest. Since both materials are principal components in quantum dot sensitized solar cells, the understanding and control of these reactions is key to increase the overall device efficiency. Furthermore, charge transfer dynamics in quantum dots used as electron acceptors will be studied as well.

2.- The charge transfer dynamics will be also studied for samples prepared using different deposition methods, including Direct Adsorption (DA), Linked Adsorption (LA), Successive Ionic Layer Adsorption and Reaction (SILAR), Chemical Bath Deposition (CBD) and Electro-phoretic deposition (EPD). Finally, the influence of passivating coatings, such as, ZnS or amorphous TiO_x, on the recombination kinetics for quantum dot sensitised TiO_2 films will be also investigated. It is known that these coatings lead to improvement in device efficiency, the main reasons forthis improvement will be discussed.

3.- The interaction between quantum dots and molecular dyes in co-sensitised mesoporous TiO_2 films will be analysed. The purpose to combine quantum dots and molecular dyes is to increase the spectral absorption range in quantum dot sensitised solar cells and to reduce the internal recombination process in quantum dots. In this case, fast scavenging of photogenerated holes in quantum dots by a molecular dye can balance the competition between electron transfer from quantum dots to TiO_2 and the internal relaxation of the quantum dot excited state, leading to higher electron injection yields. This provides a particularly powerful route to create novel composite heterostructure with enhanced photon to current conversion efficiency.

4.- The kinetics of quantum dot ground state regeneration will be investigated for a specific case. We will study the kinetics of regeneration of iodine/ iodide in the presence of an amorphous titanium dioxide layer as protecting barrier for the nanocrystals.

2. Theoretical considerations.

2.1. Laser-Transient Absorption Spectroscopy

Transient absorption spectroscopy was originally developed by Lord Porter in the 1950s,[1] for which he was awarded the Nobel prize for Chemistry in 1967. This technique can be defined as an elaborate spectrophotometer that is able to detect the spectra of short lived transitory species and their decay kinetics.[2] This technique has been widely employed during the last decade to study charge recombination dynamics in dye sensitized solar cells.[3, 4]

The technique involves the irradiation of a sample with a short light pulse while the sample is continuously illuminated with monochromatic light provided by a probe lamp. The changes in optical density observed in the sample after the short light pulse are recorded using an oscilloscope. This technique provides information not only of the kinetic decay over a wide timescale (from μs to s) of the transient species at single excitation and probe wavelength, but also, the probe wavelength can be changed over a broad range (from 400 to 1000 nm) by the use of a monochromator giving the absorption spectrum of the transient species at a chosen time.

In our case, the data collected is treated using TakeWave(C) software from Costronics Electronics, converting the electrical signal to units of optical density (Δ O.D.) employing Equation 1:

$$\Delta O.D.(t) = -\log\left[\frac{I_{probe}}{I_{ref}}\right] \approx \frac{1}{\ln(10)}\frac{I_{probe} - I_{ref}}{I_{ref}} \approx \alpha \cdot \left[\frac{\Delta V(t)}{V_0}\right] \qquad \text{(Eq. 1)}$$

where $\Delta V(t)$ is the transient signal size which is proportional to the light intensity, V_0 is the DC voltage level, which is proportional to the intensity of the light probe and α is the amplification factor constant, which was set to 0.00174 and depends on the apparatus used. This amplification factor constant was set for our equipment by Dr. Javier Perez.

Transient Absorption Spectroscopy is often employed to elucidate charge transfer kinetics, for example, to study the kinetic competition between different charge transfer processes in molecular photovoltaics. The obtained decays are frequently fitted to a mathematical function which describes the dynamics of the studied charge transfer process. It is well known that in dye sensitized solar cells the recombination dynamics between the electrons in the TiO_2 conduction band and the oxidised dyes follow a Stretch Exponential Function[5] (Equation 2), while in

organic photovoltaics these dynamics are better described by a Power Law Function (Equation 3).[6]

$$y = A \cdot \exp\left(-\frac{t}{\tau}\right)^{\beta} \qquad \text{(Eq. 2)}$$

,where A is a constant, τ is the decay lifetime and β is the stretch exponential factor.

$$y = A(t)^{\alpha} \qquad \text{(Eq. 3)}$$

,where A is a constant and α is the power of the function.

The stretched exponential function is very often used in systems with dispersive relaxation dynamics since the stretch exponential factor is able to describe relaxation in disordered systems efficiently. However, the power law is more related to bimolecular relaxation events. In this, the frequency of relaxations events varies as a power of time of relaxation.

In quantum dot sensitised solar cells it has been found that the dynamics of recombination between the electrons in the TiO_2 conduction band and the holes in the valence band of the quantum dots are usually described by a stretch exponential function.[7] This function is a modification of the exponential function with one additional parameter, the stretching exponent (β). In physics, the stretched exponential is often used as a phenomenological description of relaxation in disordered systems. With $\beta = 1$, the usual mono-exponential function is recovered. The compressed exponential function (with $\beta > 1$) has less practical importance, with the exception of $\beta = 2$, which gives the normal distribution. However, in this case, the stretching exponent β will be in the range $0 < \beta < 1$. The physical meaning of $\beta < 1$, in our systems, arises from global relaxation of a system which contain independently exponential relaxing species with different probability distribution of relaxation rates. In other words, the stretching factor will give us an idea of the dispersive of the system, indicating that the recombination process comes from multiple and different pathways.

2.2. Quantum Dot Size Estimation.

The quantum dot size can be determined either by Transmission Electron Microscopy (TEM) or by means of sizing curves using their first excitonic peak positions, which are obtained from literature values or determined by TEM. These curves can be expressed as empirical fitting functions. We have selected the empirical fitting function (Equation 4) proposed by Xiaogang Peng and coworkers[8] to estimate the colloidal CdSe quantum dot size:

$$D = \left(1.6122 \times 10^{-9}\right)\lambda^4 - \left(2.6575 \times 10^{-6}\right)\lambda^3 + \left(1.6242 \times 10^{-3}\right)\lambda^2 - \left(0.4277\right)\lambda + \left(41.57\right) \quad \text{(Eq.4)}$$

,D (nm) is the quantum dot estimated size and λ (nm) is the wavelength of the last excitonic absorption peak of the CdSe quantum dot.

3. Experimental section.

Either quantum dots or the quantum dot sensitised films were always prepared at ICIQ unless otherwise stated in this thesis.

The colloidal CdSe quantum dots were prepared by the traditional hot-injection method.[7] In brief, 0.4 g of Se powder (99.99%) was solved in 10 mL Tri-Octylphosphine (TOP) (90%) and 0.2 mL of anhydrous Toluene. On the other hand, 20 g of Tri-Octylphosphine Oxide (TOPO) (90%) and 0.25 g of Cadmium acetate (97%) were placed in a three-necked flask. At certain temperature the Se solution was quickly added to the Cadmium solution. The reaction must be carried out at different temperatures and reaction times depending on the desired quantum dot size. For example, the biggest colloidal CdSe quantum dots were synthesised at 290ºC for 15 minutes, however, the smallest are synthesised at 250ºC for 1 minute. After synthesis the nanocrystals were precipitated in methanol and recovered by centrifugation. The nanocrystals were re-dispersed in chloroform and precipitated in methanol again. This cleaning procedure was repeated 3 times to ensure complete elimination of the capping ligand excess .

The CdS and CdSe nanocrystals deposited by SILAR were prepared following the procedure described by Yi-Siou Lo and collaborators.[9] In this, ethanol solution containing $Cd(NO_3)_2$ (0.5 M) and methanol solution of Na_2S (0.5 M) were used to deposite the CdS nanocrystals. For the CdSe deposition, sodium selenosulphate was used as Se source (0.3 M) in water, and ethanol solution containing $Cd(NO_3)_2$ (0.5M) for the Cd^{+2}. The PbS nanocrystals were prepared following the Md. K. Nazeeruddin and coworkers protocol. In brief, two methanol solutions were prepared containing $Pb(NO_3)_2$ and Na_2S at 0.02 M concentrations.[10]

The ZnS coating were prepared dipping twice alternatively into 0.1 M Zn $(CH_3COO)_2$ and Na_2S solution for 1 minute.[11]

The TiO_2 films were prepared from Titanium dioxide paste purchased in Dyesol(R). The paste was deposited on pre-cleaned substrates by Doctor Blade technique and annealed at 500ºC. The area of the films was usually 1 cm^2, and the film thickness was 4 µm, unless otherwise was stated.

The photophysical characterisation has been carried out using L-TAS. The excitation source used was a PTI GL-3300 Nitrogen Laser, which produced pulses at a wavelength of 337 nm with an energy of 1.45 mJ. The pulse is controlled by a TG330 function generator from Thurlby Thandar Instruments(c) at 1 Hz. A PTI GL-301 dye laser head is used in conjunction with the nitrogen laser to provide a

variable source of excitation wavelength, from 360 to 750 nm. A PTI 150W tungsten lamp is used as the probe light source. The probe light from the lamp is selected by using a monochromator. A second monochromator is used after the sample to reduce the noise from laser light scattering. The optical detector is based on a silicon photodiodide, which transform the optical signal into an electrical signal. This electric signal is amplified and filtered by an electronic system provided by Costronics(c). Finally, the signal acquisition is carried out by a TDS 2022 oscilloscope from Tektronix electronics(c).

The set up is shown in Figure 1. The sample is placed between the monochromators with a sample holder. The laser pulse hits the sample with an 45º angle respect the probe light direction. The absorption spectra of transient species can be measured changing the probe wavelength and recording the signal intensity at a particular time delay. Once the transient absorption spectrum is measured, the transient kinetic decay can be measured at its maximum.

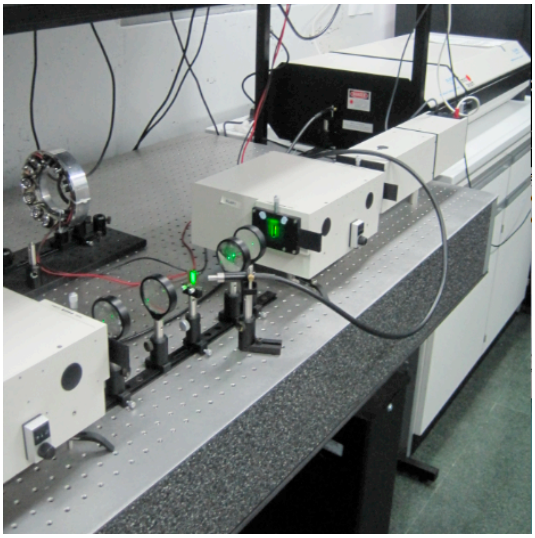

Figure 1. Digital photography of ICIQ L-TAS system used in this Ph.D.

A more complete description of the signal treatment can be found in the annexes.

A typical transient spectrum of the dye molecule N719 onto TiO_2 at t = 0.5 ms is represented in Figure 2.

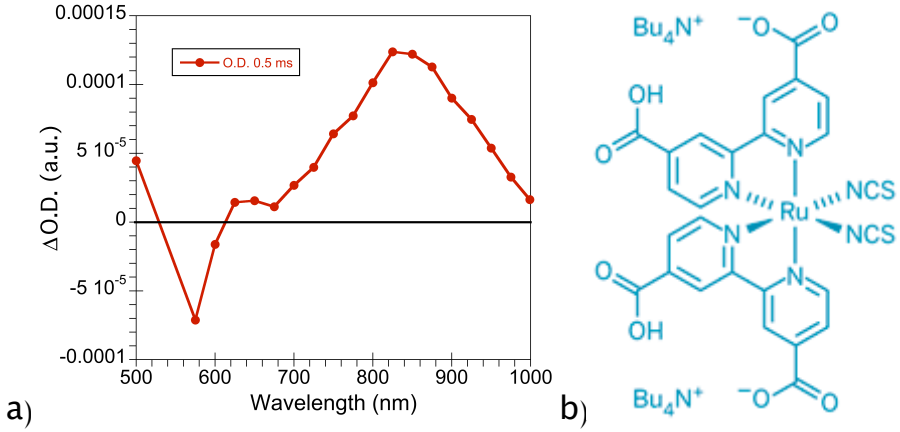

Figure 2. (a) Transient absorption spectrum of the N719 dye molecule on TiO_2. (b) Molecular structure of the N719 dye.

A typical transient absorption decay fitted to a stretch exponential is represented in Figure 3:

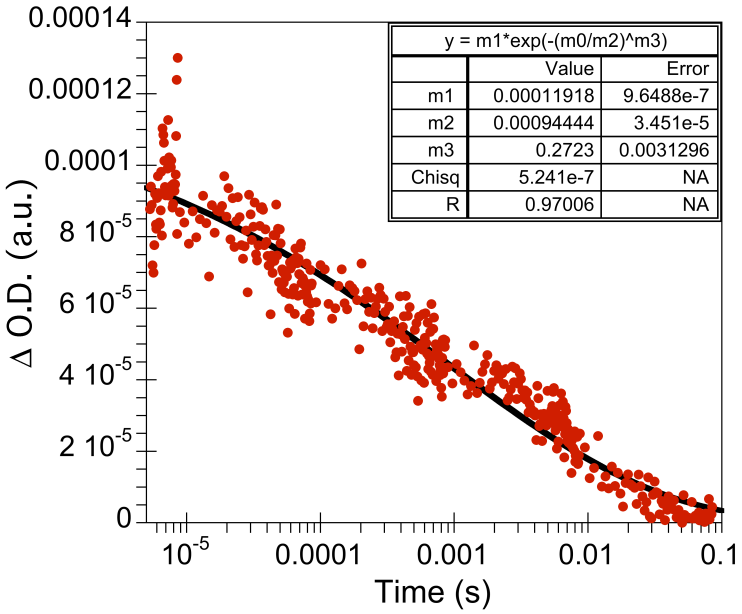

Figure 3. Transient absorption decay of the N719 dye molecule on TiO_2 and fitted to a stretch exponential function.

4. Results.

4.1. Charge Transfer Reactions Involving Colloidal CdSe Quantum Dots.

It has been described in the introduction that nanocrystalline quantum dots are able to act as electron donors or acceptors, depending on the electron affinity of the material which the quantum dots are surrounded. Charge transfer reactions where colloidal CdSe quantum dots have been put in contact with an electron donor, on the one hand, and with an electron acceptor, on the other hand, have been investigated. In the case of quantum dots as electron acceptors, an organic molecule was linked to the CdSe nanocrystal surface. The organic molecule was able to inject electrons into the CdSe quantum dot conduction band. On the other hand, CdSe quantum dots were adsorbed on TiO_2 nanoparticles by means a bi-functional linker molecule. In this case the nanocrystals acted as electron donors. The back-electron transfer reactions in both systems have been studied in detail.

4.1.1. Quantum Dots as Electron Acceptors.

In order to study the charge transfer reactions of CdSe quantum dots as electron acceptors a squarilium methoxy cyanide dye, namely MSqb, was linked to the quantum dots surface. The chemical structure of the dye is shown in Figure 4. This molecule has been previously synthesised in our group and used in dye sensitised solar cells.[12]

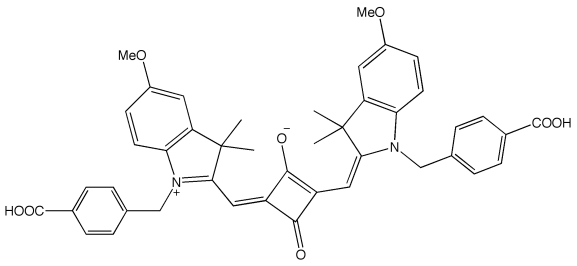

Figure 4. Structure of the squalirilium methoxy cyanide dye (MSqb)

The CdSe quantum dots were synthesised using TOPO as a capping ligand. The absorption maximum of the last excitonic peak was located at $\lambda = 580$ nm, indicating that the nanocrystal size was 4 nm. This value was obtained applying Equation 4 as described before. The UV-Vis absorption spectra of the MSqb molecule and the CdSe quantum dots in solution are showed in Figure 5. The molecule was anchored to the quantum dot through the carboxylate groups of the MSqb. The ligand exchange was performed under inert conditions stirring a mixture of both solutions for 24 hours. After that, the solution was precipitated and centrifuged with methanol, where the quantum dots with the anchored molecule were precipitated and the unattached MSqb molecules reminded in the solution. Three cleaning steps were performed to completely remove the free molecules from the quantum dots

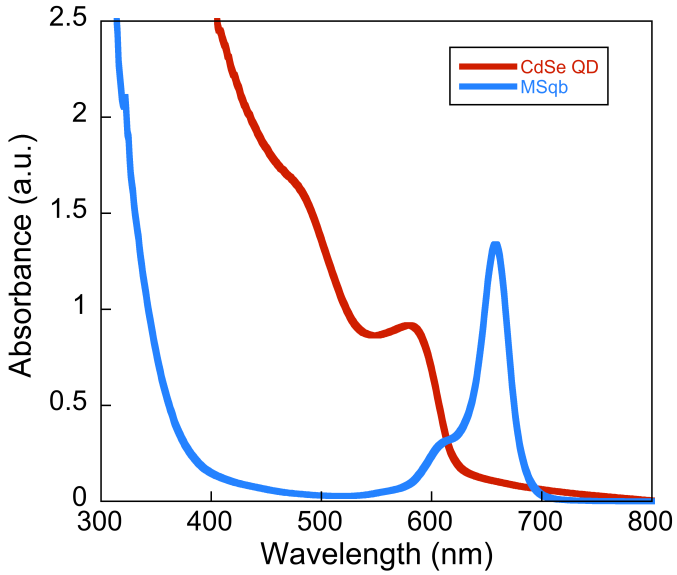

Figure 5. UV-Vis spectra of CdSe quantum dots and the MSqb molecule in solution.

In Figure 6, it is presented a comparison of the linked MSqb–QD and a mixture of both solutions by UV–Vis spectroscopy. As can be seen in Figure 6, noticeable differences can be seen between solutions where the ligand exchange has been successfully performed and where the molecule and the quantum dots are just mixed. While in the solution mixture the spectrum appears as the addition of both, the characteristic last excitonic peak of the quantum dots is not clearly identified in the MSqb–QD solution. This could indicate some electronic interaction between both materials.

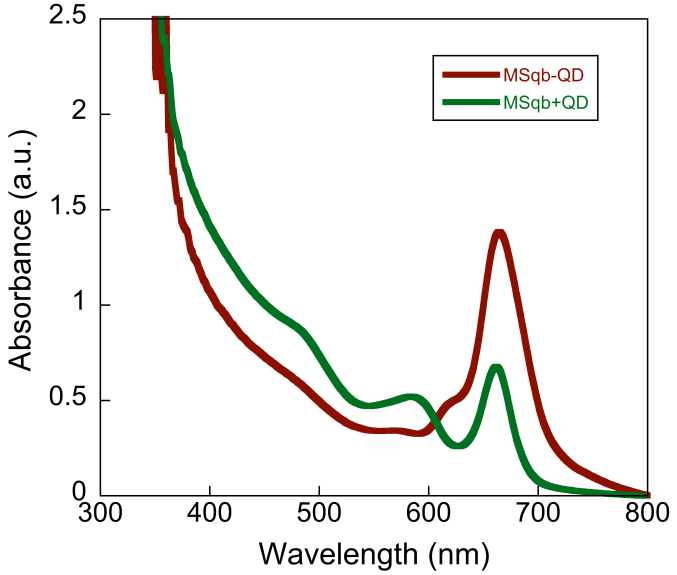

Figure 6. UV-Vis spectra of linked MSqb-QD solution and a mix of MSqb plus CdSe quantum dots solutions.

In order to investigate the charge transfer reactions that might take place between both materials Laser–Transient Absorption Spectroscopy was performed in

MSqb–QD solution in Chloroform. The possible reactions are depicted in Figure 7. In summary, after MSqb excitation (Process 1) a kinetic competition between electron injection from the dye excited state to the CdSe conduction band and electron decay from the MSqb excited state to the ground state (radiatively or non-radiatively) can occur (Processes 2 and 3). If the electron injection reaction is faster than the excited state deactivation the radical cation of the MSqb will be formed, and thus, a L-TAS positive signal corresponding to the absorption of the MSqb cation will be observed. Moreover, since the electrons in the QD conduction band have no selective contacts where to be collected, these charges only can recombine with the cation of the molecule (Process 4) and, thus, the kinetics of the back-electron transfer will be recorded too.

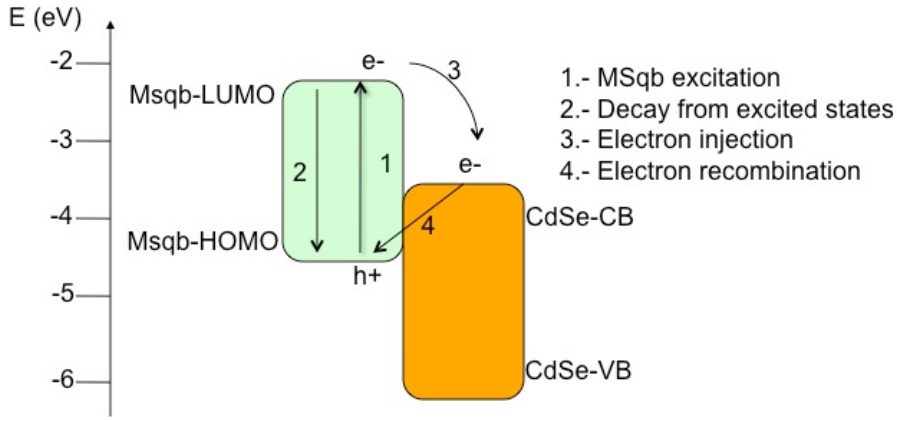

Figure 7. Scheme of the charge transfer processes in the system MSqb-CdSe quantum dot.

As it has been described by S. Tatay et al. the radiative decay of electrons from the excited states to the ground state in the MSqb molecule in solution is < 0.1 ns,[12] therefore, the charge injection (Process 3) should happen on the picosecond time scale. Figure 8 shows the transient absorption spectra of CdSe-MSqd, measured at 1 ms.

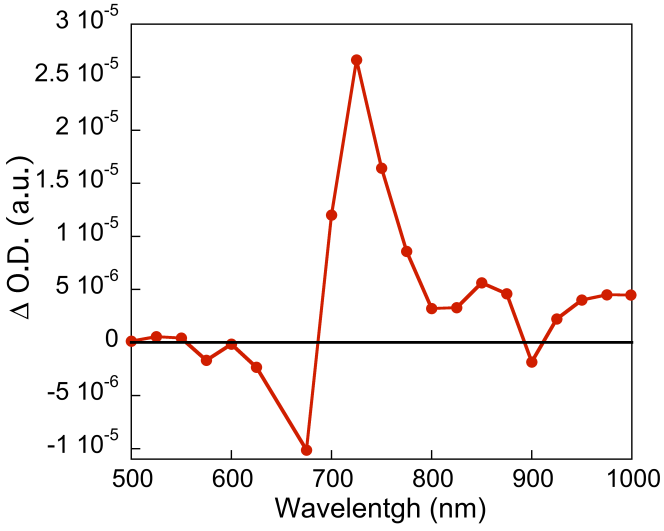

Figure 8. Transient absorption spectra of MSqb linked to CdSe quantum dots. The excitation wavelength was λ = 650 nm. Acquisition time 1 ms.

This spectra is in good agreement with the one published by S. Tatay in the system MSqb–TiO_2 at 100 μs. Consequently, the excited electrons in the MSqb are injected in the QD conduction band rather than decaying from it excited state.

As can be seen in Figure 8, the cation spectra presents a maximum in the near IR range at 725 nm. Therefore, the transient absorption decay was measured at this wavelength, and it is shown in Figure 9. This decay describes the recombination kinetics (Process 4) between the electrons at the CdSe conduction band and the radical cation of the MSqb (Process 4 in figure 7).

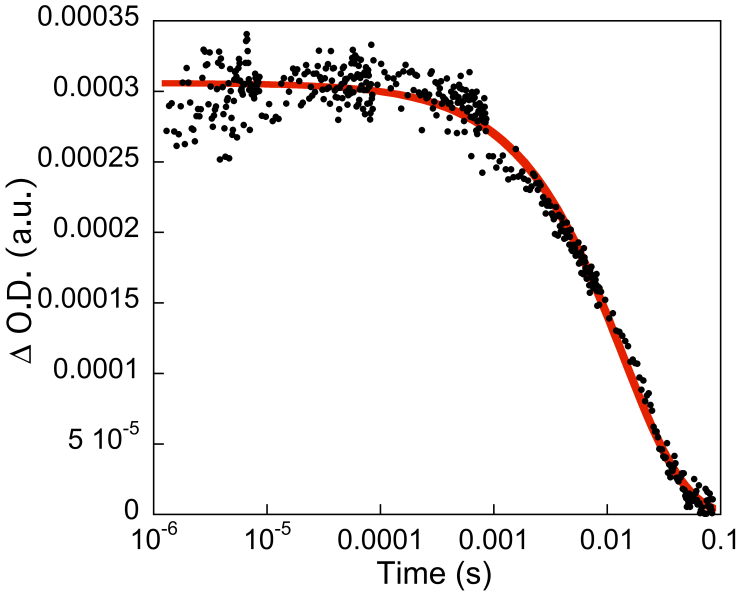

Figure 9. Transient absorption decay of MSqb linked to CdSe quantum dots. The excitation wavelength was λ = 650 nm, and the probe was λ = 725 nm.

The MSqb transient decay was fitted using a stretch exponential function (Eq. 2), and the fitting parameters are shown below:

$$\Delta O.D. = 3.06 \cdot 10^{-4} \exp\left(-\frac{t}{13.8 \cdot 10^{-3}}\right)^{0.79} \quad ; R=0.992$$

,where the decay lifetime is of τ = 13.8 ms and the stretched factor, β is 0.79. Notice the high value for the stretched exponential factor, which is close to unit. As we have explained before, stretched exponential functions with β values of one are related to bimolecular recombination processes. That means that the excited electrons, which are immediately injected in the quantum dot conduction band, after a certain period of time (τ) go back to the previously oxidised molecule.

Thin films (100 nm) of the MSqb–QD were prepared by spin coating, and the recombination kinetics measured, see Figure 10. Although the decay lifetime in film

is about 3 times shorter than in solution, both are in the same time range (milliseconds), and thereby, the charge transfer kinetic properties of the couple MSqb–QD still work in solid state. In general, we can say that electron injection from the MSqb molecule to the quantum dot take places in picoseconds and the electron back reaction in milliseconds in both solution and in thin films.

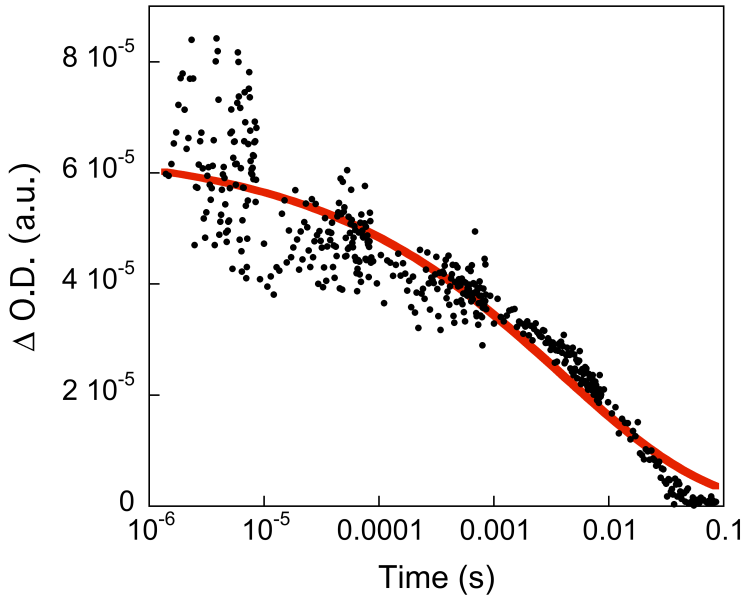

Figure 10. Transient absorption decay of a MSqb linked to CdSe quantum dots thin film. The excitation wavelength was λ = 650nm, and the probe was λ = 725 nm.

The transient decay was again fitted to a stretch exponential function, which parameters are:

$$\Delta O.D. = 6.42 \cdot 10^{-5} \exp\left(-\frac{t}{3.96 \cdot 10^{-3}}\right)^{0.34} \quad ; R=0.949$$

Furthermore, if we compare the stretched exponential factors, both in solution as in thin film, it is clear that the system in solution has completely different recombination dynamics than in solid state. This is, while in solution $\beta = 0.79$, in film $\beta = 0.34$. While in solution β is close to one, in thin film the recombination dynamics become more dispersive. In the films, the dielectric media is different from solution and the excited molecules produce excitons (electron–hole pair) which must travel up to the quantum dot interface to split into positive and negative polarons. Then, the generated polarons, must cover different distances to find the holes in the oxidised molecules, depending on how long it takes the excitons to find an interface. In addition in all these processes, the intrinsic electron and hole mobility of the different materials must be take into consideration. As a conclusion, since the electrons in the quantum dot conduction

band may take different times to find a hole, the recombination dynamics become dispersive instead of bimolecular.

The study of semiconductor quantum dots as electron acceptor has not been only restrained to the MSqb molecule. The ruthenium complex known as N719 (cis-$RuL_2(SCN)_2$(L=2,2'-bipyridyl-4,4'-dicarboxylic acid)) was also linked to the CdSe quantum dot surface in the same way, and similar results were obtained in solution, see Figure 11.

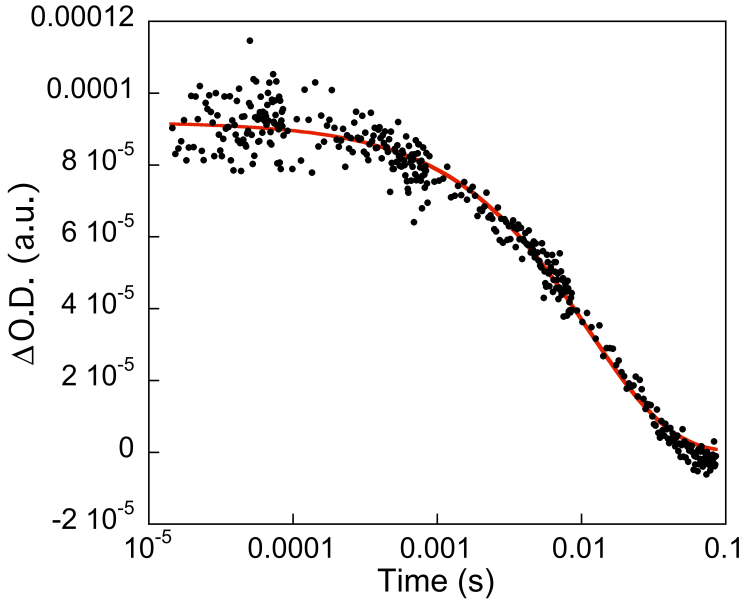

Figure 11. Transient absorption decay of N719 linked to CdSe quantum dots. The excitation wavelength was 535 nm, and the probe was 800 nm.

The parameter of the stretch exponential fit are shown below:

$$\Delta O.D. = 9.19 \cdot 10^{-5} \exp\left(-\frac{t}{11.3 \cdot 10^{-3}}\right)^{0.77} ; \text{R=0.989}$$

Notice that the values of the lifetime decay and the stretched factor are very similar to the ones obtained for the MSqb molecule. This indicates that the material which controls the recombination dynamics is the semiconductor nanocrystal, and not the dye molecule.

4.1.2. Quantum Dots as Electron Donor.

Semiconductor quantum dots can act as electron donors too. The electron injection reaction between quantum dots and semiconductor metal oxides have been widely studied by Kamat and coworkers.[13] In these studies it has been demonstrated that the quantum dot size influences the electron transfer rate (K_{ET}). When the quantum dot size is increased the K_{ET} decrease. This is due to the lower

energy gap that the quantum dots present when its size is increased. Since the energy gap decrease with the increase of size, the energy driving force $(-\Delta G^{o})$ for the electron transfer is reduced as well.

We have studied the electron recombination from the electrons injected in the TiO_2 conduction band to the quantum dot valence band.

A scheme of these reactions as a function of the quantum dot size is depicted in Figure 12.

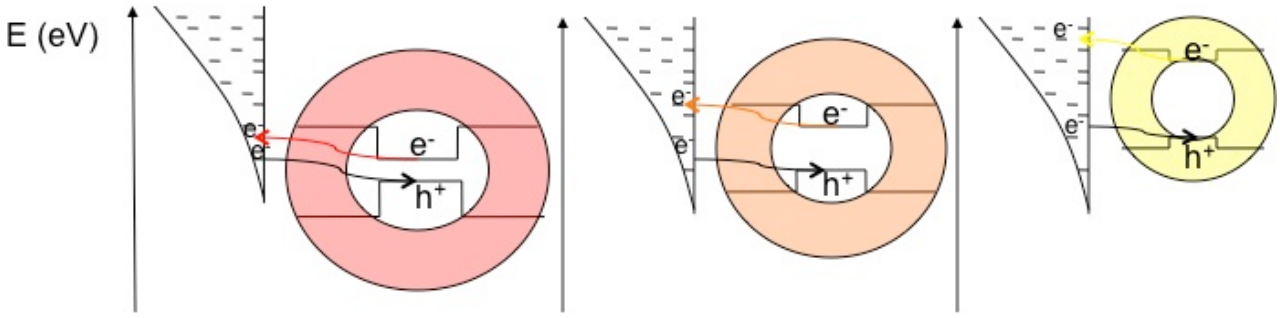

Figure 12. Scheme of the charge transfer processes in QD-TiO_2 films for different QD sizes. The coloured arrows indicate electron injection and the black arrows electron recombination.

In order to study this charge recombination process we have sensitised three different size CdSe quantum dots. In Figure 14 (a) the UV-Vis spectra of the three quantum dots anchored to mesoporous TiO_2 films are shown. The quantum dot size has been calculated from the wavelength of the maximum of the last excitonic peak. The TOPO capped CdSe quantum dots had 2.2, 2.6 and 3.5 nm size. The colloidal quantum dot was linked to the titanium nanoparticles with the bi-functional molecule 3-Mercaptopropionic acid (MPA) (see Figure 13). The TiO_2 films were treated for 24 hours with MPA (0.1 M), after that, quantum dot sensitisation was performed for 24 hours more.

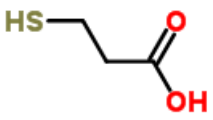

Figure 13. Molecular structure of the 3-Mercaptopropionic acid.

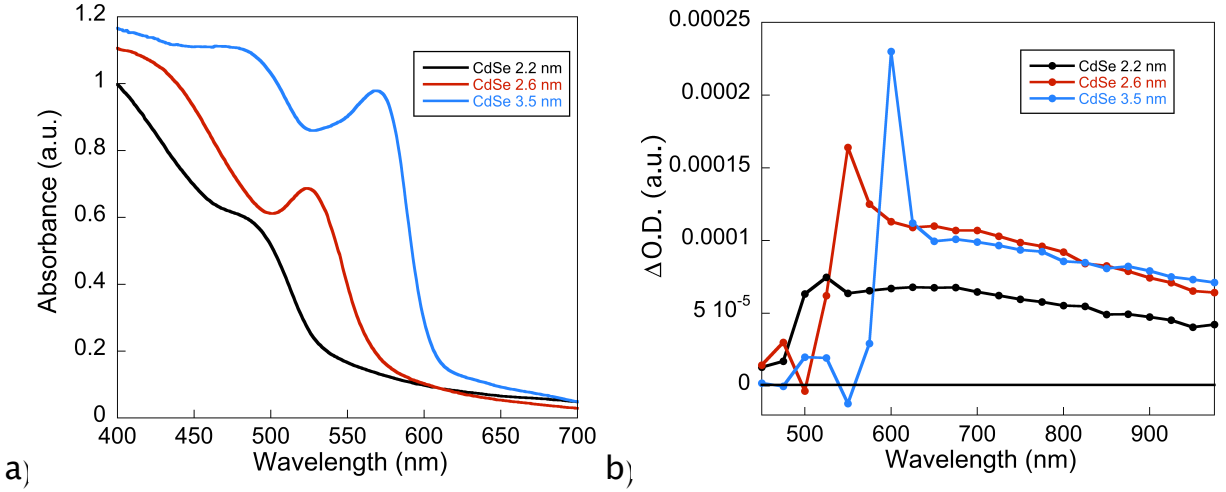

Figure 14. UV-Vis spectra (a) and transient absorption spectra (b) of the three different sized CdSe quantum dots linked to TiO_2 mesoporous films. The excitation wavelength was λ = 405 nm and the acquisition time 100 μs.

The transient absorption spectra of the colloidal quantum dots were measured. The spectrum of the oxidised quantum dots changed with the size. Positive signals in the L-TAS spectra were recorded, indicating electron injection. Moreover, a red-shift of the transient absorption can be observed when the quantum dot size is increased, Figure 14 (b). The transient lifetime decay of the three samples was also recorded, see Figure 15.

The O.D. amplitude of the samples in the transient spectra and decay followed the trend of the UV-Vis absorption spectra. The fact that the K_{ET} increase when the quantum dot size decrease does not mean that the amount of injected charges also increases. K_{ET} only refers to the injection kinetics. Indeed, the extinction coefficient of quantum dots increase with the size.[8] This property and the higher absorption of the samples with biggest quantum dot size produce that the O.D. trend of the samples will be the opposite to the expected.

The transient decays were fitted to a stretch exponential function. Notice that the plateau at the beginning of the decay in this kind of measurement is not clearly identified. Probably, the recombination processes starts at time scales faster than our instrument response (μs - ms), in the ns time scale. The parameters from the fittings are shown below:

CdSe (2.2 nm) $\Delta O.D. = 1.02 \cdot 10^{-4} \exp\left(-\frac{t}{1.26 \cdot 10^{-3}}\right)^{0.31}$; R=0.98

CdSe (2.6 nm) $\Delta O.D. = 2.26 \cdot 10^{-4} \exp\left(-\frac{t}{1.05 \cdot 10^{-4}}\right)^{0.33}$; R=0.996

CdSe (3.5 nm) $\Delta O.D. = 3.05 \cdot 10^{-4} \exp\left(-\frac{t}{0.71 \cdot 10^{-3}}\right)^{0.29}$; R=0.996

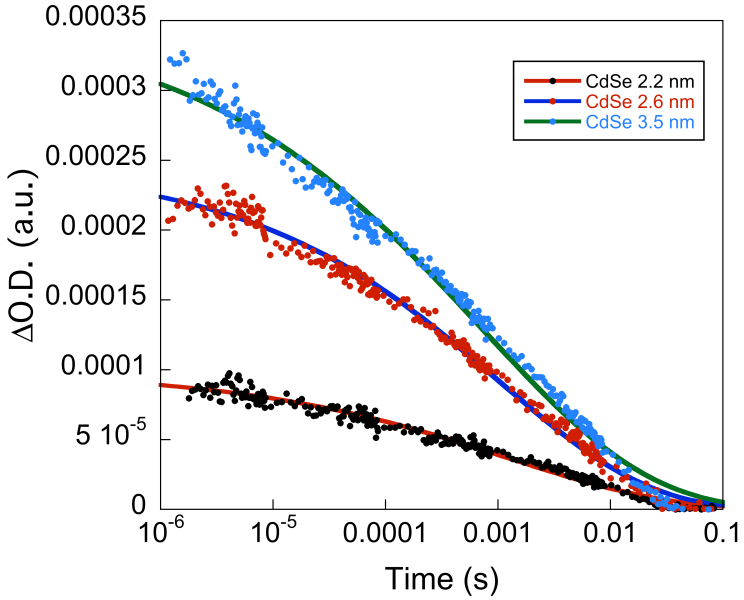

Figure 15. Transient absorption decay of the three different sized CdSe quantum dots linked to TiO_2 mesoporous films. The excitation wavelength was λ = 405 nm and the probe wavelengths λ = 525, 550 and 600 nm for CdSe 2.2, 2.6 and 3.5 nm, respectively.

The lifetime decay of the oxidised CdSe nanocrystals decreased when the quantum dot size was increased. However, the recombination dynamics reminded constants with quantum dot size. The stretched factors were 0.3 approximately in all cases. This is indicating that, in this case, the material which control the recombination dynamics is the semiconductor metal oxide, and not the quantum dots as it was the case of the previous section (4.1.1.). The injected electrons move through the titanium nanoparticle network, following a random walk.[14]

The increase in the recombination kinetics with the quantum dot size might be explained in energetic terms. The characteristic quantum confinement that quantum dots possess decreases in the nanocrystals bandgap when the quantum dot size is increased. Therefore, the smaller nanocrystals will have their valence band (v.b.) further from the titanium dioxide conduction band (c.b.) than the bigger quantum dots. This fact, could be the reason responsible for the slower recombination kinetics to the smaller the quantum dots.

The recombination kinetics that the molecular linked colloidal quantum dots present in contact to TiO_2, are in the range of milliseconds and the recombination mechanism can be considered as a dispersive recombination pathway, as also takes

place in DSSC. However, the efficiency of these devices has not reached yet the efficiency of the devices sensitised with molecular dyes. Accordingly, there must be other charge transfer processes that are limiting the device efficiency. The low adsorption of quantum dots by the linker adsorption technique, charge recombination processes involving electrolytes and the regeneration process of the oxidised nanocrystal could be some examples of these limiting factors.

4.2. Photo-Induced Charge Recombination in Quantum Dot Sensitized TiO_2 Films by SILAR.

It has been found that the deposition of colloidal quantum dots by Direct Adsorption and Linker Adsorption does not provide a quantum dot monolayer on the surface of the nanostructured metal oxides. This low absorption means that higher thicknesses of metal oxide layers were needed to absorb significant amounts of light. For this reason, the SILAR method has been suggested to overcome the low sensitisation issue, due to the ability of this technique to occupy more metal oxide free surface area, and thus, increasing the light absorption.

Furthermore, the SILAR method allows two approaches in order to extend the device light harvesting from the UV to the Near-IR part of the spectra. On the one hand, the co-adsorption of different but complementary materials, such as CdS + CdSe, which absorb in different regions of the spectra. On the other hand, the use of one low band gap material, for example PbS, which absorb light in the lower energy part of the solar spectrum. The charge transfer reactions of this "quantum material" with TiO_2 has been investigated for both approaches, co-adsorption of different materials and adsorption of a material with large absorption spectra. Moreover, the influence of charge recombination by the inclusion of a ZnS passivation layer in the case of co-adsorption of different materials by SILAR, has been also investigated.

4.2.1. Charge Transfer Recombination of CdS, CdSe and ZnS Nanocrystals Deposited on TiO_2 Films by SILAR

Mesoporous TiO_2 (11 μm) films were prepared. These films were sensitised with 3 SILAR cycles of CdS, 4 SILAR cycles of CdSe and 2 SILAR cycles of ZnO as it has been described by Yi-Siou Lo et al.[9] A HR-TEM image of the TiO_2 nanoparticles covered with the nanocrystals will be presented at the end of the section in Figure 21 (b). The UV-Vis spectra of the films after sensitisation is shown in Figure 16.

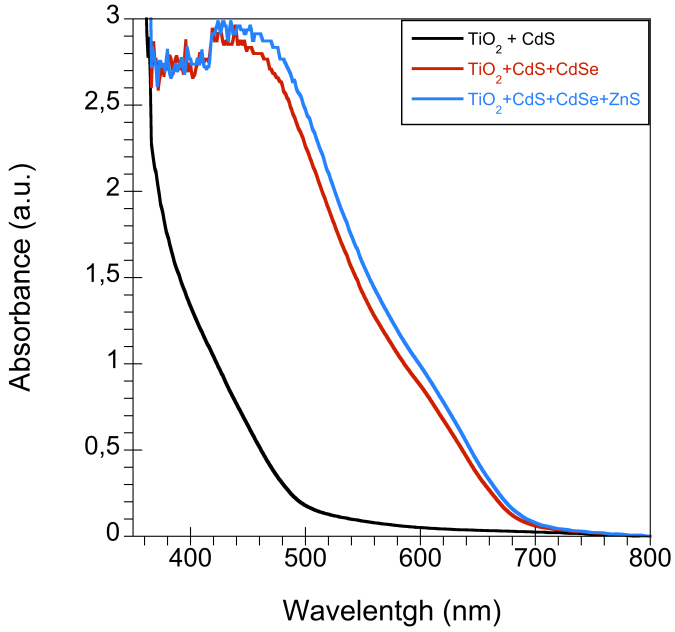

Figure 16. UV-Vis spectra of deposited TiO_2 films of CdS, CdS + CdSe and CdS + CdSe + ZnS deposited by the SILAR method.

From the UV–Vis spectra we can see that the in situ quantum dot growth by SILAR technique does not display the narrow and characteristic peak that we can see in the colloidal quantum dots. This is due to the wide size distribution that this technique provides. The addition of the different materials to the titanium films extends the absorption through the visible range. The addition of CdSe to CdS shifts the absorption band by around 200 nm. The addition of ZnS does not promote a much higher shift of the absorption on set. However, it is known[11] that the ZnS forms a passivating layer on the top of the QD–TiO_2 surface. This thin layer (~ 2 nm) plays the role, on the one hand, of passivating trap states in the quantum dot surface which promote exciton annihilation, and in the other hand, avoiding recombination charge losses between the electrons in the TiO_2 conduction band and the electrolytes in the quantum dot sensitised solar cells. We will focus on the charge transfer processes between electrons at the titania conduction band and the oxidised quantum dots.

The transient absorption spectra of the CdS, CdS + CdSe and CdS + CdSe + ZnS coated TiO_2, respectively, are showed in Figure 17.

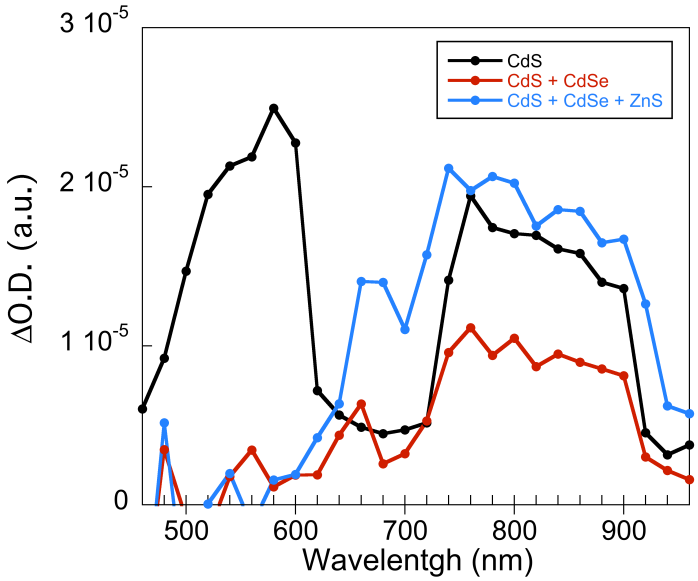

Figure 17. Transient absorption spectra of CdS, CdS + CdSe, CdS + CdSe + ZnS coated TiO_2. The excitation wavelength was λ = 405 nm. The acquisition time was 100 μs.

If we first focus in the transient absorption spectra of the CdS sample (spectrum in black, Figure 17) two absorption bands can be identified. The first one with maximum at λ = 580 nm, and the second one at λ = 780 nm. The fact that two absorption bands appear in the spectrum could be due to the existence of two main quantum dot populations of different sizes. SILAR provides a wider load of nanocrystals on the titanium dioxide surface, nonetheless, a poor control on the quantum dot size distribution is achieved with this technique.[15] In order to confirm whether the two bands correspond to the same species the transient decay in the two maximums was measured and is shown in Figure 18. These decays do not shows significant differences, therefore, it is believed that both absorption bands correspond to oxidised CdS quantum dots with two main sizes. The decays were fitted to stretch exponential function and the fittings revealed very similar parameters with cation lifetimes (τ) in the millisecond time scale and stretched factors between β = 0.20 – 0.29. In the same way that we have seen in the recombination kinetics of colloidal quantum dots linked to TiO_2, the bigger quantum dots (which cationic absorption band must be located in the red part of the transient spectrum) showed faster recombination kinetics (7.5 ms) than the smaller ones (which band is in the blue part), that showed slower recombination kinetics (33.3 ms).

Now, we look at the transient absorption spectrum of the CdS + CdSe–TiO_2 sample (spectrum in red in Figure 17). The band with maximum at λ = 580 nm has disappeared, corresponding to the smallest quantum dot population. In addition, the band assigned to the bigger ones with maximum at λ = 780 nm has decreased

in intensity, and a new small shoulder between λ = 620 and 680 nm has appeared, where there was no absorption before. The transient lifetime decay at λ = 780 nm of CdS + CdSe–TiO_2 is compared with the CdS one in Figure 19.

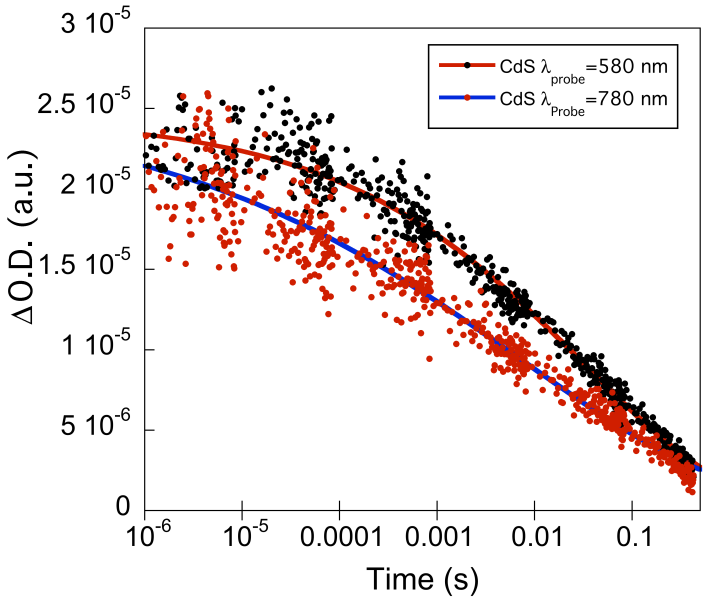

Figure 18. Transient absorption decay of CdS-TiO_2 film with light probe at λ = 580 and 780 nm. The excitation wavelength was λ = 405 nm.

In this case the dynamics looks completely different. The CdS + CdSe–TiO_2 decay belongs to a process that probably starts several orders of magnitude faster than our instrument response (I.R. ≈ 1 μs), and the only thing that we can see is the tail of the decay. In this case, from the transient spectrum and the decay we can only suggest that the CdSe has reduced the oxidised CdS. The hole in the CdS valence band has passed to the CdSe.

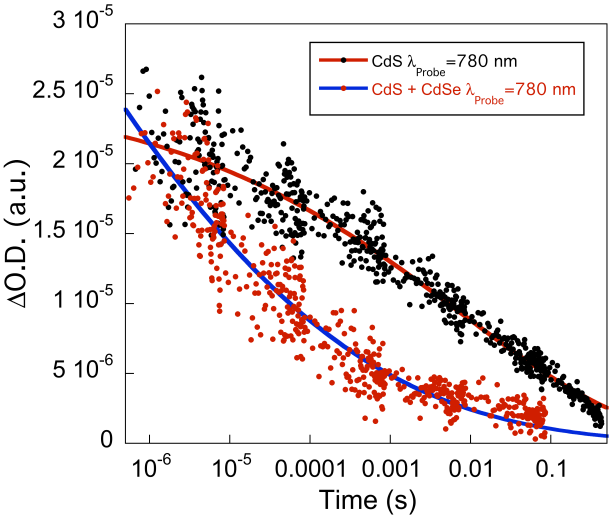

Figure 19. Transient absorption decay of CdS and CdS + CdSe - TiO_2 films with light probe at λ = 780 nm. The excitation wavelength was λ = 405 nm.

For this reason, the transient spectrum of the CdS can not be seen and the spectrum that we are observing belongs to the oxidised CdSe. Although $CdSe^+$ has a spectrum very similar to the oxidised CdS there is a feature that points to this hypothesis: the apparition of a new shoulder at 660 nm. In addition, the new created specie ($CdSe^+$) has a very short lifetime. We have fit the CdS + CdSe–TiO_2 decay, and the lifetime obtained is in the order of nanoseconds time scale (0.17 ns). This could be due, on the one hand, to the new scenario created with the addition of a second material to the system, where the oxidised CdSe can accept electrons from the TiO_2 conduction band, or from the CdS valence band and from its own excited states. On the other hand, to the generation of trap states in the quantum dot surface due to photo–oxidation associated to these materials in the presence of light and oxygen.[16] The charge transfer processes produced by the addition of a second sensitiser are illustrated in Figure 20.

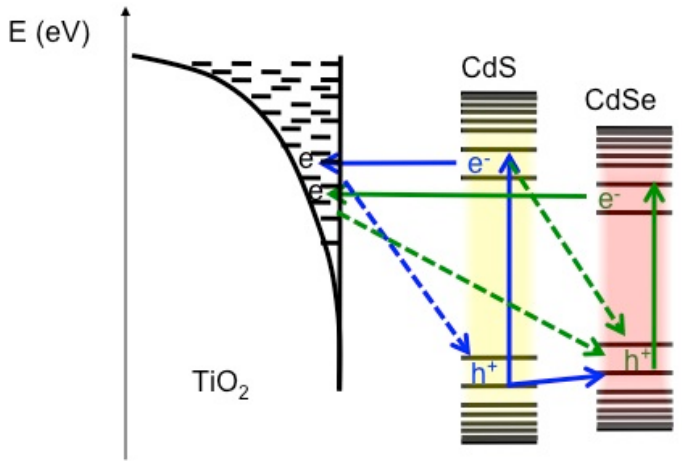

Figure 20. Scheme of the charge transfer processes involving CdS-TiO_2 and CdS + CdSe-TiO_2. The blue arrows corresponds to the photo-induced charge processes for CdS and the green arrows to the addition of CdSe to the system. The deactivation of excited electron in the nanocrystal conduction band to the ground state has not been depicted in any case. The dotted arrows corresponds to recombination processes.

Finally, after addition of the ZnS layer the transient absorption spectrum maintained the shape of the CdS + CdSe one, but with higher intensity. The decay of this transient was measured at λ = 780 nm as well, and it is shown in Figure 21. As can be seen the dynamics in the TAS signal are identical, but noticeable differences in the kinetics can be extracted from the fitting. The addition of the ZnS layer slows down the decay from nanoseconds to microseconds. Since this layer is covering the surface of the in situ growth quantum dots on the titanium nanoparticles and the free TiO_2 (non–covered with CdS + CdSe quantum dots), as can be seen in Figure 21 (b), it is logical to think that this layer is passivating trap states in the quantum dots, avoiding photo–oxidation, and so, making longer the oxidised CdSe lifetime.

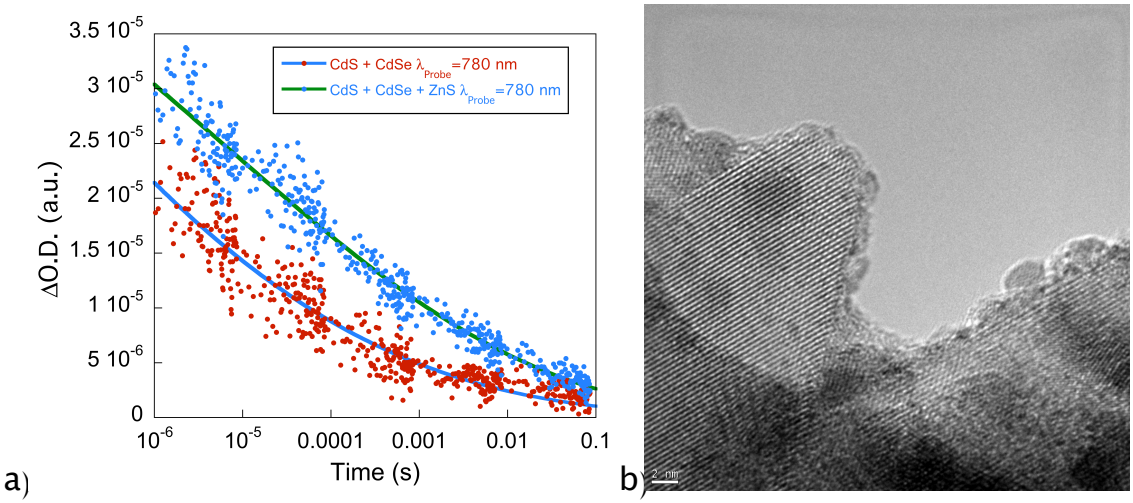

Figure 21. (a) Transient absorption decay of CdS + CdSe and CdS + CdSe + ZnS-TiO_2 film with light probe at λ = 580 and 780 nm. The excitation wavelength was λ = 405 nm. (b) High Resolution Transmission-Electron Microscopy (HR-TEM) image of a CdS + CdSe + ZnS-TiO_2 film.

4.2.2. Charge Transfer Recombination of PbS Nanocrystals Deposited on TiO_2 Films by SILAR

Mesoporous TiO_2 films were sensitised with PbS quantum dots by the SILAR technique. Figure 22 depicts the UV–Vis spectra of the PbS–TiO_2 films, when the number of SILAR cycles were increased.

It is widely known in the bibliography that the maximum of the transient absorption spectrum of PbS quantum dots is located in the near infra–red part of the spectrum, depending on the nanocrystal size.[17] Unfortunately, our system is only able to measure up to λ = 980 nm. However, the beginning of the absorption band starts at wavelengths in the visible. Therefore, we measured this part of the transient absorption spectrum of the PbS–TiO_2 films with 6 SILAR cycles, and it is shown in Figure 23.

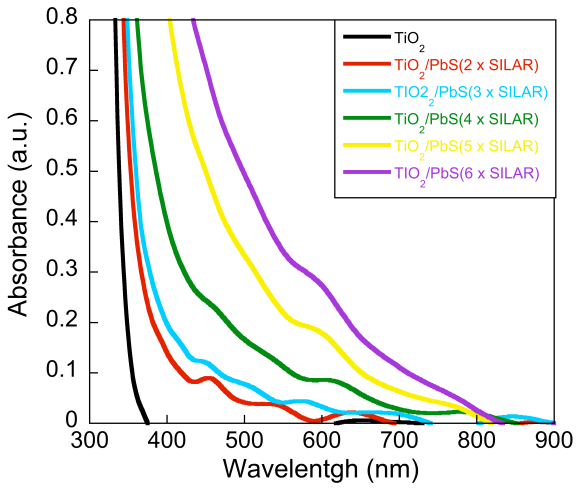

Figure 22. UV-Vis spectra of the PbS-TiO_2 film when the number of SILAR cycles is increased.

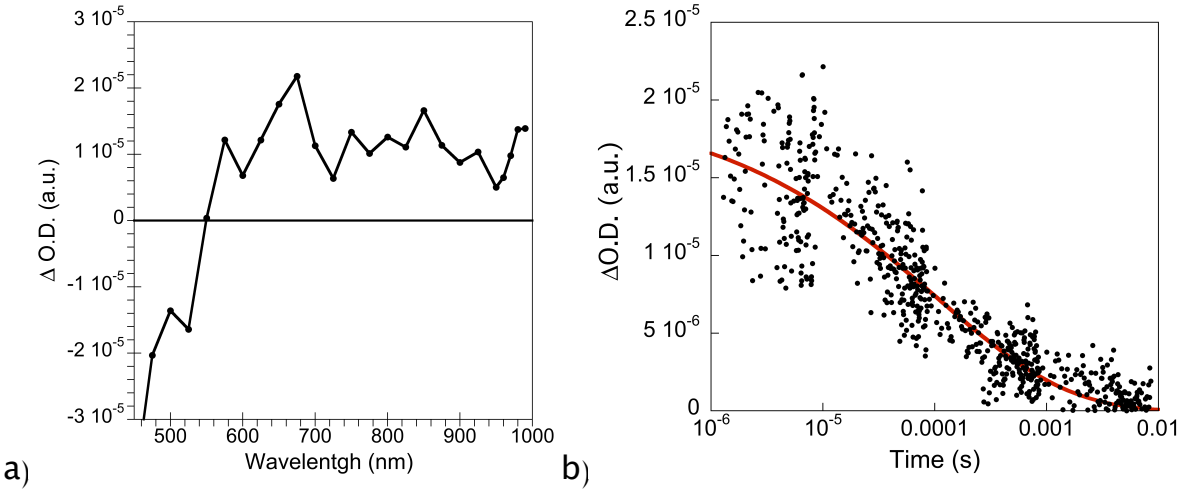

Figure 23. Transient absorption spectrum (a) and decay (b) of PbS-TiO_2 film with 6 SILAR cycles. The excitation wavelength was λ = 405 nm in both measurements. The acquisition time was 10 μs in the spectrum, and the probe wavelength in the decay was λ = 675 nm.

The obtained transient spectrum was not very intense and quite noisy. Nevertheless, the recombination kinetics could be measured at λ = 675 nm. The transient lifetime decay was fitted to a stretch exponential function. The decay presented faster recombination kinetics than in the CdS SILAR deposited case, but similar dynamics. The oxidised PbS lifetime was of τ = 104 μs and the stretched factor of β = 0.37. The faster recombination kinetics could be due to the lower energy which the electrons are injected in the titanium conduction band compared with the one of the CdS. The charge recombination was also measured for films with different number of SILAR cycles. Figure 24 shows the transient lifetime decay of the TiO_2–PbS films sensitised with different SILAR cycles at λ = 675 nm. The lifetime decays were fitted to stretch exponential functions. The parameters obtained from the fits are shown below:

TiO_2–PbS(2 X SILAR); $\Delta O.D. = 8.6\cdot10^{-6}\exp\left(-\frac{t}{3.6\cdot10^{-3}}\right)^{0.352}$; R = 0.82

TiO_2–PbS(4 X SILAR); $\Delta O.D. = 4.97\cdot10^{-5}\exp\left(-\frac{t}{2.2\cdot10^{-5}}\right)^{0.13}$; R = 0.957

TiO_2–PbS(6 X SILAR); $\Delta O.D. = 1.98\cdot10^{-5}\exp\left(-\frac{t}{1.04\cdot10^{-4}}\right)^{0.37}$; R = 0.92

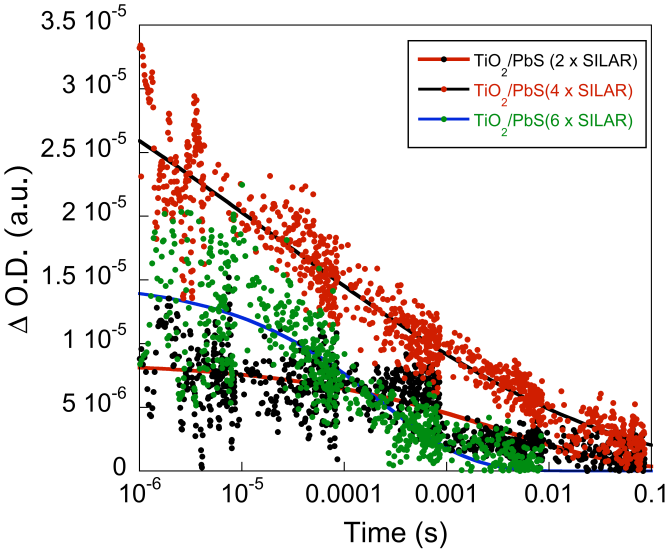

Figure 24. Transient absorption decay of PbS-TiO_2 films with different SILAR cycles. The excitation wavelength was λ = 405 nm and the probe λ = 675 nm.

As can be appreciated from the lifetime decays in Figure 24 and in the stretch exponential functions obtained from the fit of the decays, the amplitude of the oxidised PbS grows from 2 to 4 SILAR cycles but decreases from 4 to 6. The UV–Vis absorption spectra shown in Figure 22 show that the absorption is increased with the number of SILAR cycles. However, the transient absorption amplitude increased up to 4 cycles and after that, decreased. This could be due to the fact that successive SILAR cycles may grow new nanocrystals both in free TiO_2 surface and on already grown PbS nanocrystals. The overall absorbance is increased in every cycle, but the saturation of free TiO_2 surface and subsequent growth over other nanocrystals means that the oxidised species in contact with other nanocrystals may be quickly deactivated. Therefore, the O.D. signal of transient species was decreased when this phenomena arises. This have been observed by HR–TEM. The pictures of HR–TEM of PbS–TiO_2 with 2 and 6 SILAR cycles are shown in Figure 25.

While in Figure 25 a) a few PbS nanocrystals can be identified in the TiO_2 surface, in Figure 25 b) the metal oxide appears almost covered by nanocrystals of very different sizes. Since in the SILAR method we can not select were the nanocrystals are going to be deposited, the successive depositions could be on the more and more limited free space on the TiO_2 or on the already created nanocyrstals. This not only affects the number of oxidised species generated, but also the recombination dynamics, as can be seen in Figure 24 and in the fit parameters. The optimum number of SILAR cycles will be the one where higher number of oxidised species will be formed without an increase in the recombination kinetics dramatically. In this case, 5 SILAR cycles have been found to be the optimum in terms of charge generation and recombination. This optimum number of SILAR cycles has been selected without taking into account other device

components such as electrolytes and counter electrodes. Therefore, this conclusion must be reviewed in complete devices.

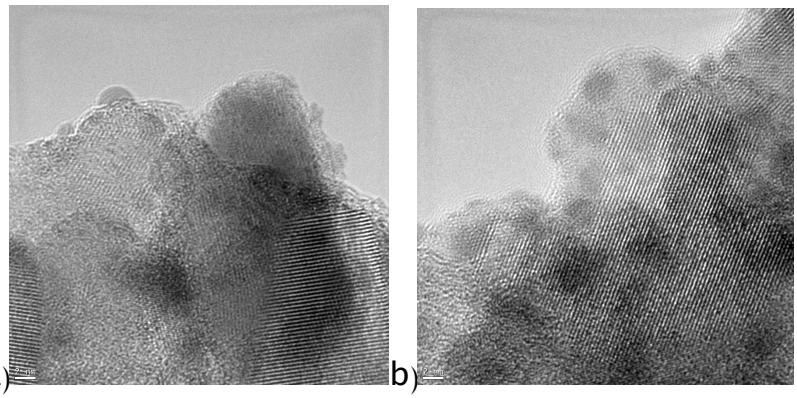

Figure 25. PbS-TiO_2 HR-TEM pictures of (a) 2 cycles and (b) 6 cycles of SILAR.

4.3. Charge Recombination Comparison in CdSe Quantum Dot TiO_2 by Three Different Deposition Methods.

Mesoporous thin films of titanium dioxide were prepared and sensitised with colloidal CdSe quantum dots by Direct Absorption (DA) and Linked Adsorption Absorption (LA). The linker molecule was Cysteine, whose structure is shown in Figure 26. TiO_2 films were also sensitised with CdSe by Chemical Bath Deposition (CBD). Then, the sensitised films were coated with a thin ZnS layer (~2 nm). The charge recombination kinetics of CdSe quantum dots deposited by these methods with and without ZnS layer were studied. Moreover, the Black Dye molecule was anchored to the films with and without ZnS in order to study its influence in the recombination dynamics of these systems. The CdSe–TiO_2 films sensitized by three different methods were supplied by Professor Juan Bisquert group in Universitat Jaume I de Castelló. The Black dye sensitisation was performed at ICIQ.

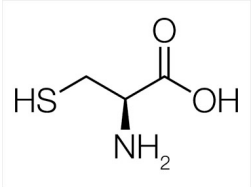

Figure 26. Molecular structure of Cysteine molecule.

The transient absorption spectra of CdSe quantum dots deposited on TiO_2 by the three different methods were measured. All spectra in this section were obtained with a excitation pulse of λ = 440 nm and acquired at 100 µs. The transient spectra of the CdSe quantum dots deposited by Direct Absorption, Linked Adsorption and Chemical Bath Deposition are shown in Figure 27.

From the transient spectra, it can be observed that the absorption feature correspond to a wide absorption band from the range of the visible which is extended up to the Near IR in all cases. However, in the case of DA and LA the absorption of the oxidised quantum dots is shifted towards 500 nm, respect to the one deposited by CBD.

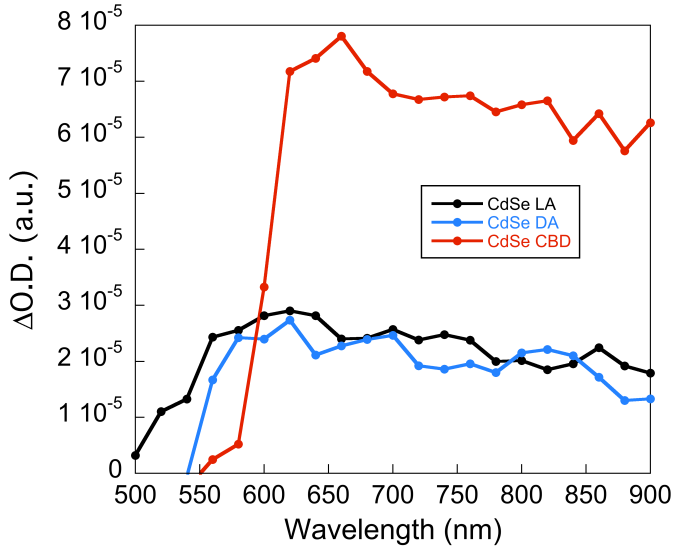

Figure 27. Transient absorption spectra of CdSe quantum dots deposited on TiO_2 by LA, DA and CBD. Excitation wavelength λ = 440 nm. Acquisition time 100 μs.

In addition, the absorption of the oxidised CdSe had double intensity in the case of CBD than in DA and LA. This is not surprising since in the CBD technique a higher amount of quantum dots are deposited rather than in LA and DA, which are the techniques where less nanocrystal load is present. The kinetics of recombination in the three deposition techniques were measured at λ = 620 nm and are presented in Figure 28. The kinetics of recombination of colloidal quantum dots deposited both DA and LA were very similar. However, the ones deposited by CBD presented faster recombination kinetics. The decays were fitted to stretch exponential functions. The parameters are presented below:

Linked adsorption: $\Delta O.D. = 1.14 \cdot 10^{-4} \exp\left(-\frac{t}{2.65 \cdot 10^{-8}}\right)^{0.06}$; R = 0.898

Direct absorption: $\Delta O.D. = 1.84 \cdot 10^{-4} \exp\left(-\frac{t}{1.05 \cdot 10^{-8}}\right)^{0.07}$; R = 0.929

Chemical Bath Deposition: $\Delta O.D. = 8.64 \cdot 10^{-4} \exp\left(-\frac{t}{2.59 \cdot 10^{-10}}\right)^{0.09}$; R = 0.975

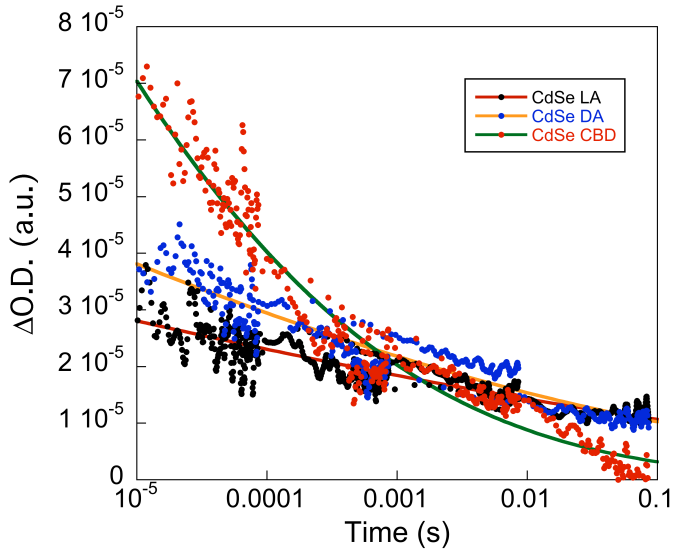

Figure 28. Transient absorption decay of CdSe quantum dots deposited by LA, DA and CBD. The excitation and the probe wavelengths were λ = 440 and 620 nm, respectively.

In all cases, the CdSe quantum dots presented similar dynamics and fast kinetics of recombination. Indeed, the lifetime decay of the oxidised colloidal nanocrystals were in the order of nanoseconds. However, the nanocrystals deposited by CBD presented 100 times faster recombination kinetics than the colloidal quantum dots. This behaviour has been described elsewhere,[18] and these experiments confirm such hypothesis.

We then studied the behaviour of the back-electron reactions when the films were coated with a thin ZnS layer. The transient absorption spectra of CdSe-TiO_2 films, deposited with the different techniques, and coated with ZnS are shown in Figure 29.

Notice that the transient spectra of the sample prepared by CBD with (Figure 29) and without (Figure 27) ZnS are not different neither in shape nor signal intensity. However, the samples prepared by the other methods (DA and LA) present an enhancement of signal intensity, which means that more oxidised CdSe quantum dots are present in this time range with the coating rather than without.

The ZnS coating is passivating the quantum dots from trap states in the surface of the nanocyrstals, allowing more electrons to be injected into the titanium conduction band instead of recombing with those trap states. Therefore, more signal from transient species can be detected. This behaviour have been already seen in section 4.2.1 with CdSe quantum dots deposited by SILAR. In the case of the CdSe deposited by CBD, no change in the signal intensity means that the ZnS layer is not playing a major role in the recombination dynamics between the electrons in

the TiO_2 conduction band and the oxidised CdSe. Therefore with this technique a passivating layer to avoid the presence of trap states, is not crucial.

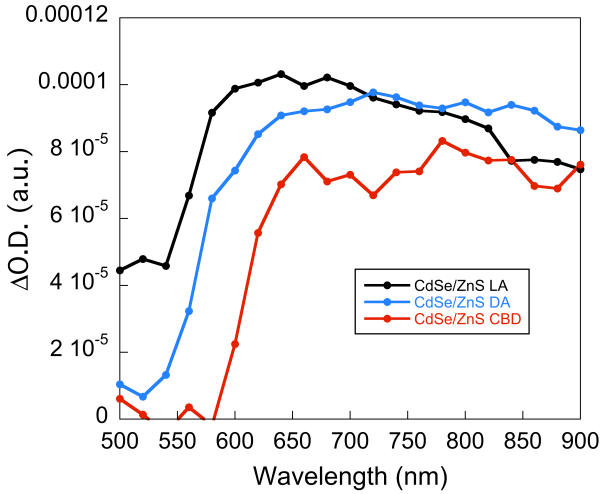

Figure 29. Transient absorption spectra of CdSe-TiO_2 films, deposited with different techniques, and coated with ZnS. The excitation wavelength was λ = 440 nm, and the acquisition time 100 μs.

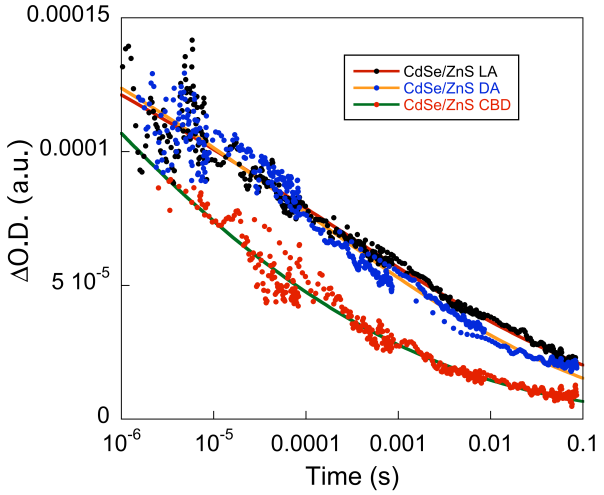

Figure 30. Transient absorption decay of CdSe quantum dots deposited by LA, DA and CBD. The excitation and the probe wavelengths were 440 and 620 nm, respectively.

The kinetics were also measured, and are shown in Figure 30. In this case, in all samples the recombination kinetics are slower than the ones without the ZnS coating. But, while the recombination dynamics with DA and LA techniques are practically identical, the kinetics with CBD are still much faster than the other two. The decays were fitted to stretch exponential functions, and presented the following parameters:

$$\text{Linked Adsorption: } \Delta O.D. = 2.09 \cdot 10^{-4} \exp\left(-\frac{t}{1.24 \cdot 10^{-4}}\right)^{0.13} \text{; R} = 0.9$$

Direct absorption: $\Delta O.D. = 2.09 \cdot 10^{-4} \left(-\frac{t}{1.03 \cdot 10^{-4}} \right)^{0.14}$; R = 0.98

Chemical Bath Deposition: $\Delta O.D. = 6.06 \cdot 10^{-4} \exp\left(-\frac{t}{1.32 \cdot 10^{-9}} \right)^{0.08}$; R = 0.981

As can be seen, the addition of the ZnS layer has slowed the back-electron transfer from nanoseconds to microseconds for colloidal quantum dots. However, for CBD quantum dots the kinetics remains very similar. Furthermore, the stretch exponential factors for LA and DA are very similar and slightly higher than for CBD. This could point to a reduction of superficial defects in the colloidal nanocrystals which reduce recombination sites.

We also added a dye molecule to the system. The molecule is the Black Dye (see structure in Figure 32), which is able to absorb light up to the near infrared region (~800 nm) and it has been widely employed for DSSC.[19] The transient spectra of CdSe colloidal quantum dots (LA) with and without ZnS in the presence of the organic molecule is shown in Figure 31 (a):

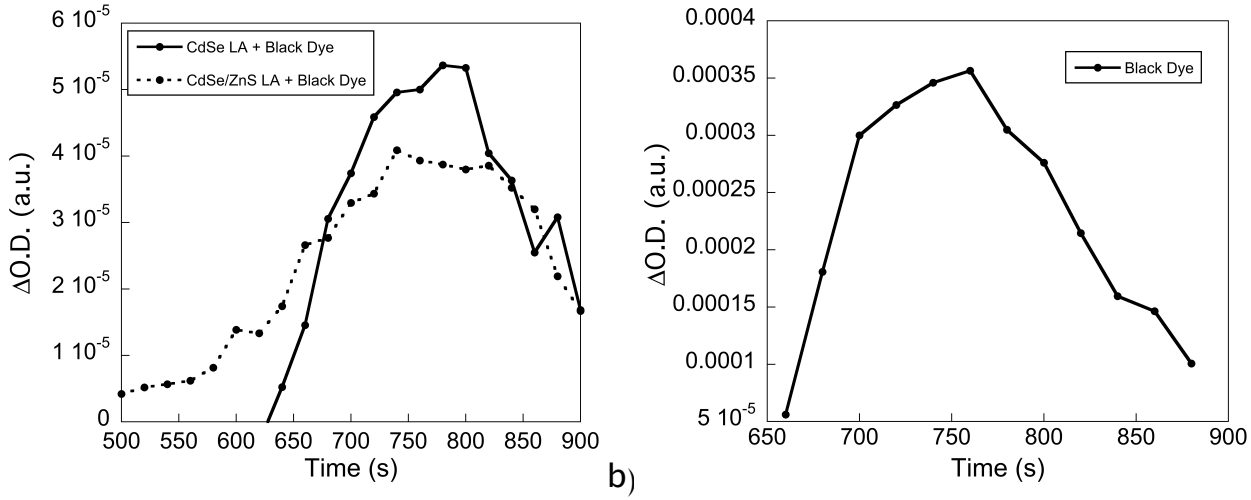

Figure 31. Transient absorption spectra of: (a) a CdSe-TiO_2 film deposited by linker adsorption technique, with and without ZnS, and sensitised with Black Dye. (b) Black Dye-TiO_2. The excitation wavelength was λ = 440 nm and the acquisition time 100 μs in all cases.

The characteristic CdSe transient absorption was not observed any more, and a new absorption band with maximum at λ = 780 nm has appeared. This transient absorption corresponds to the Black Dye one, as can be seen in Figure 31 (b). In the case of the CdSe/ZnS LA sample this band has also appeared, but is wider than without ZnS. The fact that the only transient species present in this new scenario was the black dye cation can be explained by the fact the the Black Dye is

regenerating the oxidised CdSe quantum dots, that means, that it is extracting the hole from the nanocrystal, and therefore, the organic molecule is the one which is in its oxidised form now. A representative scheme of all these reactions is depicted in Figure 32.

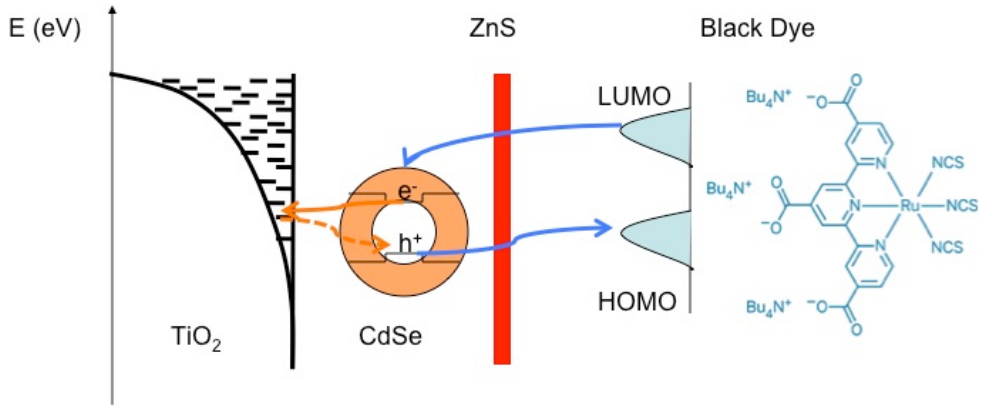

Figure 32. Scheme of the charge transfer reaction involving CdSe quantum dots coated with a thin layer of ZnS and with the Black Dye molecule.

The kinetics in samples prepared with the three methods, with and without ZnS, in the presence of the organic dye were measured (Figure 33).

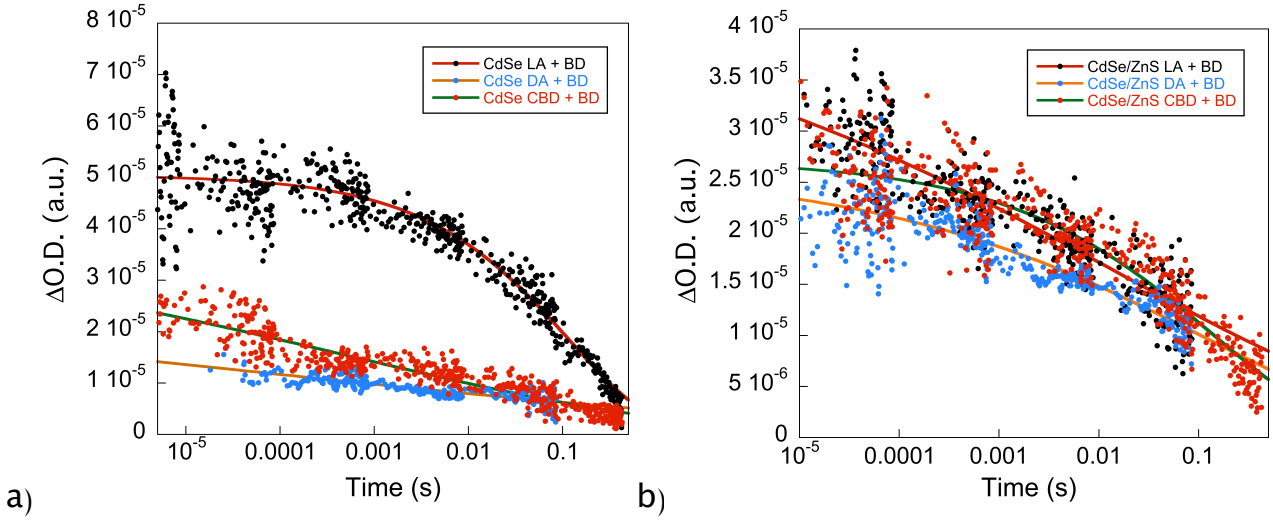

Figure 33. Transient absorption decay of CdSe quantum dots deposited by LA, DA and CBD (a) without ZnS and (b) with ZnS layer. The excitation and the probe wavelengths were λ = 440 and 780 nm, respectively.

From Figure 33 we can observe that the lifetime of the Black Dye cation lives longer in the case of LA rather than in DA and CBD. We must take into account that the dye molecule is absorbed both in the free titanium dioxide and in the quantum dot surfaces, due to the low QD adsorption. Therefore we could be observing a mix of the back-electron reaction of electrons in the TiO_2 conduction band and the Black Dye cation, and the hole extraction from the CdSe to the dye. In the case of CBD, the Black Dye is mainly absorbed in the CdSe, since with this technique a

higher nanocrystal load is achieved, and not many free titanium is left. For this reason, the transient observed should be mainly from regeneration of the semiconductor nanocrystal. The case of DA should be similar to the LA, since the load of quantum dots is quite similar. However, the dynamics and kinetics are more similar to the CBD case. This is not completely understood and it could be attributed to some experimental error in the measurement or a low absorption of the molecule in the film.

On the other hand, when a thin ZnS layer is deposited in between the nanocrystals and the free titanium dioxide, and the dye, the three decays become similar. The Black Dye is now anchored in the ZnS layer in all cases, and the dynamics and kinetics are similar independent of the quantum dot deposition method. The Black Dye cation lifetime is quite long in these cases. This might be due to the ZnS barrier between the electrons in the TiO_2 and quantum dots conduction bands and the molecule cation, which slow down back-electron reaction. This phenomena has been also observed in dye sensitized solar cells, when a thin alumina layer was deposited between the titanium dioxide and the dye. [20] The transient lifetime decays were fitted to the stretch exponential function. A summary of the parameters is shown in Table 1.

Table 1. Parameters extracted from the fitting to the stretch exponential function of the transient decays in Figure 33.

Sample	ΔO.D. (a.u.)	τ (s)	β	R
CdSe LA + BD	$5 \cdot 10^{-5}$	0.115	0.477	0.946
CdSe DA + BD	$3.42 \cdot 10^{-5}$	$3.38 \cdot 10^{-5}$	0.07	0.798
CdSe CBD + BD	$4.15 \cdot 10^{-5}$	$5.48 \cdot 10^{-3}$	0.123	0.929
CdSe/ZnS LA + BD	$4.48 \cdot 10^{-5}$	0.013	0.141	0.902
CdSe/ZnS DA + BD	$2.65 \cdot 10^{-5}$	0.118	0.221	0.876
CdSe/ZnS CBD + BD	$2.72 \cdot 10^{-5}$	0.142	0.357	0.914

4.4. Charge Recombination and Regeneration in CdS Quantum Dot Sensitized Solar Cells Deposited by EPD.

Mesoporous thin films of titanium dioxide were prepared and sensitised with CdS quantum dots by EPD. The films were prepared at the A. Zaban group in IBar-Ilan University. The charge recombination and regeneration kinetics were measured at ICIQ. The regeneration process is usually carried out in DSSC using a liquid electrolyte based in the redox couple I^-/I_3^-. However, this electrolyte can not be used in quantum dots due to the fast degradation that the Iodine/Iodide causes to

the quantum dots. For this reason the polysulfide electrolyte has been the most common redox mediator in this kind of solar cell although this is not as efficient as regenerator agent as I^-/I_3^-. Zaban and co-workers developed a coating method to protect the quantum dots from the Iodine/Iodide, keeping the regenerator properties of this electrolyte. This method consists of the electrochemical growth of a thin amorphous titanium dioxide layer between the CdS quantum dots and the electrolyte.[21] The idea is very similar to the one developed by Palomares et al. in dye sensitized solar cells.[20] The transient absorption spectra of CdS quantum dots with and without the coating is presented in Figure 34 (a).

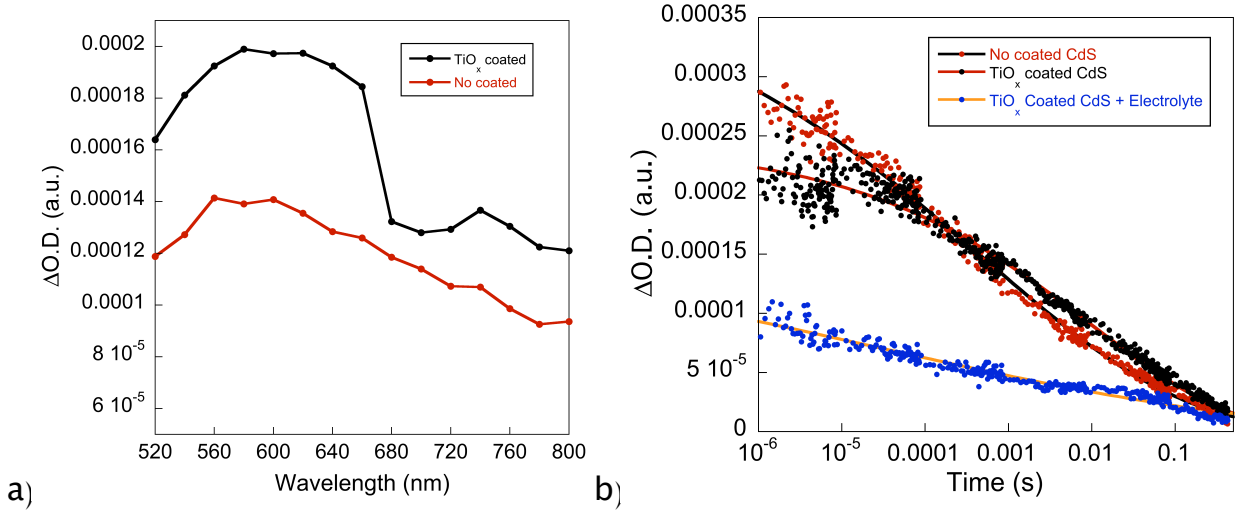

Figure 34. Transient absorption spectra (a) of CdS quantum dots with and without the presence of amorphous titanium dioxide layer. (b) Transient lifetime decay of CdS quantum dots coated and non-coated and the coated sample in presence of I^-/I_3^- based electrolyte. The excitation wavelength in all cases was λ = 440 nm. The acquisition time in the spectra was 1 ms, and the probe wavelength in the decay was λ = 560 nm.

The transient absorption spectra of samples coated and non-coated showed similar features. The coated sample presented higher transient absorption. This behaviour has been previously shown with ZnS coating. The kinetics were measured at λ = 560 nm. The oxidised CdS had a lifetime 2 orders of magnitude slower when it was coated, as has been seen for other coatings on quantum dots. In addition, I^-/I_3^- based electrolyte was added to the coated sample, and the lifetime of the oxidised CdS was dramatically reduced. The electrolyte has efficiently regenerated the oxidised quantum dot. The parameters extracted from the stretch exponential fitting are shown below:

$$\text{No coated CdS: } \Delta O.D. = 3.98\cdot10^{-4}\exp\left(-\frac{t}{5.06\cdot10^{-4}}\right)^{0.18};\ R = 0.996$$

Coated CdS: $\Delta O.D. = 2.44 \cdot 10^{-4} \exp\left(-\frac{t}{0.010}\right)^{0.26}$; R = 0.989

Coated CdS + electrolyte: $\Delta O.D. = 1.96 \cdot 10^{-4} \exp\left(-\frac{t}{2.3 \cdot 10^{-5}}\right)^{0.09}$; R = 0.976

So, we can conclude that the recombination kinetics of electrons in the TiO_2 conduction band and the oxidised CdS take place in milliseconds and the regeneration of the oxidised species by the electrolyte take place in microseconds. Therefore, the electrolyte is regenerating the sensitiser before it recombines. And thanks to the amorphous titanium layer, the nanocrystals are not damaged by the Iodide/Iodine electrolyte.

The dye molecule N719 (molecular structure showed previously in Figure 2) was added to the CdS–TiO_2 films with two purposes: on the one hand to increase the light harvesting in the visible range, where the CdS can not absorb, and thus, increase the charge injection; on the other hand, to improve the charge regeneration, since, as it has been seen in previous sections, the addition of organic molecules to the quantum dot surface contributes to the hole extraction from the nanocrystal Valence Band. The transient spectra of the coated and non-coated samples in the presence of the dye are shown in Figure 35.

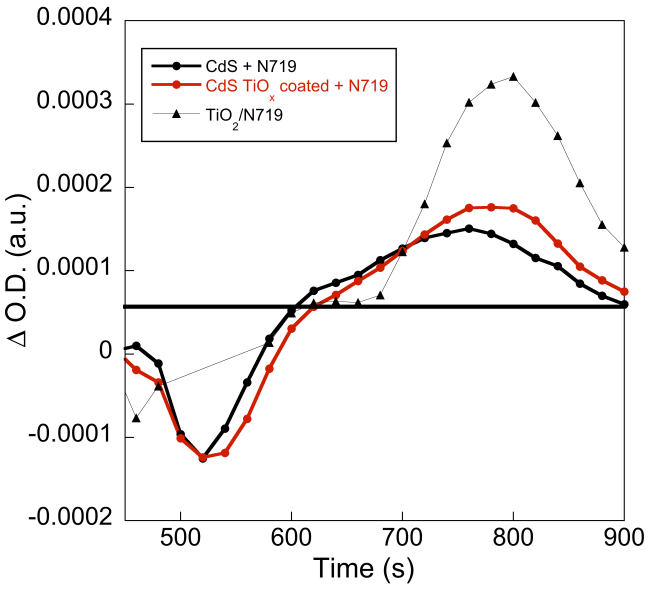

Figure 35. Transient absorption spectra of TiO_2-CdS films TiO_x coated and non-coated, and sensitised with N719 dye molecule. The transient absorption spectrum of the N719 in TiO_2 is also included. The excitation wavelength CdS and N719 films were 440 and 535 nm, respectively. The acquisition times were 1 ms and 0.5 ms for CdS and N719, respectively.

As can be clearly seen, the CdS spectrum features are not present at 1 ms already, and the only transient specie formed is the radical cation of the N719 dye.

The molecule has extracted the hole from the quantum dot, regenerating the nanocrystal. The kinetics are shown in Figure 36. The N719 cation lifetime is longer than the oxidised CdS lifetime not only when it is coated but when is not as well. Consequently, the results reveal significantly faster hole extraction from the oxidised quantum dots by the dye, which contributes to the good device performance. The addition of the N719 dye has a positive effect on the kinetic competition between the regeneration and the recombination processes. Since, the lifetime of the oxidised specie is extended, the electrolyte has more time to regenerate it. The parameters from the stretch exponential fits are shown below:

CdS without coating: $\Delta O.D. = 3.98 \cdot 10^{-4} \exp\left(-\frac{t}{5.06 \cdot 10^{-4}}\right)^{0.18}$; R = 0.996

N719 without coating: $\Delta O.D. = 2.28 \cdot 10^{-4} \exp\left(-\frac{t}{9.54 \cdot 10^{-3}}\right)^{0.17}$; R = 0.987

CdS with coating: $\Delta O.D. = 2.44 \cdot 10^{-4} \exp\left(-\frac{t}{0.01}\right)^{0.26}$; R = 0.989

N719 with coating: $\Delta O.D. = 1.97 \cdot 10^{-4} \exp\left(-\frac{t}{0.197}\right)^{0.33}$; R = 0.981

In addition, the kinetics were also measured at 560 nm, where the CdS transient specie absorbs, and at 780 nm, where the N719 cation absorb (Figure 36). At 560 nm, we can only observe the bleach of the CdS decay, that corresponds to the CdS due to the fast hole regeneration. The negative signal feature has been previously reported for DSSC as a feature of hole transfer between dyes. However, if we look at 780 nm, the N719 cation lifetime is in milliseconds time scale. The hole in the CdS is extracted very quickly by the molecule. The presence of the amorphous coating increase the differences in lifetime, that is, the CdS lifetime is shorter than without the coating, and the N719 cation has longer lifetime than without the coating. This behaviour has been observed for other quantum dots with other coatings. In conclusion, the conformal amorphous TiO_x layer not only creates the possibility for sequential co-sensitisation but also slows the back electron transfer to the dye. Moreover, the addition of the N719 molecule on the TiO_x coating enhance the CdS regeneration and increase the N719 cation lifetime, making it suitable of efficient regeneration by the electrolyte.

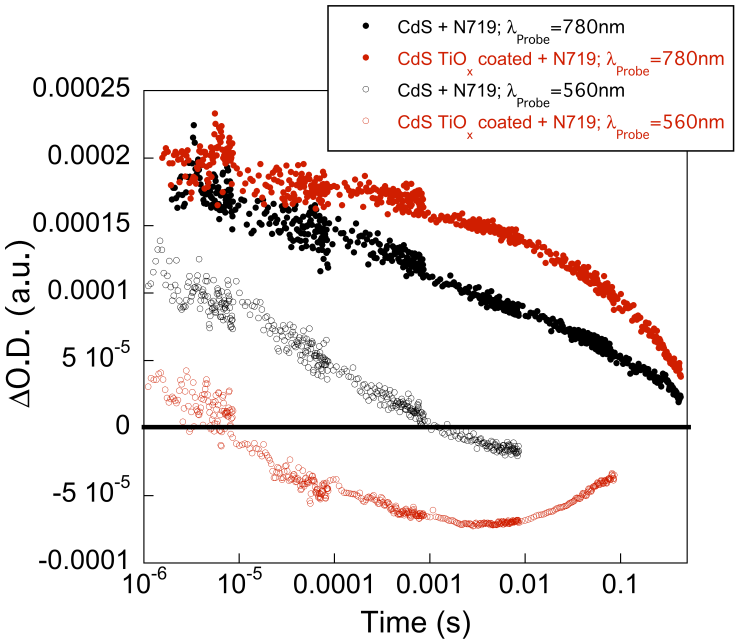

Figure 36. Transient absorption decay of CdS coated and non-coated in the presence of N719 measured at two different probes wavelengths, 560 nm where the oxidised CdS absorb and at 780 nm where the N719 cation absorb. The excitation wavelength in all cases was 440 nm.

In order to check the N719 cation regeneration a I^-/I_3^- based electrolyte was added to the TiO_2–CdS–TiO_x–N719 system, see Figure 37. The N719 cation lifetime, when the electrolyte is added, is 10 times faster. Which means that the regeneration of the N719 by the electrolyte is a magnitude order faster than the recombination with the TiO_2 or the CdS, and several orders of magnitude slower than the hole extraction from the CdS. This indicates that the devices built with this architecture are designed to work efficiently, since the kinetic competition between the different thermodynamical processes are adequately controlled.

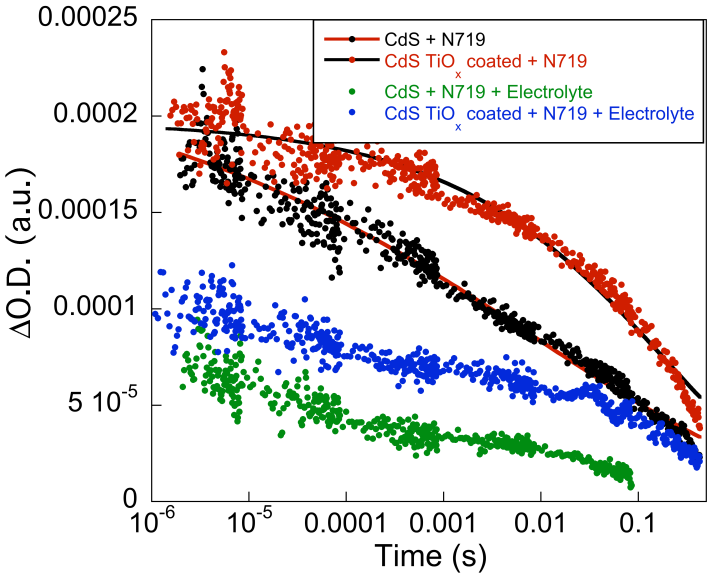

Figure 37. Transient absorption decay of CdS with and with out coating, sensitized with N719, and with and without electrolyte. All transients were recorded at 780 nm and excited at 440 nm.

5. Conclusions.

Semiconductor nanocrystals were sensitised and tested as electron acceptors and donors. The electron transfer dynamics for MSqb–CdSe quantum dots were studied. In this case, the organic dye was able to inject electrons in the nanocrystals conduction band faster than the excited states deactivation (< 0.1 ns). The back electron reaction kinetics were measured, and it was found to be on the millisecond time scale. The recombination kinetics were measured in solution and thin films, showing similar behaviour.

Nanocrystal CdSe quantum dots were linked to titanium dioxide nanoparticles by means of a molecular linker. In this case, three different sized nanocrystals showed electron injection into the TiO_2 conduction band. The recombination kinetics were investigated, showing that the quantum dot size has influence not only in the injection kinetics but also in the recombination kinetics.

The photo–induced charge recombination in quantum dot sensitised TiO_2 films, deposited by the SILAr technique, have been investigated. It has been found that a ZnS coating in co–sensitised CdS + CdSe nanocrystals has a beneficial effect in the recombination kinetics. This ZnS layer is passivating trap states in the nanocrystal surface, and thus, enhancing the formation of long–live oxidised CdSe nanocrystals. The transient lifetime decay of CdSe has been increased by 1.000 times with the inclusion of this passivating layer. On the other hand, it has been checked, for PbS nanocrystals, that the addition of successive SILAR cycles to increase the light harvesting, is limited by the films saturation, which promote an increase in the recombination kinetics.

The charge recombination kinetics has been also compared for CdSe quantum dots deposited by Direct Adsorption, Linker adsorption and Chemical Bath Deposition. The latter, in spite of showing an increase in nanocrystal load on the films, compared with the other two techniques, results in faster recombination kinetics. This is probably due to the direct contact of nanocrystals with the metal oxide that this technique causes. It has been confirmed that the addition of a ZnS passivating layer to CdSe surface states, slows down the recombination dynamics for quantum dots deposited by Direct Adsorption and Linker Adsorption, but not for Chemical Bath Deposition, where no change was found.

It has been also investigated the role of ruthenium molecular dye co–sensitised in the quantum dot films. It has been found a fast photo–induced hole transfer from quantum dots to the dye molecules, in all deposition methods, that

act as regenerating agents of the quantum dot sensitisers and promote charge separation in the dye/QD/TiO_2 system.

Finally, co-sensitised TiO_2 films with CdS quantum dots, using Electrophoretic Deposition, and a ruthenium molecular dye, were studied. The addition of the molecular dye has a beneficial effect in the oxidised nanocrystals regeneration, as it has already seen for quantum dots deposited by other techniques. In this case, an amorphous TiO_2 coating was used with 2 principal purposes. On the one hand, to passivate superficial trap states in the nanocrystals and, on the other hand, to increase the stability of the nanocrystals in the presence of Iodide/Iodine based electrolytes. This configuration offers a method of slowing the interfacial charge recombination and thus allowing efficient charge regeneration.

Bibliography.

1. G. Porter, *Proc. R. Soc. A*, 1950, **200**, 284-300.
2. Y. Tachibana, J. E. Moser, M. Grätzel, D. R. Krug and J. R. Durrant, *J. Phys. Chem.*, 1996, **100**, 20056-20062.
3. E. Palomares, J. N. Clifford, S. A. Haque, T. Lutz and J. R. Durrant, *J. Am. Chem. Soc.*, 2003, **125**, 475-482.
4. S. A. Haque, Y. Tachibana, D. R. Krug and J. R. Durrant, *J. Phys. Chem. B*, 1998, **102**, 1745-1749.
5. J. Nelson, S. A. Haque, D. R. Krug and J. R. Durrant, *Phys. Rev. B*, 2001, **63**, 205321.
6. T. M. Clarke, F. C. Jamieson and J. R. Durrant, *J. Phys. Chem. C*, 2009, **113**, 20934-20941.
7. H. J. Lee, J.-H. Yum, H. C. Leventis, S. M. Zakeeruddin, S. A. Haque, P. Chen, S. I. Seok, M. Gratzel and M. K. Nazeeruddin, *J. Phys. Chem. C*, 2008, **112**, 11600-11608.
8. W. W. Yu, L. Qu, W. Guo and X. Peng, *Chem. Mat.*, 2003, **15**, 2854-2860.
9. Y.-L. Lee and Y.-S. Lo, *Adv. Func. Mater.*, 2009, **19**, 1-6.
10. H. Lee, H. C. Leventis, S.-J. Moon, P. Chen, S. Ito, S. A. Haque, T. Torres, F. Nüesch, T. Geiger, S. M. Zakeeruddin, M. Graetzel and M. K. Nazeeruddin, *Adv. Func. Mater.*, 2009, **19**, 2735-2742.
11. L. J. Diguda, Q. Shen, J. Kobayashi and T. Toyoda, *Appl. Phys. Lett.*, 2007, **91**, 023116.
12. S. Tatay, S. A. Haque, B. O'Regan, J. R. Durrant, W. J. H. Verhees, J. M. Kroon, A. Vidal-Ferran, P. Gavina and E. Palomares, *J. Mat. Chem.*, 2007, **17**, 3037-3044.
13. K. Tvdy, P. A. Grantsuzov and P. V. Kamat, *PNAS*, 2011, **108**, 29-34.
14. J. Nelson, *Phys. Rev. B*, 1999, **59**, 15374-15380.
15. H. M. Pathan, B. R. Sankapal, J. D. Desai and C. D. Lokhande, *Mat. Chem. Phys.*, 2002, **78**, 11-14.
16. W. G. J. H. M. v. Sark, P. L. T. M. Frederix, D. J. V. d. Heuvel and H. C. Gerritsen, *J. Phys. Chem. B*, 2001, **105**, 8281-8284.
17. H. C. Leventis, F. O'Mahony, J. Akhtar, M. Afzaal, P. O'Brien and S. A. Haque, *J. Am. Chem. Soc.*, 2010, **132**, 2743-2750.
18. I. Mora-Sero, S. Gimenez, F. Fabregat-Santiago, R. Gomez, Q. Shen, T. Toyoda and J. Bisquert, *Acc. Chem. Res.*, 2009, **42**, 1848-1857.
19. M. K. Nazeeruddin, P. Pechy, T. Renouard, S. M. Zakeeruddin, R. Humphry-Baker, P. Comte, P. Liska, L. Costa, V. Shklover, L. Spiccia, G. B. Deacon, C. A. Bignozzi and M. Grätzel, *J. Am. Chem. Soc.*, 2001, **123**, 1613-1624.
20. E. Palomares, J. N. Clifford, S. A. Haque, T. Lutz and J. R. Durrant, *Chem. Comm.*, 2002, 1464-1465.
21. M. Shalom, S. Dor, S. Ruhle, L. Grinis and A. Zaban, *J. Phys. Chem C*, 2009, **113**, 3895-3898.

Chapter 3 - Photo-Induced Charge Transfer Reactions In P3HT/CdSe Quantum Dots Films.

Important research efforts into nanocrystal/polymer solar cells have been carried out in order to increase the device efficiency. Several approaches have been developed in order to overcome the low light-to-energy conversion that these devices has presented up to now. Even though, quantum dot / polymer solar cells has only lead to power conversion efficiencies of 4.1% under standard solar simulated light irradiation. However, less attention has been paid to the study of the fundamental interfacial charge transfer reactions between the quantum dots and the polymer that limits the device performance. We have studied the charge transfer reactions at the interface between the (P3HT) polymer and the CdSe semiconductor nanocrystals employing spectroscopic techniques such as Time Correlated Single Photon Counting (TCSPC) and L-TAS. The relationship between film morphology and charge recombination dynamics was studied also.

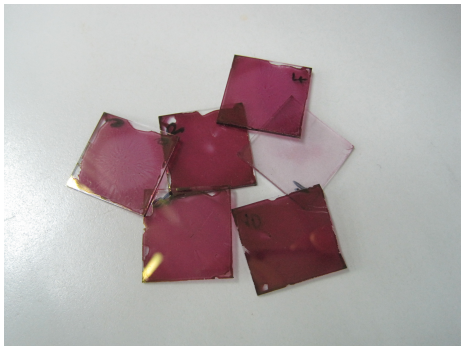

TABLE OF CONTENTS

1. Objectives.

Since the demonstration of photo-induced charge generation in polymer:nanocrystal composite films, an increasing number of different nanocrystal:polymer hybrid solar cells have been investigated. During the last decade efficiencies up to 4% have been achieved combining different semiconductor nanocrystal materials and morphologies with several semiconductor polymers. However, considerably less attention has been paid to the photo-induced processes occurring in these films. This chapter aims to shed more light on the charge transfer reactions that take place at the interface between CdSe nanocrystals and the semiconductor polymer P3HT.

In particular, we have focused on the study of the charge separation and undesired charge recombination reactions by monitoring these processes occurring at the nanocrystal:polymer interface using spectroscopic techniques. The use of fluorescence spectroscopy to study the charge transfer processes has been employed in different fields from biological labeling to photovoltaics. In addition, Time Correlating Single Photon Counting (TCSPC) has been widely employed in the study of charge injection process in dye sensitised solar cells during the last decades. For this reason, we believe that this technique can be very useful in the study of charge separation processes in such composite films. On the other hand, the Laser-Transient Absorption Spectroscopy has been found to be a powerful tool in the study of charge recombination dynamics not only in dye sensitised solar cells but also in organic photovoltaics. The combination of both techniques will provide substantial information on the charge transfer reactions that take place at the interface of both materials.

We first study the photo-induced processes as a function of the quantum dot concentration. It is well stablished the strong dependency that device efficiencies show upon quantum dots concentration. The charge separation and charge recombination processes will be studied for P3HT:CdSe quantum dot blend films at different ratios. The relationship between quantum dot concentration, charge recombination and film morphology will be discussed as well.

Following this study, the influence of the capping molecules anchored to the CdSe quantum dot surface over the charge separation and charge recombination dynamics in CdSe:P3HT blend films is also reported. The modification of this passivating layer on the nanocrystal surface is key in quantum dot/polymer interfaces to achieve efficient charge separation and slow back electron transfer. We

check if the dipole moment that these molecules possess is able to modify the interfacial charge transfer dynamics and if they are providing further effects.

Finally, we studied which is the role of the nanomorphology of semiconductor nanocrystals in the interfacial charge transfer processes in hybrid nanocrystal:polymer bulk heterojunction thin films. CdSe quantum dot, nanorods and tetrapods will be mixed in different ratios with P3HT. The charge separation and charge recombination reactions at the interface of the different nanocrystals and the polymer are investigated.

2. Practical considerations.

2.1. Time Correlated Single Photon Counting (TCSPC).

The time correlated single photon counting is a technique that allows time-domain lifetime measurements. An excitation source, in our case a pulsed diode laser at 405 nm, excites the sample and the emission time is measured. TCSPC is a digital technique, counting photons which are time-correlated in relation to the excitation pulse. The key of this method is a time-to-amplitude converter (TAC).

The sample is repetitively excited using the pulse light source. Each pulse is optically monitored, by a high-speed photodiode or photomultiplier, to produce a start signal which is used to trigger the voltage ramp of the TAC. The voltage ramp is stopped when the first fluorescence photon from the sample is detected. The TAC provides an output pulse whose voltage is proportional to the time between the start and stop signals. A multichannel analyser converts this voltage to a time channel using an analog-to-digital converter. The addition of many pulses, the multichannel analyser builds up a probability histogram of counts versus time channels. The experiment is continued until one has collected a determined number of counts or a desired time. The histogram of photon arrival times represents the intensity decay of the sample.[1]

We use a LifeSpec-ps apparatus from Edinburgh Instruments(c), with wavelength response from 200 to 850 nm and lifetime range from 350 picoseconds to 10 microseconds. Appropriate filters can be placed in front of the detector channel in order to block undesired laser reflections. TCSPC is used in order to measure emission lifetimes. But, electron injection experiments can be performed with this equipment too. The emission decay of a material with fluorescent properties (dyes, semiconductor polymers, semiconductor nanocrystals) can be measured for a fix number of counts. Then, we put this fluorescent material in intimate contact with an electron acceptor material. Finally, we measure the emission lifetime of the fluorescent material in contact with the electron acceptor for the same acquisition time that it took to measure the emission lifetime of the fluorescent material alone. The comparison between the two emission decays may give us information about the electron transfer process.

2.2. Fitting of Emission Decay.

The LifeSpec-ps apparatus contains software which is able to fit the decays to de-convoluted functions (Equation 1).

$$F(t) = A + \sum_i B_i \cdot \exp\left(-\frac{t}{\tau_i}\right) \qquad \text{Eq. (1)}$$

,where A and B are constant and τ is the lifetime.

This expression is used to obtain the emission lifetime of a material. Usually, an excited material shows several de-activation mechanisms.[1, 2] In this case, the decays have more than one radiative recombination mechanism, and this is expressed by more than one emission lifetime. For example, for the CdSe quantum dots we have measured up to three different mechanisms with our instrument, but it has been reported up to five, using equipment with faster instrument response. Each one of the processes have a different lifetime with a different relative weight in the overall complete decay. Very often, a percentage is presented with the lifetime for multiexponential decays, indicating the relative weight of this lifetime in the complete decay.

When the lifetime decay of different samples are going to be compared, it is worth having an unique value. For decays which present more than two mechanisms or where relative weight in the decay is very similar, an average lifetime[3] can be calculated employing Equation 2.

$$\langle \tau \rangle = \frac{\sum_i B_i \tau_i^2}{\sum_i B_i \tau_i} \qquad \text{Eq. (2)}$$

,where $\langle \tau \rangle$ is the average emission lifetime, B_i is a constant and τ_i the emission lifetime.

However, if the emission decay shows only two components, where one of them has a smaller relative weight than the other, the lifetime can be calculated treating the decay as mono-exponential,[1] using Equation 3.

$$I(t) = I_0 \cdot \exp\left[-\left(\frac{\tau}{t}\right)\right] \qquad \text{Eq. (3)}$$

,where $I(t)$ is the emission intensity in function of time, I_0 is the emisison intensity at $t=0$ and τ is the emission lifetime.

2.3. Mathematical Procedure to Estimate Charge Injection Kinetics.

Sara E. Koops and James R. Durrant developed a method to calculated electron injection kinetics employing TCSPC for dye sensitised solar cells.[4] In this method, by the use of a non-injecting reference film and a simple stretched

exponential fitting procedure with only two fitting parameters it is possible to resolve electron injection half-times down to the TCSPC instrument response. This provides a potentially cheaper and experimentally easier approach to monitor such dynamics compared to more widely used ultrafast pump/probe laser spectroscopy.

In this procedure the emission decay of a reference sample is measured. In this reference sample electron transfer processes must be avoided. For example, in dye sensitised solar cells a mesoporous film of a wide bandgap metal oxide (alumina or zirconia) is used to adsorbed a dye. The dye will not be able to inject electrons in the high conduction band of the isolator, therefore, all the emission will come from the radiative relaxation of the excited dye. In our case, a pristine film of P3HT polymer will be the reference.

The reference decay is fitted to a stretch exponential function (Equation 4). From the fitting we can obtain the signal amplitude (ΔOD), the lifetime (τ) and the stretch exponential factor (β).

$$F(t) = \Delta OD \cdot \exp\left(-\frac{t}{\tau}\right)^{\beta} \qquad \text{Eq. (4)}$$

The emission decay of the investigated material is now measured in the presence of the electron acceptor. For example, in the case of dye sensitised solar cells the emission decay of the dye is measured again but on titania. In our case, the polymer will be measured but forming a mix with the nanocrystals. The decay is fitted again to equation 4, but in this case ΔOD will be fixed to the value previously obtained from the reference. Thus, the function will have only two free parameters, τ and β. The obtained τ is thus correlated to the injection process, and is defined as the time at which the amplitude of the signal decay to half the initial amplitude of the non-injecting data.

This procedure enables fits to the experimental data to be undertaken with only two free fitting parameters, thereby greatly increasing the reliability and validity if the fitting procedure.

A more complete description of the signal treatment can be found in the Annexes.

3. Experimental section.

The colloidal CdSe quantum dots were prepared by the traditional hot-injection method.[5] In brief, 0.4 g of Se powder (99.99%) was solved in 10 mL Tri-Octylphosphine (TOP) (90%) and 0.2 mL of anhydrous Toluene. On the other hand, 20 g of Tri-Octylphosphine Oxide (TOPO) (90%) and 0.25 g of Cadmium acetate (97%) were placed in a three-necked flask. At 280ºC the Se solution was quickly added to the Cadmium solution. The reaction was carried out for 15 minutes. The nanocrystals were precipitated and centrifuged in Methanol. This cleaning step was repeated 3 times.

The CdSe nanorods were prepared mixing 0.2 g of CdO, 0.71 g of TetraDecyl Phosphonic acid (TDPA), 0.16 g of Hexylphosphonic acid (HDA) and 3 g of TOPO in a three neck flask to degas for 60 minutes and purged 30 minutes with Argon. Then, the mixture is heated up to 300ºC until it becomes colourless. At this point, 1.5 g of TOP was added, and we waited 10 minutes for the TOP to be fully mixed with the rest of the compound. On the other hand, 0.062 g of Se and 0.351 g of TOP were mixed under Argon conditions until Se was completely dissolved. The Selenium solution was injected into the Cd solution at 300ºC. The final solution was stirred fast and the nanocrystals were left to grow for 5 minutes. The reaction was stoped removing the heat and cooling down to 70ºC. At this temperature 4 mL of Anhydrous Toluene and 8 mL of isopropyl alcohol (IPA) were added to the solution. The nanocrystals were recovered by centrifugation. This process was repeated 3 times for complete nanocrystal cleaning.[6]

The CdSe tetrapods were synthesised with the same procedure of the nanorods just changing the amount of the reagents of the Cd solution. In this case, 0.4 g of CdO, 1.4 g of TDPA, 0.32 g of HPA and 6 g of TOPO were mixed to obtain the Cd solution. The rest of the procedure remained exactly the same.[6]

After that, the CdSe nanocrystals were re-disolved in the desired capping molecule (Pyridine or molecules with end-thiol groups), in the presence of anhydrous Toluene, for ligand exchange. The solutions were refluxed at 90ºC for 12 hours under inert conditions. Finally, the nanocrystals were precipitated and centrifuged in Hexane 3 times in order to remove the non-linked capping molecules. Finally, the quantum dots were dissolved in Chloroform at 30 mg/ml concentration.

The poly(3-hexylthiophene-2,5-diyl) (P3HT) was purchased from Rieke Metals, Inc.(c). The polymer poses highly regioregular Electronic Grade (typical

results between 90% and 94% regioregularity). The average molecular weight is 50.000 g/mol.

P3HT/CdSe thin films were prepared over pre-cleaned 2x2 cm glass substrates by spin coating. P3HT and CdSe solutions were mixed at the desired proportions and spin cast at 1000 r.p.m. for 60 seconds. Then, the films were annealed in a hot plate at 150ºC for 20 minutes. The thickness analysis carried out using a profilomter with AFM technology indicate that the thickness of the films was around 100 nm independent on the nanoparticle concentration.

The UV-Visible and fluorescence spectra were recorded, under ambient conditions, using a 1 cm path length quartz cell (for the CdSe solution) or a holder (for films) on a Shimadzu UV spectrophotometer 1600 and an Aminco-bowman Series 2 luminescence spectrometer with temperature controller, respectively.

Time Correlated Single Photon Counting experiments were carried out with Lifespec picosecond fluorescence lifetime spectrophotometer from Edinburgh Instruments (C). As excitation source a diode laser with 405 nominal wavelength was used. The instrument response measure at the FWHM was below 350 ps. The laser power was 5 mW. The spot area was 3 mm^2.

The electrochemical data were obtained employing a conventional three-electrode cell connected to a CH Instruments(c) 660c potentiostat-galvanostat. The working electrode consisted of a carbon while auxiliary electrode was platinum. The reference electrode was Ag/AgCl. The solvents used were purged under argon prior the use. Cyclic voltametries were carried out in the presence of 0.1 M TBA·PF_6 supporting electrolyte.

The recombination kinetics were measured for the P3HT/CdSe films with L-TAS experiments. They were recorded using a home-built system as reported before. The samples were measured with a probe wavelength of 980 nm and an excitation source of 470 nm. The laser intensity pulse was 86.7 μJ/cm^2, repetition rate 1 Hz.

Transmission electron microscopy measures were done using JEOL 1011 microscope. Atomic Force Microscopy was also used. A Molecular Imaging Pico SPMII apparatus was used to obtain AFM images of the topography of the P3HT/CdSe blend films.

4. Results.

4.1. Influence of the Quantum Dot Concentration.

Semiconductor CdSe quantum dots were synthesised at ICIQ. The nanocrystals showed a wavelength at the maximum of the last excitonic peak of 565 nm, obtaining a mean quantum dot size of 3.4 nm by the procedure previously described in this Thesis. This nanocrystal size was confirmed with the analysis of TEM image (see Figure 1). This analysis gave an average size of 3.5 ± 0.5 nm after 50 measurements.

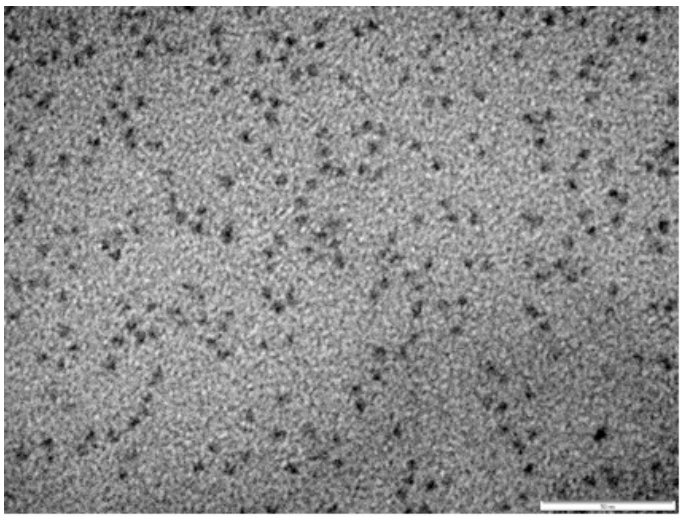

Figure 1. TEM image of the CdSe nanocrystals dispersed in Chloroform. The scale bar is of 50 nm.

The absorption and emission spectra of CdSe quantum dots is illustrated in Figure 2. The emission spectrum shows a maximum at 605 nm.

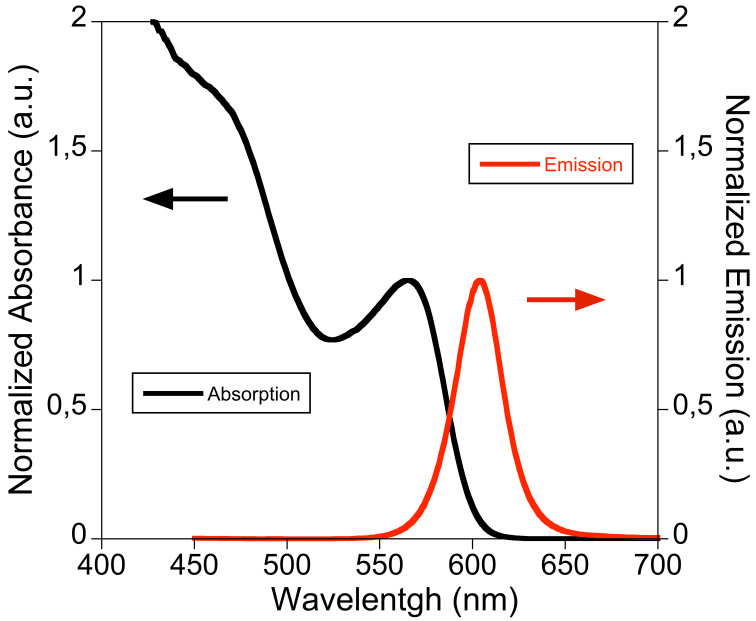

Figure 2. UV-Vis absorption and emission spectra of CdSe quantum dots in Chloroform. The excitation wavelength for the emission spectrum was λ = 405 nm.

The emission spectrum showed a narrow band at the maximum wavelength, with 30 nm of Full Width at Half Maximum (FWHM). This is a typical value, from which we can assume monodisperse size of quantum dots.[7]

The decay curve of the exciton emission is depicted in Figure 3. The emission intensity recorded at the emission maximum exhibited a multi-exponential decay and was analysed using a de-convoluted fit.

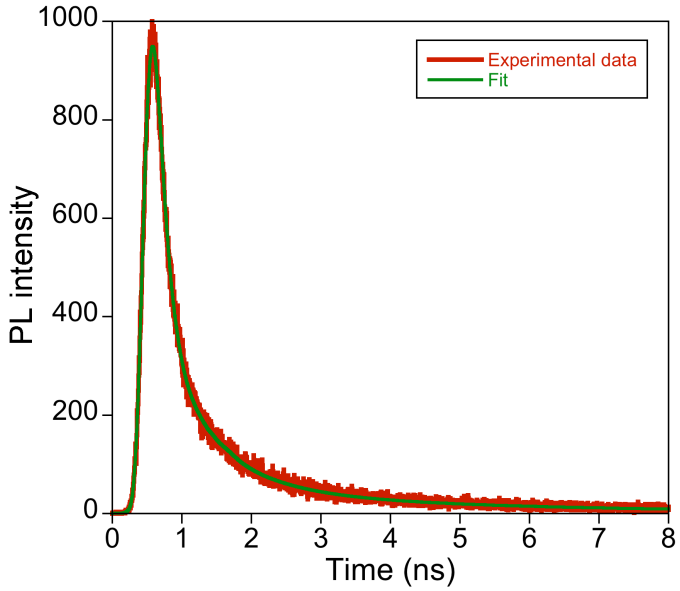

Figure 3. Photoluminiscence decay of CdSe quantum dots in Chloroform and the de-convoluted fit. The excitation wavelength for the emission decay was λ = 405 nm, the probe wavelength was λ = 605 nm

The emission decay parameters of the CdSe quantum dots were obtained from the fitting of the experimental points, and are shown in Table 1. The origin of multiexponential emission decay of nanocrystal semiconductors in solution has been previously studied in detail and ascribed to the trapping sites within the nanocrystal surface.[2, 8] These surface defects give rise to trap states that lie within the band gap, and are the reason responsible for these characteristic emission dynamics.

Table 1. Fluorescence decay fitted with three exponential kinetic. The relative % are the percentage for each τ in the decay. A and B are constants. And χ is the goodness of fit.

τ_i	Value (ns)	B_i	Value	Rel %
τ_1	0.1	B_1	0.025	(41.03)
τ_2	3.95	B_2	0.00044	(28.3)
τ_3	0.79	B_3	0.0024	(31.5)
χ = 1.14			**A =** 0.85	

The E_{0-0} transition has been found to be of 2,16 eV from the intersection of the absorption and emission spectra. Cyclic voltammetry of the pyridine coated CdSe quantum dots was carried out. A oxidation potential of 1.05 V vs. KCl saturated Ag/AgCl electrode was obtained. This potential is 5.95 eV vs. vacuum. Hence, the reduction potential has been estimated to be 3.79 eV by subtracting the E_{0-0} transition to the oxidation potential.

The P3HT from Rieke Metals, Inc.(c). was used in anhydrous Chlorobenzene and spin cast over glass substrates. The molecular structure of the P3HT polymer is presented in Figure 4.

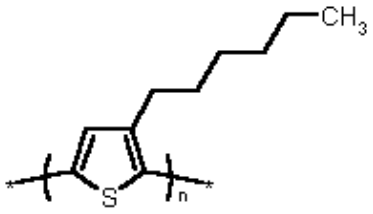

Figure 4. Molecular structure of the P3HT semiconductor polymer.

Morphology studies on films have revealed that the crystallinity of P3HT is increased upon thermal treatment, resulting in stronger interchain interactions and enhanced hole mobility. The crystalline properties of P3HT can be followed by UV-Vis absorption, since the absorption spectrum of P3HT films show significant changes after thermal annealing. It is known, that the unannealed films have a maximum absorbance at ~485 nm, and two shoulders can be also observed at 550 and 610 nm. The intrachain exciton ($\pi - \pi^*$ transitions) is responsible for the two first features, while the latter has been assigned to a regioregular P3HT interchain excitation. After annealing, the two shoulders become more pronounced and the absorbance maximum red-shifts up to 525 nm. The interchain excitation at 610 nm does not shift after annealing. All three P3HT transitions show an increase in oscillator strength upon annealing, which has been attributed to the improved chain stacking and crystallinity of the annealed films.[9-11] The absorption spectrum of an annealed film of P3HT showing a maximum absorbance at 525 nm and a lowest energy band at 610 nm is displayed in Figure 5 (a).

The emission spectrum is also shown. This displays a emission maximum located at λ = 670 nm. The fluorescence decay is depicted in Figure 5 (b). The emission intensity recorded at the emission maximum exhibited a bi-exponential decay and was analysed using a de-convoluted fit. The emission decay parameters of the P3HT were obtained from the fitting of the experimental points, and are shown below:

$$F(t) = 0.781 + 0.00148 \cdot \exp\left(-\frac{t}{0.542}\right) + 0.0237 \cdot \exp\left(-\frac{t}{0.118}\right); \chi = 0.953$$

, where τ is in ns, and the relative percentage of each τ is 22.3 and 77.7, respectively.

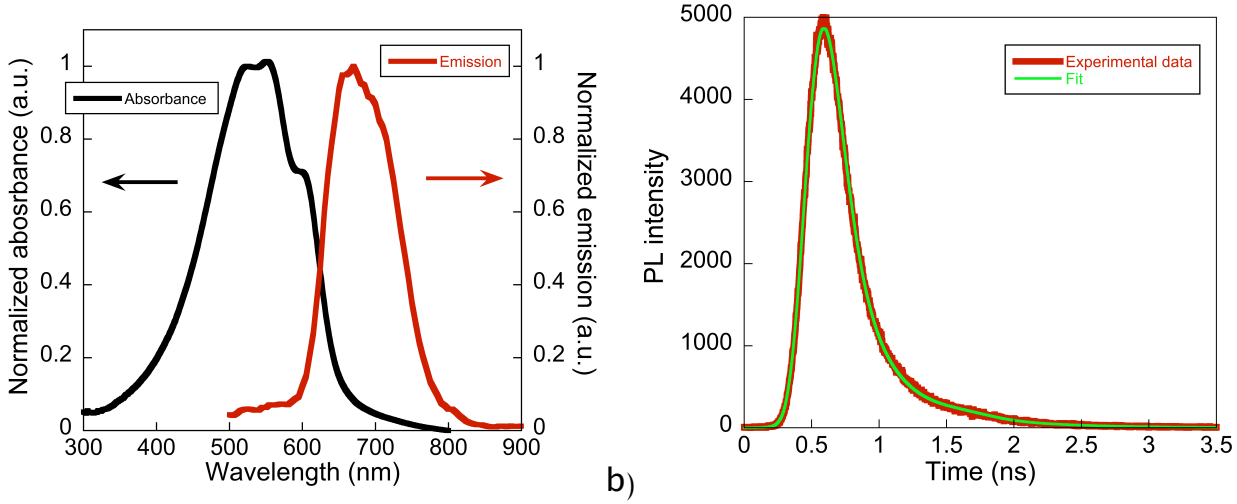

Figure 5. UV-Vis absorption and emission spectra (a) and the emission decay (b) of a P3HT annealed thin film. The excitation wavelength for the emission spectra and decay was λ = 405 nm, and the probe wavelength for the decay was λ = 670 nm.

The E_{0-0} transition has been found to be approximately of 1.99 eV. The P3HT values of highest occupied molecular orbital (HOMO) and lowest unoccupied molecular orbital (LUMO) vary notably in the bibliography, depending on the measuring and preparation methods. Typically, a LUMO of 3.1 eV and a HOMO of 5 eV from the vacuum level have been assigned.[12, 13] Therefore, the energetic scheme of the donor polymer and the acceptor quantum dots is depicted in Figure 6. In this, the charge transfer reactions that are going to be studied are also indicated.

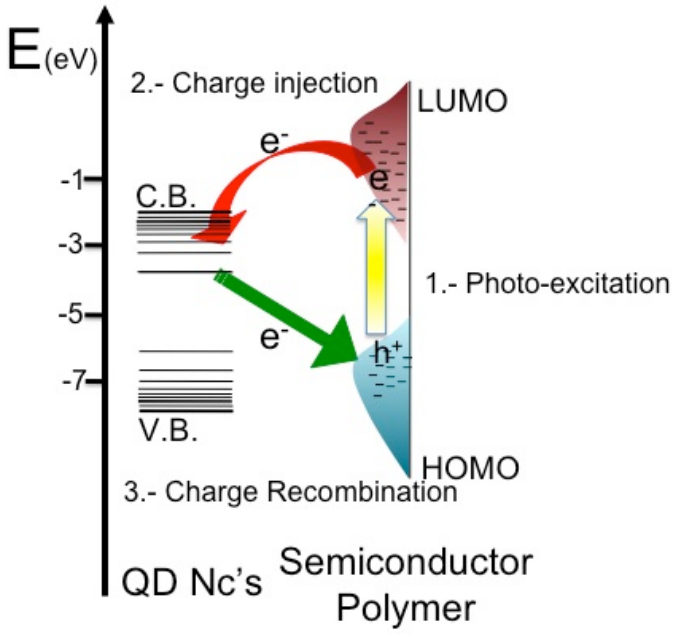

Figure 6. Energy diagram and charge transfer processes in polymer / quantum dot system.

Since the P3HT LUMO is approximately at 3.1 eV and the conduction band of these CdSe quantum dots is close to 3.79 eV, we can assume that there is enough driving force to induce charge separation ($-\Delta G^{o} \approx 0.69$ eV). In this process the photogenerated excitons must travel to the P3HT/QD interface and there split into negative and positive polarons efficiently. In order to monitor this process we have employed fluorescence spectroscopic techniques. P3HT/CdSe quantum dot blend films were prepared with different P3HT:CdSe ratios. In Figure 7 can be seen the UV-Vis spectra of the P3HT/CdSe films with different quantum dot concentrations.

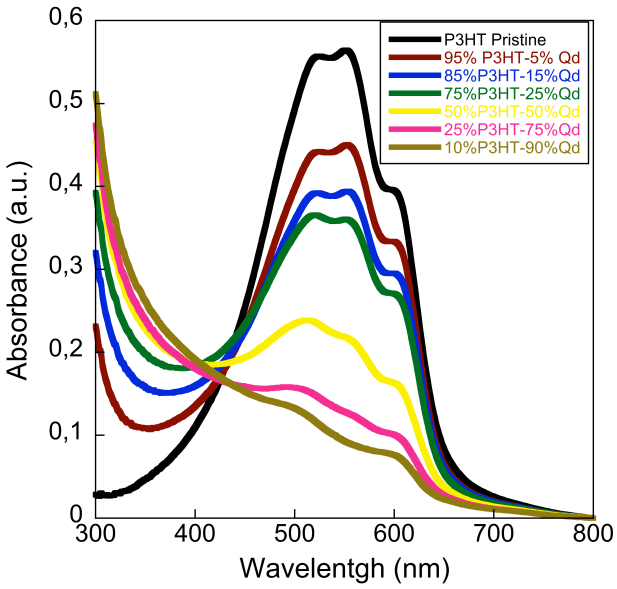

Figure 7. UV-Vis spectra of the P3HT/CdSe quantum dots blend films with different ratios.

The contribution of the P3HT in the blend spectra decreases when the CdSe concentration is increased. However, even in the less concentrated sample, the absorption features of the P3HT are still present. However, the addition of nanocrystals to P3HT shows an increase in optical absorption in the UV region, where the P3HT do not absorb, indicating proper contribution of the quantum dots in the overall light absorption.

The emission spectra of these films were also measured (see Figure 8 (a)). The quenching of the fluorescence of the P3HT in the presence of CdSe nanocrystals could be related to the electron transfer from the polymer to the quantum dots.[14] Figure 8 (b) shows the emission decay of P3HT in the presence of different amounts of CdSe quantum dots upon excitation with a diode laser ($\lambda_{Ex.}$= 405 nm), with an instrument response of 350 ps. Notice that the excitation wavelength, both in steady state and in time resolved techniques, has been selected where all the films absorbs approximately the same amount of light. Thus, we can infer that the decay amplitude decreases with the increasing QD concentration, and this amplitude decrease is not due to dilution effects.

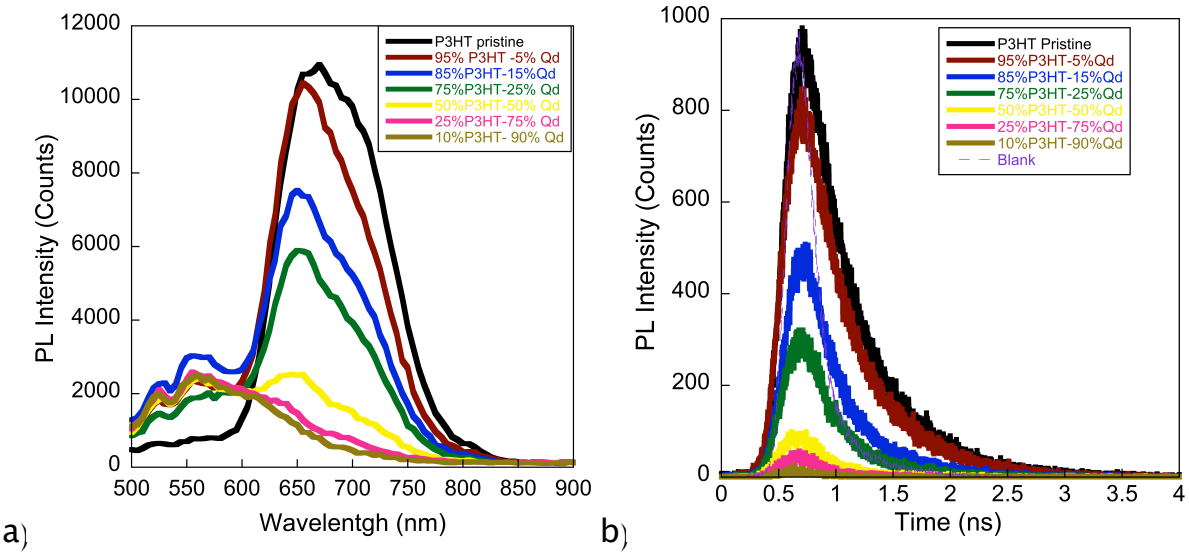

Figure 8. Emission spectra of the blend films (a), and emission kinetics adjusting the decay measurements to the same acquisition time (21 s) in a linear-linear plot. $\lambda_{Ex.}$= 405 nm, λ_{Probe}= 670 nm.The dashed purple line corresponds with the instrumental response.

This is in good agreement with previous reported emission steady–state measurements of P3HT/Quantum Dots. The emission decay parameters are listed in Table 2 and were obtained from the fitting of the experimental data to Equation3.

From this data, we can infer that the yield for electron injection from the P3HT excited state to the CdSe nanocrystals conduction band is higher than 90% already in the 50:50 (w:w) rate and occurs faster than our instrument response (350 ps). The former hypothesis is based on the integration of the areas below the emission decay curves while the later one is based on the mathematical procedure published previously by Koops et al,[4] from which the calculated electron transfer must occur faster than 200 ps. The electron injection yields as well as the injection kinetics, calculated with this method, are shown in Table 2. In addition, we have determined the apparent rate constants for charge injection process, K_{et},[15] using Equation 5.

$$K_{et} = \frac{1}{[\tau]} - \frac{1}{[\tau_{P3HT}]} \qquad \text{Eq. 5}$$

The values of k_{et} represent the rate constant at which electron injection occurs. In Table 2 we can observe that when the amount of quantum dots increase in the blend the rate of electron injection is higher up to 90% weight.

In conclusion, we have verified that efficient charge separation takes place in CdSe:P3HT blends for ratios equal or higher than 50:50 (w:w). In addition, the electron transfer kinetics are very fast, taking place in the picosecond time scale.

However, the use of photoluminiscence spectroscopy to elucidate the charge separation kinetics, by itself, has became quite controversial lately. This is due to the lack of information that this technique provides, about the de-activation of the excited states by other mechanisms than luminescence or if the electrons are transferred (desired process) or if the entire electron-hole pairs are transferred by Förster resonance energy transfer, for example.[16] For this reason, we cannot completely exclude other non-radiative processes competing with the charge transfer that might have also an influence on the decreasing intensity of the photoluminiscence measurements.

Table 2. The de-convulted emission decay lifetimes measured at $\lambda_{Ex.}$= 405 and λ_{Probe}= 670 nm for P3HT/CdSe hybrid films calculated with Equation 1. The electron injection kinetics obtained with the mathematical procedure of Koops (τ_{EIK}). The electron injection yields of the blend films, and the apparent rate constants for charge injection.

	P3HT	5% QD	15% QD	25% QD	50% QD	75% QD	90% QD
τ (ps)	395	282	263	255	222	226	209
Yield (%)	-	15.85	56.95	73.96	92.78	96.41	98.61
τ_{EIK} (ps)	-	105	157	131	106	91.3	88
K_{et}(ps^{-1})	-	0.0010	0.0013	0.0014	0.0019	0.0019	0.0023

We have also studied the interfacial charge recombination processes between the free carriers at the CdSe/P3HT heterojunction as a function of the quantum dot concentration using L-TAS. In Figure 9 (a) the measurement of the transient absorption spectrum of a 90:10 (w:w) CdSe:P3HT film is shown. The positive signal in the L-TAS spectrum denotes charge separation as it has been explained in previous chapters of this thesis.

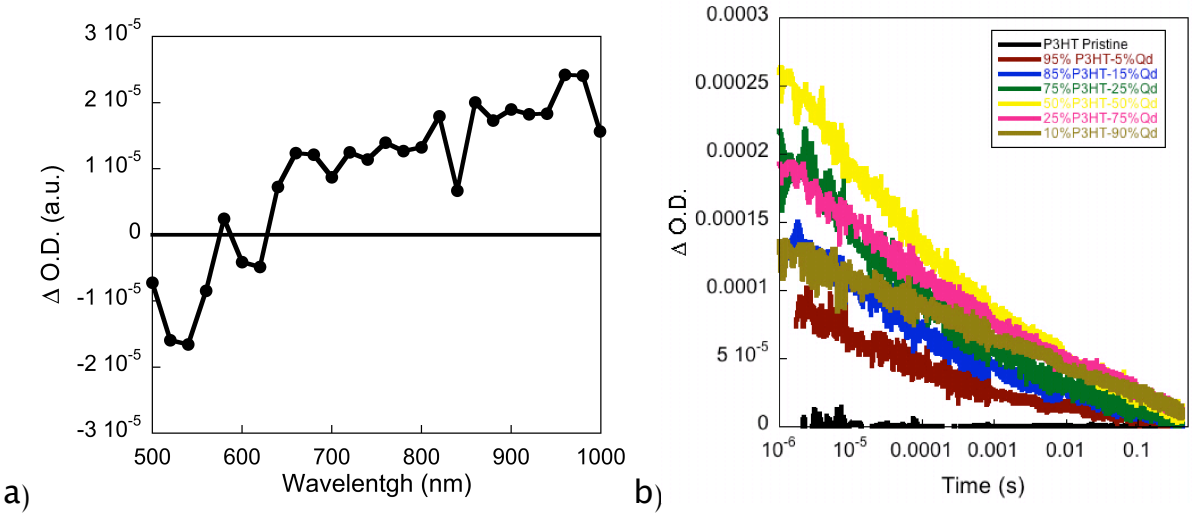

Figure 9. (a) Transient absorption spectrum of a P3HT:CdSe thin film, measured at 1 ms. The composition of the film was 10:90 (w:w). $\lambda_{Ex.}$= 470 nm. (b) Transient absorption decays of P3HT/CdSe films with different ratios. $\lambda_{Ex.}$= 470 nm, λ_{Probe}= 980 nm.

The transient absorption spectrum is in good agreement with reported literature previously for P3HT/PCBM (PCBM : 1-(3-methoxycarbonyl)propyl-1-phenyl-[6,6]methanofullerene), blends assigning the observed signal at 980 nm to positive polarons at the P3HT.[17, 18]

We have measured the decay of this transient signal for all films and we found that the dynamics can be fitted to a stretched exponential function (see Figure 9 (b)). This finding is contrary to previously published reports on transients decays of PCBM/P3HT films which display power law exponential decay dynamics ($\Delta O.D. = A \cdot t^{-\alpha}$) after low intensity laser excitation (17 μW). The nature of such exponential decay dynamics has been assigned to the presence of bimolecular charge recombination of long-lived separated charge species.[17, 19] In addition, the MDMO-PPV/CdSe (Weight ration 1:4, MDMO-PPV: poly(2-methoxy-5-(3',7'-dimethyl-octyloxy)-p-phenylenevinylene) and APFO-3/CdSe blend (1:6 w:w, APFO-3 chemical name: poly(2,7-(9,9-dioctyl-fluorene)-alt5,5'-4(4',7'-di-2-thienyl1-2',1',3'-benzothiadiazole) displays a biphasic dependence on the laser intensity.[14, 20] At intensities lower than 1 mW/cm^2 or 30 mW/cm^2, respectively, the intensity dependence of the PIA signal ($-\Delta T/T$) with power follows a power law behaviour assigned to monomolecular decay process ($\alpha = 1$), while at higher intensities it is bimolecular ($\alpha = 0.5$).

In contrast, we found that for CdSe/P3HT blends the electron recombination dynamics are more dispersive and are best fitted to stretched exponential decay dynamics suggesting that there are multiple decay processes in the blend film probably due to the different energy of the traps of charges at the nanocrystals. We employed low laser excitation energy, 0.087 mW, in the experiments to ensure that the densities of photogenerated charge carriers are below of those generated under solar irradiation resulting in excitation of a small fraction of the polymer. The analysis of our experimental decays using power law dynamics, as reported for other hybrid systems above, resulted in unsatisfactory fits. In Figure 10, we show experimental data of L-TAS decay of CdSe:P3HT films with 75:25 and 90:10 ratios, fitted to both power law and stretch exponential functions. As can be seen, the stretched exponential function shows a better fit to the experimental data rather than the power law. The rest of the samples showed an identical trend.

We want to highlight that not only the P3HT polaron lifetime varied with the quantum dot ratio but also the exponential factor of the stretched exponential decay, probably due to the differences in trap filling in the hybrid film. The decay lifetime ($\tau_{1/2}$) and the stretch exponential factor (β) parameters, extracted from the fitting to the experimental points, are presented in Table 3. We believe that it can

be directly correlated to the formation of aggregates on the hybrid films which promote the electron movement between nanocrystals. To correlate this hypothesis a morphologic study was carried out. Moreover, it must be remarked that all decays were far from being mono-exponential (β=1) which is different from what has been previously observed for different blends at low laser intensities.

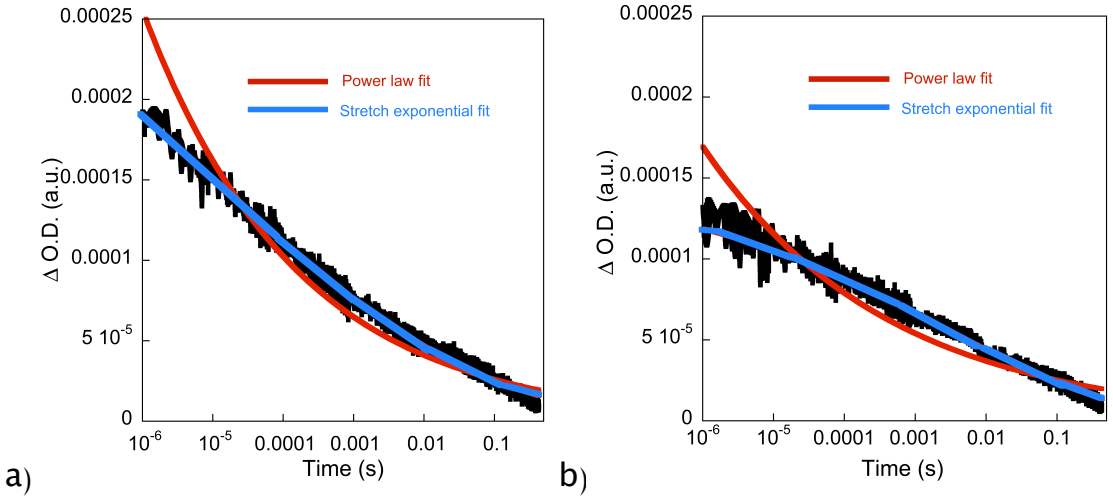

Figure 10. Transient absorption decay of CdSe/P3HT (a) 75:25 and (b) 90:10 w:w fitted both Power law (red) and Stretch exponential (blue) functions. $\lambda_{Ex.}$= 470 nm, λ_{Probe}= 980 nm.

Table 3. Decay-lifetime ($\tau_{1/2}$) measured at FWHM and β, stretch exponential factor, for different CdSe/P3HT films, calculated from fitting of experimental data in Figure 9.

%CdSe	5%	15%	25%	50%	75%	90%
$\tau_{1/2}$ (ms)	0.04	0.09	0.09	0.1	0.3	2
β	0.08	0.09	0.1	0.1	0.11	0.17

Thin film Atomic Force Microscopy (AFM) morphological characterisation was made to the CdSe/P3HT samples. The AFM measurements were performed on a 5x5 μm area in tapping mode. The AFM revealed that the increase in nanocrystals in the samples results in the formation of aggregates (see Figure 11). These agglomerations leads to the unexpected planarisation of the hybrid films, shown by the Roughness Mean Square (RMS), which describes the roughness of the surface of a sample, which decreases from 29 nm for pure P3HT to 14 nm for the 90% CdSe sample.

These results are directly related with the charge recombination dynamics in this kind of blend. As can be seen in Table 3, the increase of CdSe concentration promotes the formation of aggregates in the films that may be responsible for the higher dispersive behaviour observed in the L-TAS measurements. It seems obvious that 5% of semiconductor CdSe quantum dots is sufficient to create a CdSe/P3HT interface capable to dissociate excitons into free carriers. However, as it can be

observed in Figure 11, with 5% of nanocrystals, the recombination kinetics is in the order of microseconds. Nonetheless, increasing the CdSe nanocrystals in the blend slows down the charge recombination dynamics between photo-injected electrons at the CdSe and the P3HT polarons to the millisecond time scale.

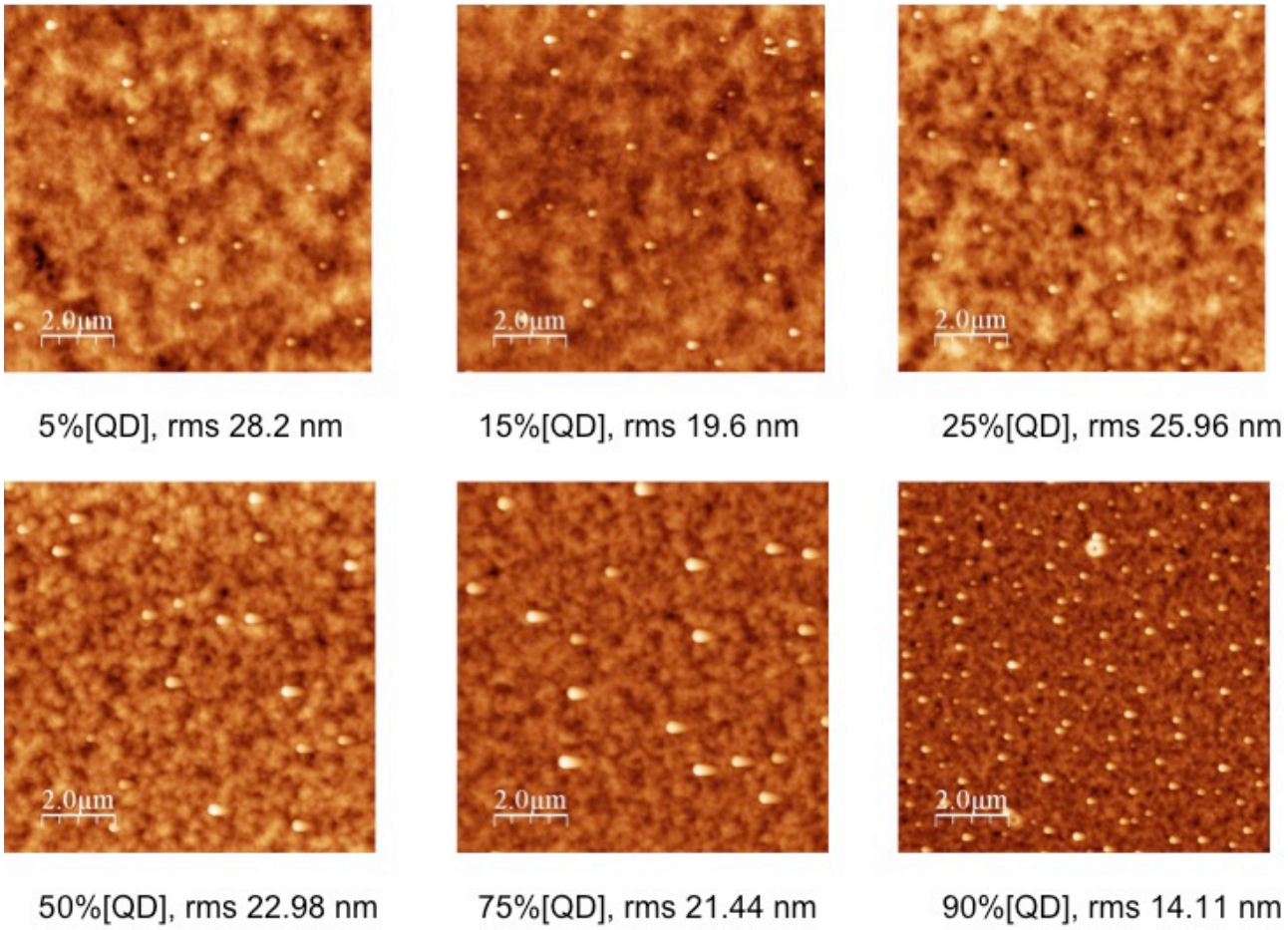

Figure 11. AFM images for the CdSe/P3HT films with different polymer:nanocrystal ratio. The Roughness Mean Square (RMS) of every film is showed.

The fast back electron transfer in blend films with low CdSe weight could be due to the lack of percolation routes for the electrons and, therefore, the electrons are trapped at the nanocrystals surface and recombine with the P3HT positive polarons before they can move to another nanocrystal. Thus, we can assign these decays to fast recombination between CdSe and P3HT where most of the P3HT polarons have recombined before tenths of microseconds. On the other hand, increasing the CdSe weight in the blend to 90%, promotes the formation of aggregates creating sufficient percolation routes between the CdSe nanocrystals and allowing a random walk of electrons between the different quantum dots, and thus, slowing recombination, as can be seen in Figure 12.

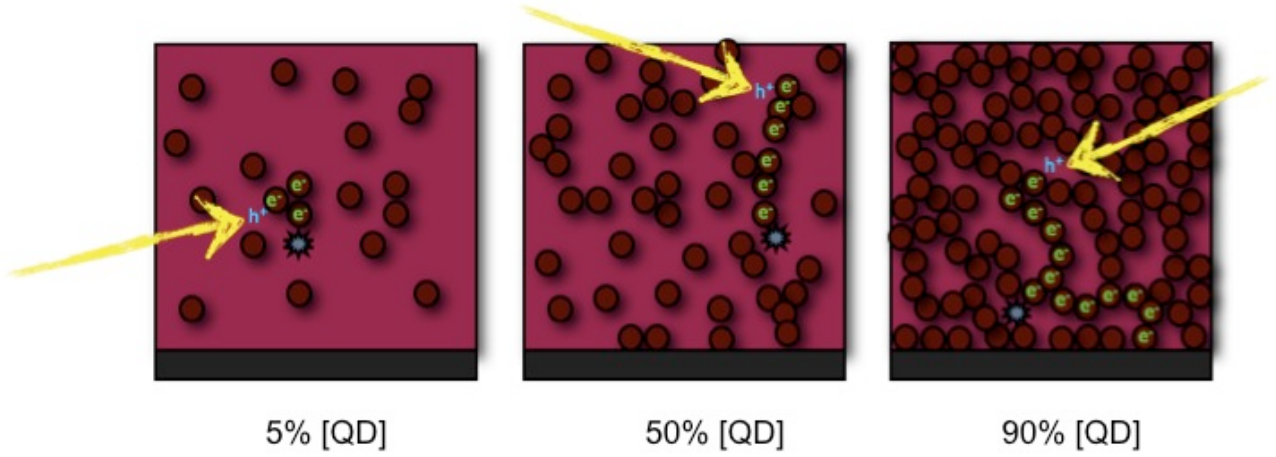

Figure 12. Illustration of the origin of the dispersive behaviour of the charge recombination dynamics as a function of the quantum dot concentration for CdSe/P3HT blend films.

4.2. Influence of the Molecule Capping Ligand

We have already studied the influence of the quantum dot concentration in the polymeric matrix of P3HT:CdSe blend films on the charge transfer dynamics, both charge separation and recombination. Now, we investigate how the capping molecules of the CdSe nanocrystals modulate the interfacial charge transfer dynamics in quantum dot:polymer blend films.

CdSe quantum dots were prepared as has been reported in the previous section, using the organic ligand TOPO. In order to study the influence of the organic coating the TOPO molecule has been exchanged with other organic molecules. One of the exchanged molecules is pyridine, since it has been reported as one of the best molecules to improve charge transfer reactions in polymer:quantum dot systems. The other molecules are based on an aromatic ring with two different functional groups in the –para positions. On the one hand, thiol–end group, which is well known to strongly attach to the CdSe nanocrystals, and on the other hand, different electron withdrawing or donor groups (–H, –F, –Cl, $–NH_2$), which provide different dipole moments to the molecules. Theoretical calculations kindly provided by Prof. Anton Vidal, employing Spartan'06 (B3LYP 6–31g* basis set) predicted the different dipole moment for the molecules illustrated in Figure 13.

The ligand exchange has been characterised by Fourier Transform Infrared Spectroscopy (FTIR). For this, a liquid holder with KBr windows was used in a NICOLET 5700 FT–IR. The results are shown in Figure 14.

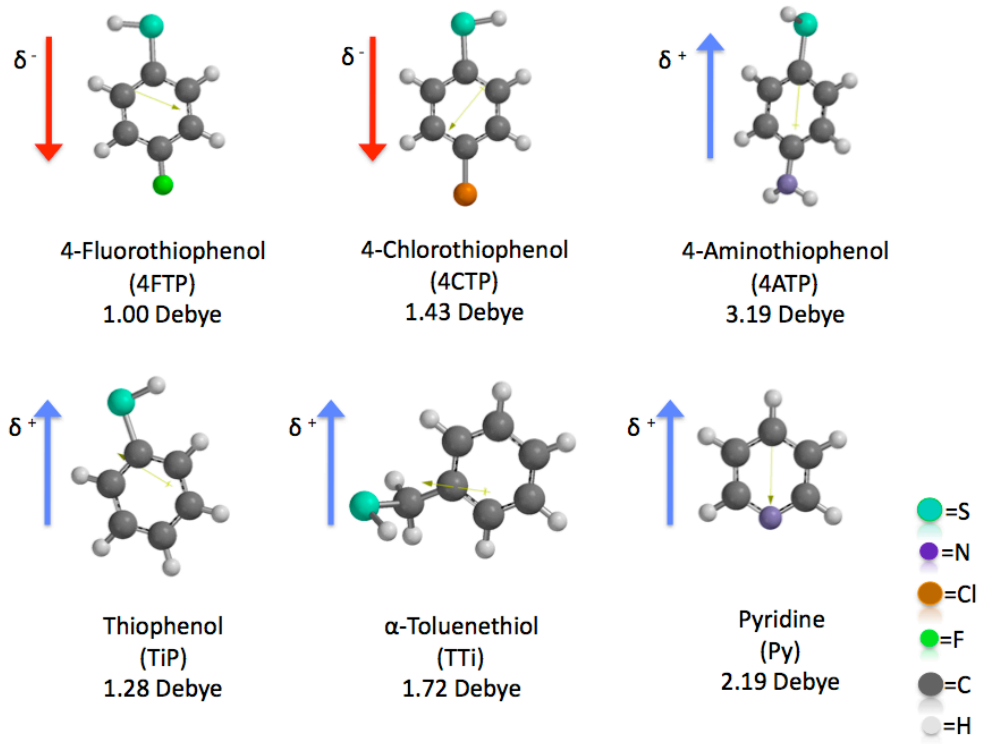

Figure 13. Aromatic thiol derivates used to coat the surface of the CdSe nanocrystals in this study. The arrows indicate the direction of the dipole moment respect the quantum dot surface. The calculated dipole moment is also shown for each molecule.

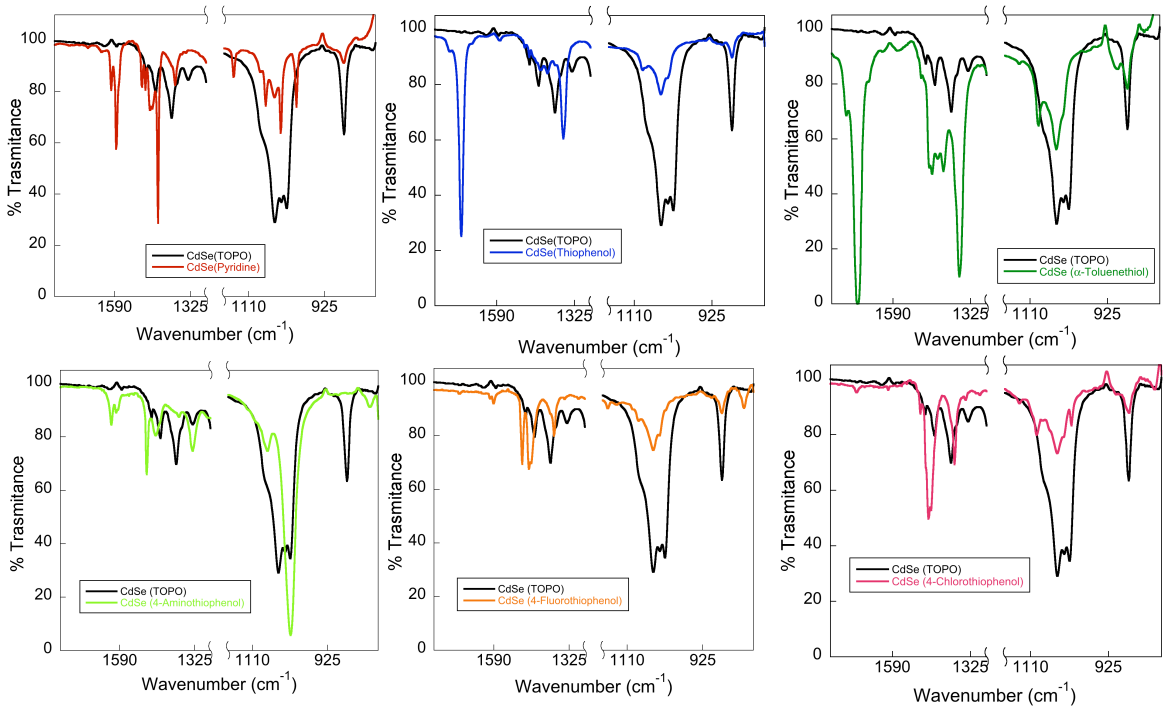

Figure 14. FTIR spectra of CdSe quantum dots coated with different molecules in $CHCl_3$.

The TOPO capped CdSe quantum dot spectrum showed an intense peak between 1010 and 1100 cm^{-1}, which has been related to the vibrational stretch of the P=O (1080 cm^{-1}) and the alkyl chains in the TOPO molecule.[3] There is another

feature characteristic of TOPO, centred at 874 cm^{-1}, which has been assigned to alkyl chains too. Notice that it has been deleted the region from 1170 to 1270 cm^{-1} , where the solvent absorbs, in order to make the spectra more clear. The peaks related to the TOPO molecule appeared in the other FTIR spectra with much less intensity, suggesting the removal of TOPO from the surface of the nanocrystals. New peaks related to the aromatic rings (1590 and 1438 cm^{-1}) and with the functional groups in the exchanged molecules appeared in the other spectra. For example in the 4ATP sample a signal corresponding to the primary amine bond, at 1020 cm^{-1}, was found. Unfortunately, the signal from the C–Cl and C–F bonds were overlapped with signals from the solvent and the TOPO alkyl chains, respectively. It is worth point out, that the ligand exchange was not complete, and a small percentage of TOPO, which cannot be removed, reminded on the quantum dot surface after ligand exchange, as has been reported previously.

The UV–Visisble spectra for all CdSe nanocrystals in chloroform are shown in Figure 15. The typical spectrum for CdSe quantum dots, with the excitonic peak at λ_{abs}= 565 nm can be observed. Notice the broadening of the absorption band for the CdSe nanocrystals coated with the Fluor–, and Amino– derivates of the aromatic thiol. This broadening cannot be assigned to the differences either in the dipole moment or the dipole direction. However, it is clear that the presence of 4FTP and 4ATP substituted molecules is responsible for the change.

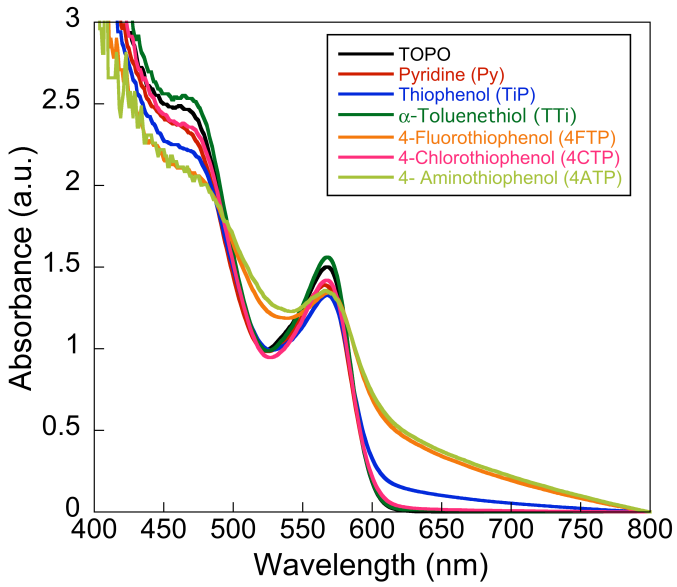

Figure 15. UV-Vis spectra for the different CdSe quantum dots in $CHCl_3$.

Nonetheless, the UV–Vis spectra of the different modified CdSe nanocrystals showed no shift in the excitonic peak or further modification. Photoluminiscence spectroscopy measurements were performed in order to obtain more information. The photoluminiscence in steady state is illustrated in Figure 16.

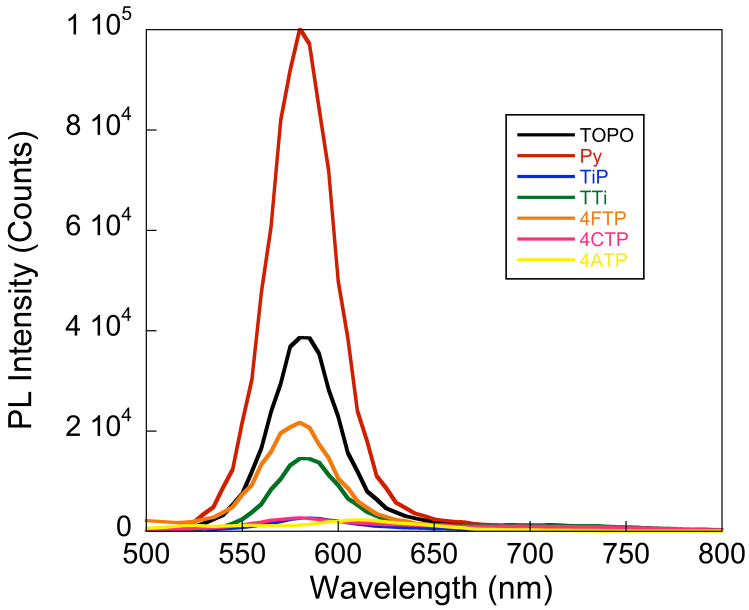

Figure 16. Emission spectra of the CdSe nanocrystals capped with different molecules. $\lambda_{Ex.}$= 405 nm.

As can be clearly seen from Figure 16, the substitution of the capping molecules on the nanocrystal surface causes important changes in the photoluminiscence of the quantum dots. Therefore, from the TOPO sample, which was used as a reference, the Py coated quantum dots showed an enhancement of the photoluminiscence intensity. This could be due to a better coverage of the nanocrystal surface, which provide better passivation of surface trap states. However, the rest of the molecules produced a quenching of the nanocrystal fluorescence with respect to the reference. This could be due to the efficient hole scavenging that these aromatic molecules with thiol groups produce, as it has been previously reported.[3] Nevertheless, the most quenched samples were 4FTP, TiP and 4ATP, and therefore, this quenching phenomena cannot be attributed to differences in dipolar moments or dipole directions of the molecules.

From the absorption and emission spectra we determined the E_{0-0} of the different capped CdSe nanocrystals. Then, cyclic voltammetry of the different coated CdSe quantum dots was carried out, using as reference an Ag/AgCl KCl saturated electrode. From the E_{0-0} and the electrochemistry we estimated the energy level diagram for all quantum dots used in this study, see Figure 17.

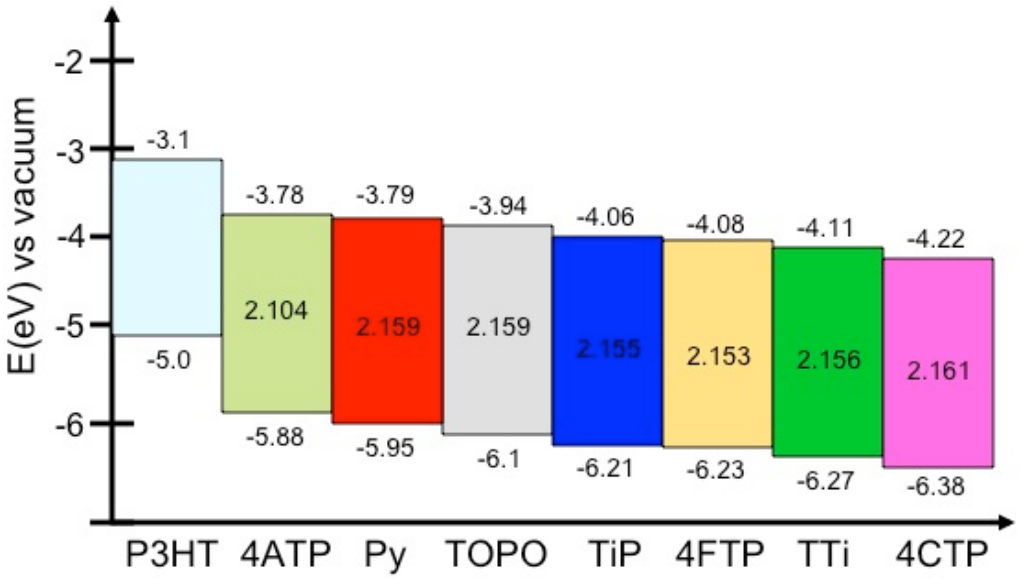

Figure 17. Energy level diagram for the different capped quantum dots and the polymer P3HT. The P3HT values come from the literature and the capped nanocrystal values have been estimated from cyclic voltammetry using as reference an Ag/AgCl KCl saturated electrode.

From Figure 17 we can conclude that the P3HT polymer was suitable to study the photoinduced charge transfer reactions with the modified CdSe quantum dots. The differences in band alignment of the nanocrystals with respect the polymer could influence both in charge separation as in charge recombination. In order to study these processes CdSe/P3HT 90:10 (w:w) blend films were prepared with all capped quantum dots. The UV-Vis spectra for he different films is shown in figure 18.

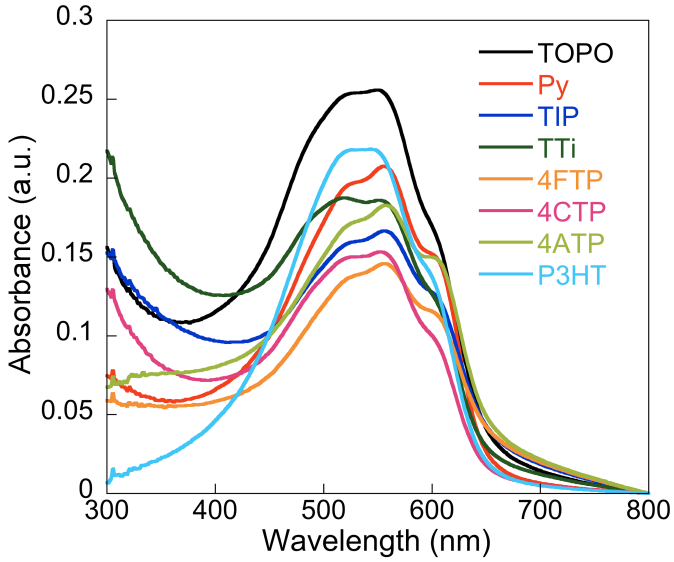

Figure 18. UV-Vis spectra of the capped CdSe:P3HT (90:10) blend films. The P3HT film absorbance is included for comparison.

The UV-Vis spectrum of the CdSe/P3HT shows mostly the features of the polymer. All films were prepared in identical conditions, and a final thickness near to 100 nm was obtained for all of them. Thus, it is interesting to notice that the

absorption intensity varies very much depending on the CdSe capping agent i.e. the para-substituted aromatic ring (4FTP, 4CTP and 4ATP) ones showed less absorption and TOPO and TTi showed higher absorption.

The study of the influence of the capping ligand over the spectroscopical characteristics of the films, was carried out by measuring steady state fluorescence emission spectroscopy firstly. The photoluminiscence of the different CdSe:P3HT films is shown in Figure 19.

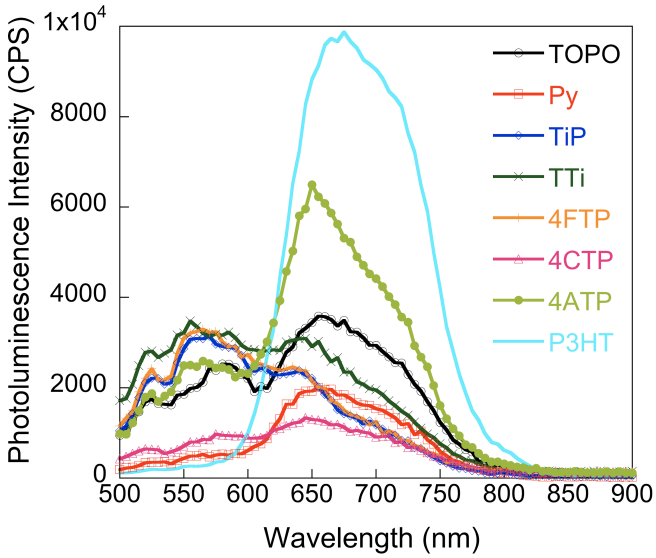

Figure 19. Photoluminescence spectra for all the different CdSe/P3HT thin films. $\lambda_{Ex.}$ = 560 nm.

The emission spectra of the different films show that there is effective quenching of the P3HT fluorescence (λ_{max} = 670 nm) in all cases the 4FTP capping agent is the strongest quencher, while 4ATP the weakest of the P3HT emission deactivation. The photoluminescence quenching has been assigned to charge transfer from the polymer to the nanocrystals. The charge separation yield was further estimated by TCSPC by measuring the films emission decay dynamics at λ_{Probe} = 670 nm, after excitation at 405 nm, while keeping the acquisition time constant (t= 600 s) and integrating the area under the decay. The charge separation yield values are listed in Table 4.

As can be seen from Figures 19 and 20, both steady state and dynamic results are in complete agreement. The emission lifetime of the hybrid films was calculated with Equation 3. The electron transfer kinetics were also calculated with the mathematical procedure published by Koops et al. The results are compared with de dipole moment of the capping molecules in Table 4. Notice that the values of the TOPO sample have been omitted for the charge separation and charge recombination results. The TOPO molecule possess a very different chemical

structure which could add stearic and insulator effects, making it not suitable for fair comparison of charge transfer processes.

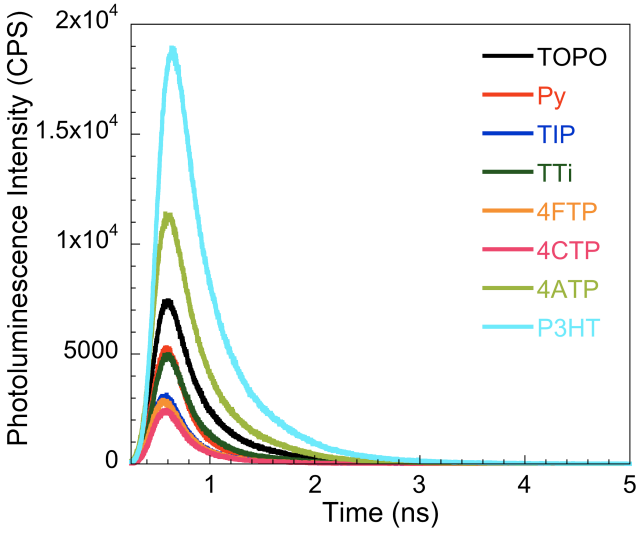

Figure 20. Photoluminiscence decay measurements for the different CdSe:P3HT films. $\lambda_{Ex.}$= 405 nm, λ_{Probe} = 670 nm, acquisition time 600 s.

Table 4. Charge transfer yield and kinetics and emission lifetime of the different CdSe:P3HT films. The dipole moment of the capping molecules is also included. τ is the P3HT emission lifetime and τ_{EIK} is the electron injection kinetic.

Sample	Dipole(D)	Yield(%)	τ (ps)	τ_{EIK} (ps)
4ATP	-3.19	43	805	389
Py	-2.19	80	774	284
TTi	-1.72	79	711	319
TiP	-1.28	88	675	278
4FTP	1.00	91	614	299
4CTP	1.43	90	645	277

We found that the molecules which posses the higher dipole moment pointing to the nanocrystal (4ATP) were not favouring the electron injection. On the contrary, the molecules which electronic density was far from the quantum dot surface enhanced the charge separation yield. The same trend was followed for the electron injection kinetics. The molecule 4ATP, with higher dipole moment pointing out the nanocrystal showed the slower kinetics. However, the molecules 4FTP and 4CTP, which have dipole moment pointing out in the opposite direction, showed the faster kinetics.

This behaviour have been previously observed in the system TiO_2/P3HT by McGehee et al.[21] In this work, a monolayer of dipole molecules were attached to

titanium dioxide surface. Then a film of polymer was deposited on the top of the coated metal oxide. They observed that when the dipole was directed toward the TiO_2, the band edge potential of TiO_2 was shifted away from the local vacuum level of the polymer. Thus, the effective gap between the conduction band of the metal oxide and the HOMO of the polymer was reduced if compared to unmodified TiO_2, increasing the driving force for electron injection. If dipoles were pointing away from titanium dioxide, the band edge of TiO_2 was shifted closer to the vacuum level of the polymer, and the gap between the TiO_2 conduction band and P3HT HOMO increases. Moreover, they also performed emission quenching experiments where dipole molecules with electron acceptor groups, such as NO_2, were able to quench more the fluorescence of the P3HT than molecules with electron donor groups, such NH_2, as is happening in our case.

If we look again to Figure 17, we can observe that the trend that McGehee observed for TiO_2 is also working for our colloidal semiconductor nanocrystals. The 4ATP sample, with dipole moment –3.19 D, was found to have the biggest gap between the CdSe conduction band and the P3HT HOMO (1.22 eV), decreasing the driving force ($-\Delta G^{o}$) for electron injection. However, the sample 4CTP, with dipole moment 1.43 D, had the smallest gap between the nanocrystal conduction band and the polymer HOMO (0.78 eV), increasing the $-\Delta G^{o}$. The disagreement with the TTi sample from the general trend could be due to experimental error. It must be take into account that the ligand exchange is never complete, and some TOPO molecules remain in the quantum dot surfaces. In addition, different degrees of molecule substitution may take place, which could influence some measurements.

The back electron transfer processes between the photo-injected electrons at the P3HT and the oxidised quantum dots was also studied by L-TAS. Figure 21 shows the recombination decay for all the samples when monitoring at 980 nm, which corresponds to the absorption of the P3HT polarons, formed by charge separation after excitation at 470 nm.

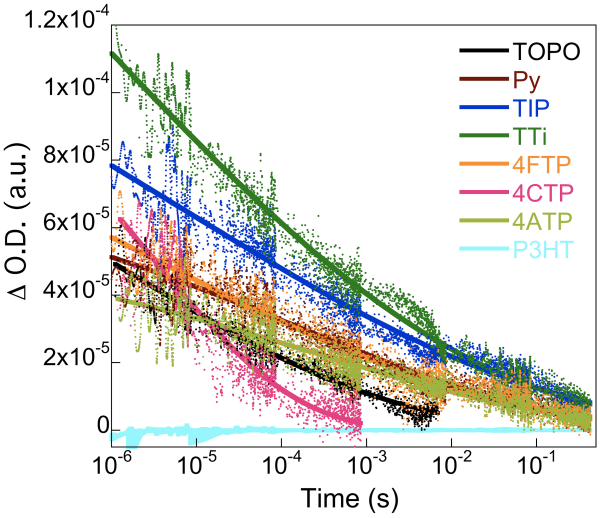

Figure 21. L-TAS decay measurements for the different films. $\lambda_{Ex.}$= 470 nm, λ_{Probe} = 980 nm. The solid lines are the fitting to stretch exponential function.

As can be seen, the kinetics expands from microseconds to hundred of microseconds and can be fitted to a stretch exponential function as we have previously shown. It is worth noticing that it was not possible to fit the transient decays to a power-law expression, which has been typically used to fit polymer-fullerene bulk-heterojunction films. Thus, we can infer that the recombination kinetics in all cases studied here are controlled by the number of traps at the CdSe nanocrystals in much extend that the traps situated at the tail of the density of states of the P3HT polymer.

In this case, we did not find a clear correlation between the dipole moment of the ligands and the lifetime of the recombination decays. The parameters from the fit to the stretch exponential are listed in Table 5.

Table 5. L-TAS decays fitting parameters from stretch exponential function.

Sample	Dipole (D)	τ (μs)	β
4ATP	-3.19	297	0.15
Py	-2.19	164	0.15
TTi	-1.72	0.55	0.10
TiP	-1.28	6.43	0.10
4FTP	1.00	1.73	0.10
4CTP	1.43	2.62	0.25

In previous sections, we have demonstrated that changes in morphology, due to different quantum dot concentration in the blends, were able to modify back

electron transfer dynamics. In this case, we believed that the capping molecules, in addition of affect the nanocrystals with its own dipole moment, also played a role on the film morphology, which is directly affecting the recombination dynamics. In order to probe this hypothesis AFM measurements were performed to some capped CdSe:P3HT films. The AFM measurements were performed to a 5 x 5 μm area in tapping mode, see Figure 22.

As can be seen in Figure 22, big aggregates of different sizes are present in the blend films. These big aggregates may be responsible for the different recombination kinetics. Notice that the bigger clusters were found when the thiol-end molecules with the para-substitution in the aromatic ring were used as capping ligands (4FTP, 4CTP and 4ATP). However, the other molecules, with different structures, showed less prominent agglomerates.

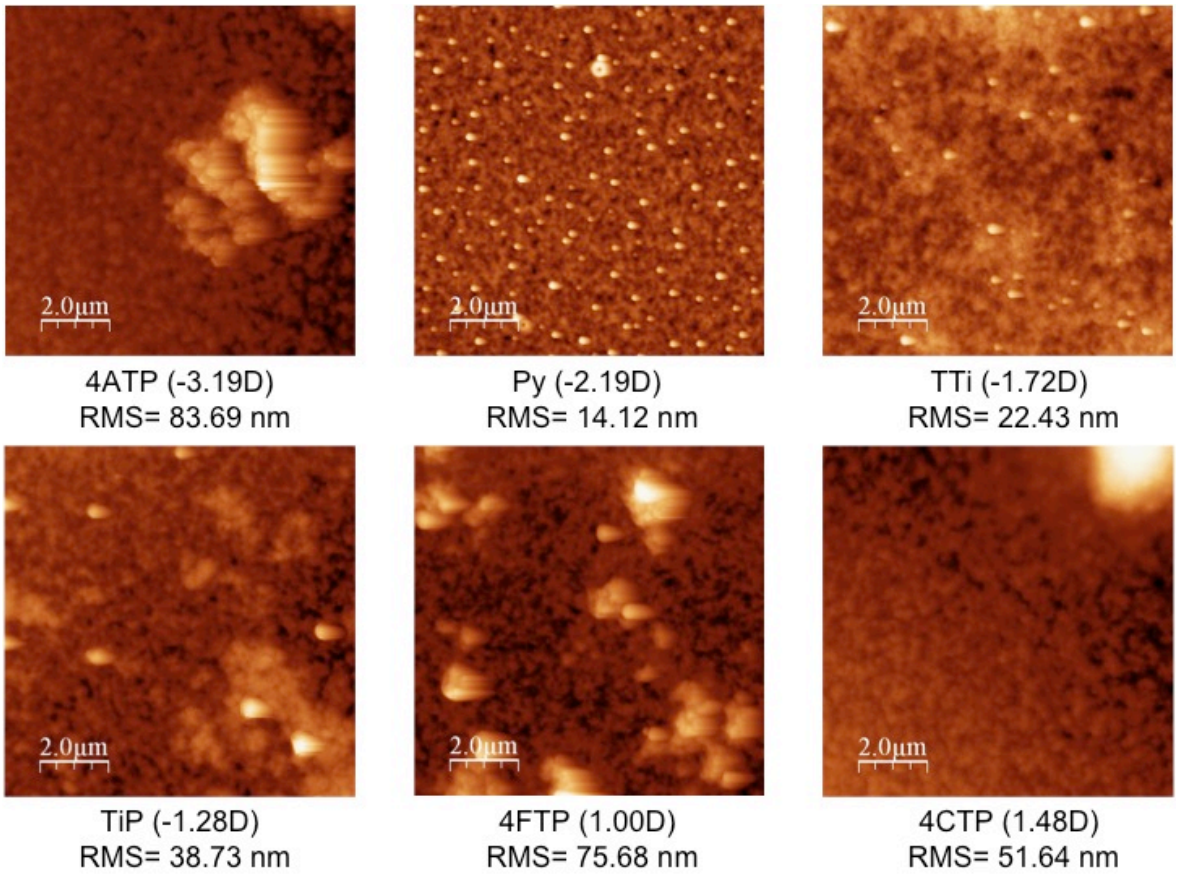

Figure 22. AFM images for the different capped CdSe/P3HT films. The roughness mean square (RMS) of every film and the dipole moment (in brackets) of the dipole molecules are shown.

In order to study the origin of the formation of these aggregates Single Fluorescence Microscopy was performed on some of the ligand exchanged CdSe quantum dots by Dr. Daniela Iacopino in Tyndall National Institute, Cork (Ireland). The single fluorescence microscopy to 4FTP and Py samples are shown in Figure 23.

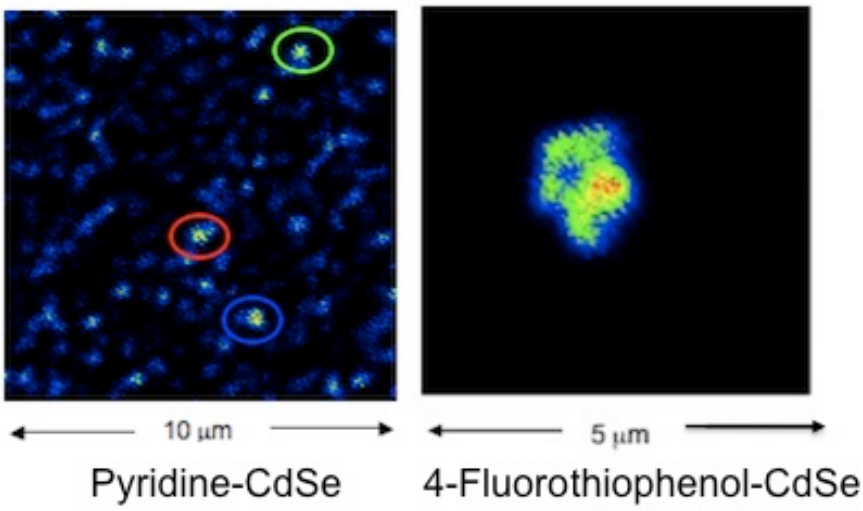

Figure 23. Fluorescence microscope image of Py-CdSe and 4FTP-CdSe from solutions, spin coated on glass coverslips.

The Single Fluorescence Microscopy revealed that already in solution the 4FTP–CdSe nanocrystals presented aggregates of approximately 1 μm. However, the Py–CdSe exhibited smaller aggregates. These aggregates could also be the origin in the UV–Vis and emission spectra that the different capped CdSe presented in solution. It seems clear that the formation of these aggregates in the quantum dot solutions affects the morphology of the films, which is directly related with the charge recombination dynamics.

In clear contrast with previous work in other heterojunctions,[21, 22] where dipole molecules were used, we did not observe any correlation between the charge recombination reaction and the modified interface between the polymer and the nanocrystal with the dipoles. This is attributed to the quantum dot agglomeration that those dipole molecules present for the molecules with the para-substituted groups in the aromatic ring (4ATP, 4FTP, and 4CTP). The prepared films, with quantum dots and such molecules, presented high roughness caused by the formation of bigger nanocrystal clusters. For the rest of the molecules the nanomorphology presented better phase segregation with less aggregates.

4.3. Influence of the Morphology.

Finally, we have investigated the influence of the nanocrystal morphology on the charge transfer reactions in P3HT: CdSe nanocrystals blend films.

First of all, CdSe quantum dots, nanorods and tetrapods were synthesised and characterised at ICIQ. All CdSe nanocrystals were synthesised using TOPO as the capping ligand. After synthesis and washing, the capping ligand was exchanged by pyridine for the three morphologies. TEM images of the three different CdSe nanocrystal morphologies are shown in Figure 24.

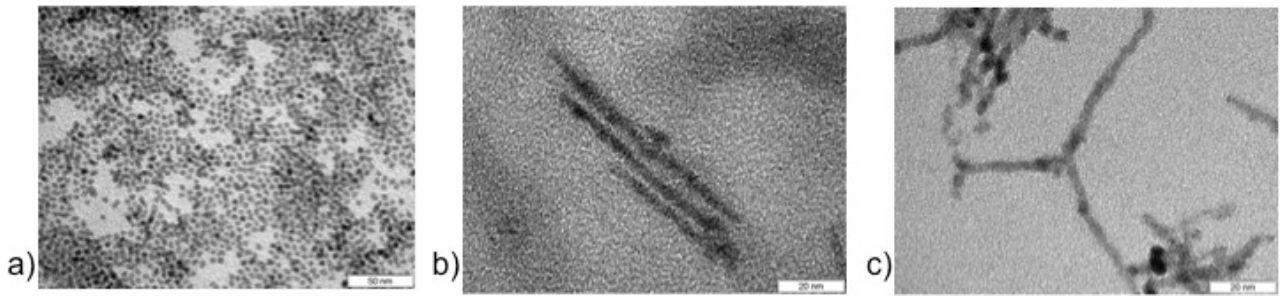

Figure 24. TEM images of CdSe quantum dots (a), nanorods (b) and tetrapods (c).

The CdSe quantum dot presented a mean size of 3.7 nm. The absorbance maximum of the last excitonic peak was located at 577 nm, and the emission maximum at 601 nm. The nanorods showed a mean diameter of 3.6 nm and an average length of 50 nm. The maximum in the absorption peak was 572 nm, and the emission peak presented a maximum at 595 nm. The tetrapods had 3.4 nm in diameter and an length average of 60 nm. The maximum in absorbance was located at 566 nm and the emission at 608 nm. In Figure 25 the absorption and emission spectra of the three CdSe nanocrystals is presented. Notice from the absorption and emission spectra that the nanorods presented higher size distribution than the quantum dots, and the tetrapods showed a even higher size distribution than the nanorods and quantum dots, respectively. We want to highlight that in the tetrapods syntheses, a population of nanorods were also growth, forming mixed solutions. Some quantum dots may be present in the nanorods solutions too. Moreover, both nanorods and tetrapods solutions presented a wide dispersion in the arm lengths.

Excitons in nanorods and in the branched nanocrystals are confined mostly along the diameter since the length often exceeds the excitation radius by several times. Therefore, the length of the arms does not affect the absorption, and so, the emission spectra.[23] The three morphologies where synthesised with very similar diameters. And so, differences on the charge transfer reactions are only due to nanocrystals morphology, but not because of differences in energy levels.

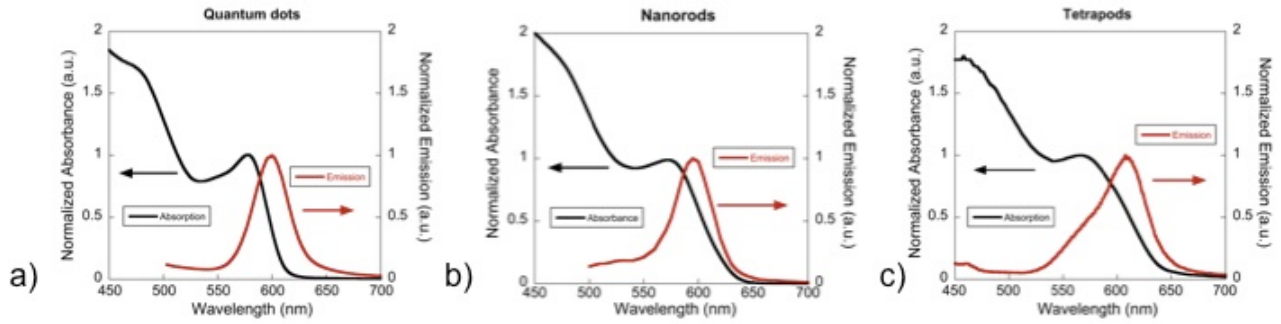

Figure 25. UV-Vis and emission spectra of CdSe quantum dots (a), nanorods (b) and tetrapods (c).

The emission lifetime was also measured for the three CdSe morphologies. The decays are showed in Figure 26. As can be seen the quantum dots presented the shorter emission lifetime, and the tetrapods the longest. This behaviour has been already seen elsewhere, and it is explained by the larger number of exciton states in the tetrapods (compared with the nanorods and quantum dots), due to the splitting of the degeneracy of the states in the dots as a result of the decrease in symmetry.[24–26] The emission decays were fitted to de-convoluted functions, and the parameters obtained from the fittings are shown below:

Quantum dots:

$$F(t) = 0.85 + 2.5\cdot10^{-2}\exp\left(-\frac{t}{0.1}\right) + 2.4\cdot10^{-3}\left(-\frac{t}{0.79}\right)0.44\cdot10^{-3}\exp\left(-\frac{t}{3.95}\right);\chi = 1.14$$

τ_1 (41%), τ_2 (28%), τ_3 (31%).

Nanorods:

$$F(t) = 29.92 + 3.49\cdot10^{-3}\exp\left(-\frac{t}{0.192}\right) + 1.88\cdot10^{-3}\exp\left(-\frac{t}{1.079}\right) + 2.96\cdot10^{-2}\exp\left(-\frac{t}{7.68}\right);\chi = 1.19$$

τ_1 (13.5%), τ_2 (40.8%), τ_1 (45.7%).

Tetrapods:

$$F(t) = 34.32 + 3.85\cdot10^{-3}\exp\left(-\frac{t}{0.323}\right) + 2.79\cdot10^{-3}\exp\left(-\frac{t}{2.02}\right) + 1.15\cdot10^{-3}\exp\left(-\frac{t}{10.56}\right);\chi = 1.26$$

τ_1 (6.5%), τ_2 (29.6%), τ_1 (63.9%).

, where the lifetime (τ) are in nanoseconds.

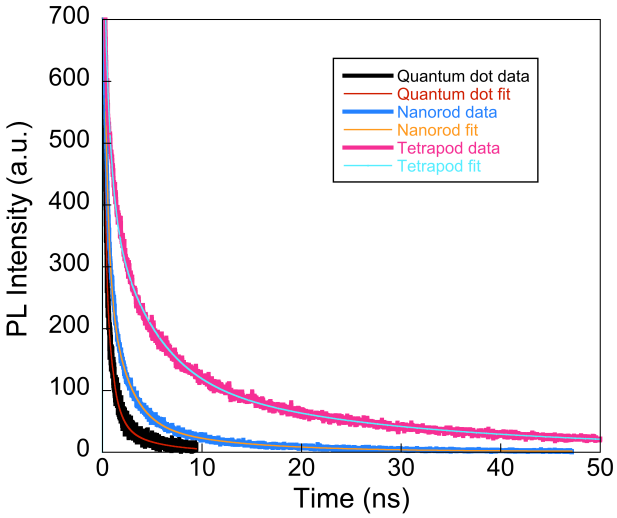

Figure 26. Emission decay of CdSe quantum dots, nanorods and tetrapods. In all cases, the excitation wavelength was $\lambda_{Ex.}$= 405 nm, and the λ_{Probe}= 600 nm.

The CdSe nanocrystals with different morphologies were mixed with the P3HT polymer. In addition, each class of nanocrystal has been mixed with the polymer in different ratios. Finally, the mixed nanocrystals and polymer were spin cast on glass substrates and annealed at 150ºC for 20 minutes. The absorption spectra of the blend films with different CdSe morphologies are shown in Figure 27.

It is worth pointing out that the P3HT shoulder located at 550 nm, related to intrachain exciton (π–π* transition), increases in intensity with respect to the one at 500 nm when the P3HT was mixed with CdSe quantum dots. However, these remained unchanged in the case of nanorods and tetrapods. It is obvious that the spheric nanocrystals have some influence in the electronic structure of the P3HT that the other morphologies have not.

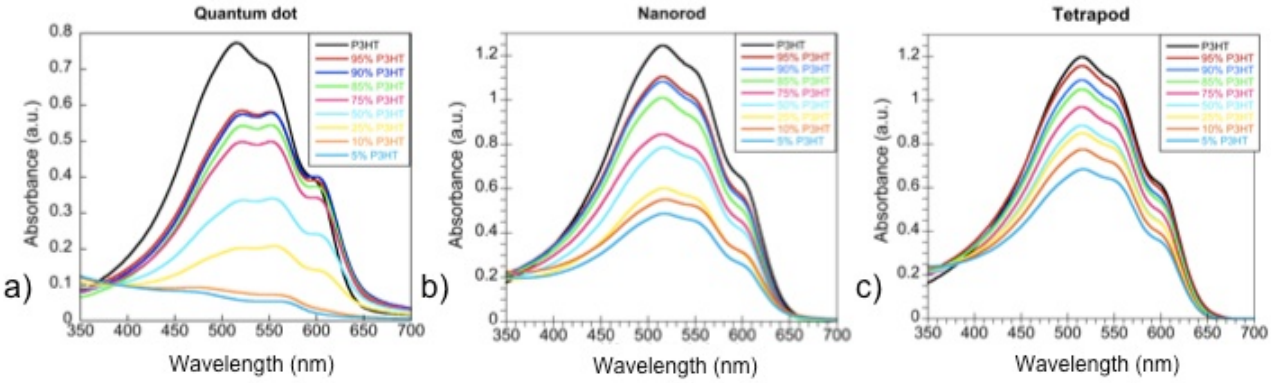

Figure 27. UV-Vis spectra of blend films of CdSe quantum dots (a), nanorods (b) and tetrapods (c) mixed with P3HT at different ratios.

Moreover, in the samples with higher quantum dot load (10% and 5% P3HT) the absorption spectra becomes more similar to the nanocrystal one rather than the polymer. However, this is not the case for the other morphologies.

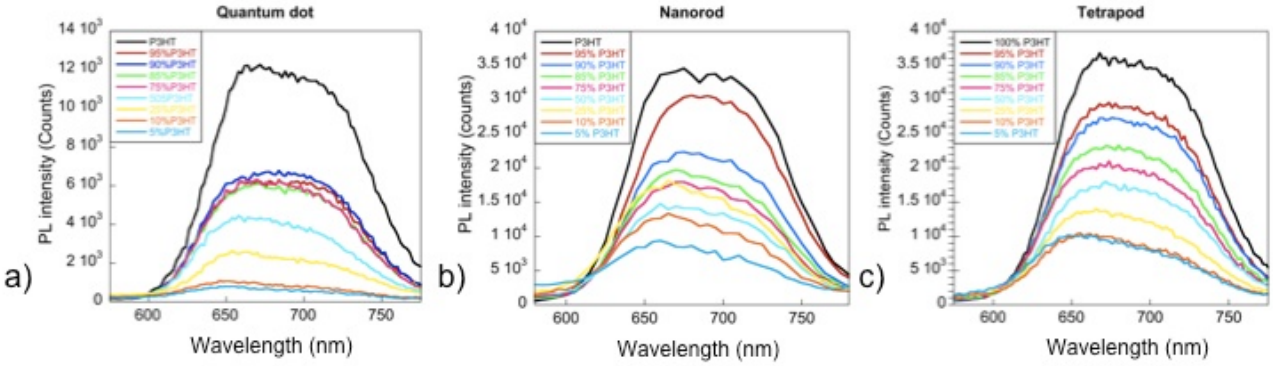

Figure 28. Emission spectra of blend films of CdSe quantum dots (a), nanorods (b) and tetrapods (c) mixed with P3HT at different ratios. $\lambda_{Ex.}$= 405 nm.

The emission spectra of the blend films was also measured and is shown in Figure 28. As we have previously commented in this thesis, the P3HT emission quenching has been related to the electron transfer from the polymer excited state

to the nanocrystal conduction band. The emission spectra of the P3HT was immediately quenched to approximately 50% by the presence of the quantum dots. However, higher nanocrystal loading (50:50, w:w) was necessary for further fluorescence quenching. The films with the higher quantum dot ratio presented almost complete emission quenching (more than 90%). In the case of nanorods and tetrapods the emission was sequentially quenched when the nanocrystal concentration was increased. However, in these cases the fluorescence was not completely quenched at high leading. Specifically, in the case of nanorods, the P3HT:CdSe 90:10 (w:w) sample reached approximately 50% of the emission fluorescence. In the case of tetrapods higher nanocrystal load (50:50, w:w) was necessary to quench the 50% of the P3HT fluorescence. The final quenching of samples containing nanorods and tetrapods did not exceed the 90%.

The emission lifetime decays were also measured for the blend films with nanocrystals of different morphologies. The emission decays are in good agreement with the emission spectra, and are shown in Figure 29.

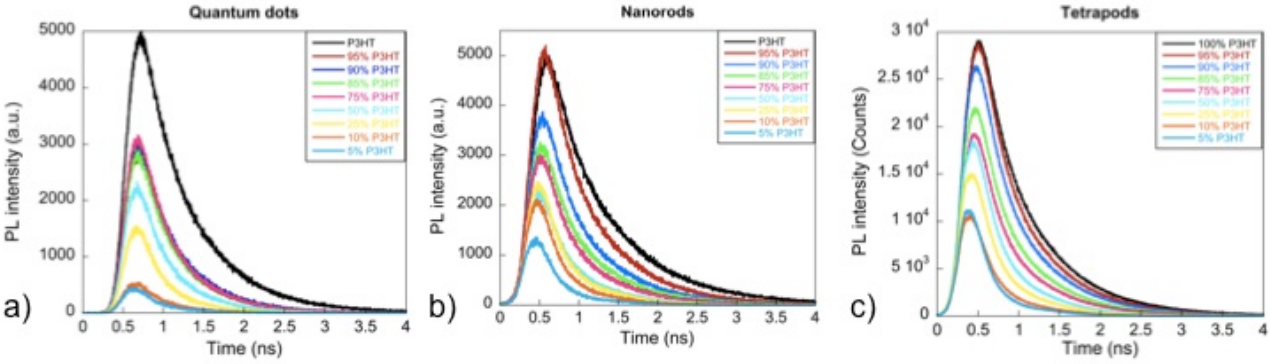

Figure 29. Emission kinetics adjusting the decay measurements to the same acquisition time (300s for Quantum dots and Nanorods and 900s for tetrapods) in a linear-linear plot of the blend films of CdSe quantum dots (a), nanorods (b) and tetrapods (c) mixed with P3HT at different ratios. $\lambda_{Ex.}$= 405 nm, $\lambda_{Probe.}$= 670 nm.

Notice that the signal amplitude of the quantum dots samples does not correspond exactly with the data presented in the first section of this chapter (vide supra). Nevertheless, the general trend of these data are in good agreement, obtaining injection yields higher than 90% and kinetics faster than 200 ps for the more concentrated samples. The differences in the data are attributed to the intrinsic properties of the polymer batch, in the nanocrystal synthesis (where nanocrystals with different superficial trap states are formed from batch to batch), and experimental error.

While the emission decay in the CdSe nanorods and tetrapods blend films are quenched sequentially when the nanocrystal ratio is increased, in the case of

quantum dots 50% of the emission is quenched only adding a 5% of nanocrystals, as it has been previously observed in steady state.

From the emission dynamics data, we calculated the yield for electron injection from P3HT excited state to the CdSe nanocrystals conduction band and the electron injection kinetics. The electron injection yield calculation is based on the integration of the areas below the emission decay curves while the injection kinetic is based on the mathematical procedure published previously by Koops et al.. The P3HT emission lifetime was also calculated using Equation 3. In Figure 30 a summary of the electron injection yield, the P3HT emission lifetime and the kinetics of electron injection are shown.

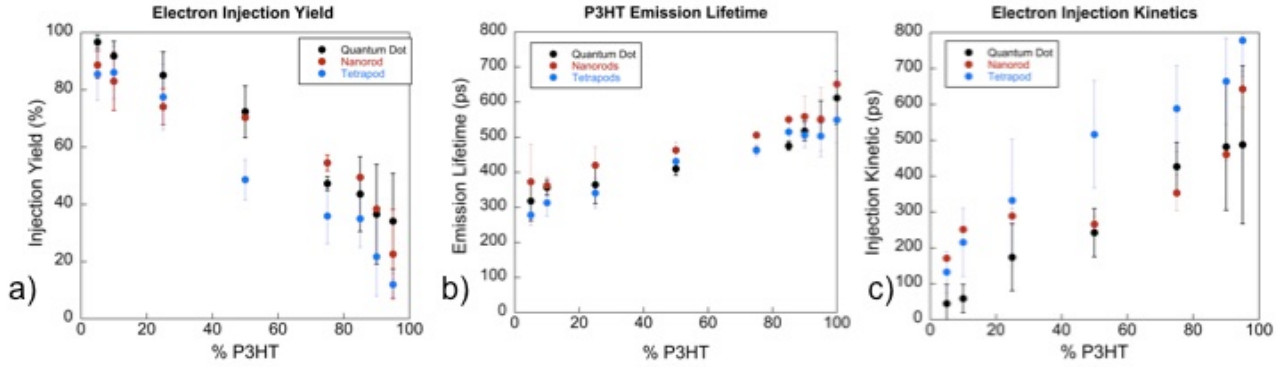

Figure 30. Summary of the electron injection yield (a), P3HT emission lifetime (b) and electron injection kinetics (c) of the three CdSe morphologies for different P3HT:nanocrystal ratios. Those values were obtained from the average of several measurements with different films of the same sample.

The electron injection yield for all morphologies was higher than 85% for samples with the highest nanocrystal load. The blend films with the highest nanocrystal ratio which showed higher injection yield were the quantum dots (96.8%), then nanorods (88.8%) and the lowest the tetrapods (85.6%). Contrary to these observations it has been previously reported by S. Dayal et al.[27] that the high aspect ratio of the nanorods and tetrapods favours charge separation. This conclusion was extracted from the signal amplitude of microwave photoconductivity measurements. However, this assessment was proposed for low excitation light intensity ($< 2 \cdot 10^{15}$ photon/cm^2/pulse). Nevertheless, the author's reported that for higher light intensities the amplitude of the signals became very similar. In our system we are using a excitation light intensity of $3.4 \cdot 10^{17}$ photon/cm^2/pulse, which explains the similar behaviour in injection yield and kinetics observed for all three morphologies in our case, and which is in good agreement with S. Dayal et al. report.

The P3HT emission lifetime was reduced for all morphologies when the nanocrystal concentration was increased. However, the variation in emission

lifetime of pure P3HT films (more than 100 ps difference) make difficult a comparison between them. If the emission lifetime of pristine P3HT films are normalised, we can conclude that all CdSe nanocrystals are able to decrease the P3HT fluorescence lifetime by half at the maximum nanocrystal ratio.

The results obtained for the electron injection kinetics showed, first of all, a elevated dispersion (as can be appreciated from the error bars). The blend films using CdSe tetrapods were the ones with higher difference in results. This could be due to the different fractions of tetrapods and nanorods obtained in the synthesis of these nanocrystals, as it has been reported before.[27] Nevertheless, we can clearly observe how the electron injection kinetics increase with the nanocrystals load. In addition, all morphologies showed very fast charge separation kinetics (< 200 ps) at high nanocrystals load.

From these results we can infer that for all morphologies the optimum P3HT:CdSe nanocrystals ratio for charge separation is 5:95, (w:w). At this concentration, the higher electron injection yield (>85%) and faster kinetics (< 200ps) were found for all cases. Nonetheless, the quantum dots presented slightly higher injection yields and faster kinetics than the other two morphologies at the same measured light intensity.

Now, we check the charge recombination dynamics of the P3HT:CdSe nanocrystals using L-TAS. Figure 31 shows the transient decay of the positive polaron of P3HT in the presence of quantum dot, nanorods and tetrapods with different concentrations. In this case we have only used compositions of 50:50, 25:75, 10:90 and 5:95 P3HT:CdSe nanocrystals for clarity, due to the use of higher P3HT concentrations resulted in negligible transient positive signals with our equipment.

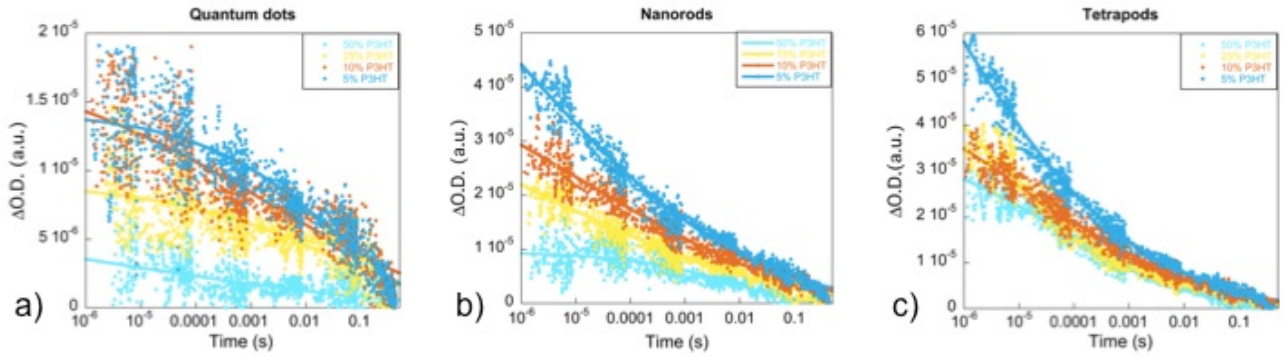

Figure 31. Transient absorption decay of P3HT:CdSe quantum dots (a), nanorods (b) and tetrapods (c) with 50:50, 25:75, 10:90 and 5:95, w:w, ratios, respectively. $\lambda_{Ex.}$= 470 nm, $\lambda_{Probe.}$= 980 nm.

From the transient decays we can observe, on the one hand, that the ΔO.D. scale for nanorods and tetrapods is higher than for quantum dots. If we consider

that the ΔO.D. is proportional to the charge density, as it is has been reported,[28] we can consider that in the microsecond time scale there are more free charges in the blends with nanorods and tetrapods than with quantum dots. On the other hand, we can also observe that the dynamics of recombination of nanorods and tetrapods are different from the quantum dots. The decays for the elongated nanocrystals looks faster than for the spheres.

We have fitted the transient decays to stretch exponential functions. The parameters extracted from the decay fitting are summarised in Table 6.

Table 6. Parameters obtained from the fit of the experimental data of the L-TAS to a stretch exponential function.

Quantum dot(%)	ΔO.D. (a.u.)	τ(s)	β	R
95	$1.4\cdot10^{-5}$	0.0379	0.287	0.89
90	$1.98\cdot10^{-6}$	0.0029	0.140	0.88
75	$9.25\cdot10^{-6}$	0.045	0.23	0.78
Nanorod (%)	**ΔO.D. (a.u.)**	**τ(s)**	**β**	**R**
95	$1.6\cdot10^{-4}$	$5\cdot10^{-8}$	0.096	0.98
90	$6.3\cdot10^{-5}$	$1\cdot10^{-5}$	0.111	0.97
75	$5.7\cdot10^{-5}$	$1.4\cdot10^{-6}$	0.099	0.96
Tetrapod (%)	**ΔO.D. (a.u.)**	**τ(s)**	**β**	**R**
95	$3.9\cdot10^{-4}$	$2\cdot10^{-10}$	0.079	0.99
90	$7.8\cdot10^{-5}$	$5.6\cdot10^{-6}$	0.12	0.99
75	$1.7\cdot10^{-4}$	$2\cdot10^{-8}$	0.097	0.98

In Table 6, if we look at mixes polymer:nanocrystal 10:90 (w:w), which has been found to be the optimum for efficient devices, we can confirm that the ΔO.D. for blends containing nanorods and tetrapods are one magnitude order higher than in quantum dots in the microsecond time scale. This is in good agreement with Dayal et al. observations, since they found also one magnitude order difference in the amplitude signal between samples using dots and elongated nanocrystals at low light intensity, as we used to use in the L–TAS experiments (approximately $2\cdot10^{14}$ photons/cm^2/pulse). The amplitude of the transient decays have been proposed to be proportional to the charge density previously. Therefore, we can conclude that there exist more long live charges (μs) when the polymer is mixed

with the elongated nanocrystals than with the quantum dots. The increase in the aspect ratio provide more surface were the excitons can be dissociated.

Nonetheless, if we look at the mean lifetime of the P3HT polarons, we can conclude that, although more free charges are created in the samples containing nanorods and tetrapods, those have shorter lifetime. In the case of mixtures with quantum dots, the P3HT polarons take millisecond in recombine, however, in the other morphologies they only take microseconds.

It is clear that when the aspect ratio of the nanocrystals is increased more charges are generated at the interface. This produce an enhancement of photo-generated charges between the interface of the polymer and the nanocrystals, but this also produces an increase of the recombination kinetics. Therefore, It will be the kinetic competition between charge recombination and charge transport which will determine the best morphology for efficient devices. It has been proved several times that the branched morphologies provide better devices, since more percolations routes are created to the electron transport. Therefore, the charge transport in these blend films must be higher than in nanorods and even higher than in quantum dots, as has been reported.

5. Conclusions.

The interfacial charge transfer reactions between the semiconductor polymer P3HT and CdSe nanocrystals have been investigated in blend films. We have observed in general sub-nanosecond electron injection. Furthermore, the charge recombination dynamics are dominated by the presence of traps states in the nanocrystals surface. This back electron transfer reactions can be optimised depending on the nanocrystal concentration and the molecules in the surface.

From our analysis, we have demonstrated the influence that the quantum dots concentration play in the charge separation and charge recombination dynamics. Our results illustrate that efficient charge separation take place already at low quantum dot concentration. In addition, ultra fast (< 200 ps) injection kinetics have been obtained for those composites. On the other hand, we have demonstrated that even for low concentration of quantum dots the recombination dynamics are highly dispersive instead of bimolecular. We also observed that there is a relationship between the morphology and the charge recombination, which may have direct consequence in the efficiency of complete devices.

The spectroscopic measurements revealed that the orientation and the dipole moment of the capping molecules that surround the quantum dots surface causes an effect on the charge transfer reactions at the interface between P3HT polymer and the CdSe quantum dots. While charge separation seems to be influence by the displacement in the quantum dot energy gap due to the dipolar moment of the capping molecules, there is not a linear and direct relationship between the dipole moment strength and direction and the recombination reactions. This has been explained by the different chemical nature of the molecules, which produce a strong effect over the quantum dot agglomeration and film nanomorphology. The molecules that show para-substitution in the aromatic ring showed higher film roughness caused by the formation of bigger nanocrystal clusters. However, molecules with different structures presented better phase segregation with less nanocrystals aggregates.

Finally, the role of the nanocrystal morphology on the photo-induced charge transfer reactions was studied. Although the fluorescence measurements revealed no significative differences neither on the charge separation yield nor on the injection kinetics, the L-TAS experiments, performed at lower light intensity, showed one magnitude order difference in the signal amplitude between the spheric and the elongated nanocrystals, indicating that there are 10 times more long-lived charges in nanorods and tetrapods rather than in quantum dots. Nevertheless, the transient decays showed faster recombination dynamics for

elongated nanocrystals compared with the quantum dots. Probably, the higher number of charges is accelerating the recombination dynamics in those blend films. Therefore, it must be the kinetic competition between the charge recombination and charge transport which determine the best nanocrystal morphology for polymer:nanocrystal bulk heterojunction solar cells, since the improved charge separation from spheric nanocrystals to nanorods and tetrapods is compensated by the faster recombination dynamics that those present.

Bibliography.

1. Lakowicz, J. R., *Principles of Fluorescence Spectroscopy*. Kluwer Academic/ Plenum Publishers: New York, 1999.
2. Wang, H.; Donegá, C. d. M.; Meijerink, A.; Glabeek, M. *J. Phys. Chem. B* **2006,** 110, (2), 733-737.
3. Liu, I.-S.; Lo, H.-H.; Chien, C.-T.; Lin, Y.-Y.; Chen, C.-W.; Chen, Y.-F.; Su, W.-F.; Liou, S.-C. *J. Mater. Chem.* **2008,** 18, (6), 675-682.
4. Koops, S. E.; Durrant, J. R. *Inorg. Chim. Acta* **2008,** 361, 663-670.
5. Lee, H. J.; Yum, J.-H.; Leventis, H. C.; Zakeeruddin, S. M.; Haque, S. A.; Chen, P.; Seok, S. I.; Gratzel, M.; Nazeeruddin, M. K. *J. Phys. Chem. C* **2008,** 112, (30), 11600-11608.
6. Milliron, D. J.; Hughes, S. M.; Cui, Y.; Manna, L.; Li, J. B.; Wang, L. W.; Alivisatos, A. P. *Nature* **2004,** 430, (6996), 190-195.
7. Bruchez, M.; Moronne, M.; Gin, P.; Weiss, S.; Alivisatos, A. P. *Science* **1998,** 281, 2013-2016.
8. Bawendi, M. G.; Carroll, P. J.; Wilson, W. L.; Brus, L. E. *J. Phys. Chem.* **1992,** 96, 946-954.
9. Brown, P. J.; Thomas, D. S.; Köhler, A.; Wilson, J. S.; Kim, J.-S.; Ramsdale, C. M.; Sirringhaus, H.; Friend, R. H. *Phys. Rew. B* **2003,** 67, 064203.
10. Kline, J.; McGehee, M. D.; Nadnikova, E. N.; Liu, J.; Fréchet, J. M. J. *Adv. Mater.* **2003,** 15, (18), 1519-1522.
11. Verma, D.; Dutta, V. *J. Renew. Sustain. Energ.* **2009,** 1, 023017.
12. Zhou, Y.; Eck, M.; Krüger, M. *Energy Environ. Sci.* **2010,** 3, 1851-1864.
13. Saunders, B. R.; Turner, M. L. *advances in Colloid and Interface Science* **2008,** 138, (1), 1-23.
14. Wang, P.; Abrusci, A.; Wong, H. M. P.; Svensson, M.; Andersson, M. R.; Greenham, N. C. *NanoLett.* **2006,** 6, 1789-1793.
15. Kamat, P. V. *J. Phys. Chem. C* **2008,** 112, (48), 18737-18753.
16. Borchert, H. *Energy Environ. Sci.* **2010,** 3, 1682-1694.
17. Clarke, T. M.; Jamieson, F. C.; Durrant, J. R. *J. Phys. Chem. C* **2009,** 113, 20934-20941.
18. Clarke, T. M.; Ballantyne, A. M.; Nelson, J.; Bradley, D. D. C.; Durrant, J. R. *Adv. Func. Mater.* **2008,** 18, 4029-4035.
19. Ohkita, H.; Cook, S.; Astuti, Y.; Duffy, W.; Tierney, S.; Zhang, W.; Heeney, M.; McCulloch, I.; Nelson, J.; Bradley, D. D. C.; Durrant, J. R. *J. Am. Chem . Soc* **2008,** 130, 3030-3042.
20. Han, L.; Qin, D.; Jiang, X.; Liu, Y.; Wang, L.; Chen, J.; Cao, Y. *Nanotechnology* **2008,** 178, 4736.
21. Goh, C.; Scully, S. R.; McGehee, M. D. *J. Appl. Phys.* **2007,** 101, 114503.
22. Shalom, M.; Rulhe, S.; Hod, I.; Yavah, S.; Zaban, A. *J. Am. Chem. Soc.* **2009,** 131, 2258-2271.
23. Milliron, D. J.; Gur, I.; Alivisatos, A. P. *MRS Bulletin* **2005,** 30, 41-44.
24. Talapin, D. V.; Nelson, J. H.; Shevchenko, E. V.; Aloni, S.; Sadtler, B.; Alivisatos, A. P. *NanoLett.* **2007,** 7, (10), 2951-2959.
25. Mohamed, M. B.; burda, C.; El-Sayed, M. A. *NanoLett.* **2001,** 1, (11), 589-593.
26. Müller, J.; Lupton, J. M.; Lagoudakis, P. G.; Schindler, F.; Koeppe, R.; Rogach, A. L.; Feldmann, J. *NanoLett.* **2005,** 5, (10), 2044-2049.
27. Dayal, S.; Reese, M. O.; Ferguson, A. J.; Ginley, D. S.; Rumbles, G.; Kopidakis, N. *Adv. Func. Mater.* **2010,** 20, 2629-2635.

28. Clarke, T. M.; Ballantyne, A.; Shoaee, S.; Soon, Y. W.; Duffy, W.; Heeney, M.; McCulloch, I.; Nelson, J.; Durrant, J. R. *Adv. Mater.* **2010,** 22, (46), 5287-5291.

Chapter 4 - Photo-Induced Charge Recombination In Polymer/Quantum Dot Solar Cells.

The interfacial charge transfer recombination processes under working conditions that limit the device performance in polymer:quantum dot bulk heterojunction solar cells have been investigated. We have employed conventional spectroscopic techniques such as charge extraction, transient absorption spectroscopy and transient photovoltage. From the charge extraction technique we have observed an exponential charge accumulation in the device when light intensity is increased, as has been desserved in organic solar cells. The transient photovoltage studies showed us that the devices were limited by non-geminative recombination dynamics, with a stronger carrier lifetime dependency upon charge density than in polymer:fullerene solar cells. The comparison between recombination dynamics extracted from the transient absorption and transient photovoltage techniques allowed us to elucidate the role of the metal contacts on the device recombination dynamics.

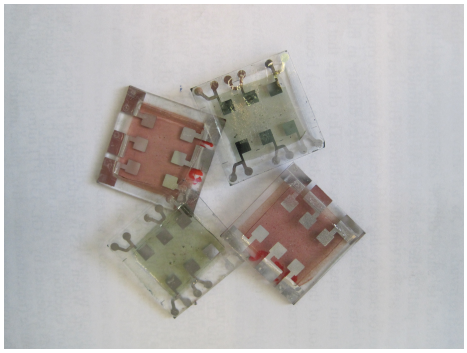

TABLE OF CONTENTS

1. Objectives.

The main objective in this chapter is the analysis of the working principle and the origin of the main losses that limit the efficiency in polymer:quantum dot bulk heterojunction solar cells.

PCPDTBT polymer : CdSe quantum dot bulk heterojunction solar cells will be fabricated and characterised. The role of the semiconductor nanocrystals in the charge photogeneration will be investigated. The dependence of the photocurrent and the photovoltage with the light intensity will be discussed.

The charge extraction technique, which has been widely employed in dye sensitised solar cells and organic photovoltaics, will be used to study the behaviour of the charge density as a function of the light intensity for PCPDTBT:CdSe quantum dot solar cells. Depending on the charge density behaviour a working mechanism based on electric fields generated between the metal contacts or based on the charge accumulation in the active layer will be suggested.

The recombination dynamics which limit the device efficiency will be studied in devices under working conditions. Transient photovoltage experiments will be carried out in order to investigate the recombination dynamics and the carrier lifetime dependency upon the charge density in the devices.

Transient absorption spectroscopy will be used as well to investigate the influence of the electrodes on the charge recombination processes. The comparison between the recombination dynamics in thin films without the presence of metal contacts and in complete devices will show us the influence of the electrodes on the device charge losses.

2. Theoretical considerations.

2.1. The Charge Extraction Technique (CE).

The charge extraction technique was developed by L. M. Peter and coworkers in 2000 to study the transport, trapping and back reactions of photogenerated electrons in dye sensitised solar cells under operation conditions.[1, 2] Later, J. R. Durrant and coworkers also employed this technique to analyses the charge carrier densities in polymer:fullerene solar cells.[3]

The potential advantages of this technique over the others employed for this purpose(i.e. Impedance spectroscopy) from the experimental point of view are the short accumulation times necessary and a relatively simple setup. In physical therms, it is a direct measure of the charges accumulated on the device due to the photovoltaic process under light conditions. We would like to stress the fact that the acquisition time used in the CE technique is the fastest procedure to measure the device charge (Q) and the device capacitance (C), which implies that the device physical parameters remain constant during the measurements, a unique property of this time-resolved technique.

Basically, charge extraction is a measurement in which a solar cell is initially under continuous illumination at open circuit conditions. The device is then switched to short-circuit (zero bias) while at the same time the light is switched off. The initial illumination produces charge accumulation in the device, which generate a light induced voltage or light bias at open circuit conditions. The switch to short circuit creates a current transient as the device discharges. The integral of this current transient provides an estimate of the excess charge in the cell due to the initial illumination, minus any charge losses incurred during the measurement.

The setup is an illumination system consisting of a white light LED ring (containing 6 LED's) from Luxeon Lumileds, which are focussed onto the device and connected to a DC power supply, a function generator TGP110. Finally, an oscilloscope TDS 2022 from Tektronix(C) register the drop in voltage between a resistance of 50 Ω. Figure 1 shows a digital image of the charge extraction setup at ICIQ.

The measurements start in short circuit and dark conditions. The pulse generator triggers the open circuit conditions on the device and switch on the LED's during the necessary time to reach steady state conditions, typically a few seconds is enough. Immediately after the pulse, the system goes to the initial conditions (short-circuit device and darkness) in less than 300 ns.

Figure 1. Digital photography of ICIQ CE system used in this Thesis.

The excess of charges generated on the device due to the photovoltaic effect flow through the external circuit and are recorded as the drop in voltage through resistance over time. When this procedure is repeated using different light intensities, an estimation of the accumulated charge on the device over light bias can be obtained. An example of the recorded voltage decays in a typical CE measurement of one quantum dot:polymer device is depicted in Figure 2.

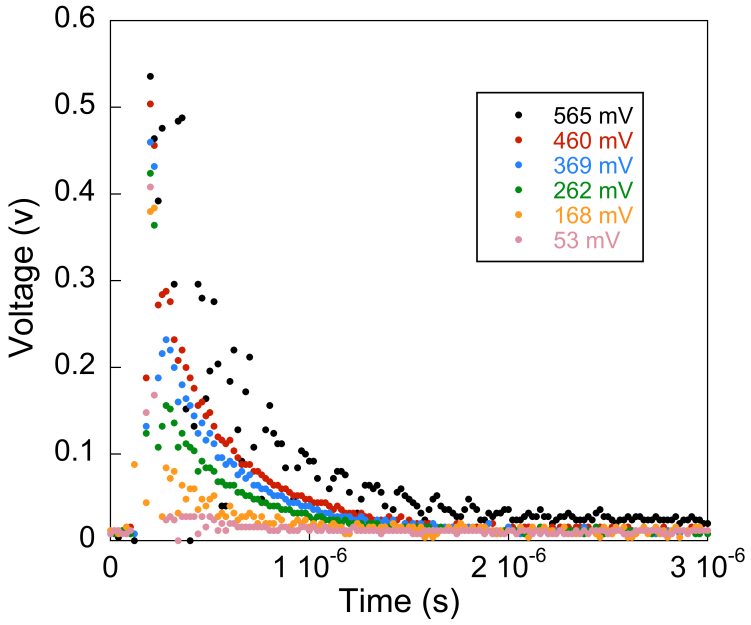

Figure 2. Voltage decay in a charge extraction experiment in a quantum dot:polymer device for different light bias.

The data obtained from the oscilloscope, at different applied light bias, is the variation of the voltage over time. In order to convert this data in charge (Q) we integrate the area under the voltage decay, Equation 1:

$$Q = \frac{1}{R}\int_{t=0}^{t=t} V(t)\,dt \qquad \text{Eq. 1}$$

,where R is the resistance (50 Ω) and V(t) is the voltage measured at every time.

Since the charge depends on the active layer's volume the accumulated charge can be also expressed as electron density. Therefore, the charge is converted in electron density taking into account the elementary electron charge ($1.60217646 \cdot 10^{-19}$ Coulomb) and the film volume. The electron density or charge density (e^-/cm^3) is thus used to define the charge accumulated in the film, allowing fair comparisons between devices.

The electron density vs. applied light bias, obtained from the CE measurements, is usually represented in a linear–linear plot, as shown in Figure 3. It can also be fitted to a exponential distribution of the form of Equation 2:

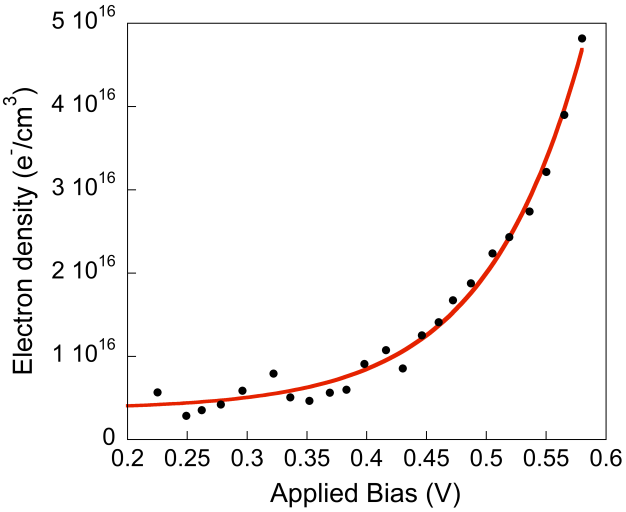

Figure 3. Charge density of a PCPDTBT:CdSe device extracted from the CE measurement and fitted to an exponential function.

$$n(V) = n_0 \cdot \exp\left(\gamma V_{OC}\right) \qquad \text{Eq. 2}$$

,where n_0 is the initial number of charges in the absence of light bias, and γ is the characteristic energy which describes the curvature distribution.

The experimental points can be also extrapolated to a Gaussian function. With this procedure, the shape of the Density of States (D.O.S.) may be estimated. It must be taken into consideration that the exponential behaviour of the charge density here may not be representative for all solar cells. It has been described that

devices, whose working principle is due to electric fields between electrodes, posses a linear relation between the charge density and the light bias.

A more complete description of the signal treatment can be found in the annexes.

2.2. Evaluation of Losses During Charge Extraction Measurement.

It is worth stoding that an underestimation of the total charge due to the internal recombination during the extraction of the excess of charges generated in the CE experiment could lead to inaccurate results. However, the short circuit and dark conditions of the CE technique provide a preferential pathway for charges.

We can observe qualitatively these losses comparing the time to extract 50% of the charge in the device at 100 mW/cm^2 (1 sun) with the corresponding carrier lifetime at V_{OC} obtained from the Transient Photovoltage measurement (vide infra). If the time to extract 50% of the charge is lower than the carrier lifetime we can assume that the losses during extraction will be negligible. An example of this is depicted in Figure 4.

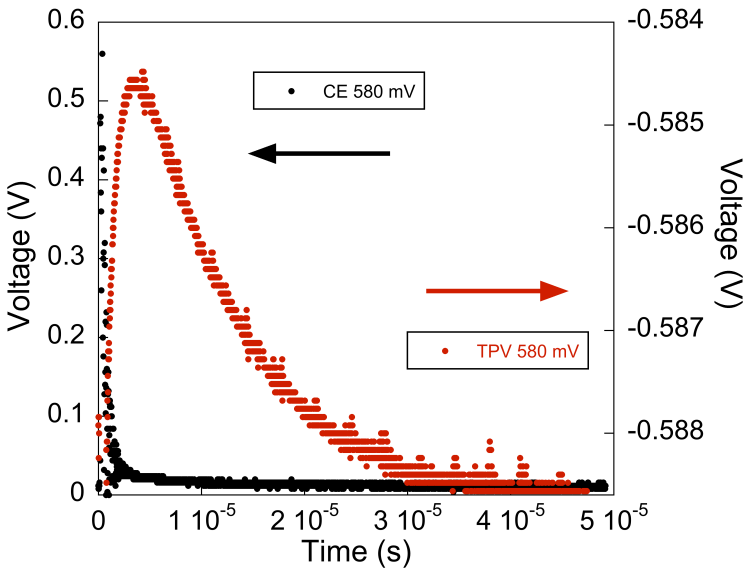

Figure 4. Comparison of a CE and TPV decay of a quantum dot:polymer device at 1 sun.

Nonetheless, if a quantitative determination of the charges lost during extraction is desirable, we can quantify the incurred charge losses using the procedure reported by Shuttle et al.[3] In this, the extracted charge density as a function of time gives a first estimate of the initial charge $n_{ext(\infty)}$ and the remaining charge density $n_{device(t)}$ in the device at each time, see Equation 3:

$$n_{device}(t) = n_{ext}(t = \infty) - n_{ext}(t) \qquad \text{Eq. 3}$$

,where $n_{ext(t=\infty)}$ represent the total charge density extracted. In Figure 5 it is presented the $n_{ext(t)}$ and $n_{device(t)}$ for a representative quantum dot:polymer device at 1 sun light illumination.

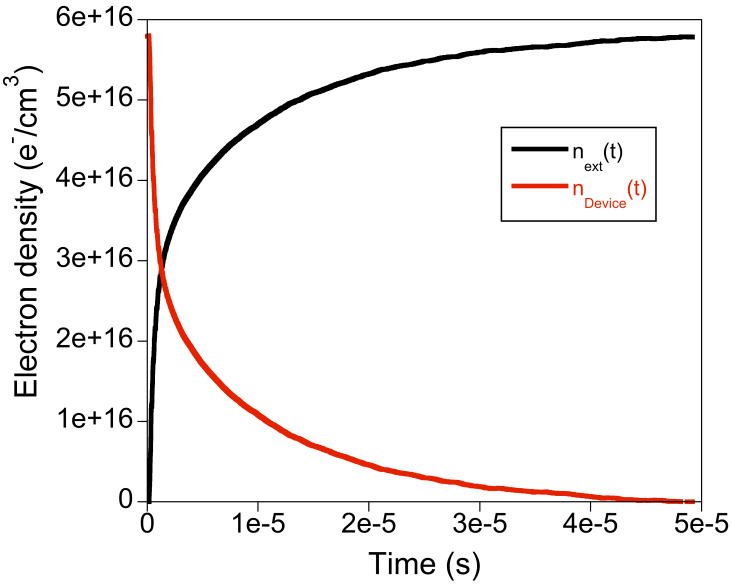

Figure 5. A typical initial CE plot is shown for a device under 1 sun and an initial estimate of the amount of charge present in the device as a function of time.

By performing TPV studies in the same device, combined with this initial estimate of the initial charge density present in the device at V_{OC}, an expression for the carrier decay dynamics in the device at V_{OC} is obtained, Equation 4:

$$\frac{dn}{dt} = -\frac{n_{Device}(t)^{1+\lambda}}{(1+\lambda)\tau_{\Delta n_0} n_0^{\lambda}} \qquad \text{Eq. 4}$$

,where $\lambda=\beta/\gamma$, β is extracted from the TPV and γ from the CE measurements. $\tau_{\Delta no}$ is the initial carrier lifetime and n_0 the initial charge density.

Since TPV is performed as a function of light bias, this may be used to determine the incurred losses during these CE measurements. The carrier lifetime versus light bias of a typical device is depicted in the following section (vide infra).

Using the derived expression for the carrier decay dynamics dn/dt, an initial estimation of the incurred carrier losses (n_{losses}) of the device can be made, see Figure 6.

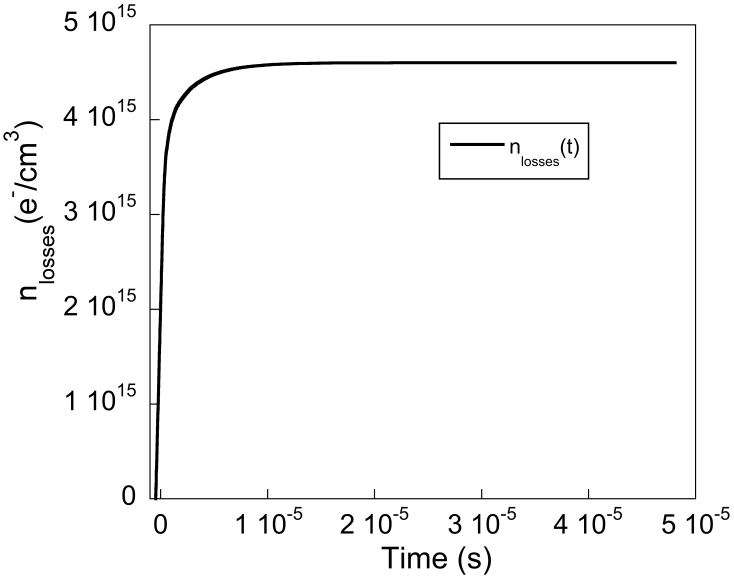

Figure 6. Carrier losses of a quantum dot:polymer device at 1 sun obtained by using the derived expression for the carrier decay dynamics dn/dt.

The expression for $n_{Device}(t)$ can be thus corrected for these losses, and the same process repeated for several iterations (i) until the evaluated carrier losses are convergent, $n_{losses}[i] - n_{losses}[i-1] \sim 0$. For a typical device, the procedure is repeated for 10 times to ensure convergence, as shown Figure 7.

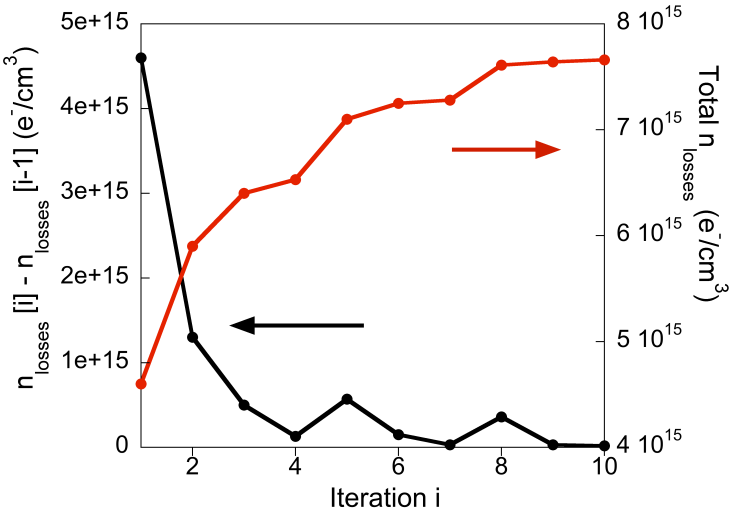

Figure 7. Additional incurred losses n_{losses} [i] - n_{losses} [i-1] between iteration i-1 and the total losses incurred during the charge transient on the expresion of dn/dt converges to a fixed value.

If this procedure is repeated for each of the light biases employed in CE, we can obtain the n_{losses} at each point. These values are then added to the initial charge density n_{ext}, obtaining a new CE curve. A new expression for dn/dt is then re-evaluated to account for this modification (n_0, γ and therefore λ will change). The procedure was then repeated iteratively until consistency is achieved, which provides the finalised values for n_{losses}. By correcting for the determined n_{losses}, we

obtain an estimate of the total excess charge density present in the device given by Equation 5:

$$n_{Device} = n_{ext} + n_{losses} \qquad \text{Eq. 5}$$

A comparison between $n_{ext}(V)$ before and after correcting for the total determined charge losses can be made. This correction is relatively small for low light intensities, however, at 1 sun, where the charge densities present in the device under operating conditions are maximum, larger incurred carrier losses are expected. We found that n_{losses} at 1 sun are usually $<$10% of n_{Device}.

2.3. Transient Photovoltage Measurements (TPV).

Transient Photovoltage was developed by B. O'Regan et al. for measurements of carrier lifetimes in dye sensitised solar cells in open circuit conditions. Nevertheless, this technique has been lately used on the characterisation of the recombination dynamics of organic solar cells.

Basically, the measurement consists of the application of small perturbations of light to the device at open circuit conditions, while a constant steady state voltage by background illumination is held. The steady state condition is set by the observed constant V_{OC} of the device and is governed by the equilibrium between the photogenerated charges and its internal recombination. The small perturbation created by pulsed light induces the formation of additional charges. These extra charges will be forced to recombine in order to recover the equilibrium since the open circuit conditions avoid any possibility of charge extraction. If the perturbation is small enough, the rate at which these extra charges recombine can be related to the device recombination process governing the device performance under operating conditions. Variations on the background illumination allows to monitor the carrier lifetime over several light biases.

For the TPV measurements the device is connected to the 1 MΩ input terminal of an oscilloscope TDS 2022 from Tektronix(C). The background illumination was obtained from a ring of 6 white LED's from LUXEON(R), the photovoltage generated by the white light source is referred to as the light bias. The source of the small perturbation was a Nitrogen pump dye laser. The intensity of the laser pulse was attenuated as necessary to keep ΔV_0 smaller than typically 5 mV using a gradient neutral density filter. The optical perturbation resulted in a voltage transient with amplitude $\Delta V_0 \ll V_{0C}$. By restricting measurements to the small perturbation regime, the profile of the measured decay is forced to take the

form of a single exponential (i.e. pseudo-first order behaviour), simplifying quantitative analysis.

A typical measurement consist of the illumination of the solar cell at 1 sun. The maximum applied light bias is usually the V_{OC} of the device. A short pulse of light (~50 ns) is generated by the LASER and its intensity varied to induce a 2-3 mV increase of V_{OC}. The drop in voltage over time is recorded using an oscilloscope. This procedure is repeated by decreasing the light intensity, obtaining the corresponding kinetics at different device applied light bias as shown in Figure 8.

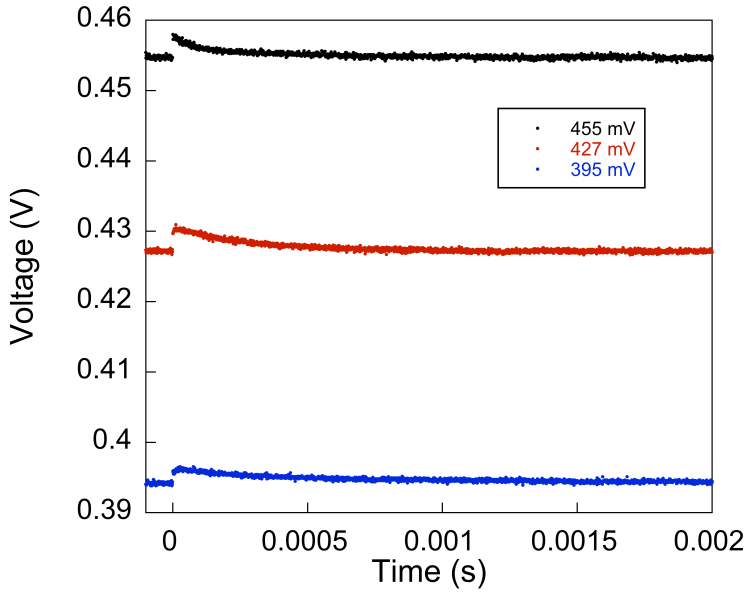

Figure 8. Transient photovoltage decays for a quantum dot:polymer device at different light bias.

The obtained data is fitted to a single exponential function of the form of Equation 6:

$$V(t) = V_0 + V_1 \cdot \exp\left(-\frac{t}{\tau}\right) \qquad \text{Eq. 6}$$

,where V_0 (V) is the voltage at open circuit, V_1 (V) corresponds to the voltage amplitude generated by the LASER pulse and τ (s) is the carrier mean lifetime.

The obtained carrier lifetimes at each light bias are plotted as in Figure 9 (a). And the experimental points are usually fitted to an exponential function as Equation 7:

$$\tau = \tau_0 \cdot \exp\left(\beta \cdot V_{OC}\right) \qquad \text{Eq. 7}$$

,where τ_0 (s) is the carrier lifetime obtained without the presence of photogenerated charges and β is a parameter of the variation of the carrier lifetime with the light bias.

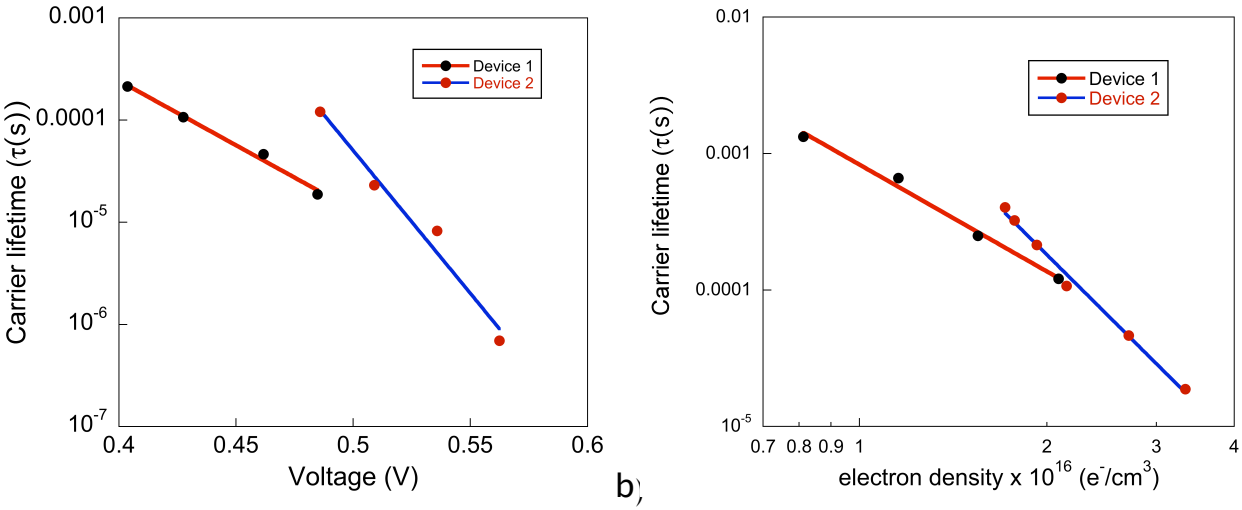

Figure 9. Carrier lifetime of quantum dot:polymer device as a function of the apply light bias (a) and as a function of the charge density (b).

It is well known that in organic solar cells the recombination kinetics are dependent on the light bias, hence on the charge density. Therefore, a fair comparison of the recombination dynamics is only achieved in the case where the recombination lifetime is plotted versus device charge density obtained from CE measurement, as can be seen in Figure 9 (b).

The carrier lifetime as a function of the charge density is usually fitted to a power law function, as shown in Equation 8:

$$\tau_n = \tau_{n_0} \left(\frac{n_0}{n} \right)^{\lambda} \qquad \text{Eq. 8}$$

,where τ_0 (s) is the carrier lifetime obtained without the presence of photogenerated charges and k is a constant.

A more complete description of the signal treatment can be found in the annexes.

3. Experimental section.

The colloidal CdSe quantum dots were synthesised with a mixture of trioctylphosphine (TOP) and oleic acid (OA) capping ligands by using a flow-through microreactor system similar to the procedure reported previously.[4, 5] The mean diameter of the nanocrystals was 4.7 nm, presenting a prominent excitonic absorption peak centred at 610 nm. After synthesis the nanocrystals were treated with hexanoic acid.[6] Briefly, 16 µL CdSe quantum dots (134 mg/mL) were added to 6 mL hexanoic acid at 105ºC and stirred for 10 minutes. 12 mL of methanol were added afterwards to precipitate the quantum dots, which were recovered by centrifugation. Then 1 mL of chloroform and 3 ml of methanol were added at 90ºC to precipitate the quantum dots again. After being recovered by centrifugation, quantum dots were finally dispersed into Chlorobencene at 23 mg/mL.

The alternating copolymer (polydithiophene)-alt-4,7(2,1,3-benzothiadiazole) (PCPDTBT) was synthesised in a Stille-type polycondensation as described before,[7] resulting in mean and weight average molecular weights of M_n=14.300 g/mol and M_w=21700 g/mol. The chemical structure is presented in Figure 10.

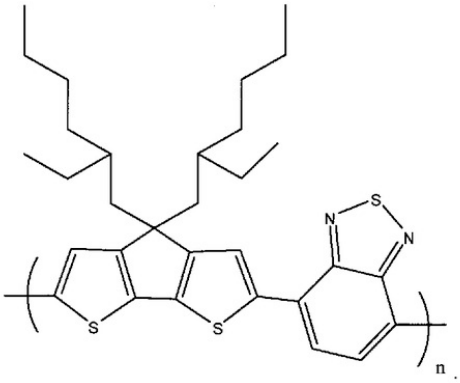

Figure 10. Chemical structure of the PCPDTBT polymer.

The active layer of the bulk heterojunction solar cells was prepared from a chlorobenzene quantum dot solution of 23 mg/ml, which was mixed with a 1,2,4-trichlorobenzene (TCB) PCPDTBT solution at 20 mg/ml, at 9:1 ratio in weight.

The ITO substrates with an area of 25x25 mm^2 were cleaned by sequential ultrasonication with different solvents (acetone, isopropanol). Before the first layer deposition, O_3 treatment was performed on the ITO substrates for 20 minutes. Immediately after this the ITO were covered with an aqueous PEDOT:PSS dispersion (Baytron AL4083, from H.C. Starck) by spin coating. The films were annealed at 150ºC for 30 minutes under N_2 conditions. Afterwards, the polymer:CdSE quantum dots solution was spin-coated onto the surface of PEDOT:PSS to form the photoactive films. The cathodes were thermally deposited onto the Polymer:CdSe

quantum dot blend, obtaining an active area of 9 mm^2. Device thermal annealing was done on a hot plate at 110ºC for 10 minutes under nitrogen atmosphere. The devices were encapsulated with an UV curing epoxy in order to ensure device stability during all the characterisation.

The solutions and films UV-Vis absorption were recorded with a Shimadzu 1600 spectrophotometer. The emission spectra was performed in a Aminco-bowman Series 2 luminescence spectrometer with temperature controller.

The measurement of incident photon-to-current conversion efficiency (IPCE) was plotted as a function of the excitation wavelength by using the incident light from a 300 W xenon lamp (ILC Technology, USA), which was focused through a gemini-180 double monochromator (Jobin Yvon Ltd.)

The J-V characteristics measurements were carried out with an ABET 150 W Xenon light source equipped with the correct set of filters to achieve the solar spectrum 1.5 AM G. The light intensity was adjusted to 100 mW/cm^2 using a calibrated Si photodiode. The applied potential and cell current were measured with Keithley model 2600 digital source meter. The current to voltage (I-V curve) was measured automatically with a home-built Labview(C) software.

L-TAS measurements were performed by excitation of the blend films at 535 nm with pulses from a nitrogen-pumped dye laser PTI GL-301 (<50 ns pulse duration, 1.5 Hz, intensity 0.09 mJ/cm^2). The resulting photoinduced changes in the optical density were monitored at different wavelengths by employing a 150 W tungsten lamp, with 1 nm bandwidth monochromators located before and after the sample, a home-built photodiode based detection system, and a TDS-200 Tecktronik(C) oscilloscope.

Charge extraction (CE) was measured with a white LED illumination source, as it has been previously explained. The devices were illuminated under different light intensities (from darkness to 1 sun intensity) at open circuit conditions, which allows the device to reach an equilibrium in open circuit voltage, depending on the applied light intensity. This applied light bias was turned off in less than μs, while simultaneously, the cell is switched from open to short circuit and the drop in voltage is recorded by the oscilloscope.

Transient photovoltage (TPV) measurements, the devices were connected to the 1 MΩ input terminal of the oscilloscope, and illuminated with the white LED to set the light bias. A small optical perturbation was applied using nitrogen pumped dye LASER as an excitation source with wavelength of 535 nm (frequency 1.5 Hz),

which resulted in voltage transient amplitude of 4 mV. The intensity of the LASER pulse was attenuated as necessary using a circular neutral density filter.

The software employed at ICIQ in order to obtain the charge losses during charge extraction measurements was developed by Dr. Javier Perez Hernandez using Matlab(C) R2009.

4. Results.

4.1. Characterisation of PDPCTBT:CdSe Devices.

The CdSe quantum dots:PCPDTBT bulk heterojunction devices were fabricated in the Freiburg Materials Research Centre (FMF) in Freiburg University. The stability of the devices after encapsulation was proved, with device physical parameters (J_{SC}, fill factor (FF) and V_{OC}) constant for longer than 10 days. All the characterisation was performed at ICIQ.

The PCPDTBT polymer has been widely used in organic photovoltaics with outstanding light-to-energy conversion efficiency close to 5.5% under 1 sun.[8, 9] The main characteristic of the polymer consists in the wide light absorption which extends from the visible to the near IR region as can be seen in Figure 10. Here, we can observe the PCPDTBT main band, which is centred at 730 nm and extends from 500 to 800 nm. When the CdSe semiconductor nanocrystals are added to the polymer at a 9:1 (w:w) ratio, and deposited on transparent substrates, blend films are formed. The absorption spectra of these films corresponds to the addition of the absorption of CdSe quantum dots last excitonic peak, centred at 610 nm, and the PCPDTBT main band, with maximum at 730 nm, as can be seen in Figure 11.

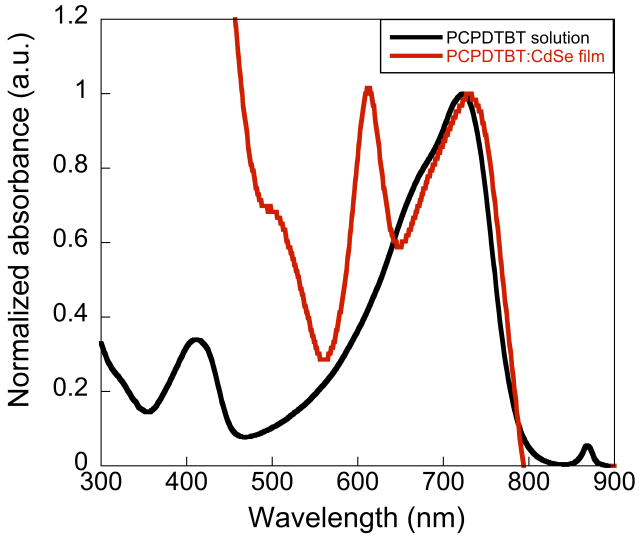

Figure 11. UV-Vis spectra of a PCPDTBT solution (chlorobencene) in black and of a PDPCTBT:CdSe blend film in red.

The incident photon to current conversion (IPCE) of one of the CdSe quantum dots:PCPDTBT solar cells is shown in Figure12 with the blend film absorption spectrum. The IPCE shows a maximum photon to current conversion of 30%, but most important is the fact that clearly both device components, the CdSe quantum dots and the semiconductor polymer, are both capable of generating photocurrent. We have also calculated the theoretical photocurrent obtained in this device from

the overlap integral between the measured IPCE spectrum and the AM1.5G global spectrum provided by the National Renewable Energy Laboratories (NREL) webpage. The theoretical value was 6.4 mA/cm^2, which is in good agreement with the measured value (6.89 mA/cm^2). The small difference between both values could be due to the spectrum mismatch between our solar simulator and the AM1.5G solar spectrum, which has been measured to be lower than 5%.

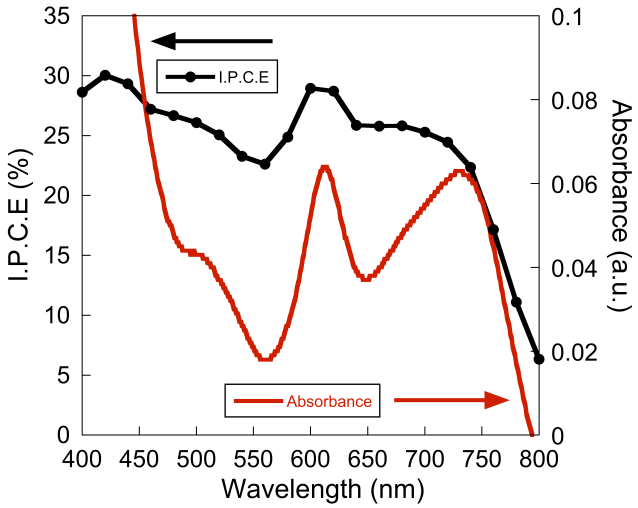

Figure 12. UV-visible spectrum and the IPCE spectrum of a typical CdSe quantum dots:PCPDTBT bulk heterojunction device.

The J–V characteristics of a PCPDTBT:CdSe quantum dot device at different light intensities are shown in Figure 13. A summary of the average physical parameters of all measured devices is presented in Table 1. The devices showed an average short circuit current density of 6.24 mA/cm^2 and an open circuit voltage of 566 mV, obtaining efficiencies of 1% at 1 sun. Although this is not the maximum efficiency reported for this kind of solar cell (2.7%),[4] these devices were efficient enough in order to measure the charge recombination dynamics, with very good signal to noise ratio.

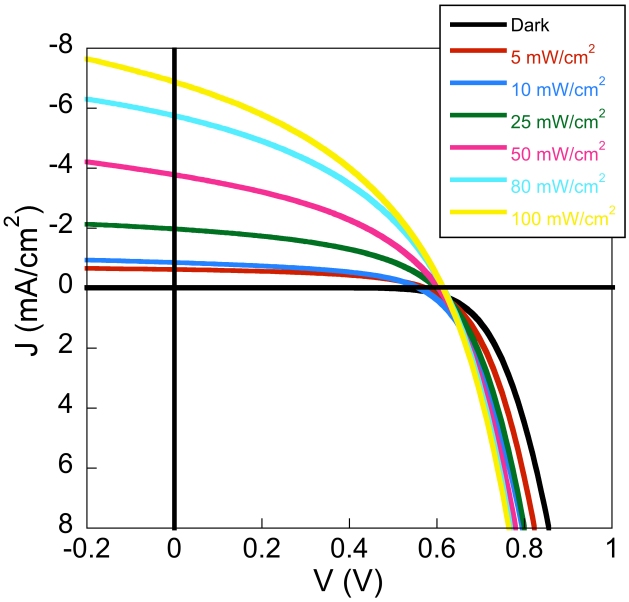

Figure 13. J-V characteristics of a PCPDTBT:CdSe quantum dots device at different light intensities.

Table 1. Characteristic parameters from the J-V curves obtained from the average values of the measurements of 15 devices at 1 sun.

Parameters	J_{SC}(mA/cm²)	V_{OC}(mV)	FF(%)	η(%)
Device average	6.24±0.33	566±0.26	28.6±1.12	1±0.08

As can be seen in Figure 14, the photocurrent density is linear with the light intensity. This observation suggests that no major losses due to non-geminative recombination processes occur at short circuit. Different behaviour has been observed for organic solar cells in polymer bulk heterojunctions, where the dependence of the current density with the light intensity follows a power law function instead.[10, 11] In those cases, a linear dependency indicates that the recombination is first order in carrier density (such as geminative recombination). Nonetheless, the open-circuit voltage on the devices do not follow this linear behaviour with the light intensity, as can be seen in Figure 14. This indicates that the major non-geminative recombination events are taking place at these conditions. For this reason, the recombination dynamics on complete devices will be investigated under open circuit conditions.

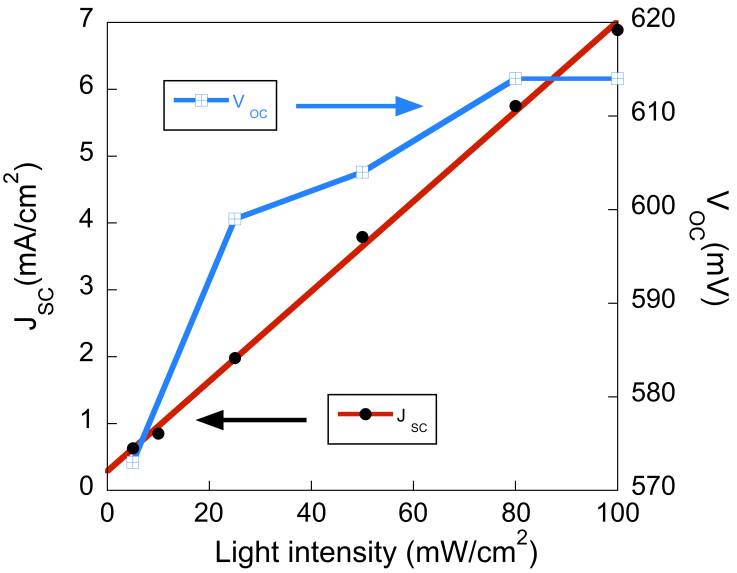

Figure 14. Dependence of J_{SC} and V_{OC} with the light intensity of a PCPDTBT:CdSe quantum dot device.

4.2. Charge Extraction Measurements of the Charge Density in the Devices.

The total charge in the device at different V_{OC} corresponding to different light intensities was measured by the charge extraction (CE) technique as described previously, and the results are shown in Figure 15 (a). The experimental points can be fitted to an exponential equation of the form of Equation 2. This exponential behaviour is usually observed when the photo-generated charges are being accumulated at the tail of the density of states (DOS) as the light intensity is raised.

In contrast, a linear behaviour with the light bias (not observed for these devices at high light intensities) would imply that the charge is accumulated at the metal electrodes and the cell photovoltage is determinates by the V_{bi} (built-in-voltage).[12]

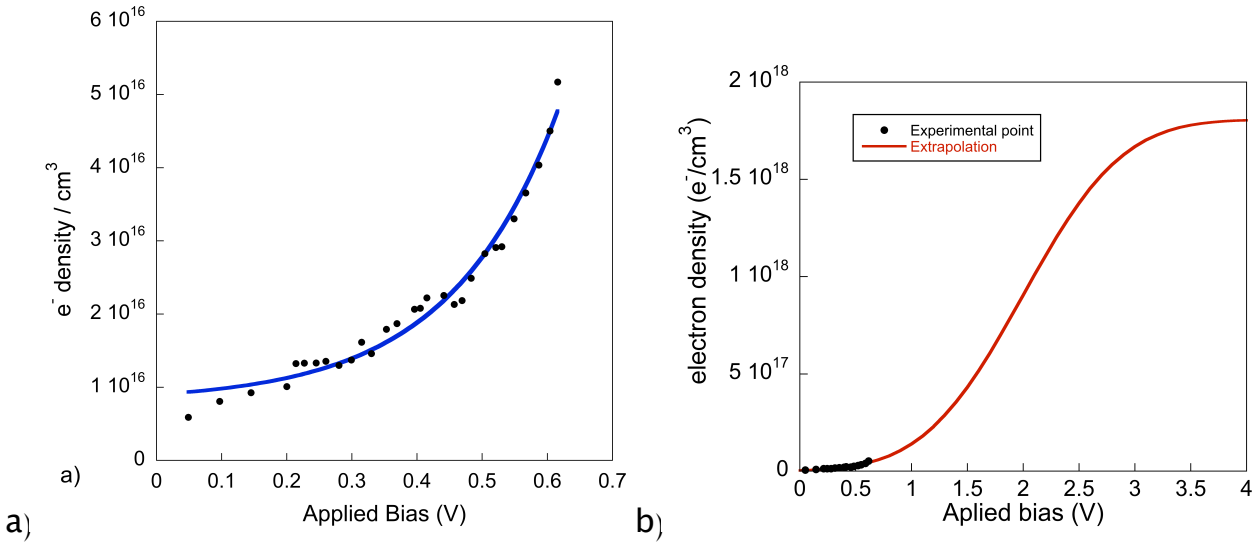

a) b)

Figure 15. Electron density measured with the charge extraction technique (a) and a extrapolation (b) of the experimental data to a Gaussian function. The blue line in (a) correspond to the data fit to an exponential function and the red line (b) correspond to the extrapolation of the experimental data to a Gaussian function.

The fitting of the experimental data from the CE measurements to several devices provides an average value of the initial carrier concentration ($n_0 = 7 \cdot 10^{15} \pm 1.7 \cdot 10^{15}$ e^-/cm^3), when no light bias is applied, and an average $\gamma = 9.42 \pm 1.95$ or $\gamma = 9.87 \pm 0.61$ if we take only into consideration the range between 0.4 and 0.62 V, where an excess of charge accumulated was found for these devices. These values have been obtained from the average of the data extracted from several devices and the good correlation of the experimental data to an exponential function implies that the device is highly p-doped as is the case in P3HT/PCBM organic solar cells,[11, 13] and the states in the tail of the DOS of the polymer are those which dominate the recombination rate.

An extrapolation of the experimental points to a Gaussian function of the form of Equation 8 was also performed, and it is shown in Figure 15 (b). This give us an estimation of the shape of the DOS in the device.

$$g_n(E - E_L) = \frac{N_n}{\sqrt{2\pi\sigma_n}} \exp\left[-\frac{(E_L - E)^2}{2\sigma_n^2}\right] \qquad \text{Eq. 8}$$

,where N_n is the total density per unit volume (for the device showed in Figure 15 (b) $N_n = 1.8 \cdot 10^{18}$ cm^{-3}) and σ_n is the disorder parameter ($\sigma_n = 0.7$). This type of distribution reflects the energy disorder caused by electrostatic and steric interactions resulting from the different environment in which each material is

placed. It should be pointed out that Equation 8 is a first approximation, and for more accurate determinations of the DOS further investigations must be correlated. [11]

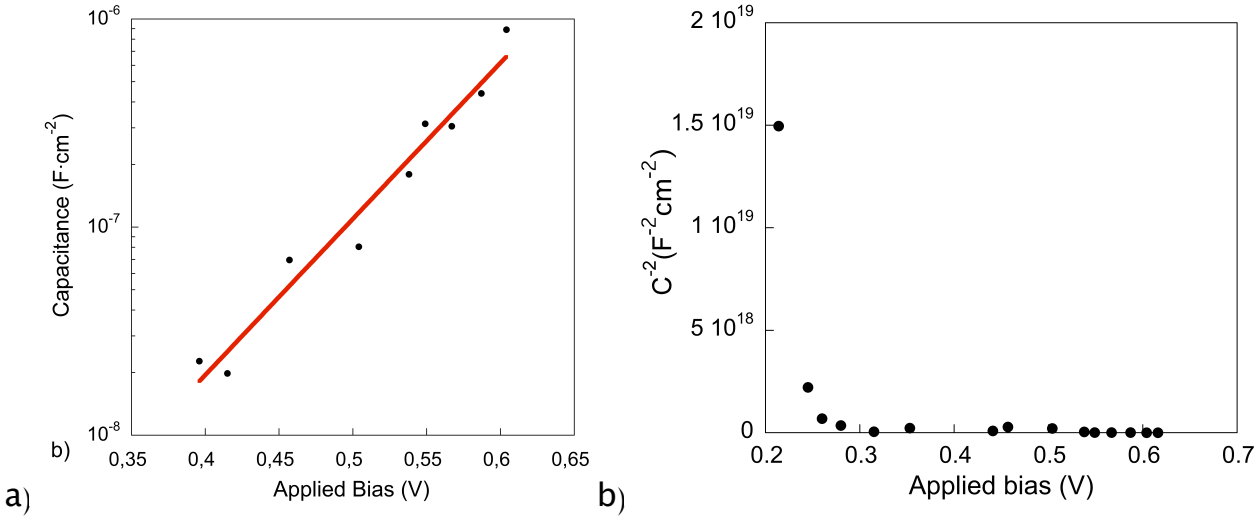

Figure 16. (a) Capacitance vs. light bias induced open-circuit voltage of complete device measured under standard operation conditions. (b) Mott-Schottky plot of the studied device.

The chemical capacitance was also calculated from the charge extraction data. The differential capacitance C is defined as the voltage change ΔV_0 when a small amount of charge ΔQ is added to the device (Equation 9). These values are shown in Figure 16 (a).

$$c = \left(\frac{\Delta Q}{\Delta V_0} \right) \qquad \text{Eq. 9}$$

ΔQ may be also obtained by integrating with respect to time the current measured obtained for each light bias applied. Figure 16 (a) shows the capacitance curve is the range from 400 to 620 mV. For lower values of voltage (V_{OC} < 400 mV) there is no excess of charge accumulated in the device layer and the capacitance obtained corresponds to the electrode capacitance, which was found to be ~10 nF/cm^2 for those devices. The device built-in-voltage (V_{Bi}, flat-band conditions at the cathode) has been extracted from a Mott-Schottky plot (Figure 16 (b)) and found to be 0.32 V. It is worth noticing that V_{Bi} refers to a particular interface and it does not limit the device V_{OC}. It is also important to highlight that at light bias higher than 400 mV the capacitance is found to increase exponentially with V_{OC}.

We have also studied the charges that may be lost before extraction due to their recombination during transport. As can be seen in Figure 17, the result is that the total amount of charge, which is lost, is negligible (less than 4%) and the major losses take place at high light intensities. In any case, these losses will affect the magnitude of the curves, however the curve shape is the same. Previous studies

showed also an error lower than 10% when employing this technique on organic bulk heterojunction solar cells.[14 15]

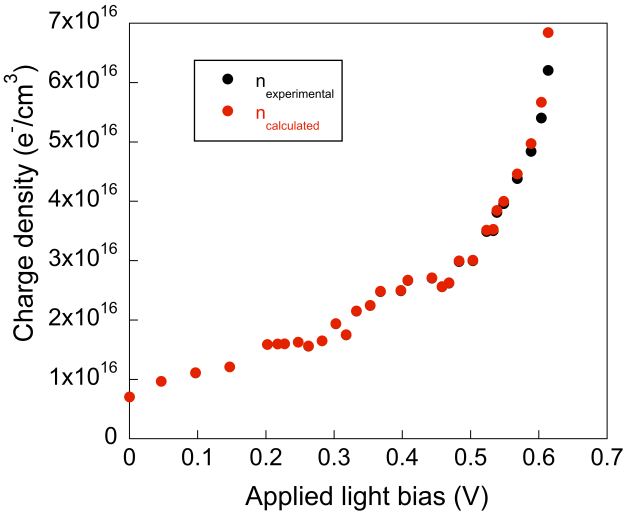

Figure 17. Comparison of the charge densities in the device by charge extraction determined experimentally and calculated from the procedure previously described.

Since the charge accumulation starts at potentials close to the V_{OC}, observed in the J–V curves at 1 sun for these devices, the light dependent charge recombination lifetimes were measured at those potentials. The calculation of the charge losses also confirms that the major charge losses due to internal recombination take place at these potential.

4.3. Charge Recombination Measurements.

Laser transient absorption spectroscopy (L–TAS) was used to study the photo–indued charge recombination dynamics in thin films, such as the ones employed in the devices, but without the presence of evaporated metal electrodes. The transient absorption spectrum, from the visible to the near IR region, is presented in Figure 18 (a), and the lifetime decay of the radical cations (PCPDTBT polarons) in blends films with CdSe quantum dots is shown in Figure 18 (b).

In the visible region of the transient spectrum the bleaching of the ground state of the PCPDTBT can be observed, and a positive signal (related to the formation of the cationic species) arises in the near IR region, as it has been previously reported.[16]

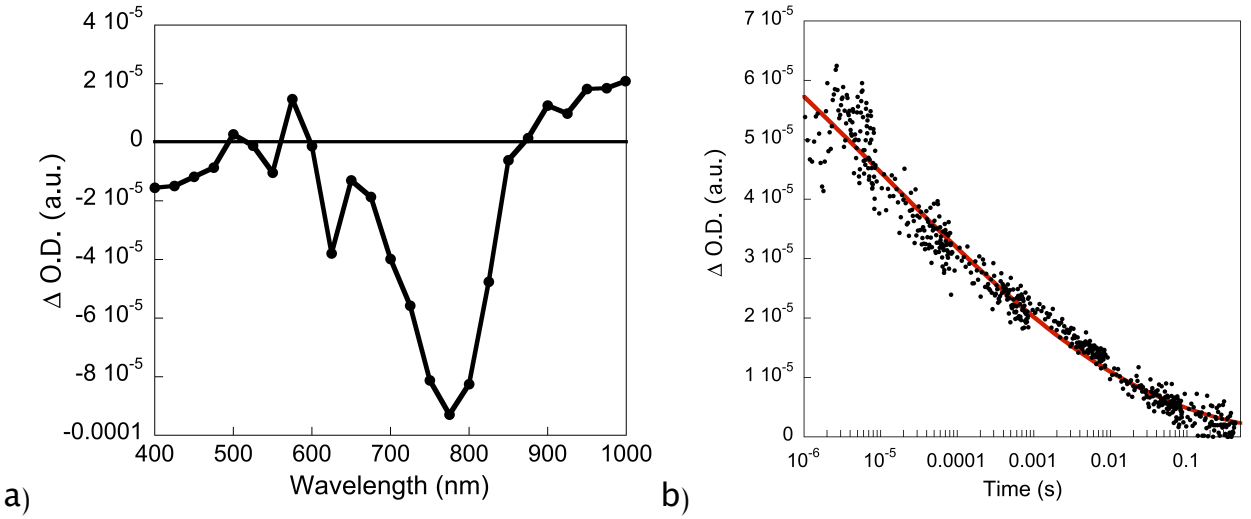

Figure 18. Transient absorption spectra (a) and decay (b) of CdSe quantum dots:PCPDTBT blend films. For the decay, the laser excitation was 535 nm and was monitored at 980 nm. For the absorption spectrum the acquisition time was 0.5 ms at the same excitation wavelength. The red line in the decay corresponds to the fitting of the experimental data to a stretch exponential function.

The decay of the transient signal in the microsecond–millisecond time scale can be fitted with a stretch exponential function, Equation 10:

$$f(t) = A \cdot \exp\left(-\frac{t}{\tau}\right)^{\alpha} \qquad \text{Eq. 10}$$

From the fit we extract the lifetime (τ) of the PCPDTBT polarons in the blend is of 11 μs and the stretched factor (α) of 0.13. This suggest that there are multiple decay processes in the blend films due to the different energies of the trap states present in the quantum dots surface. This result is in good agreement with the previous published results in polymer:CdSe quantum dots using photoinduced absorption spectroscopy (PIA), and the results presented in this Thesis in the previous chapter. As we have commented previously, the observation of stretch exponential decays in nanocrystal/polymer blend films is in contrast to the power-law decays measured in bulk heterojunction organic solar cells.[17, 18]

Now, we focus on the photo-induced charge recombination in complete devices under working conditions. The transient photovoltage (TPV) was measured over a range of light intensities corresponding to a V_{OC} range of 0.4 – 0.62 V, which is the same range we evaluate the accumulated charge, and is shown in Figure 19 (a).

The lifetime of the carriers in a complete cell (τ) was found to vary exponentially with the V_{OC} (Equation 7). Where τ_0= 23.33 ± 5.26 s and β = 29.47 ±

2.18. As the light intensity increases the carrier lifetime (τ) decreases, reaching ~ 1 μs at an intensity of approximately 1 sun.

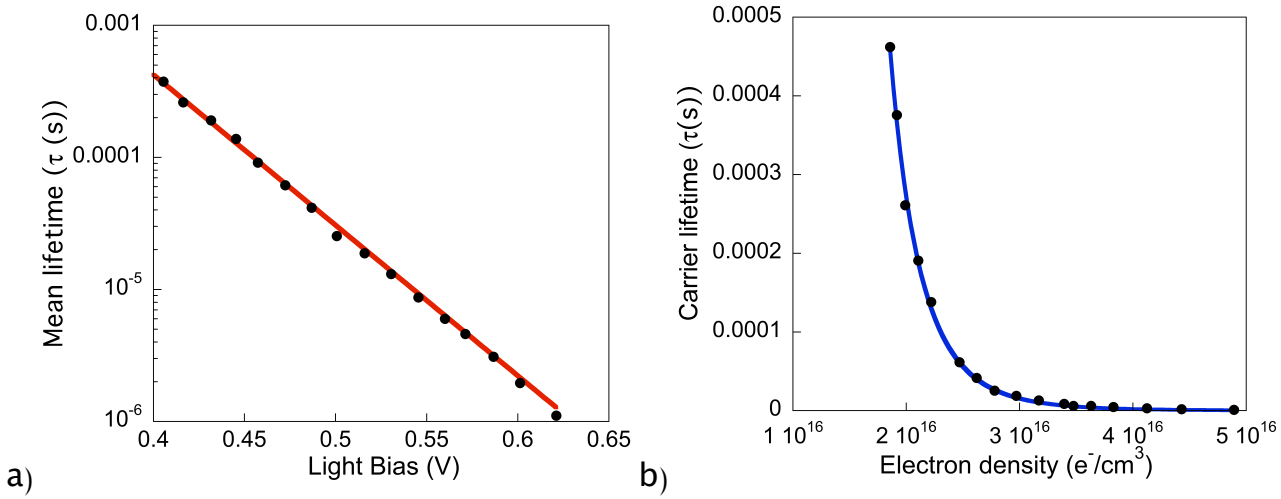

Figure 19. Recombination lifetime at open circuit conditions extracted from fitting at the transient photovoltage to a single exponential function, the red line corresponds to an exponential fit. (b) Carrier lifetime as a function of charge density with V_{OC} from 400 to 620 mV. The blue line corresponds to the data fit to Equation 8.

The recombination lifetimes were also plotted vs. charge density (Figure 19 (b)), and we found that the carrier lifetime decreased as the charges stored in the device under working conditions was increased, as expected. The relation between the charge density with the recombination lifetime follows an inverse cubic relationship with:

$$\lambda = \frac{\beta}{\gamma} \qquad \text{Eq. 11}$$

We found λ= 2.99 ± 0.14 for PDPCTBT:CdSe quantum dot bulk heterojunction solar cells. This means that the charge carrier decay dynamics shows a strong carrier density dependency. Indeed, this dependence is stronger than polymer:fullerene bulk heterojunction or small molecule:fullerene solution processable solar cells, where an inverse square relationship (λ=2) between the charge density and the recombination lifetime was found.[12, 14] In contrast, values between 3.7 and 4.3 have been shown in DSSC, depending on the electrolyte composition.[19]

In organic solar cells, bimolecular non-geminative recombination processes have been suggested to explain the inverse square relationship between the recombination rate and the charges, exhibiting a third-order dependence on charge density ($dn/dt \approx n^3$). On the other hand, a non-defined number of species in

the electrolytes of the DSSC provide multiple recombination pathways, obtaining dispersive recombination dynamics.

In PDPCTBT:CdSe quantum dot solar cells non-geminative recombination is present in the device. The exponential dependence of the carrier lifetime with the applied bias, and the fact that the recombination under operating conditions follows a power low function, points to this. However, the stronger dependence of the carrier lifetime with the charge density indicates that, in addition to the bimolecular events that govern the recombination dynamics in OPV, there are other recombination pathways in the bulk or between the photoactive materials and the electrodes that affect the recombination dynamics in these devices too. In order to confirm or dismiss the effect of the metal electrodes in the recombination dynamics a comparison of the L-TAS and TPV measures was done.

4.4. Comparison of L-TAS data in Thin Films with TPV Data in Complete Devices.

In order to analyse the effect of electrode dependent processes such as non-selective contacts, shunt resistance, or the presence of macroscopic electric fields in these devices we have compared the variation of charge carrier density (n) with time (dn/dt) obtained with from the combination of CE and TPV and the charge carrier density extracted from the L-TAS.[14, 20] The L-TAS measurements were undertaken without the presence of device metal electrodes, hence the bulk heterojunction thin film is not affected by the processes dependent on the electrodes. Therefore, if both experimental sets of data, the one provided by the combination of CE/TPV measurements in complete devices, and the one from L-TAS are in good agreement, we can conclude that non-geminative charge recombination losses are not determined by any process dependent upon device electrodes at the time scale that our charge recombination measurements have been carried out (from microsecond to milliseconds).

As reported by Shuttle et al., n(t) from CE/TPV data can be calculated by integrating Equation 4 to obtain:

$$n(t) = n_{t=0}\left[1 + \frac{\lambda n_{t=0}^{\lambda} \cdot t}{(1+\lambda)\tau_{\Delta n_0} n_0^{\lambda}}\right]^{-1/\lambda} \qquad \text{Eq. 12}$$

,where, for our devices, λ=3, n_0= $8.05 \cdot 10^{15}$ cm^{-3} and $\tau_{\Delta n0}$ = 23.33 s. Moreover, we have used several values for $n_{t=0}$ in order to see if there are substantial difference in n(t) when $n_{t=0}$ is varied. The dependence of n(t) with $n_{t=0}$ is shown in Figure 20, and as can be seen there is no difference at the lifetime time range of the carriers in our

devices. We used a value of $4 \cdot 10^{15}$ cm^{-3} for $n_{t=0}$, which it is in good agreement with the value of charge carrier density (n) obtained by the CE technique as described before (Figure 5).

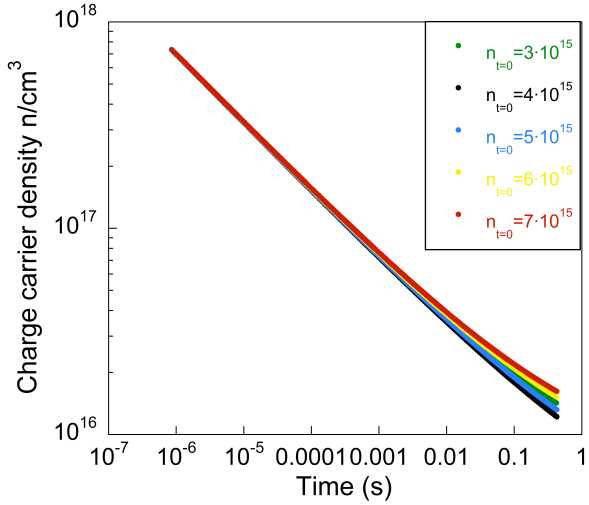

Figure 20. Charge density as a function of time extracted from CE/TPV data for several $n_{t=0}$ values.

The n(t) from L-TAS measurements can be calculated converting the L-TAS decay signal (ΔO.D. optical density) to the charge carrier density n_{TAS} by using the Lambert-Beer law, Equation 13:

$$\Delta O.D. = n_{TAS} \cdot d \cdot \varepsilon_{PCPDTBT^+} \qquad \text{Eq. 13}$$

,where d is the thickness of the films and $\varepsilon_{PCPDTBT^+}$ is the polaron molar extinction coefficient at the detection wavelength. $\varepsilon_{PCPDTBT^+}$ was not measured independently but was used as a fitting parameter to allow comparison of the TAS and CE/TPV data. The n_{TAS} as a function of $\varepsilon_{PCPDTBT^+}$ is depicted in Figure 21. The $\varepsilon_{PCPDTBT^+}$ value is independent on the decay slope, which is constant and we only observe changes in the decay amplitude. The fitting procedure yielded $\varepsilon_{PCPDTBT^+}$ ~ 20000 M^{-1} cm^{-1}.

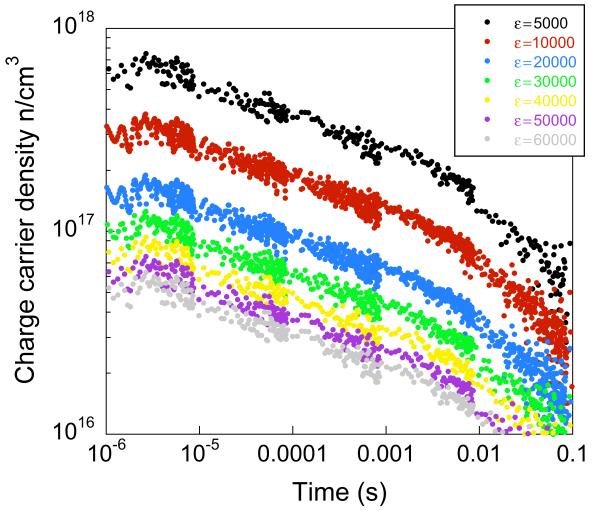

Figure 21. n(t) from L-TAS data for different $\varepsilon_{PCPDTBT^+}$ values.

Finally, the n(t) curves from CE/TPV and L-TAS were in good agreement, as it is shown in Figure 22. The experimental points were fitted to power law functions of the form:

$$n(t) = A \cdot t^{-\alpha} \qquad \text{Eq. 14}$$

,where A is a constant and $\alpha_{CE/TPV}$ ~ 0.3 and $\alpha_{CE/TPV}$ ~ 0.23. We observe similar results for both the CE/TPV data and the L-TAS measurements and thus we can conclude that the non-geminative recombination dynamics in these devices are not influenced by the presence of processes dependent on the electrodes. As such, we assign the decay dynamics observed in the TPV measurements to the same process obseved in the TAS data.

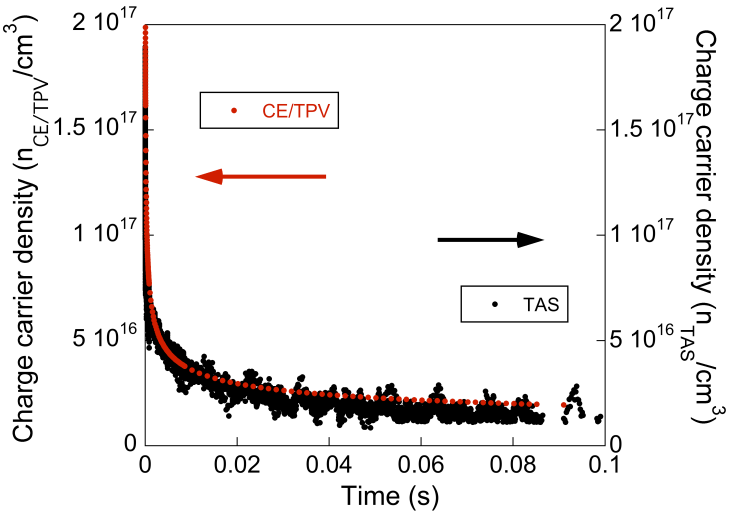

Figure 22. Comparison of charge carrier density (n) as function of the time (t) derived from CE/TPV and TAS data .

Therefore, the strong dependence of the recombination dynamics with the charge density in these devices in comparison with other OPV solar cells must be attributed to other factors, such as the nanomorphology or the presence of traps states in the quantum dot surface, rather than electric fields due to the metal electrodes at the studied time range. Different reports have obtained similar conclusions for polymer:fullerene solar cells.[20, 21] The fact that the semiconductor nanocrystals are covered with capping ligands could also contribute to the generation of different recombination pathways, which would be different from fullerene:polymer in organic photovoltaics. Although usually capping ligands, such as phosphines, phosphonic acids, amines derivates or oleic acid, are believed to be removed from the quantum dot surface when ligand exchange reactions are carried out, the fact is that there is no evidence of their complete elimination. These organic molecules may play also a role in the interfacial reactions between the nanocrystals and the polymer, and promote recombination processes that are not present in other kind of organic photovoltaic device architectures.

5. Conclusions.

The charge accumulation and the photo-induced charge recombination in polymer:quantum dots bulk heterojunction solar cells have been investigated.

Hybrid photovoltaic devices containing the low band gap semiconductor polymer PCPDTBT and CdSe quantum dots were fabricated obtaining overall efficiencies of 1%. The devices showed charge photogeneration both from the polymer and from the nanocrystals. Hence, both materials are contributing to the overall photocurrent in the devices. The current density in the devices increases linearly with the light intensity. However, the photovoltage is limited by non-geminative recombination.

The PCPDTBT:CdSe quantum dots solar cells showed charge accumulation in the active layer, which grows exponentially with increased light intensity. The devices show belong the geometrical capacitance the ability to store charges. This excess of charge accumulation produce a splitting of the quasi-Fermi levels of the electron donor and the acceptor. These energy differences are responsible for the V_{OC} in the devices. Therefore, we can conclude that the working principle of these devices is not due to the electric fields produced between the metal contacts but, because of the excess of charge accumulation, which generates the chemical capacitance.

The carrier lifetime was found to decrease with the light intensity in these devices. This behaviour is analogous to the that observed for other all organic bulk heterojunction solar cells. However, the dependence of the carrier lifetime with the charge density show an inverse cubic dependency. While in the case of the polymer:fullerene solar cells this dependency has been found to be inverse square. The stronger carrier lifetime dependency with the charge density produce faster recombination kinetics in this devices compared with the organic photovoltaics at 1 sun under operating conditions.

The origin of this stronger charge carrier density dependency upon the recombination has been investigated. In order to exclude any process related with the device electrodes (such as nonselective contacts, shunt losses or the presence of macroscopic electric fields) as the reason responsible for the device recombination dynamics, comparison between L-TAS measurements in thin films without the presence of electrodes and the combination of CE and TPV measurements in complete devices was done. The recombination in both cases followed very similar dynamics. Therefore, we can conclude that the metal contacts are not playing a major role on the strong carrier lifetime dependency upon the

charge density that these devices present. As a consequence, the non-geminative recombination processes, that are taking place in the bulk, has been pointed out as the origin of this strong dependency. We suggest, that the superficial trap states that the organic capping molecules produce in the nanocrystals could be the reason responsible for the charge recombination events, and so, for the stronger dependency of the carrier lifetime compared with organic photovoltaic solar cells.

Bibliography.

1. Duffy, N. W.; Peter, L. M.; Rajapakse, R. M. G.; Wijayantha, K. G. U. *Electrochem. Commum.* **2000,** 2, (9), 658-662.
2. Duffy, N. W.; Peter, L. M.; Rajapakse, R. M. G.; Wijayantha, K. G. U. *J. Phys. Chem. B* **2000,** 104, (38), 8916-8919.
3. Shuttle, C. G.; Maurano, A.; Hamilton, R.; O'Regan, B.; Mello, J. C. d.; Durrant, J. R. *Appl. Phys. Lett.* **2008,** 93, 183501.
4. Zhou, Y.; Eck, M.; Veit, C.; Zimmermann, B.; Rauscherm, F.; Niyamakom, P.; Yilmaz, S.; Dumsch, I.; S.Allard; Scherf, U.; Krüger, M. *Solar Energ. Mat. Solar Cells* **2011,** 95, (12), 3227-3232.
5. Chan, E. M.; Mathies, R. A.; Alivisatos, A. P. *Nano lett.* **2003,** 3, 294-302.
6. Zhou, Y.; Riehle, F. S.; Yuan, Y.; Scheleiermacher, H. F.; Niggemann, M.; Urban, G. A.; Krüger, M. *Appl. Phys. Lett.* **2010,** 96, 213506.
7. Zhu, Z.; Waller, D.; Guadiana, R.; Morana, M.; Muhlbacher, D.; Scharber, M.; Brabec, C. *Macromolecules* **2007,** 40, 1981-1986.
8. Mühlbacher, D.; Scharber, M.; Morana, M.; Zhu, Z.; Waller, D.; Gaudiana, R.; Brabec, C. *Adv. Mater.* **2006,** 18, 2884-2889.
9. Hwang, I.-W.; Cho, S.; Kim, J. Y.; Lee, K.; Coates, N. E.; moses, D.; Heeger, A. J. *J. Appl. Phys.* **2008,** 104, 033706.
10. Koster, L. J. A.; Mihailetchi, V. D.; Xie, H.; Blom, W. P. *Appl. Phys. Lett.* **2005,** 87, 203502.
11. Garcia-Belmonte, G.; Boix, P. P.; Bisquert, J.; Sessolo, M.; Bolink, H. J. *Solar Energ. Mat. Solar Cells* **2010,** 94, 366-375.
12. Antonio Sánchez-Díaz; Roberto Pacios; Udane Muñecas; Tomás Torres; Palomares, E. *Organic Electronics* **2011,** 12, 329-335.
13. Shuttle, C. G.; O'Regan, B.; Ballantyne, A. M.; Nelson, J.; Bradley, D. D. C.; Durrant, J. R. *Phys. Rew. B* **2008,** 78, 113201.
14. Shuttle, C. G.; O'Regan, B.; Ballantyne, A. M.; Nelson, J.; Bradley, D. D. C.; Mello, J. d.; Durrant, J. R. *Appl. Phys. Lett.* **2008,** 92, 093311.
15. Maurano, A.; Hamilton, R.; Shuttle, C. G.; Ballantyne, A. M.; Nelson, J.; O'Regan, B.; Zhang, W.; McCulloch, I.; Azimi, H.; Morana, M.; Brabec, C. J.; Durrant, J. R. *Adv. Mater.* **2010,** *22*, 4987-4992.
16. Hwang, I.-W.; Soci, C.; Moses, D.; Zhu, Z.; Waller, D.; Gaudiana, R.; Brabec, C. J.; Heeger, A. J. *Adv. Mater.* **2007,** 19, 2307-2312.
17. Wang, P.; Abrusci, A.; Wong, H. M. P.; Svensson, M.; Andersson, M. R.; Greenham, N. C. *Nano Lett.* **2006,** 6, 1789-1793.
18. Pientka, M.; Wisch, J.; Boger, S.; Parisi, J.; Dyakonov, V.; Rogach, A.; Talapin, D.; Weller, H. *Thin Solid Films* **2004,** 48, 451-452.
19. O'Regan, B. C.; Durrant, J. R.; Sommeling, P. M.; Bakker, N. J. *J. Phys. Chem. C* **2007,** 111, 14001-14019.
20. Maurano, A.; Shuttle, C. G.; Hamilton, R.; Ballantyne, A. M.; Nelson, J.; Zhang, W.; Heeney, M.; Durrant, J. R. *J. Phys. Chem. C* **2011,** 115, 5947-5957.
21. Bisquert, J.; Garcia-Belmonte, G. *J. Phys. Chem. Lett.* **2011,** 2, (15), 1950-1964.

Chapter 5 - General Conclusions

The conclusions extracted from the results obtained in this thesis are summarised.

In this thesis, we have prepared and characterised CdSe semiconductor nanocrystals. Those nanocrystals were prepared in different morphologies (dot, nanorods and tetrapods). Moreover, ligand exchange reactions were performed on the CdSe nanocrystal surface in order to modify their electronic properties. The nanocrystals were then utilised to study fundamental charge transfer reactions between the semiconductor nanocrystals and mesoporous titania films and polymer/quantum dots bulk heterojunction thin films.

Firstly, the CdSe nanocrystals showed excellent properties both as an electron acceptor as an electron donor. The photo-induced electron transfer between the organic molecule MSqb and the CdSe quantum dots were studied. In this case, the organic dye was able to inject electrons into the nanocrystal conduction band faster than the excited state deactivation. The back electron reaction kinetics were measured, and it was found to be on the millisecond time scale. The recombination kinetics were measured both in solution and thin films, demonstrating this system as a good candidate for photovoltaic applications. Nanocrystal CdSe quantum dots were then linked to titanium dioxide films with a molecular linker. In this case, three different size nanocrystals showed efficient electron injection into the TiO_2 conduction band. The recombination kinetics were investigated, showing that the quantum dot size influences the recombination kinetics.

The photo-induced charge recombination in quantum dot sensitised TiO_2 films, deposited by the SILAR technique, was investigated. It was confirmed that the addition of a ZnS coating layer acts efficiently on the CdSe surface trap states, slowing down the recombination dynamics in these systems. This ZnS layer is passivating trap states in the nanocrystals surface, and thus, enhancing the formation of long-live oxidised CdSe nanocrystals. The transient lifetime decay of CdSe have been increased by 1.000 times with the inclusion of this passivating layer. On the other hand, it has been checked, for PbS nanocrystals, that the addition of successive SILAR cycles to increase the light harvesting, is limited by the films saturation, which promote an increase in the recombination kinetics.

The charge recombination kinetics has been also compared for CdSe quantum dots deposited by Direct Adsorption, Linker adsorption and Chemical Bath Deposition. The latter technique, in spite of allowing an increase of nanocrystal load in the films, compared with the other two techniques, results in faster recombination kinetics. This is probably due to the direct contact of nanocrystals with the metal oxide that this technique produce.

It has been also investigated the role of ruthenium molecular dye co-sensitised with CdSe quantum dots in titania films. Fast photo-induced hole transfer from quantum dots to the dye molecules has been found. The molecule acts as a regenerating agent of the quantum dot sensitisers and promotes long life charge in the dye/QD/TiO_2 system. Co-sensitivisation of TiO_2 films with CdS quantum dots, using Electrophoretic Deposition, and a ruthenium molecular dye, were studied as well. The addition of the molecular dye has a beneficial effect in the oxidised nanocrystals regeneration, as it has already seen for quantum dots deposited by other techniques. In this case, a amorphous TiO_2 coating between both sensitisers was used with 3 principal purposes. on the hand, to passivate superficial trap states in the nanocrystals and, on the other hand, to increase the stability of the nanocrystals in front of Iodide/Iodine based electrolytes and act as platform for the dye adsorption. This configuration offers a method to slow the interfacial charge recombination and thus allowing efficient charge regeneration.

The interfacial charge transfer reactions between the semiconductor polymer P3HT and CdSe nanocrystals was investigated in blend films. Results indicate sub-nanosecond charge separation. Furthermore, the charge recombination dynamics are dominated by the presence of traps states in the nanocrystals surface. This back electron transfer reactions can be optimised depending on the nanocrystal concentration and the molecules in the surface.

From our analysis, we have observed the influence that the quantum dots concentration play in the charge separation and charge recombination dynamics. The photophysical study illustrates that efficient charge separation takes place already at low quantum dot concentration. In addition, ultra fast ($<$ 200 ps) charge separation is indicated by TCSPC for those composites. On the other hand, we have demonstrated that even for low concentration of quantum dots the recombination dynamics are highly dispersive instead of bimolecular. We also observed that there is a relationship between morphology and charge recombination, which may have direct consequence on the efficiency of complete devices.

After that, spectroscopic measurements revealed that the orientation and the dipole moment of the capping molecules that surround the quantum dot surface causes an effect on the charge transfer reactions at the interface between P3HT polymer and the CdSe quantum dots. Charge separation seems to be influenced by the displacement in the quantum dot energy gap due to the dipolar moment of the capping molecules: There is not a linear and direct relationship between the dipole moment strength and direction and the recombination reactions. Rather this has been explained by the chemical nature of the molecules, which produce a strong

effect over the quantum dot agglomeration and film nanomorphology. The capping molecules that presented para-substitution in the aromatic ring showed higher film roughness caused by the formation of bigger nanocrystal clusters. However, molecules with different structure presented better phase segregation with less nanocrystals aggregates.

Furthermore, the role of the nanocrystal shape on the photo-induced charge transfer reactions was studied. Although the fluorescence spectroscopy measurements revealed no significative differences either on the charge separation yield nor in the injection kinetics, the L-TAS experiments, performed at lower light intensity, showed one magnitude order difference in the signal amplitude between the spheric and the elongated nanocrystals, indicating that there are 10 times more long-lived charges using nanorods and tetrapods rather than with quantum dots. Nevertheless, the transient decays showed faster recombination dynamics for those elongated nanocrystals compared with the quantum dots. Probably, the higher number of charges produces an enhancement of the recombination dynamics in those blend films.

Finally, the charge accumulation and photo-induced charge recombination in polymer:quantum dots bulk heterojunction solar cells under working conditions was investigated.

Hybrid photovoltaic devices containing the low band gap semiconductor polymer PCPDTBT and CdSe quantum dots were fabricated obtaining overall efficiencies of 1% at 1 sun. The devices presented charge photogeneration both from the polymer and from the nanocrystals. Hence, both materials are contributing to the overall photocurrent in the devices. The current density in the devices increased linearly with the light intensity. However, the lose of linearity of the voltage at open circuit with the light intensity suggested that the photovoltage was limited by non-geminative recombination.

The PCPDTBT:CdSe quantum dots solar cells showed charge accumulation in the active layer, which growths exponentially with the light intensity. The devices presented belong the geometrical capacitance the ability the store charges. This excess of charge accumulation produces a splitting of the quasi-Fermi levels in the device semiconductor materials. These energy differences are the responsible of the V_{OC} in the devices. Therefore, we can conclude that the working principle of these devices is not due to the electric fields produced between the metal contacts but, because of the excess of charge accumulation photogenerated

The charge carrier lifetime was found to decrease with the light intensity in these devices. This behaviour is analogous to the one observed for other all organic bulk heterojunction solar cells. However, the dependence of the carrier lifetime with the charge density was found to follow a inverse cubic dependency. While in the case of the polymer:fullerene solar cells this dependency has been found to be inverse square.

The origin of this stronger charge carrier density dependency upon recombination was also investigated. In order to exclude any process related with the device electrodes (such as nonselective contacts, shunt losses or the presence of macroscopic electric fields) as the reason responsible of the device recombination dynamics, comparison between L-TAS measurements in thin films without the presence of electrodes and the combination of CE and TPV measurements in complete devices was done. The recombination in both cases followed very similar dynamics. Therefore, we can conclude that the metal contacts are not playing a major role on the strong carrier lifetime dependency upon the charge density that these devices present. As a consequence, the bimolecular recombination processes, that are taking place in the bulk, has been pointed out as the origin of this strong dependency. We suggest, that the superficial trap states that the organic capping molecules cause in the nanocrystals could be responsible for the charge recombination events, and so, the stronger dependency of the carrier lifetime compared with organic photovoltaic solar cells.

Annexes I

Annexes

Annexes from Chapter 2

1.- Procedure to represent a Transient Absorption Spectrum.

Firstly, open the selected files in Kaleidagraph:

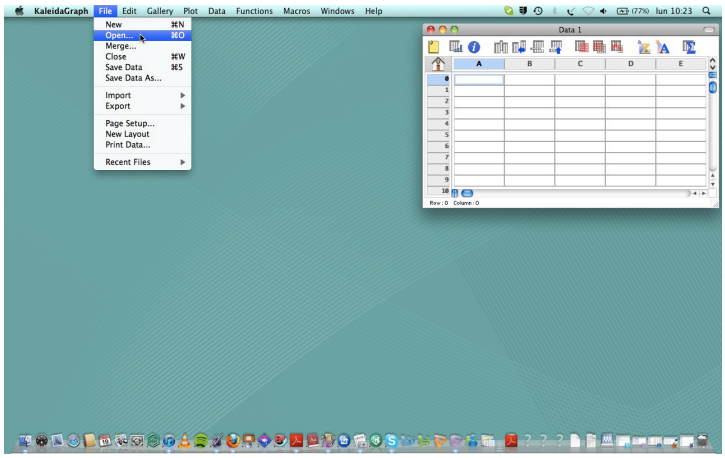

Figure A1. Open .txt files with Kaleidagraph

Secondly, you have to chose the generated .txt files in the experiment:

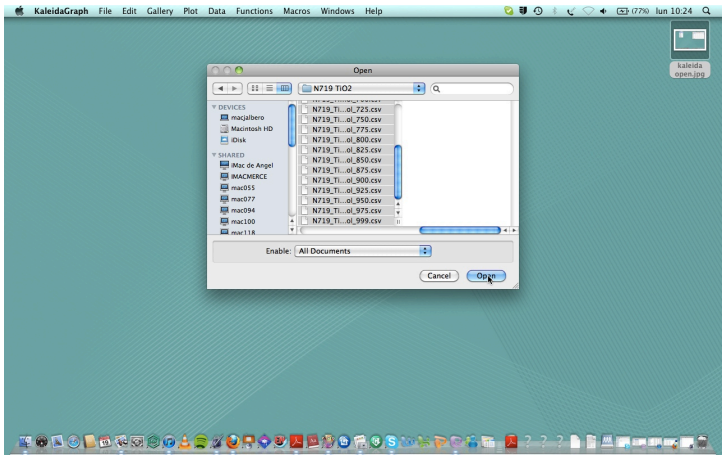

Figure A2. Open .txt files with Kaleidagraph

Thirdly, the files have to be opened in new windows:

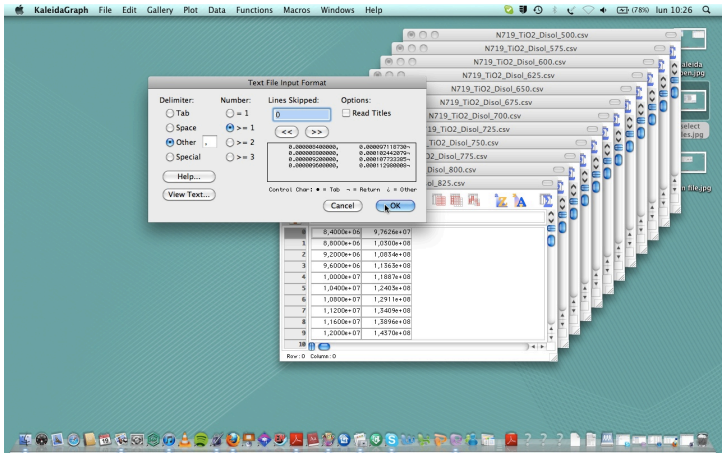

Figure A3. Open a new window for each file.

Then, in a new window copy the values of ΔO.D. at the chosen acquisition time for each measured wavelength:

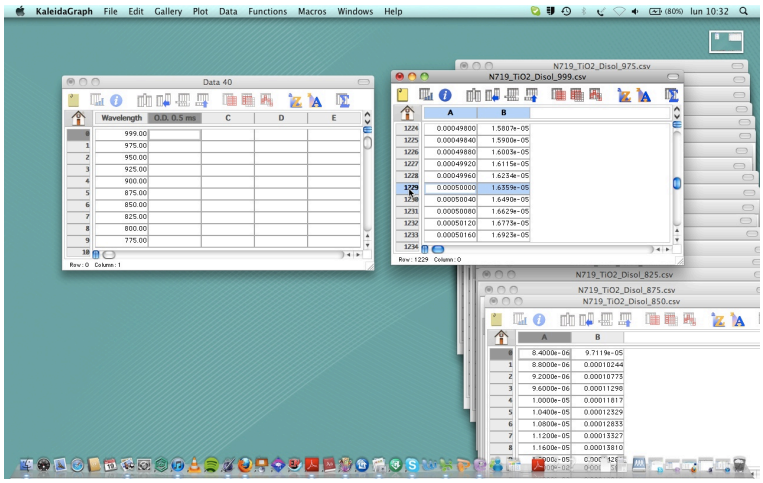

Figure A4. Selection of the desired ΔO.D value.

And complete the table:

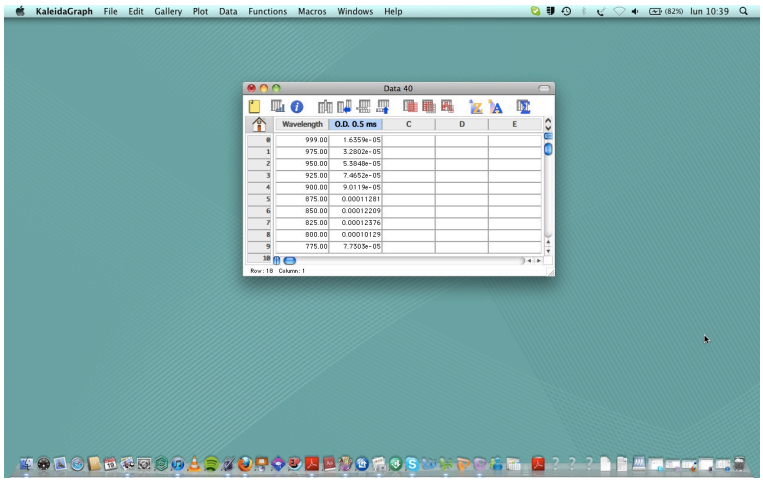

Figure A5. Final table with all values of ΔO.D. at a fix time.

Now, represent the data in a plot:

a) 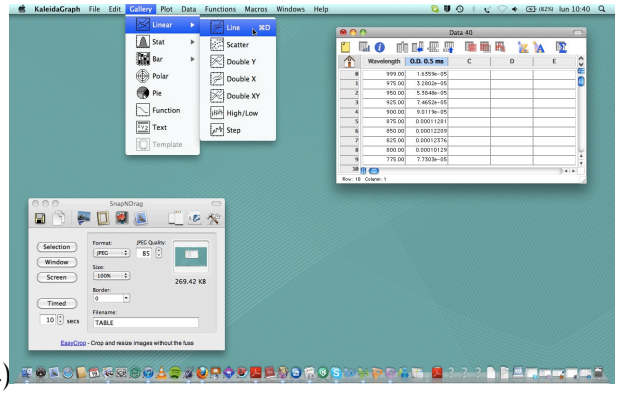 b) 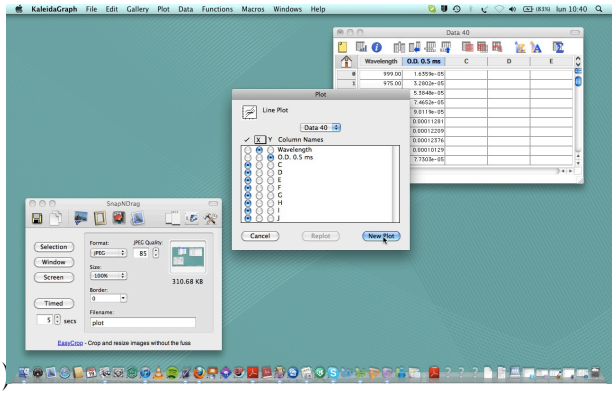

Figure A6. Plotting the data.

Finally, the transient absorption spectrum is represented at a given acquisition time:

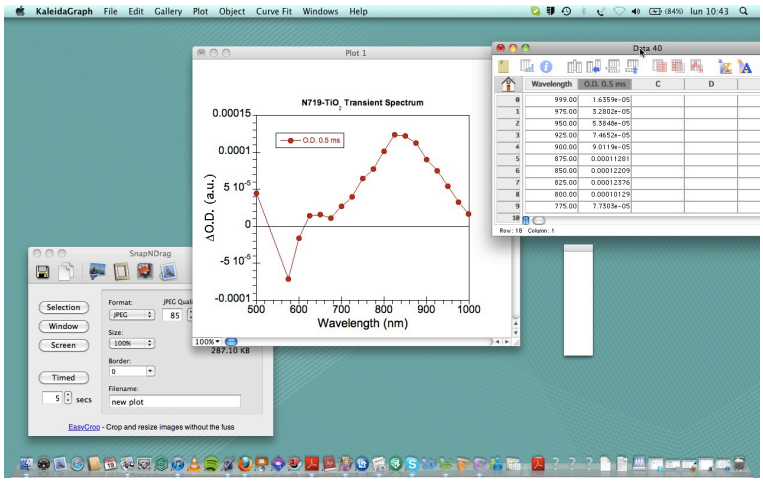

Figure A7. Final plot of a Transient spectrum.

2.- Representation of a Transient Absorption Decay

Firstly, open the selected .txt files in Kaleidagraph:

a) 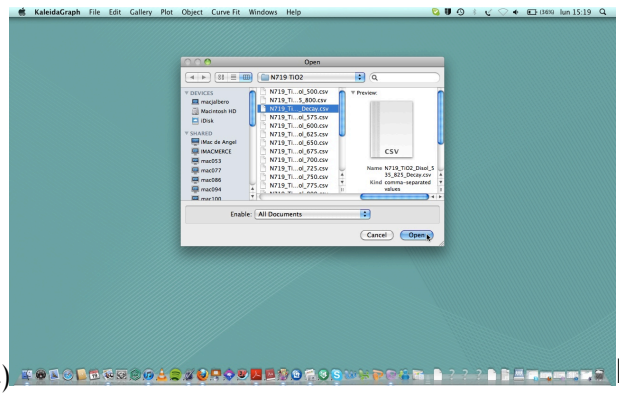 b) 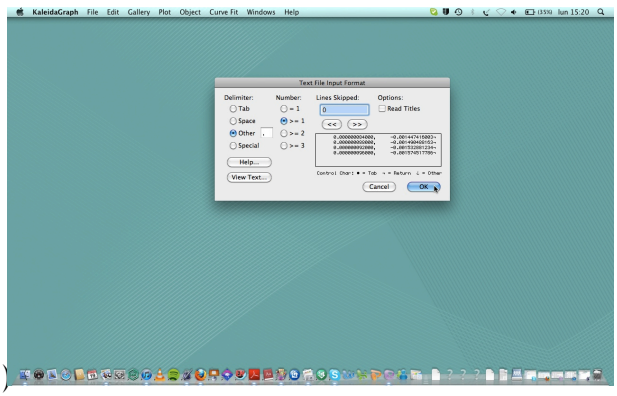

Figure A8. Opening the txt file of a transient absorption decay.

Therefore, a window with two columns will open:

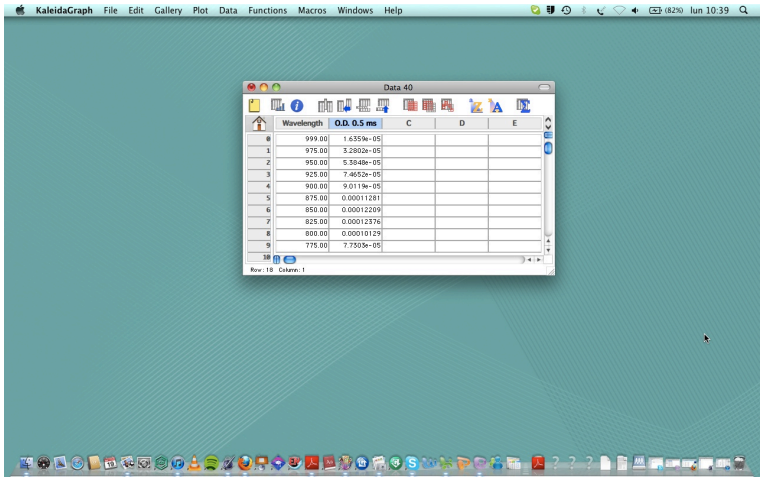

Figure A9. Table with the data extracted from the recorded decay.

Then, plot the data:

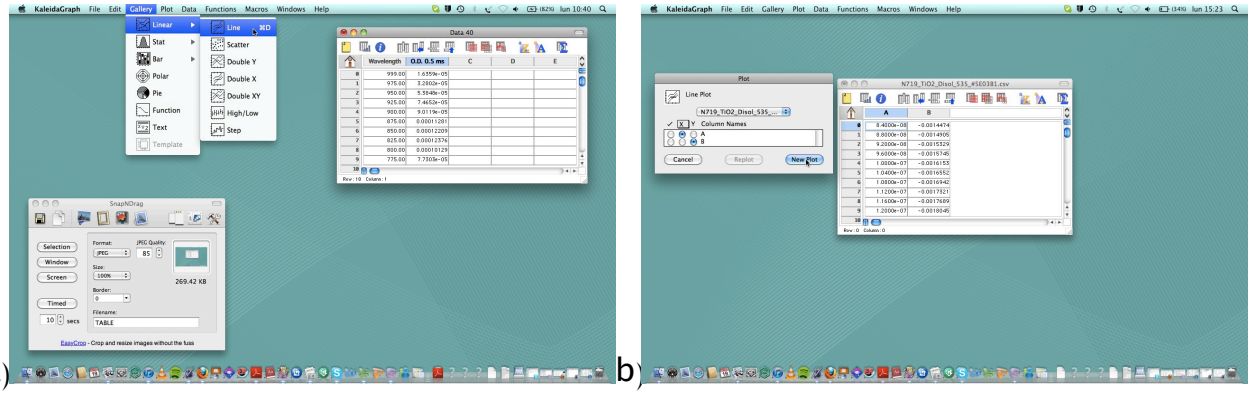

a) b)

Figure A10. Plotting the data opened in Kaleidaraph.

The x and y- axis of the obtained plot are usually plotted in linear-linear, thus, the x-axis has to be converted to log:

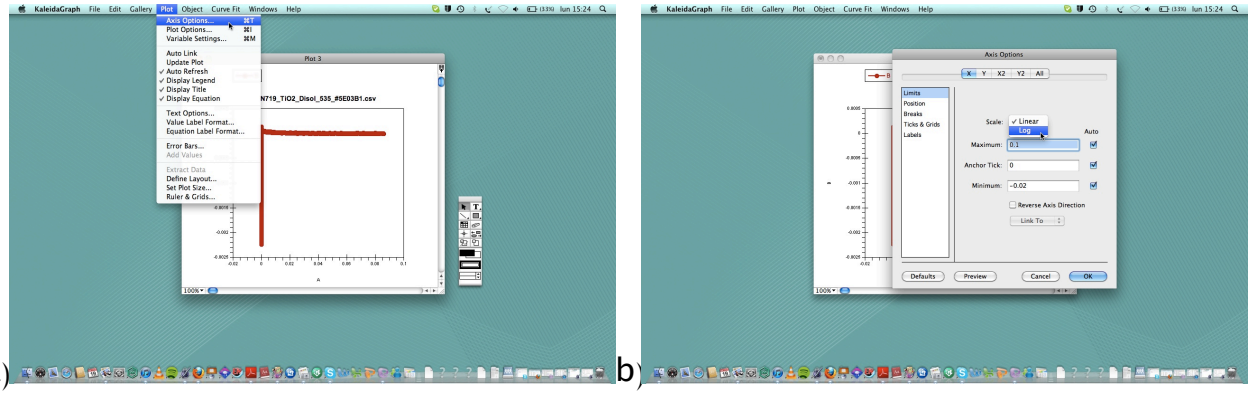

a) b)

Figure A11. Change of the x-axis from linear to log.

The obtained plot is formed by the decay and the laser rinse. This tail has to be masked, leaving the decay only. To do it, we select the proper icon and pressing continuously the alt button we select the points that we want to mask:

a) 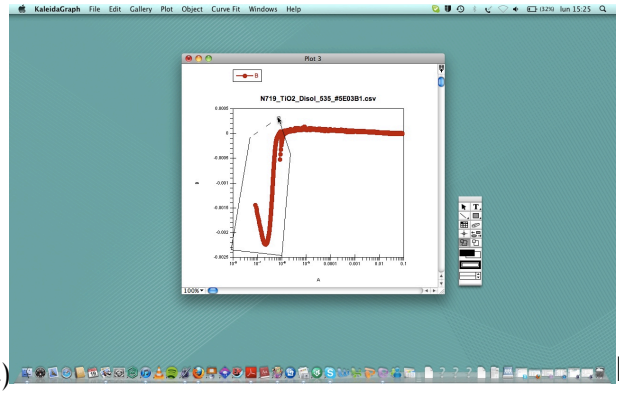 b) 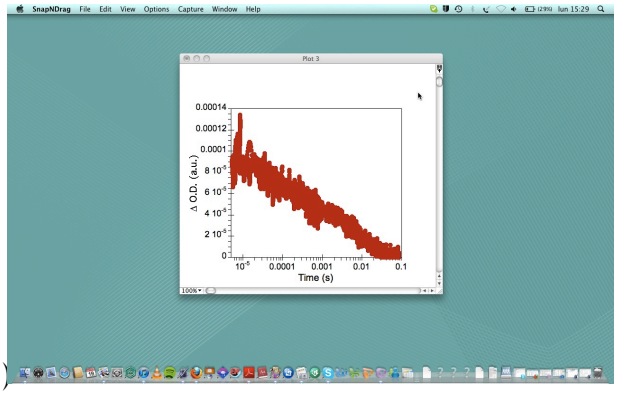

Figure A12. Erasing the tail which are not part of the decay.

Finally, the decay is usually is fitted to a function. In this case, to a Stretched Exponential function. The fitting is done as follows:

Firstly, select the function which you are going to use to fit the experimental data.

a) 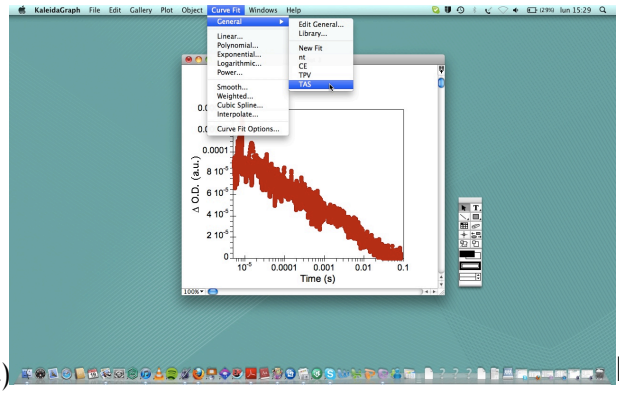 b) 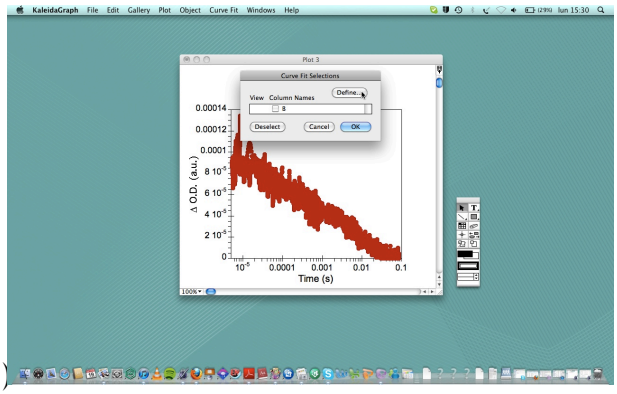

Figure A13. Fitting of a transient absorption decay to a stretch exponential function.

Notice that the function must have been previously introduced in the Kaleidagraph through Curve Fit and Edit General for the first time:

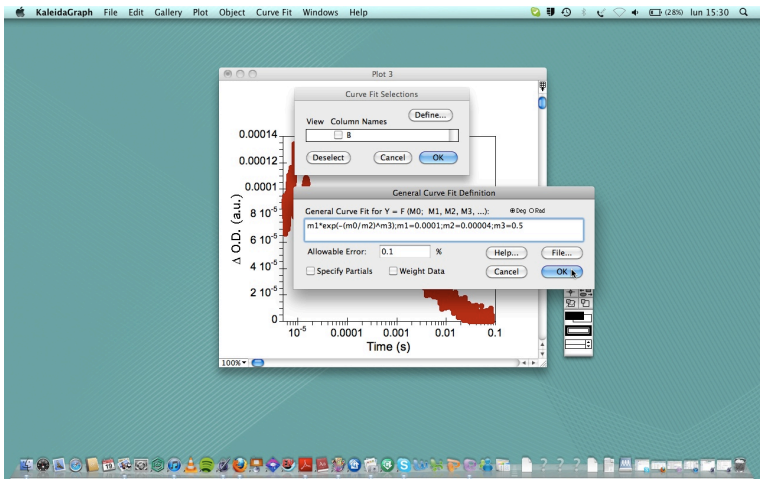

Figure A14. Defining the stretch exponential function in Kaleidagraph.

Annexes from Chapter 3

3.- Fitting an emission decay as single-exponential.

First, the desired files must be opened. Always, a window per file must be opened.

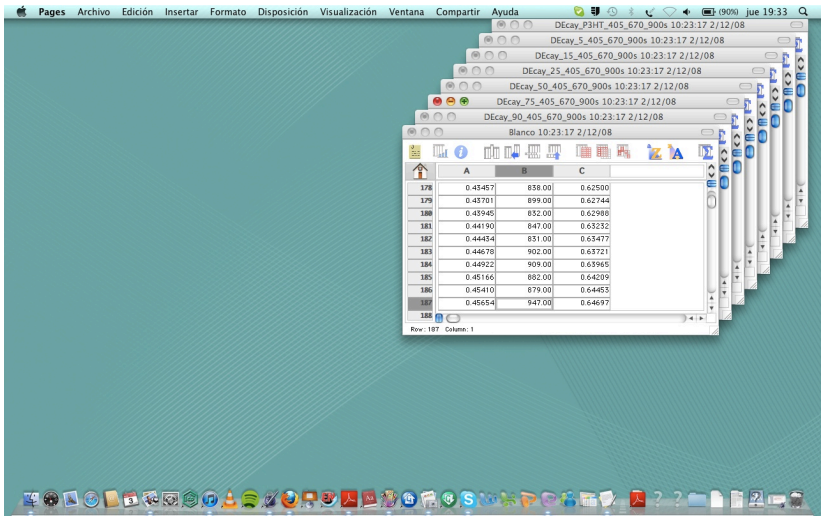

Figure A15. Tables with the data extracted from the recorded decay.

Then, select the window of the sample which we are going to calculate the emission lifetime, and mask from the table the points corresponding to the laser rise. To do that, select all the initial points up to the maximum and press the bottom for masking.

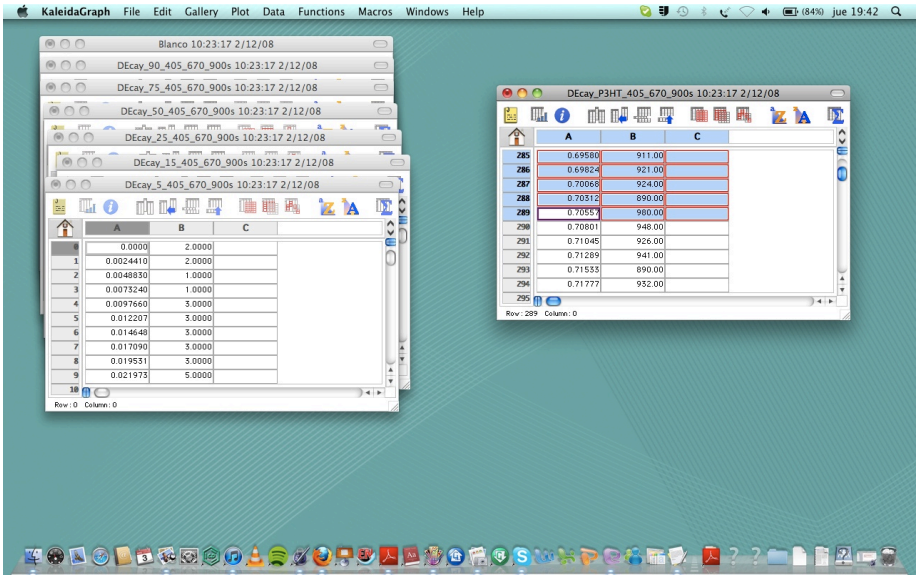

Figure A16. Masking the data corresponding to the decay rinse

Now, plot the data as it has been explained before.

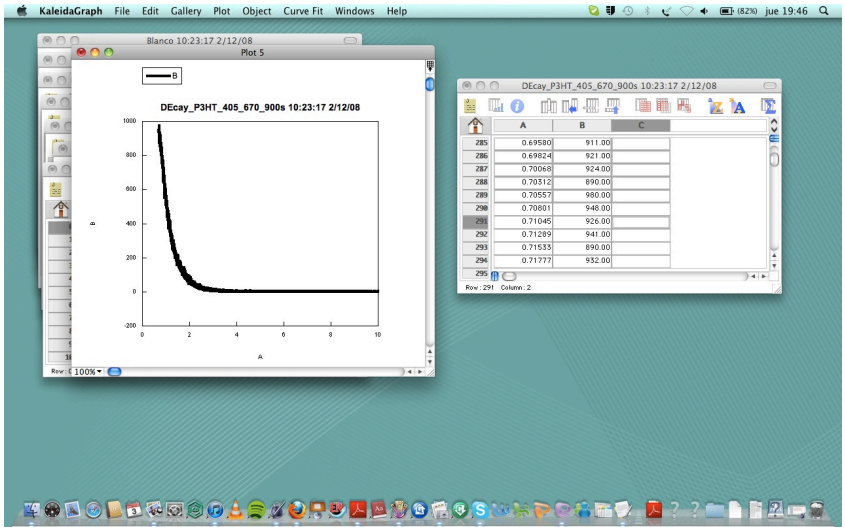

Figure A17. Plot the data after masking the non-necessary data.

Select the plot, and the option "curve fit" from the KaleidaGraph menu. Chose the function, previously edited, which contains Equation 3 from Chapter 3. The value of m2 corresponds with the emission lifetime employing Equation 3.

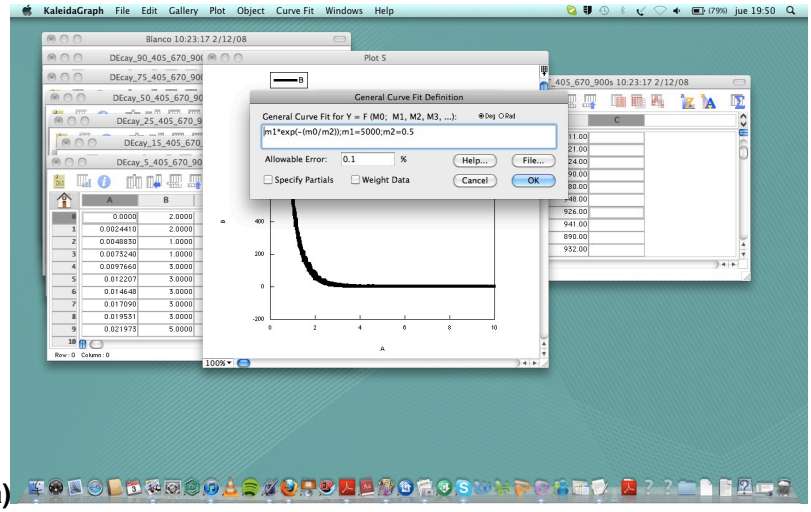

a)

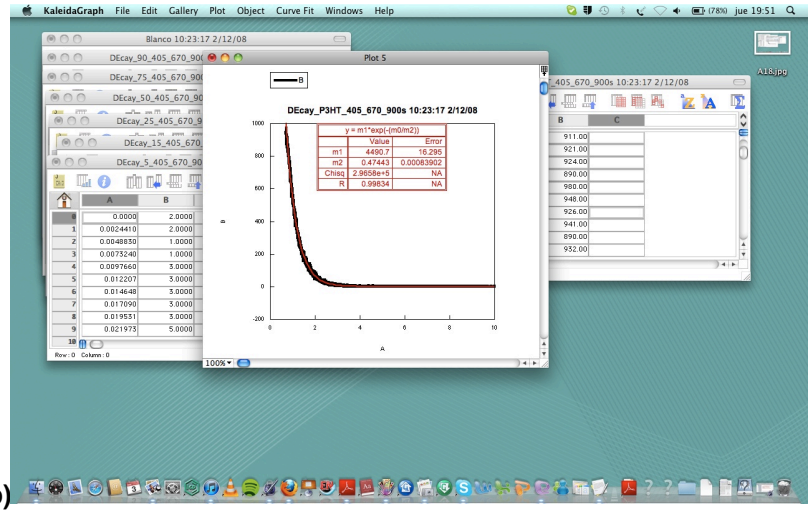

b)

Figure A18. Selection of the corresponding function (a). The result from the fitting in posted in red inside the plot (b).

4.- Calculation of the electron injection yield.

For the calculation of the injection yield, two files, corresponding to the sample reference and the one which is to be measured, must be opened. Firstly, for the reference select “Macros” in the KaleidaGraph menu. And finally select the function “Integrate”, which must be previously edited.

a)

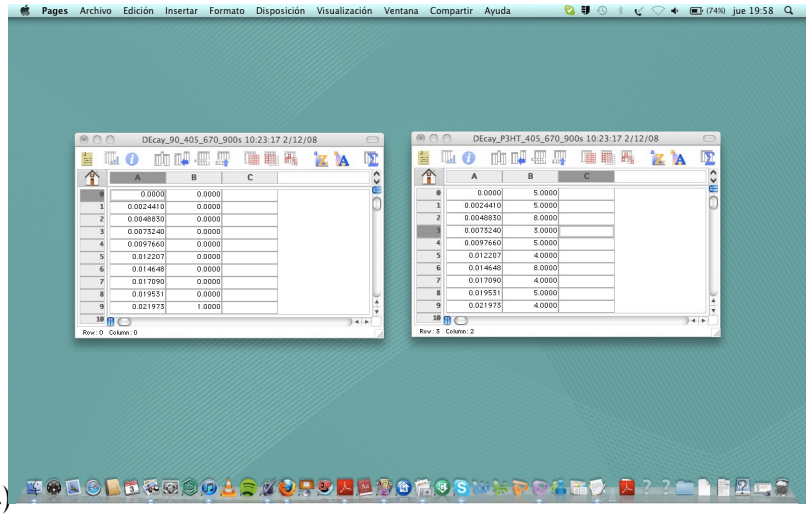

b)

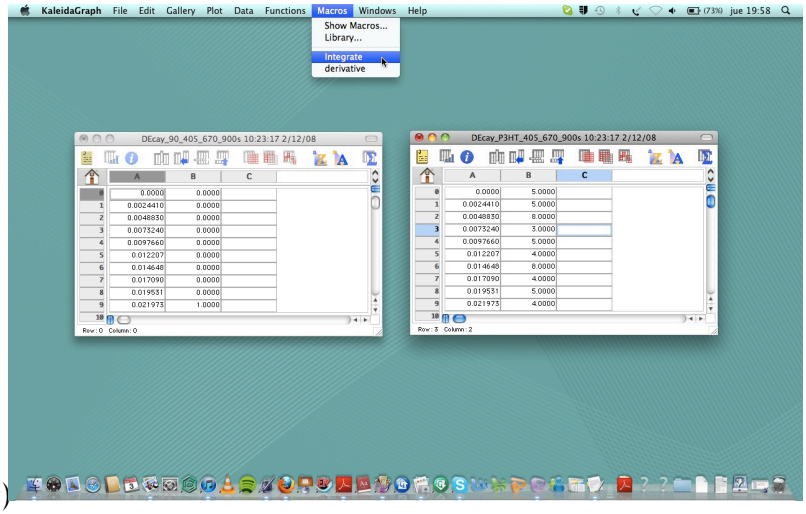

Figure A19. Files which are going to be used (a). Use of the integrate function (b).

Select the columns that are going to be used and the limits of the integration. The value of the area under the curve will appear. Save this value since it will be used later.

a)

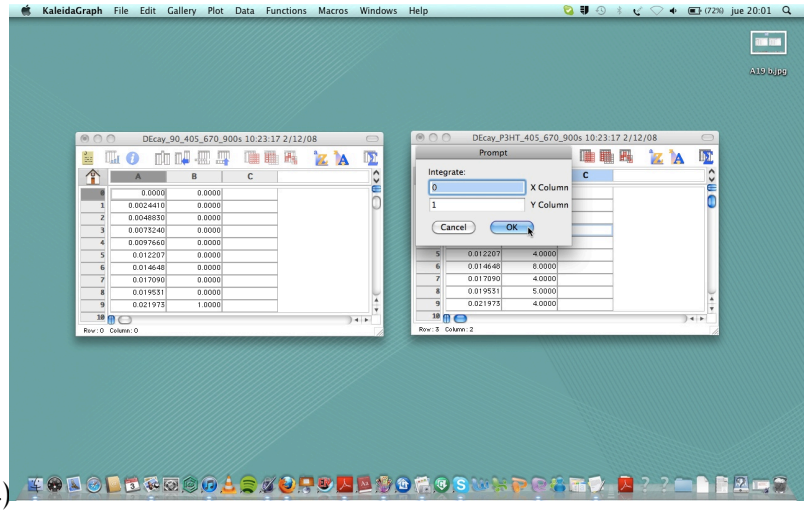

b)

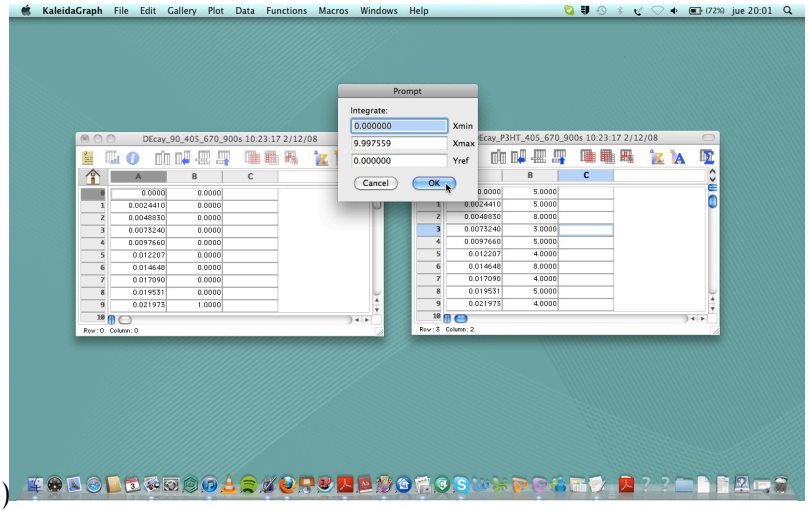

Figure A20. Selection of the suitable columns (a). Definition of the integration limits (b)

Proceed in the same way for the other data set. Finally, divide the value obtained from the sample with the one of the reference. Finally substrat this value from unit and multiply by 100 to obtain the injection yield, i.e.:

$$450/1350 = 0.33$$

$$1 - 0.33 = 0.67$$

$$0.67 \times 100 = \underline{67\%}$$

5.- Procedure for determination of electron injection kinetics.

Follow the procedure described in section 3 for estimation of emission lifetime. But in this case, fit the reference to a stretch exponential function in the same way as it has been done for the single exponential.

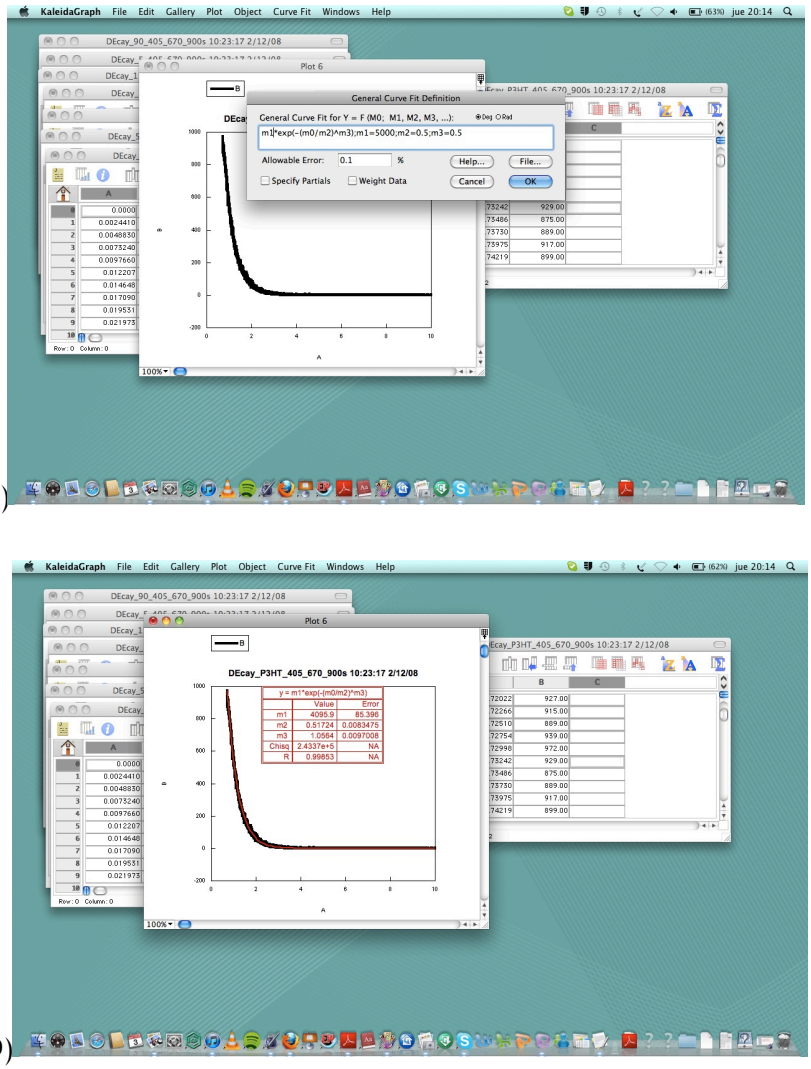

a)

b)

Figure A21. Plot the reference data (a). Fit to a stretch exponential function (b).

In this case m1 corresponds to ΔOD. Then, plot the file which sample we want to calculate the electron injection kinetics. Select “curve fit” and select the stretch exponential function. But this time we will re-define the function, fixing m1 with the value obtained from the fitting to the reference. Finally fit the curve. In this case the value of m2 corresponds to the electron injection lifetime.

a)

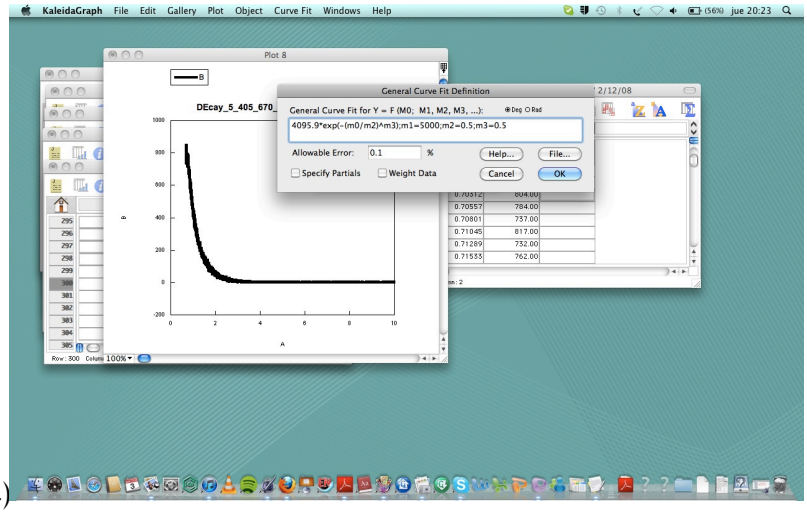

b)

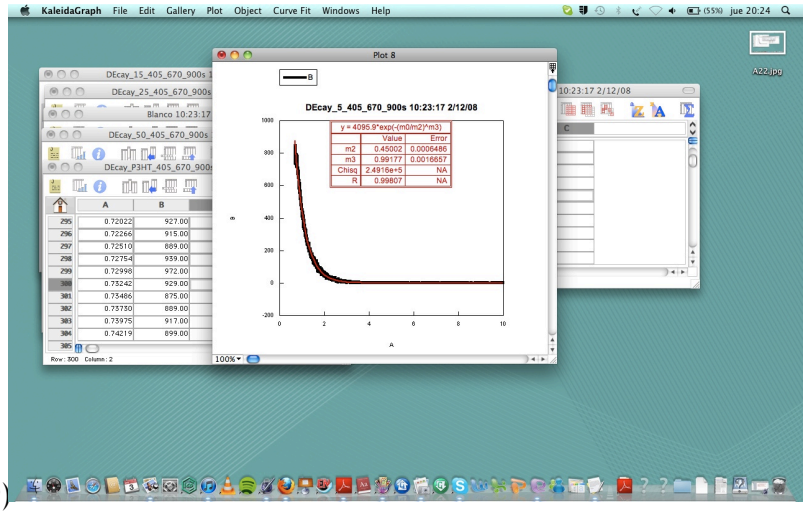

Figure A22. Plot of the investigated data (a). Fit the curve to a stretch exponential function with the parameter m1 fixed with the m1 value obtained from the reference fitting.

Annexes for Chapter 4

6. Obtaining charge density vs. light bias from charge extraction measuremetns.

To obtain the charge density from a device, charge extraction measurements are performed. This experiment generates .txt files. First step is open these files with KaleidaGraph.

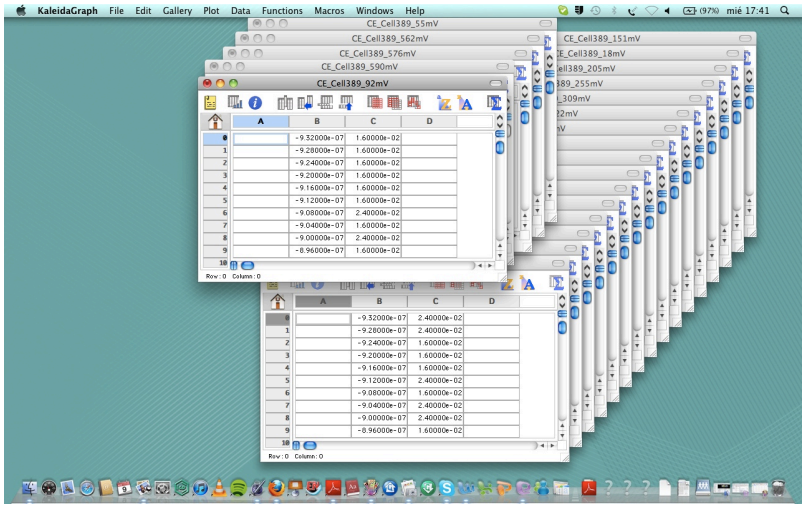

Figure A23. Files obtained from the CE technique

In a new KaleidaGraph window generate a table. The first column will contain the voltages which we have generated in the device changing the light intensity. This is directly copied from any sample. In the second column we will introduce the values obtained after integrating the voltage column. To integrate, we must select a window, and in "Macros" select integrate. This macro should have been set up previously. The integration must start at X_{Min} and Y_{Ref} =0.

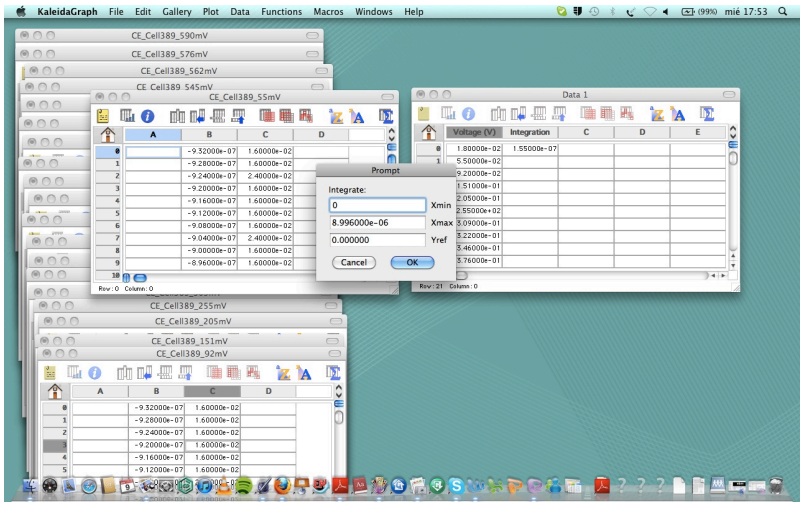

Figure A24. Integrate the voltage decay from the time of the Ce measurements.

When the second column is filled with the values of the integrals a new column is created. This new column contains the result of the subtraction of the value of the integral at V=0 from the rest of values at other V. In order to do it automatically we can create a macro. If we press button ctrl and the button F at the same time a new window it will appear.

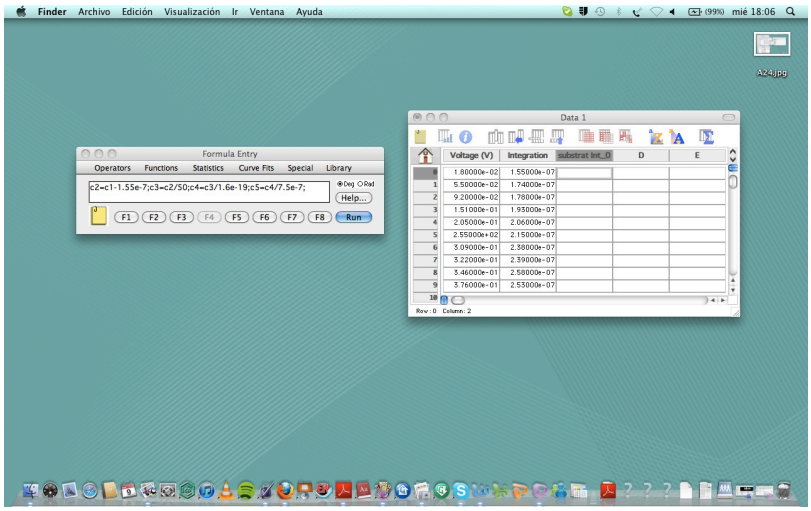

Figure A25. Program KaleidaGraph to obtain automatically charge density from the value of the integral.

If we introduce the command:

```
c2=c1-1.55e-7;c3=c2/50;c4=c3/1.6e-19;c5=c4/7.5e-7;
```

and we press run, automatically KaleidaGraph will calculate the charge density from the integral values.

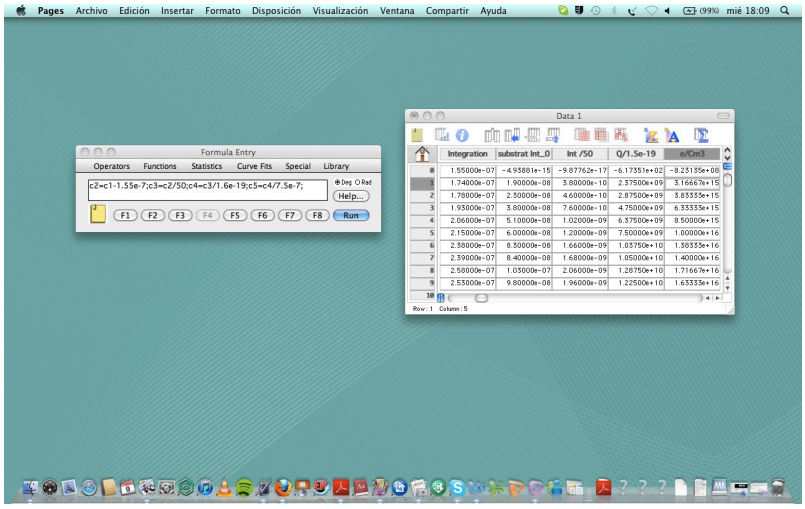

Figure A26. Complete table containing the applied bias (V), charge (Q), and charge density (e^-/cm^3).

The last generated column will correspond to the charge density. Now, we can plot the last column (n) versus of the first column (V) to obtain the desired plot.

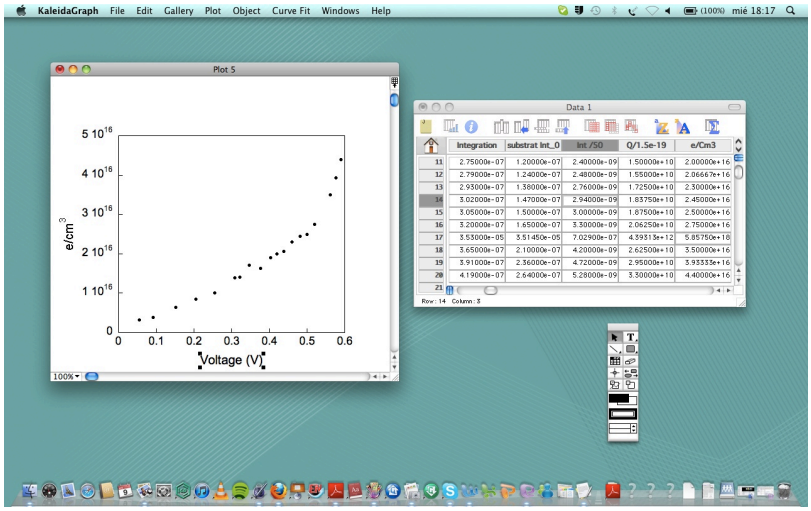

Figure A27. Plot of the chare density vs. light bias obtained from the CE technique.

The obtained points are fitted to a exponential function of the following form:

$$m1+(m2*(\exp(m3*m0))); \; m1=1e16; \; m2=1e14; \; m3=10$$

And the values from m2 and m3 correpsonds to n_0 and γ, respectively.

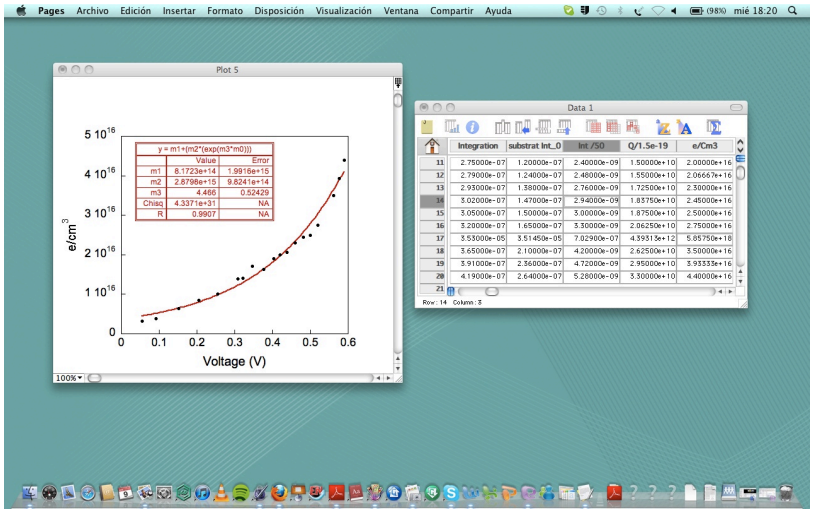

Figure A28. Fit of the experimental data to an exponential function.

7. Obtaining carrier lifetime vs. light bias.

Again, the files obtained from the TPV measurements must be opened and plotted. Then, the data coming from the laser rise must be masked. And finally, the decays must be fitted to a single exponential function of the following form:

$$m1+m2*(\exp(-(m0/m3)));m1=0.489;m2=0.002;m3=0.0001$$

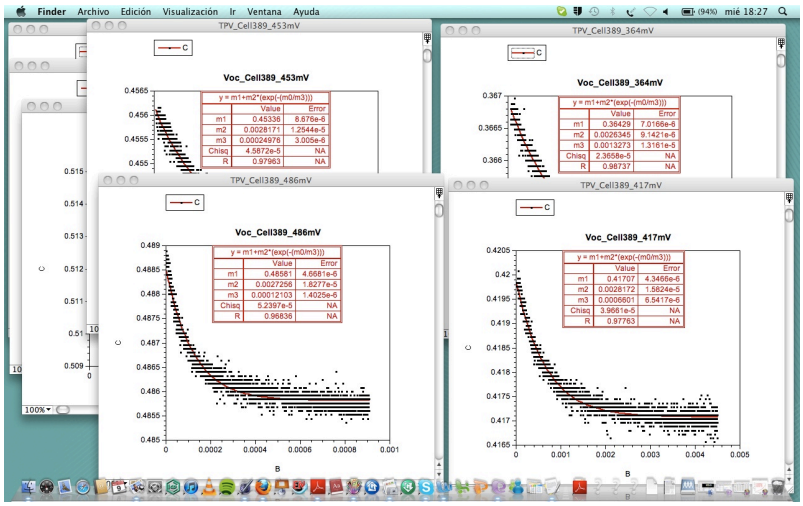

Figure A29. Fitting of the TPV decays to single exponential functions.

The m3 value corresponds to the carrier lifetime for each light bias. Now, we build a table with the values of the measured applied bias and the values obtained from the fitting lifetimes. Then, with the values of the exponential fit of the charge extraction we can convert the applied bias to charge density for this device. Finally, with this data we can plot the values of carrier lifetime vs applied bias or charge density, and fit the carrier lifetime vs. light bias with an exponential and the carrier lifeitme vs. charge density to power law functions, respectively.

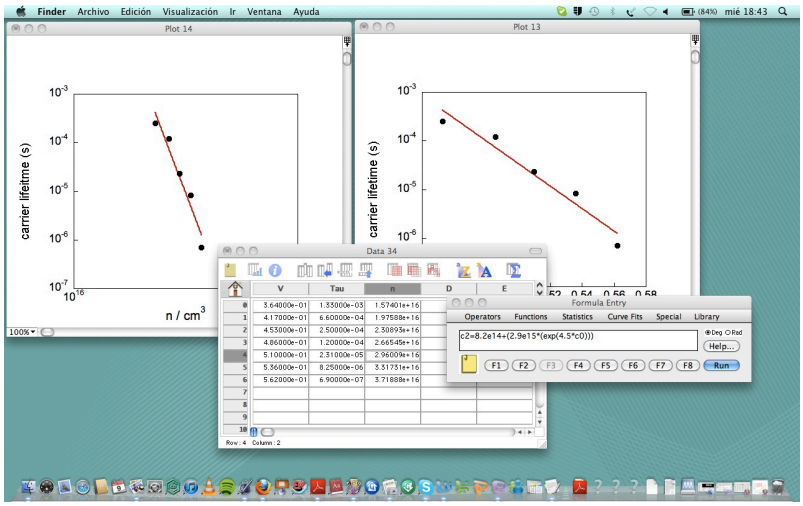

Figure A30. Plot of carrier density vs light bias or charge density.

Annexes

Annexes II

Contributions to the Scientific Community.

Publications related with this Thesis:

Photo-induced charge recombination kinetics in low bandgap PCPDTBT polymer:CdSe quantum dots bulk heterojunction solar cells. Albero, Josep; Zhou, Yunfei; Eck, Michael; Rauscher, Frank; Niyamakom, Phenwisa; Dumsch, Ines; Allard, Sybille; Scherf, Ullrich; Krueger, Michael; Palomares, Emilio.

Chemical Science, **2011**, 2(12), 2396-2401.

Interfacial charge transfer dynamics in CdSe/dipole molecules coated quantum dot polymer blends. Albero, Josep; Martínez-Ferrer, Eugenia; Iacopino, Daniela; Vidal-Ferran, Anton; Palomares, Emilio.

Physical Chemistry Chemical Physics, **2010**, 12(40), 13047-13051.

Materials, Nanomorphology, and Interfacial Charge TRansfer Reactions in Quantum Dot/Polymer Solar Cell Devices. Martinez-Ferrero, Eugenia; Albero, Josep; Palomares, Emilio.

The Journal of Physical Chemistry Letters, **2010**, 1(20), 3039-3045.

Quantum Dot-dye Bilayer-Sensitized Solar Cells: Breaking the Limits Imposed by the Low Absorbance of Dye Monolayers. Shalom, Menny; Albero, Josep; Tachan, Zion; Martinez-Ferrero, Eugenia; Zaban, Arie; Palomares, Emilio.

The Journal of Physical Chemistry Letters, **2010**, 1(7), 1134-1138.

Fast regeneration of CdSe quantum dots by Ru dye in sensitized TiO_2 electrodes. More-Sero, Ivan; Likodimos, Vlassis; Gimenez, Sixto; Martinez-Ferrero, Eugenia; Albero, Josep; Palomares, Emilio; Kontos, Athanassios G.; Falaras, Polycarpos; Bisquert, Juan.

The Journal of Physical Chemistry C, **2010**, 114(14), 6755-6761.

Charge transfer kinetics in CdSe quantum dot sensitized solar cells. Martinez-Ferrero, Eugenia; Sero, Ivan Mora; Albero, Josep; Gimenez, Sixto; Bisquert, Juan; Palomares, Emilio.

Physical Chemistry Chemical Physics, **2010**, 12(12), 2819-2821.

Photo-induced electron recombination dynamics in CdSe/P3HT hybrid heterojunctions. Albero, Josep; Martinez-Ferrero, Eugenia; Ajuria, Jon; Waldauf, Christoph; Pacios, Roberto; Palomares, Emilio.

Physical Chemistry Chemistry Physics, **2009**, 12(42), 9644-9647.

Publications not related with this Thesis:

Influence of P3HT:PCBM blend preparation on the active layer morphology and cell degradation. Balderrama, Victor S.; Estrada, Magali; Cerdeira, Antonio; Soto-Crauz, B. S.; Marsal, Lluis F.; Pallares, Josep; Nolasco, J. C.; Iñiguez, Benjamin; Palomares, Emilio; Albero, Josep;

Microelectronics Reliability, **2011**, 51(3), 597-601.

Mercury optical fiber probe based on a modified cladding of sensitized Al_2O_3 nano-particles. Perez-Hernandez, Javier; Albero, Josep; Llobet, Eduard; Correig, Xavier; Matias, Ignacio R.; Arregui, Francisco J.; Palomares, Emilio.

Sensors and Actuators, B: Chemical, **2009**, B143(1), 103-110.

Structure-Function Relationships in Unsymmetrical Zinc Phthalocyanines for Dye-Sensitized Solar Cells. Cid, Juan-Jose; Garcia-Iglesias, Miguel; Yum, Jun-Ho; Forneli, Amparo; Albero, Josep; Martinez-Ferrero, Eugenia; Vazquez, Purificacion; Graetzel, Michael; Nazzeruddin, Mohammad K.; Palomares, Emilio; Torres, Tomas.

Chemistry: A European Journal, **2009**, 15(20), 5130-5137.

Diastereoselectivity and molecular recognition of mercury(II) ions. Reynal, Anna; Albero, Josep; Vidal-Ferran, Anton; Palomares, Emilio.

Inorganic Chemistry Communications, **2009**, 12(2), 131-134.

Multivariable calibration anaysis of colorimetric mercury sensing using a molecular probe. Perez-Hernandez, Javier; Albero, Josep; Correig, Xavier; Llobet, Eduard; Palomares, Emilio.

Analytica Chimica Acta, **2009**, 633(2), 173-180.

Catalysis of recombination and its limitation on open circuit voltage for dye sensitized photovoltaic cells using phthalocyanine dyes. O'Regan, Brian; Lopez-Duarte, Ismael; Martinez-Diaz, M. Victoria; Forneli, Amparo; Albero, Josep; Morandeira, Ana; Palomares, Emilio; Torres, Tomas; Durrant, James R.

Journal of the American Chemical Society, **2008**, 130(10), 2906-2907.

Annexes

Annexes